2D and Quasi-2D Perovskites for Optoelectronic Devices

2D and Quasi-2D Perovskites

for Optoelectronic Devices

PROEFSCHRIFT

ter verkrijging van de graad van doctor aan de Technische Universiteit Eindhoven, op gezag van de rector magnificus prof.dr. S. Lenaerts, voor een commissie aangewezen door het College voor Promoties, in het openbaar te verdedigen op dinsdag 27 juni 2023 om 11:00 uur

door

Alessandro Caiazzo

geboren te Villaricca, Italië

Dit proefschrift is goedgekeurd door de promotoren en de samenstelling van de promotiecommissie is als volgt:

voorzitter: prof. dr. ir. R. P. Sijbesma
1^e promotor: prof. dr. ir. R. A. J. Janssen
copromotor: dr. ir. M. M. Wienk
leden: prof. dr. G. Grancini (University of Pavia)
         prof. dr. M. Morales-Masis (Universiteit Twente)
         prof. dr. A. P. H. J. Schenning
         prof. dr. D. Vanderzande (Universiteit Hasselt)

2D and Quasi-2D Perovskites

for Optoelectronic Devices

Table of contents

1

Introduction

1.1 MATERIALS OF THE FUTURE

Materials science has been important to humans since prehistoric times.[1,2] From the development of bronze and iron metallurgy in ancient civilizations to the development of, among others, polymers, composites, ceramics, biomaterials, and semiconductors in modern societies, the discovery of new, more advanced materials has enabled steps forward in a variety of fields, such as technology, transportation, construction, and manufacturing.[1,2] Today, research on materials science is more active than ever. Notable examples are metamaterials, engineered such that the interaction with light is artificially tuned, leading to beyond-nature properties such as negative refraction,[3] or superconductors, which power MRI machines and particle accelerators worldwide and have the potential to revolutionize power transmission.[4,5] Countless others are currently being researched and tested, such as materials for energy storage and generation,[6–8] biobased and recyclable plastics,[9] stimuli-responsive materials,[10] 2D materials.[11]

New materials for renewable energy generation will shape the future of an ever-growing energy-demanding world. It has been unequivocally demonstrated that human activities have contributed to climate change through greenhouse gas emissions, and a drastic switch to renewable energy is needed to limit the impact of climate change on our lives and the environment.[12] The net-zero emissions scenario proposed by the International Energy Agency states that solar installations should grow by 630 GW per year in this decade, which corresponds to installing one solar park every day that is the size of the world's current largest solar park.[12] Only part of this scenario (up to 2030) includes technologies already available on the market, while the remaining parts require technologies that are still in development or in research.[12] Thus, developing new semiconductor materials for solar energy generation is going to play a crucial role in how we achieve net-zero emissions.

For many years now, silicon has been the material of choice for solar cells.[13] Its price has been relatively low thanks to government subsidies and sometimes immoral practices related to cheap energy and labor.[14] In fact, the fabrication of silicon solar cells is an energy-intensive process that requires high temperatures. To keep prices low, a cheap source of energy –often coal– and a cheap source of labor are required. For silicon solar cells, modules represent roughly only 30% of the costs, while another 40% is made up of the so-called balance of system (BOS) costs that scale with the area of the photovoltaic installation.[15] This means that improvements in module efficiency are highly desired, as they would decrease BOS costs due to enhanced energy yield per unit area.[15] However, the power-conversion efficiency of silicon solar cells is particularly close to the detailed-balance limit,

which defines the maximum achievable efficiency for a semiconductor of a specific bandgap.[13,16] As a result, improvements in silicon solar cells in terms of cost are difficult to achieve with enhanced efficiency, and efforts have been focused on alternative semiconductor materials. Organic and metal halide perovskite solar cell research have made giant steps in recent years, with organic solar cells now reaching >18% and perovskite solar cells >25% efficiency.[17] These technologies have become possible competitors of silicon or even possible additions to silicon, thanks to multi-junction devices that can break the detailed-balance limit and reach >30% power-conversion efficiency, as will be described below.[18,19]

1.2 ORGANIC–INORGANIC HYBRID PEROVSKITES

Organic–inorganic hybrid halide perovskites have attracted a great deal of interest in recent years because of their exceptional optoelectronic properties and bandgap tunability.[18,20,21] When perovskites are mentioned in newspapers, it is not uncommon to read about a "miracle material".[22] Although this is quite amusing for researchers, perovskites really are a fascinating material to work with. They have been used in a plethora of applications, going from the most common solar cells to light-emitting diodes (LEDs), photodiodes, and X-Ray detectors.[23–27] With regards to solar cells, as shown in **Figure 1.1**a, perovskites recently reached 25.7% efficiency, on the verge of surpassing silicon solar cells (26.1%).[17] Less than ten years ago, in 2013, perovskite solar cells reached an efficiency of only 14%. What took only 9 years for perovskites –an increase of about 11% efficiency–, took 40 years for silicon.[17] The easy bandgap tunability makes perovskites suitable also for multi-junction devices, where semiconductor films with complementary absorption profiles are stacked on top of each other to reduce thermalization losses and drastically enhance efficiency.[18] Recently, a perovskite/silicon tandem has reached 33.7% record efficiency and, once more, perovskites have made it to the news as the miracle material that will shape the future of solar energy (Figure 1.1a).[17,28]

With regards to other optoelectronic devices: LEDs based on such material have recently reached above 25% external quantum efficiency,[24] whereas photodiodes are almost comparable in their detectivity to silicon and organic ones.[29,30]

The crystal structure of perovskites is described by the formula ABX_3. In organic-inorganic hybrid structures, A is an organic cation, such as formamidinium (FA) or methylammonium (MA), B is usually lead (Pb) or tin (Sn), and X is a halide ion, such as iodide (I) or bromide (Br) (Figure 1.1b).[20] In this work, ABX_3 structures will be referred to as 3D perovskites, because they grow in a three-dimensional octahedral framework. The choice of the A cations is dictated mostly by geometric factors, as they need to be of the right size to fit in the octahedral voids. This is well-described

by the tolerance factor, which is a function of the ionic radii of A, B, and X, and needs to be between 0.8 and 1 to obtain a perovskite in the photoactive α-phase.[31] When the tolerance factor is 1, the perovskite crystal structure in α-phase possesses a cubic symmetry, whereas it is distorted and in tetragonal or orthorhombic structures with lower tolerance factors.[31,32]
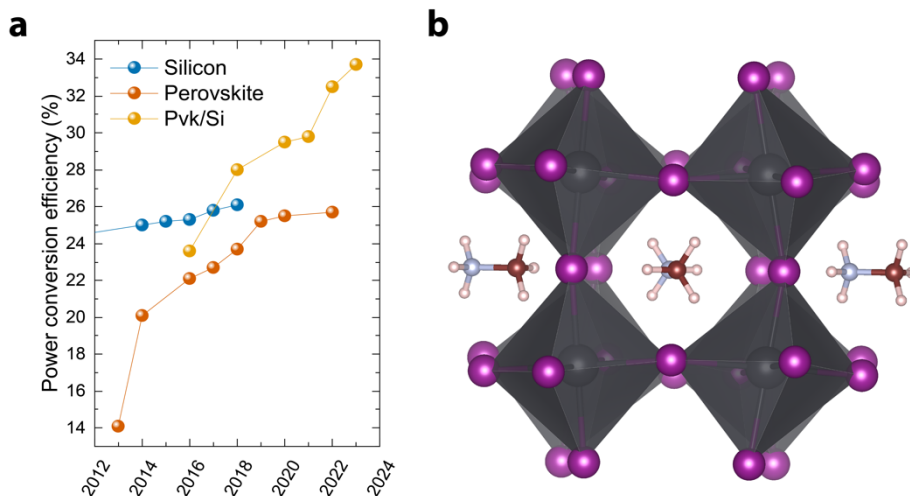
Figure 1.1. (a) Power conversion efficiency over time for silicon, perovskite, and silicon/perovskite solar cells. (b) ABX$_3$ crystal structure of an organic-inorganic hybrid perovskite (MAPbI$_3$). Color scheme: grey = lead, blue = carbon, white = hydrogen, purple = iodine, red = nitrogen.

Perovskite solar cells with the highest efficiency are obtained by using a FAPbI$_3$ composition, which allows for a bandgap energy of about 1.45 eV and – consequently– they could reach a maximum theoretical efficiency of about 32% according to the detailed-balance limit.[16] However, fabrication of FA-only perovskites has been a difficult journey, as FAPbI$_3$ tends to form a photoinactive yellow δ-phase and only reversibly converts to α-phase at 150 °C.[26,33–35] Additive engineering has proved to be crucial in this field, and nowadays photoactive FAPbI$_3$ films can be made by using additives, such as methylammonium chloride, which induce a slight octahedral tilting that inhibits conversion to δ-phase.[36] As shall be seen throughout this work, additive- and solvent-engineering have been and still are crucial to exploit the tunable properties of perovskites. A deep understanding of materials properties and crystallization mechanism will likely provide further enhancements and discoveries. For instance, a recent, insightful study on the phase evolution of FAPbI$_3$ from δ– to α–phase showed that enhancing crystal quality by slowly controlling the crystallization can have an important impact on phase stability.[37] Even the different facets of FAPbI$_3$ crystals, namely (100) and (111),

possess different degradation paths, thus inhibiting (100) facet formation *via* additive engineering has been shown to be beneficial for the stability of FAPbI$_3$ films.[38]

The focus on stability originates from the fact that traditional 3D perovskite films and devices suffer from a variety of degradation problems, which can be either intrinsic or extrinsic in nature. Intrinsically, metal halide perovskites are soft materials in which structural defects, such as vacancies, interstitials, and anti-sites, may form and in which grain boundaries exist. Specifically, ion migration under electrical bias, light-induced halide segregation, or elevated temperatures may deteriorate the quality of the semiconductor.[39–41] Extrinsic factors that can influence metal halide perovskites are oxygen and humidity. Common strategies to enhance stability involve passivation of device interfaces with capping layers, improvements of crystal quality, and encapsulation. For multi-junction devices, stability concerns become even more numerous, possible problems being –among others– brittleness, thermal expansion mismatch with silicon, and phase segregation for wide bandgap perovskites.[15] Mostly driven by enhancement in stability, researchers have recently started to explore lower-dimensional modifications of the ABX$_3$ framework, providing significant advancement to the field of so-called 2D perovskites.

1.3 2D AND QUASI-2D PEROVSKITES

The A-site in an ABX$_3$ structure imposes strict limitations on the type of organic cation that can be used to make an organic–inorganic hybrid perovskite structure. When using a bulkier organic cation (from here on, spacer) that does not fit in the octahedral void, a whole new class of lower-dimensional perovskites are formed, among which the most popular are quantum dots (0D) and 2D perovskites.[42–44]

$n = 1$ $n = 2$ $n = 3$ 3D
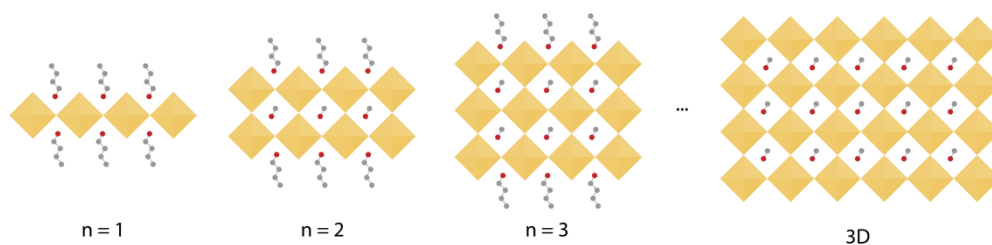
Figure 1.2. Illustration of 2D and quasi-2D perovskite crystal structures. A number of octahedral sheets (*n*) are sandwiched between a bulky organic spacer, such as butylammonium.

A 2D perovskite (**Figure 1.2**) consists of a layer of inorganic lead iodide octahedra sandwiched between bulky organic spacers, such as butylammonium (BA), phenethylammonium (PEA), or even more exotic species.[45,46] Although they are obviously still three-dimensional in nature, it is the layered structure that gives such

perovskites a "2D" nomenclature. By changing the number of layers (n) in between spacers, namely by mixing the inorganic source (*i.e.*, PbI_2) with an organic cation (*i.e.*, MA) and a spacer (*i.e.*, BA), quasi-2D perovskites are obtained. A quasi-2D perovskite possesses a small number of inorganic layers (usually between 2 and 5) between the organic spacers (Figure 1.2). The chemical formula of such 2D and quasi-2D structures is $(R)_i A_{n-1} B_n X_{3n+1}$, where R is the bulky organic spacer. With a monovalent ammonium spacer, $i = 2$ (Ruddlesden-Popper phase, RP), whereas with a divalent ammonium spacer $i = 1$ (Dion-Jacobson phase, DJ).

Overall, the change of dimensionality can be seen as an additional level of tunability of perovskites, which can be exploited by researchers for new applications. To add more complexity, 2D perovskites themselves possess a high degree of tunability because 1) there is virtually unlimited choice of organic spacers that make the crystal structure,[45] and 2) by changing the number of layers in between the spacers, the so-called n–value, the optoelectronic and physical properties of the material can be changed.[47] For example, the bandgap energy of 2D and quasi-2D perovskites decreases with increasing n, going from 2.3 eV for an $n = 1$ to 1.55 eV for a 3D perovskite ($n = \infty$). Other quantities, such as exciton binding energy, crystal orientation, and more importantly stability, change going from 2D to quasi-2D and to 3D.[48–50] 2D perovskites are well known to possess higher stability towards humidity, heat, and even light compared to their 3D counterpart.[51] For a more complete introduction to 2D and quasi-2D Ruddlesden-Popper perovskites, we refer the reader to Chapter 2.1. There, an in-depth analysis of RP perovskites is given, with a particular focus on stability, crystal orientation, and a peculiar phenomenon of phase distribution, which involves the formation of multiple quasi-2D structures (with different value of n) during crystallization.

2D and quasi-2D perovskites can be used as a photoactive layer in solar cells,[52] photodiodes,[29,53–56] or LEDs[23,24,57,58]. However, with regards to solar cells, they have mostly been used for passivation purposes.[59–62] The interfaces between perovskite and electron- and hole-transport material represent a crucial source of recombination losses in a perovskite solar cell, thus passivating such interfaces with another material has become a routine method to improve performance.[63,64] Two related passivation strategies can be distinguished that are commonly used for this purpose; one that forms a thin layer of 2D on top of a 3D perovskite (**Figure 1.3**) and one that uses organic cations as passivating agents without forming a 2D structure. Presently, virtually every high-efficiency solar cell contains a lower-dimensional passivation layer.[26,61,65,66] Once more, understanding the formation mechanism of 2D/3D heterostructures is crucial to fully exploit the passivation properties of 2D perovskites. 2D interlayers are usually solution-processed from isopropanol, with the

organic cations either reacting with excess PbI_2 or replacing the A^+ cation in the perovskite lattice. This reaction usually leads to a 2D/3D heterostructure without control on thickness and homogeneity. However, in recent studies, such interlayers have been processed on top of 3D films *via* hot–press or by using solvents that are incompatible with 3D perovskites, hence showing the possibility to form well-defined and tunable 2D/3D heterostructures.[61,67] Furthermore, because of energy alignment reasons, 2D interlayers have been traditionally most common in solar cells with *n–i–p* configuration, where the perovskite film is processed on top of an electron-transport layer. A fine control of the *n*-value in (quasi-)2D interlayers, again thanks to a sapient use of solvent engineering, has made it possible to exploit the passivation properties of lower-dimensional perovskites also in *p–i–n* cells, which are more suitable for multi-junction devices.[66]
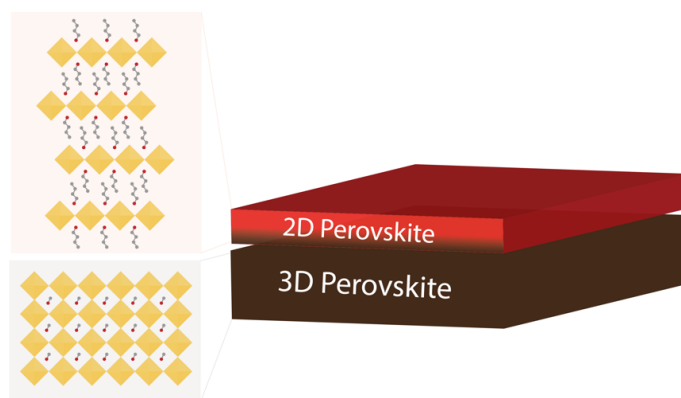
Figure 1.3. Schematic illustration of a 2D/3D heterostructure.

1.4 AIM, CONTENT, AND STRUCTURE OF THIS THESIS

The aim of this work is to explore 2D and quasi-2D perovskites and integrate them in optoelectronic devices, such as solar cells or photodiodes. The approach behind this thesis is to first understand and then apply. The crystallization mechanism of such quasi-2D perovskites, for instance, is important with regards to tuning their phase distribution. As a result, a few chapters are dedicated to understanding the crystallization pathway and then to the application of this knowledge in devices. Main questions that this work tries to answer are related to the phase distribution and purity of quasi-2D perovskites, to their stability under illumination in view of the application of such materials in multijunction solar cells, to the possibility to exploit bandgap graded structures for photodiodes, and to the nature of 2D/3D heterostructures that are so important for high efficiency devices.

This work contains lots of information; reading all of it in one go is virtually impossible. Because of this, every Chapter is intended to be a stand-alone read.

Different chapters will contain introduction sections that will mention–and sometimes repeat–all that is needed to understand the experimental results. The reader is hence encouraged to read what they find most interesting.

Chapter 1 is a general introduction to materials science and perovskites and contains a general outline and introduction to this work. Chapter 2 is a published literature review about high efficiency solar cells based on quasi-2D perovskites. The review contains a detailed introduction to quasi-2D Ruddlesden-Popper perovskites. It is followed by a description of additives and fabrication methods that are relevant to achieve high efficiency devices; mind that this second part does not involve any experimental result performed within this work. Chapter 3 describes the effect of co-solvents on phase distribution and crystallization of quasi-2D perovskites. Chapter 4 digs deeper into the fascinating crystallization mechanism of Ruddlesden-Popper perovskites and introduces the concept of reverse-graded quasi-2D perovskite films. Based on the solvent engineering and the understanding of the crystallization mechanism developed in Chapters 3 and 4, quasi-2D perovskite films with finely-tuned phase distributions were used in Chapters 5 and 6 to fabricate photodiodes with low dark-current and to study halide segregation. As any perovskite researcher also needs high efficiency devices to boost their mood; Chapter 7 describes FAPbI$_3$-based solar cells, largely improved by a benzotriazole-based 2D passivation layer.

A summary, followed by my curriculum vitae, scientific contributions, and acknowledgments–by far the most read and fun part of any PhD thesis–, will conclude this work.

1.5 REFERENCES

[1] "Materials Science," can be found under https://www.newworldencyclopedia.org/entry/Materials_science.
[2] "History of materials science," can be found under https://en.wikipedia.org/wiki/History_of_materials_science.
[3] "Explaining metamaterials and metasurfaces – properties and applications," can be found under https://www.nanowerk.com/what-are-metamaterials.php.
[4] "Superconductivity: What Is It and Why It Matters to Our Future," can be found under https://interestingengineering.com/science/superconductivity-what-is-it-and-why-it-matters-to-our-future, **2019**.
[5] "Physicists hunt for room-temperature superconductors that could revolutionize the world's energy system," can be found under https://theconversation.com/physicists-hunt-for-room-temperature-superconductors-that-could-revolutionize-the-worlds-energy-system-80707, **2020**.
[6] A. S. R. Bati, Y. L. Zhong, P. L. Burn, M. K. Nazeeruddin, P. E. Shaw, M. Batmunkh, *Commun. Mater.* **2023**, *4*, 2.
[7] I. Massiot, A. Cattoni, S. Collin, *Nat. Energy* **2020**, *5*, 959.
[8] T. Leijtens, K. A. Bush, R. Prasanna, M. D. McGehee, *Nat. Energy* **2018**, *3*, 828.
[9] J. M. Garcia, M. L. Robertson, *Science* **2017**, *358*, 870.

[10] X. Kuang, D. J. Roach, J. Wu, C. M. Hamel, Z. Ding, T. Wang, M. L. Dunn, H. J. Qi, *Adv. Funct. Mater.* **2019**, *29*, 1805290.

[11] N. R. Glavin, R. Rao, V. Varshney, E. Bianco, A. Apte, A. Roy, E. Ringe, P. M. Ajayan, *Adv. Mater.* **2020**, *32*, 1904302.

[12] International Energy Agency, *Net Zero by 2050 - A Roadmap for the Global Energy Sector*, **2021**.

[13] L. C. Andreani, A. Bozzola, P. Kowalczewski, M. Liscidini, L. Redorici, *Adv. Phys. X* **2019**, *4*, 1548305.

[14] M. Shellenberger, "China Helped Make Solar Power Cheap Through Subsidies, Coal And Allegedly, Forced Labor," can be found under https://www.forbes.com/sites/michaelshellenberger/2021/05/19/china-made-solar-cheap-through-coal-subsidies--forced-labor-not-efficiency/, **2021**.

[15] L. Duan, D. Walter, N. Chang, J. Bullock, D. Kang, S. P. Phang, K. Weber, T. White, D. Macdonald, K. Catchpole, H. Shen, *Nat. Rev. Mater.* **2023**, DOI 10.1038/s41578-022-00521-1.

[16] W. Shockley, H. J. Queisser, *J. Appl. Phys.* **1961**, *32*, 510.

[17] National Renewable Energy Laboratory (NREL), "Best Research-Cell Efficiencies," can be found under https://www.nrel.gov/pv/cell-efficiency.html.

[18] X. Wu, B. Li, Z. Zhu, C.-C. Chueh, A. K. Y. Jen, *Chem. Soc. Rev.* **2021**, *50*, 13090.

[19] M. T. Hörantner, T. Leijtens, M. E. Ziffer, G. E. Eperon, M. G. Christoforo, M. D. McGehee, H. J. Snaith, *ACS Energy Lett.* **2017**, *2*, 2506.

[20] M. Saliba, J.-P. Correa-Baena, M. Grätzel, A. Hagfeldt, A. Abate, *Angew. Chem. Int. Ed.* **2018**, *57*, 2554.

[21] P. K. Nayak, S. Mahesh, H. J. Snaith, D. Cahen, *Nat. Rev. Mater.* **2019**, *4*, 269.

[22] A. Cuthbertson, "Solar power world record broken with 'miracle material,'" can be found under https://www.independent.co.uk/tech/perovskite-solar-cell-power-world-record-b2196762.html, **2022**.

[23] Q. Van Le, H. W. Jang, S. Y. Kim, *Small Methods* **2018**, *2*, 1700419.

[24] D. Ma, K. Lin, Y. Dong, H. Choubisa, A. H. Proppe, D. Wu, Y.-K. Wang, B. Chen, P. Li, J. Z. Fan, F. Yuan, A. Johnston, Y. Liu, Y. Kang, Z.-H. Lu, Z. Wei, E. H. Sargent, *Nature* **2021**, *599*, 594.

[25] J. J. Yoo, G. Seo, M. R. Chua, T. G. Park, Y. Lu, F. Rotermund, Y.-K. Kim, C. S. Moon, N. J. Jeon, J.-P. Correa-Baena, V. Bulović, S. S. Shin, M. G. Bawendi, J. Seo, *Nature* **2021**, *590*, 587.

[26] J. Jeong, M. Kim, J. Seo, H. Lu, P. Ahlawat, A. Mishra, Y. Yang, M. A. Hope, F. T. Eickemeyer, M. Kim, Y. J. Yoon, I. W. Choi, B. P. Darwich, S. J. Choi, Y. Jo, J. H. Lee, B. Walker, S. M. Zakeeruddin, L. Emsley, U. Rothlisberger, A. Hagfeldt, D. S. Kim, M. Grätzel, J. Y. Kim, *Nature* **2021**, *592*, 381.

[27] M. Saliba, J.-P. Correa-Baena, C. M. Wolff, M. Stolterfoht, N. Phung, S. Albrecht, D. Neher, A. Abate, *Chem. Mater.* **2018**, *30*, 4193.

[28] "World record back at HZB: Tandem solar cell achieves 32.5 percent efficiency," can be found under https://www.helmholtz-berlin.de/pubbin/news_seite?nid=24348;sprache=en, **2022**.

[29] R. Ollearo, A. Caiazzo, J. Li, M. Fattori, A. J. J. M. van Breemen, M. M. Wienk, G. H. Gelinck, R. A. J. Janssen, *Adv. Mater.* **2022**, *34*, 2205261.

[30] R. Ollearo, J. Wang, M. J. Dyson, C. H. L. Weijtens, M. Fattori, B. T. van Gorkom, A. J. J. M. van Breemen, S. C. J. Meskers, R. A. J. Janssen, G. H. Gelinck, *Nat. Commun.* **2021**, *12*, 7277.

[31] W. Travis, E. N. K. Glover, H. Bronstein, D. O. Scanlon, R. G. Palgrave, *Chem. Sci.* **2016**, *7*, 4548.

[32] M. A. Green, A. Ho-Baillie, H. J. Snaith, *Nat. Photonics* **2014**, *8*, 506.

[33] G. Kim, H. Min, K. S. Lee, D. Y. Lee, S. M. Yoon, S. I. Seok, *Science* **2020**, *370*, 108.

[34] G. Yang, H. Zhang, G. Li, G. Fang, *Nano Energy* **2019**, *63*, 103835.

[35] Z. Wang, Y. Zhou, S. Pang, Z. Xiao, J. Zhang, W. Chai, H. Xu, Z. Liu, N. P. Padture, G. Cui, *Chem. Mater.* **2015**, *27*, 7149.

[36] T. A. S. Doherty, S. Nagane, D. J. Kubicki, Y.-K. Jung, D. N. Johnstone, A. N. Iqbal, D. Guo, K. Frohna, M. Danaie, E. M. Tennyson, S. Macpherson, A. Abfalterer, M. Anaya, Y.-H. Chiang, P. Crout, F. S. Ruggeri, S. Collins, C. P. Grey, A. Walsh, P. A. Midgley, S. D. Stranks, *Science* **2021**, *374*, 1598.

[37] D. P. McMeekin, P. Holzhey, S. O. Fürer, S. P. Harvey, L. T. Schelhas, J. M. Ball, S. Mahesh, S. Seo, N. Hawkins, J. Lu, M. B. Johnston, J. J. Berry, U. Bach, H. J. Snaith, *Nat. Mater.* **2023**, *22*, 73.

[38] C. Ma, F. T. Eickemeyer, S.-H. Lee, D.-H. Kang, S. J. Kwon, M. Grätzel, N.-G. Park, *Science* **2023**, *379*, 173.

[39] K. Datta, B. T. van Gorkom, Z. Chen, M. J. Dyson, T. P. A. V. D. Pol, S. C. J. Meskers, S. Tao, P. A. Bobbert, M. M. Wienk, R. A. J. Janssen, *Appl. Energy Mater.* **2021**, *4*, 6650.

[40] U. Krishnan, *J. Photonics Energy* **2019**, *9*, 1.

[41] M. V. Khenkin, E. A. Katz, A. Abate, G. Bardizza, J. J. Berry, C. Brabec, F. Brunetti, V. Bulović, Q. Burlingame, A. Di Carlo, R. Cheacharoen, Y.-B. Cheng, A. Colsmann, S. Cros, K. Domanski, M. Dusza, C. J. Fell, S. R. Forrest, Y. Galagan, D. Di Girolamo, M. Grätzel, A. Hagfeldt, E. von Hauff, H. Hoppe, J. Kettle, H. Köbler, M. S. Leite, S. Liu, Y.-L. Loo, J. M. Luther, C.-Q. Ma, M. Madsen, M. Manceau, M. Matheron, M. McGehee, R. Meitzner, M. K. Nazeeruddin, A. F. Nogueira, Ç. Odabaşı, A. Osherov, N.-G. Park, M. O. Reese, F. De Rossi, M. Saliba, U. S. Schubert, H. J. Snaith, S. D. Stranks, W. Tress, P. A. Troshin, V. Turkovic, S. Veenstra, I. Visoly-Fisher, A. Walsh, T. Watson, H. Xie, R. Yıldırım, S. M. Zakeeruddin, K. Zhu, M. Lira-Cantu, *Nat. Energy* **2020**, *5*, 35.

[42] L. Mao, C. C. Stoumpos, M. G. Kanatzidis, *J. Am. Chem. Soc.* **2019**, *141*, 1171.

[43] A. Krishna, S. Gottis, M. K. Nazeeruddin, F. Sauvage, *Adv. Funct. Mater.* **2019**, *29*, 1.

[44] Y. Chen, Y. Sun, J. Peng, J. Tang, K. Zheng, Z. Liang, *Adv. Mater.* **2018**, *30*, 1703487.

[45] X. Li, J. M. Hoffman, M. G. Kanatzidis, *Chem. Rev.* **2021**, *121*, 2230.

[46] P. Gao, A. R. Bin Mohd Yusoff, M. K. Nazeeruddin, *Nat. Commun.* **2018**, *9*, 5028.

[47] C. Ortiz-Cervantes, P. Carmona-Monroy, D. Solis-Ibarra, *ChemSusChem* **2019**, *12*, 1560.

[48] M. C. Gélvez-Rueda, E. M. Hutter, D. H. Cao, N. Renaud, C. C. Stoumpos, J. T. Hupp, T. J. Savenije, M. G. Kanatzidis, F. C. Grozema, *J. Phys. Chem. C* **2017**, *121*, 26566.

[49] R. Quintero-Bermudez, A. Gold-Parker, A. H. Proppe, R. Munir, Z. Yang, S. O. Kelley, A. Amassian, M. F. Toney, E. H. Sargent, *Nat. Mater.* **2018**, *17*, 900.

[50] A. Z. Chen, M. Shiu, X. Deng, M. Mahmoud, D. Zhang, B. J. Foley, S.-H. Lee, G. Giri, J. J. Choi, *Chem. Mater.* **2019**, *31*, 1336.

[51] L. N. Quan, M. Yuan, R. Comin, O. Voznyy, E. M. Beauregard, S. Hoogland, A. Buin, A. R. Kirmani, K. Zhao, A. Amassian, D. H. Kim, E. H. Sargent, *J. Am. Chem. Soc.* **2016**, *138*, 2649.

[52] M. Shao, T. Bie, L. Yang, Y. Gao, X. Jin, F. He, N. Zheng, Y. Yu, X. Zhang, *Adv. Mater.* **2022**, *34*, 2107211.

[53] L. Min, W. Tian, F. Cao, J. Guo, L. Li, *Adv. Mater.* **2021**, *33*, 2101714.

[54] H. L. Loi, J. Cao, X. Guo, C. K. Liu, N. Wang, J. Song, G. Tang, Y. Zhu, F. Yan, *Adv. Sci.* **2020**, *7*, 1.

[55] R. Li, Y. Xu, W. Li, Y. Li, J. Peng, M. Xu, Q. Lin, *J. Phys. Chem. Lett.* **2021**, *12*, 1726.

[56] Y. Wang, L. Song, Y. Chen, W. Huang, *ACS Photonics* **2020**, *7*, 10.

[57] S. Yuan, Z. K. Wang, L. X. Xiao, C. F. Zhang, S. Y. Yang, B. B. Chen, H. T. Ge, Q. S. Tian, Y. Jin, L. S. Liao, *Adv. Mater.* **2019**, *31*, 1.

[58] Y. Han, S. Park, J. Wang, S. Jariwala, K. Lee, C. G. Bischak, S. Kim, J. Hong, S. Kim, M. J. Lee, D. S. Ginger, I. Hwang, *Adv. Mater. Interfaces* **2020**, *7*, 1.

[59] H. Zhu, Y. Liu, F. T. Eickemeyer, L. Pan, D. Ren, M. A. Ruiz-Preciado, B. Carlsen, B. Yang, X. Dong, Z. Wang, H. Liu, S. Wang, S. M. Zakeeruddin, A. Hagfeldt, M. I. Dar, X. Li, M. Grätzel, *Adv. Mater.* **2020**, *32*, 1907757.

[60] F. Zhang, S. Y. Park, C. Yao, H. Lu, S. P. Dunfield, C. Xiao, S. Uličná, X. Zhao, L. Du Hill, X. Chen, X. Wang, L. E. Mundt, K. H. Stone, L. T. Schelhas, G. Teeter, S. Parkin, E. L.

Ratcliff, Y.-L. Loo, J. J. Berry, M. C. Beard, Y. Yan, B. W. Larson, K. Zhu, *Science* **2022**, *375*, 71.

[61] Y.-W. Jang, S. Lee, K. M. Yeom, K. Jeong, K. Choi, M. Choi, J. H. Noh, *Nat. Energy* **2021**, *6*, 63.

[62] P. Chen, Y. Bai, S. Wang, M. Lyu, J. Yun, L. Wang, *Adv. Funct. Mater.* **2018**, *28*, 1706923.

[63] A. Fakharuddin, L. Schmidt-Mende, G. Garcia-Belmonte, R. Jose, I. Mora-Sero, *Adv. Energy Mater.* **2017**, *7*, 1700623.

[64] S. Shao, M. A. Loi, *Adv. Mater. Interfaces* **2020**, *7*, 1901469.

[65] Y. Liu, S. Akin, L. Pan, R. Uchida, N. Arora, J. V. Milić, A. Hinderhofer, F. Schreiber, A. R. Uhl, S. M. Zakeeruddin, A. Hagfeldt, M. Ibrahim Dar, M. Grätzel, *Sci. Adv.* **2019**, *5*, 1.

[66] H. Chen, S. Teale, B. Chen, Y. Hou, L. Grater, T. Zhu, K. Bertens, S. M. Park, H. R. Atapattu, Y. Gao, M. Wei, A. K. Johnston, Q. Zhou, K. Xu, D. Yu, C. Han, T. Cui, E. H. Jung, C. Zhou, W. Zhou, A. H. Proppe, S. Hoogland, F. Laquai, T. Filleter, K. R. Graham, Z. Ning, E. H. Sargent, *Nat. Photonics* **2022**, *16*, 352.

[67] S. Sidhik, Y. Wang, M. De Siena, R. Asadpour, A. J. Torma, T. Terlier, K. Ho, W. Li, A. B. Puthirath, X. Shuai, A. Agrawal, B. Traore, M. Jones, R. Giridharagopal, P. M. Ajayan, J. Strzalka, D. S. Ginger, C. Katan, M. A. Alam, J. Even, M. G. Kanatzidis, A. D. Mohite, *Science* **2022**, *377*, 1425.

2

High Efficiency
Quasi-2D Ruddlesden-Popper
Perovskite Solar Cells

Abstract

Even though photovoltaic devices based on quasi-2D Ruddlesden-Popper perovskites (RPP) are still lagging behind traditional 3D perovskites, they have experienced a dramatic increase in power-conversion efficiency, recently reaching >20%. As knowledge develops, the toolbox of RPP researchers is steadily growing in terms of organic spacers, additives, and characterization methods. This review aims to describe the use of such a toolbox to achieve high efficiency solar cells. The use of additives, functionalized spacers, and novel fabrication techniques are explored to control morphology, crystallinity, crystal orientation, interlayer interaction, and phase distribution. Moreover, methods to achieve the coveted phase purity in RPPs and its implications on both single- and multi-junction solar cells are discussed. By describing successful cases of high efficiency solar cells combined with in-depth knowledge of material properties, it is shown that there are still several open research questions that need exploring to further develop this fascinating class of perovskites.

2.1 INTRODUCTION

Perovskite solar cells have attracted enormous interest because of their steep increase in photovoltaic performances, from 4% in 2009 to 25.7% in 2020.[1] Such a photovoltaic "miracle" is due to the outstanding optoelectronic properties of this material: low exciton binding energy at room temperature, high absorption coefficient, high carrier mobility, and ability to tune the bandgap of the material by changing its composition.[2] Multijunction solar cells—consisting of a perovskite over a silicon solar cell or multiple perovskites—are also gaining interest because of their chance to overcome the detailed-balance limit of single absorbers and provide >30% power conversion efficiency (PCE).[3] Despite these advantages, perovskite solar cells suffer from instability when exposed to ambient air, high temperature, high relative humidity, and even light.[4] Because of this, layered 2D perovskites have appeared on the scene with the promise of improving the stability of the material.[5,6]

Traditional organic-inorganic hybrid perovskites possess an ABX_3 chemical structure that describes a three-dimensional (3D) framework. Here, A consists of an organic cation, such as formamidinium (FA) or methylammonium (MA), B is usually lead (Pb) or tin (Sn), and X is a halide ion, mostly iodide (I) or bromide (Br). The choice of organic cation for 3D perovskites is dictated by a geometric tolerance factor based on the radii of ions, which should be in the range of 0.8 and 1, meaning that cations that are too-small or too-large cannot be incorporated in the crystal lattice and cannot be used to make 3D perovskites.[2] When using larger cations, such as butylammonium (BA) or phenethylammonium (PEA), that cannot be accommodated in the 3D perovskite, the 3D framework can be sliced along the (100) plane direction to form a layered, 2D or quasi-2D perovskite.[7–9] The chemical formula of 2D and quasi-2D perovskites is $(R)_mA_{n–1}B_nX_{3n+1}$, where R represents the bulkier spacer. Monovalent or divalent ammonium spacers have been reported to form Ruddlesden-Popper (RP, $m = 2$ in the chemical formula above) or Dion-Jacobson (DJ, $m = 1$) perovskites, respectively, where lead halide octahedral sheets are sandwiched between the larger organic cations (**Figure 2.1**).[10–13]

The number of octahedra between the spacers (which we will refer to as n-value) dramatically changes the optoelectronic properties of the materials. For example, a pure 2D $n = 1$ perovskite possesses a bandgap energy (E_g) of about 2.3 eV and a high exciton binding energy >300 meV, whereas by increasing n, the bandgap and exciton binding energy decrease to those of a 3D perovskite ($n = \infty$) (**Table 2.1**).[12,14] As a result, for solar cell applications, n-values between 3 and 5 are often used to achieve an absorption spectrum that has reasonable overlap with the spectral solar

irradiance and to avoid the excitonic nature of small-n perovskites.[14] Such perovskite structures are often referred to as quasi-2D perovskites.
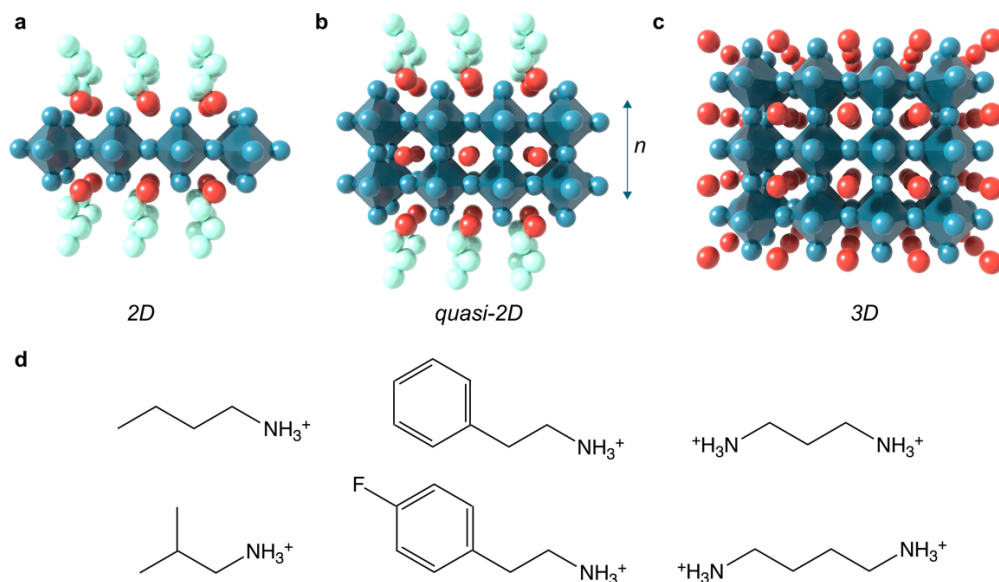
Figure 2.1. Illustration of a (a) 2D, (b) quasi-2D, and (c) 3D perovskite crystal structure. (d) Some cations used for fabrication of 2D and quasi-2D perovskites: butylammonium, phenethylammonium, 1,3-propane-diammonium, iso-butylammonium, para-fluorophenethylammonium, 1,4-butane-diammonium.

Table 2.1. Bandgap energy of RPPs with increasing n-value.

Perovskite	Bandgap energy (eV)
$n = 1$	~2.3
$n = 2$	~2.2
$n = 3$	~2.0
$n = 4$	~1.9
$n = 5$	~1.8
3D	~1.55 eV

While 3D perovskites are limited to a handful of A-site cations, namely MA, FA, and Cs, RP and DJ perovskites possess a chemical tuneability that is virtually boundless. A large variety of organic spacers has already been used for the

formation of RP and DJ perovskites either as active layer or passivation layer.[15–18] Although clear structure-property relationships–one of the main research questions for the field–are yet to be identified, the variety of spacers that can be employed makes this class of perovskites an interesting field of research with chance of impactful discoveries. Even though processing of lower-dimensional perovskites creates new challenges, such as tuning phase distribution and controlling crystal orientation, these perovskites show promise with a rapidly-increasing PCE, and enhanced stability compared to 3D perovskites, as we will discuss below.

In this Chapter and Review, we focus on Ruddlesden-Popper perovskites (RPPs), possessing a monovalent organic spacer, and refer the reader to other reviews for DJ perovskites.[18–20] Even though DJ and RP phases share similar challenges regarding fabrication of high efficiency devices, such as crystal orientation and phase distribution, RPPs have been more investigated and represent a more mature field. Furthermore, RPPs have shown enhanced stability compared to DJ phases.[21] However, DJ perovskites also possess promising features. For instance, the presence of a divalent ammonium spacer leads to shorter distances between the inorganic layers of PbI_2 compared to RPPs and provides better orbital overlap and enhanced charge transport. As a result, this class of materials is promising for optoelectronics devices, and we expect much more studies in the following years.[18]

2.1.1 PHASE DISTRIBUTION IN RP PEROVSKITES

There is a competition between the crystallization of 2D, quasi-2D, and 3D perovskites when fabricating quasi-2D RP films. Take, for example, a precursor solution containing BAI, MAI, and PbI_2 in the appropriate ratio to form a quasi-2D perovskite with $n = 4$. During solvent evaporation, crystallization can lead to $(BA)_2PbI_4$ (2D), $(BA)_2MA_{n-1}Pb_nI_{3n+1}$ structures with different n-values (quasi-2D), and $MAPbI_3$ (3D).[22] Strategies to avoid a mixture of phases are being developed, as will be discussed below, but usually a combination of all of these appears in the film, effectively forming a multidimensional perovskite with both 2D, quasi-2D, and 3D phases, and–in the specific example– an average n-value of $<n> = 4$. The film crystallization usually starts as a 3D perovskite at the liquid-air interface and proceeds toward the substrate forming multiple quasi-2D and 2D phases.[23] As a result, there are two processes to analyze: a) phase distribution of structural phases with different n-values (mostly at the bottom) and b) vertical phase segregation of (quasi-)2D and 3D phases (**Figure 2.2**a).[24–26] Both are responsible for a bandgap gradient in the film that leads to ultrafast charge carrier migration from small-n to large-n phases (Figure 2.2b),[27] which makes the analysis of phase distribution experimentally challenging. For instance, photoluminescence (PL) spectra display

emission peaks derive mostly from low-E_g perovskites (Figure 2.2c), making it impossible to quantify the phases through this routine technique.[28] Ultrafast transient absorption (TA) measurements are often better suited to determine how phases are distributed by measuring the absorption profile just after excitation in the span of hundreds of femtoseconds (Figure 2.2d)[26], which allows to analyze the charge carrier migration process and its rate. Apart from optical measurements, phase distribution can also be analyzed by angle-dependent grazing-incidence wide-angle X-ray scattering (GIWAXS), where probing with angles lower than the critical angle provide information only of the film's very top surface, while higher angles probe the whole thickness.[29] This method is independent of carrier migration and provides information also on the crystal orientation, which, as we will see below, is of crucial importance for charge transport in RPPs.
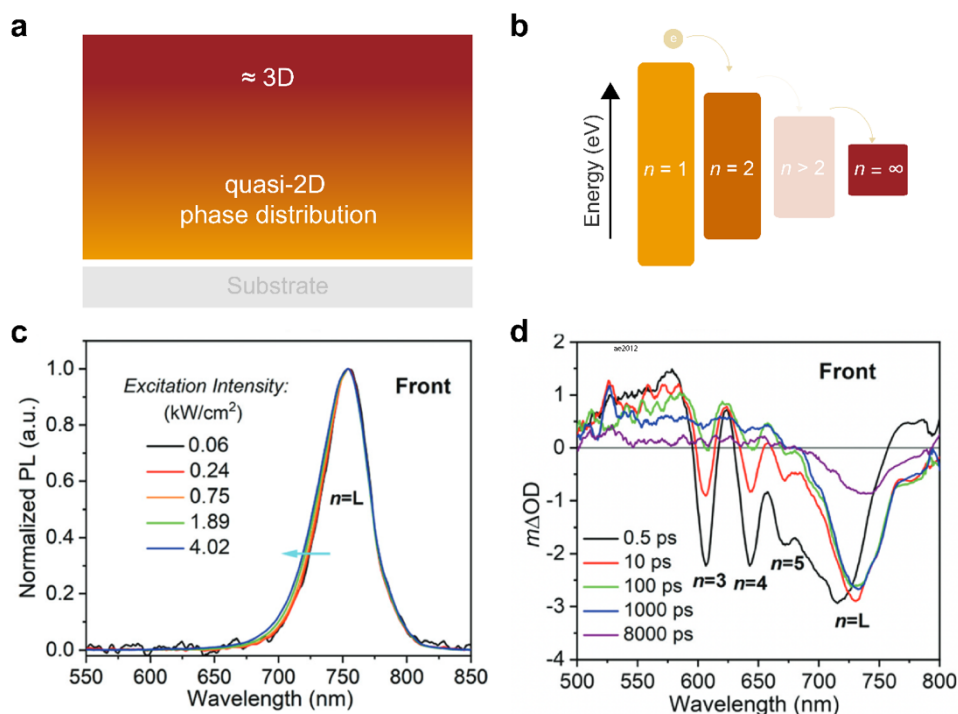
Figure 2.2. (a) Schematic illustration of vertical 2D-3D phase segregation and (quasi-)2D phase distribution at the bottom of the film. (b) Schematic illustration of the charge transfer from small-n to large-n phases. (c) PL spectra from top of a quasi-2D perovskite with emission coming from a large-n (~3D) phase. Reprinted with permission from [26]. Copyright 2021 Royal Society of Chemistry (d) Same film as in (c) but analyzed with ultrafast TA display the presence of multiple structural phases with different n-value. Reprinted with permission from [26]. Copyright 2021 Royal Society of Chemistry.

The reasons behind vertical phase distribution have been debated in the literature. It is thought that this process takes place already during the gel stage, which corresponds to the first seconds of the spin-coating process and can be modulated via solvent-precursors interactions.[22,30] Liu *et al.* proposed that differences in cation diffusivity are behind the formation of vertical phase segregation, which is exacerbated at high temperatures or with large cations.[30] For example, they found that the flux of MA cations to the surface of the film is much higher than for BA, which explains the prevalent presence of MA at the top interface and the vertical 2D-3D gradient that is so often observed. Nevertheless, this diffusivity model could not explain the formation of phases of different *n*-values at the bottom. Recently, Hoffman *et al.* studied the mechanism behind phase distribution and analyzed the evolution of the perovskite precursors to the final crystal structures.[22] One finding was that intermediate phases need free molecules of MAI and BAI to form the final perovskite structures. Based on these results, our group demonstrated that the molecules' availability to react and the resulting phase distribution at the bottom of the film depend on their interaction with solvents and co-solvents, pointing once more to the importance of studying precursor solutions to understand phase distribution.[29] Similarly, in a comprehensive study published by Quintero-Bermudez and co-workers, these large complexes of precursors and solvents were thought to provide a framework that facilitates the formation of quasi-2D and 2D RPPs).[27] Overall, the solvent was found to be crucial in determining the phase distribution and crystallinity.

While 2D-3D graded perovskites, with 2D phases at the bottom, are by far the most common encountered in the literature, recent studies have also highlighted the possibility of obtaining reverse-graded 3D-2D perovskites. For example, by using cyclohexylmethylammonium iodide as spacer, Wei *et al.* have shown that it is possible to obtain films where the 3D perovskite is at the bottom.[31] These authors demonstrated that such a gradient is optimal for solar cells in *n-i-p* configuration, obtaining a PCE of 15% with TiO_2 and Spiro-OMeTAD as electron- and hole-transport layer, respectively.[31]

Efforts have also been made by many groups to avoid phase distribution altogether and to achieve phase-pure perovskites. In a pioneering work published in 2016, Kanatzidis' group fabricated phase-pure 2D and quasi-2D perovskites single crystals by exploiting the solubility difference of structural phases with different *n*-values.[12] However, to deposit a perovskite film *via* spin-coating, crystals still needed to be dissolved in a solvent such as *N-N*–dimethylformamide (DMF), which often compromises phase purity. Recently, butylammonium acetate (BAAc) has been proposed as an alternative precursor to the iodide salt to form phase-pure

perovskites.[32] We will describe the use of single crystals and acetate salts in Section 2.2.4 and 2.3.1, respectively, and we will broadly discuss phase purity in Section 2.4.

2.1.2 CRYSTAL ORIENTATION

Compared to thin-film 3D perovskites,[33] crystal orientation has a more profound effect on charge transport in thin-film RPPs because the bulky organic spacers in layered perovskites hinders the charge transport between layers. In this case, a vertical orientation of the RPP crystals is desirable to assure that the transport of charges between electron- and hole-transport layers at top and bottom is not negatively impacted (**Figure 2.3**).[34] While the analysis of vertical orientation is often reported in the form of GIWAXS measurements, an accurate representation of the RP microstructure is complicated, again, by the presence of multiple phases with various n-values. It is often reported in the literature that the appearance of (0k0) diffraction planes in the out-of-plane direction represents the formation of parallel-oriented small-n phases. However, high efficiency RP cells are usually made of vertically oriented films that also contain a variety of structural phases. To carefully characterize which RP phases are formed in such films, one should look at the (0k0) peaks in the in-plane direction, which unfortunately are often obscured by the substrate horizon in conventional GIWAXS equipment.[35] As a result, an accurate characterization of the RPP phases present in the film is rarely provided and very often RPPs are described with a specific n-value even though little characterization is available on which phases are present. Because characterizing RPP films is difficult via both optical and crystallographic methods, these materials are often described by an average n-value ($<n>$, based on the stoichiometry of the precursor solution) that implies the presence of multiple phases.

The mechanism behind vertical orientation has been investigated. As mentioned before, the crystallization of RPPs starts at the liquid-air interface. When studying a BA-based system with in-situ GIWAXS, Chen and co-workers found that BA molecules are not able to form a monolayer at the liquid-air interface due to interaction with the solvent or due to complexation with PbI$_2$.[23] This leads to a scenario where BA molecules are oriented parallel to such interface and vertical orientation of the perovskite crystals is favored. Once the nucleation at the liquid-air interface has started, a completely vertical orientation can be obtained if low supersaturation makes crystal growth preferred over additional bulk nucleation processes, which instead inevitably lead to a random orientation of the crystals.[36] In situ GIWAXS measurements have proven themselves useful to understand such crystallization mechanism. In the abovementioned study, vertical orientation could

thus be linked to experimental parameters, such as solvent removal rate. Apart from these studies, many groups have reported different processing techniques that can enhance vertical orientation, although they seldom report the underlying mechanism. Among these techniques are hot casting,[37] spin-coating with antisolvent,[34,38] use of co-solvents,[39] and use of pressure and heat.[40]
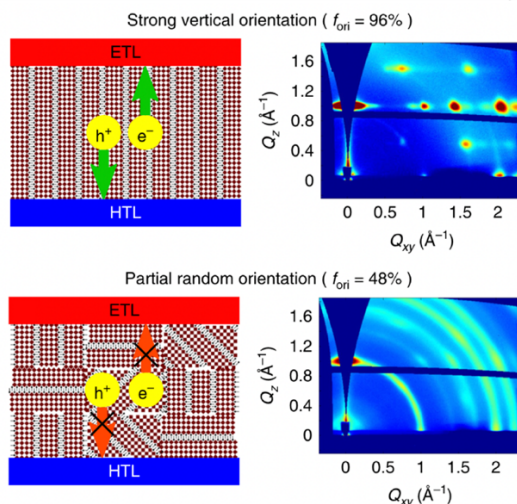
Figure 2.3. Charge transport in quasi-2D perovskites depends on crystal orientation: vertical- (top) and random- (bottom) oriented RPP with correspondent GIWAXS pattern. Reprinted with permission from [23].

2.1.3 STABILITY OF RP PEROVSKITES

Despite their lower efficiencies in solar cells compared to 3D perovskites, RPPs have attracted enormous interest in the perovskite research field because of their promise to improve the intrinsic and extrinsic stability of this material.[4] In 2014, Smith *et al.* first reported the superior stability of a PEA-based $<n>$ = 3 RPP compared to MAPbI$_3$ when exposed to ambient humidity.[41] More specifically, for at least 46 days the RPP displayed no changes in X-ray diffraction (XRD) patterns, while the 3D counterpart showed significant amounts of PbI$_2$. Later, Sargent's group investigated the stability of the same RPPs via density functional theory (DFT) and found a 6-fold decrease of PEAI desorption rate compared to MAI, which significantly decreased the film decomposition.[42] Furthermore, they analyzed the stability of the solar cells in function of the n-value and found a decrease in stability when increasing n, as expected. Nevertheless, an RPP with $<n>$ = 10 still displayed higher long-term air stability compared to MAPbI$_3$. Overall, lower n-values have typically led to solar cells with poorer efficiency but higher stability, thus the recently-

observed drastic increase in PCE of RPPs with n between 3 and 5 makes this class of material extremely promising.

Recently, RPP solar cells with efficiency >18% have been published, which all display enhanced stability compared to traditional 3D perovskites.[43–45] To visualize such enhancement, we selected a few studies with the highest reported PCEs in which the stability of RPPs was compared with that of 3D perovskites (**Figure 2.4**). Most of the shelf-life studies were in the range of 500–1000 h and showed a PCE loss >60% for 3Ds and <20% for RPPs. It is worth mentioning that most data was obtained by storing an unencapsulated solar cell in relative humidity (RH) between 25 and 65% and measuring PCE at different points in time. Stability measurements at high temperature, instead, were often performed in an N_2-filled glovebox or low-humidity atmosphere. Finally, even though we analyzed only a few reports, we note that all followed different, sometimes arbitrary, procedure to evaluate stability. As a result, it is impossible to establish which RPP, in terms of composition or phase purity, possesses higher stability. Applying a consistent method to evaluate stability and to effectively compare results among the literature is thus necessary.[46]
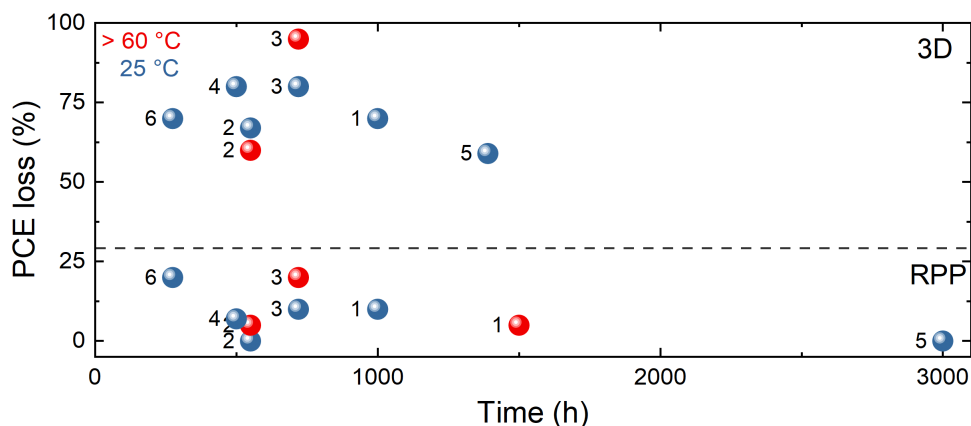
Figure 2.4. Stability comparison between unencapsulated RPP and 3D perovskite solar cells at room temperature (RT, 25 °C and >60 °C). References are the following: 1[43], 2[44], 3[47], 4[48], 5[49], 6[50].

As mentioned before, RPPs possess a large chemical tuneability because of the number of organic spacers that can be used. Changes in molecular stacking, crystallinity, charge transport properties impact the stability of the solar cells as well, apart from their efficiency. A comparison between 2-(methylthio)ethylammonium (MTEA) and BA, for example, has indicated better stability for MTEA when exposed to air and under heat stress conditions.[51] Formation of PbI_2 was inhibited under these conditions when using MTEA, because S-S inter-spacer interactions provide

stabilization of the RPP framework against humidity and heat. Fluorination of PEA in the para position has also been shown to improve the thermal stability of the perovskite layer compared to non-fluorinated PEA, whereas halogenation of PEA with F, Cl, and Br improved stability towards humidity.[47] Similar findings have recently been published for fluorinated benzylammonium (FBZA).[52] Zhang *et al.* reported that fluorination of PEA affects the phenyl-ring stacking, which is parallel slip-stacked in FBZA and edge-to-face in BZA. The better stacking allows for maximization of π-orbital overlap and leads to better charge transport and stability.[53] The A site plays a relevant role in stability as well. FA-based quasi-2D RPPs appear to be more stable than MA-based ones, in line with the higher thermal stability of $FAPbI_3$ compared to $MAPbI_3$ and the volatility of MA cations.[43] Similarly as before, fluorinated-FA-based RPPs have also displayed enhanced stability, due to increased dipole-dipole and hydrogen bonding interactions in the perovskite framework.[54] Overall, it seems that inter-spacer and spacer–perovskite interactions are key to enhanced the intrinsic stability of the RPP crystal lattice and deserve more investigation. With this in mind, further development of functionalized organic spacers will likely provide new insights also into perovskite stability, apart from photovoltaic performances. Nevertheless, to make RPPs even more stable and to avoid an endless trial-and-error process with numerous organic spacers, a comprehensive understanding of their degradation path is needed, yet is still lacking.

Finally, apart from stability against humidity and high temperature, RPPs have been shown to possess additional stability towards ion migration. Lin *et al.* have reported absence of ion migration up to 330 K for $BA_2MA_3Pb_4I_{13}$, showing promise for device based on RPPs to not suffer from any ion migration phenomena, such as photocurrent hysteresis.[55,56] In addition, wide-bandgap 3D perovskites containing large amounts of Br ions undergo photoinduced halide segregation, whereas recent studies have demonstrated that such a phenomenon is largely inhibited for 2D perovskites and at least reduced for lower dimensional perovskites with high *n*-value.[57] Generally, RPPs possess higher stability compared to 3D perovskites under a variety of conditions. It is likely that with further work this enhanced stability will be pushed even further.

2.1.4 TOOLBOX FOR HIGH-EFFICIENCY RP PEROVSKITES

Solar cells based on 3D perovskites have experienced a steep increase in photovoltaic performance during the last ≈10 years. Nowadays, solar cells with efficiency higher than 20% are the norm, and multiple publications have recently demonstrated efficiencies >25%.[58–60] Similarly, RPPs have improved from less than

4% in 2014 to more than 21% in 2021 (**Figure 2.5**). Despite significant less work on RPPs compared to 3Ds, this class of solar cells has experienced a steeper enhancement in performance in the last decade. Furthermore, while most high efficiency 3D perovskites are developed in *n-i-p* configuration, RPPs are broadly used in *p-i-n* solar cells, which are more suitable for multijunction applications. With further developments, RPPs have the potential to be stable and efficient perovskites for such applications.

The introduction of new fabrication methods, the use of new additives and spacers, and a more thorough understanding of crystallization mechanism, vertical orientation, and phase purity are behind this substantial increase of PCE in RPPs. Together with PCE, the toolbox of RPP researchers is also steadily growing in terms of fabrication methods to use or molecules to employ as additives or spacers.
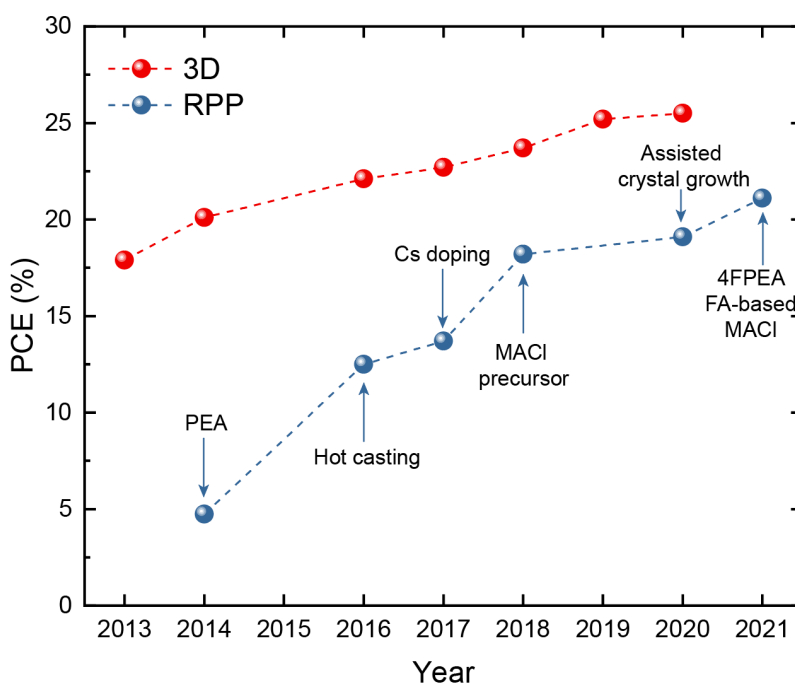
Figure 2.5. Evolution of power conversion efficiency (PCE) over time for 3D (from NREL[1]) and RP perovskites. For the latter, a brief description of the materials and fabrication method is given. References are the following: PEA,[41] hot casting,[37] Cs doping,[61] MACl precursor,[62] assisted crystal growth,[44] and 4FPEA.[43] All 3D perovskites are in *n-i-p* configuration, whereas all RPPs are in *p-i-n*.

Furthermore, as RPPs represent a complex and multifaceted system, such a toolbox now also contains a broad variety of characterization techniques, among others GIWAXS, confocal PL microscopy, dynamic light scattering (DLS), ultrafast

TA, all of which will be discussed. This review aims to describe successful methods of fabricating high efficiency solar cells based on RPPs amongst such a plethora of options. We will discuss the impact of molecular and additive engineering and new fabrication methods on both film properties, such as crystal orientation and phase distribution, and solar cell properties, such as charge transport and photovoltaic performance.

With this work, we summarize where this field is currently standing, and which research questions need answering to reduce the gap between 3D and RP perovskites and to further develop this exciting field.

2.2 MOLECULAR AND ADDITIVE ENGINEERING

RPPs show an outstanding structural variety compared to traditional 3D perovskites because of the possibility to use an enormous assortment of organic spacers. The organic spacer in 2D and quasi-2D perovskites does not only slice the perovskite framework but also has important consequences on the optoelectronic and crystalline properties of the material, such as bandgap energy, charge transport, molecular packing, and phase distribution, that can be tuned to achieve higher PCEs. For the readers who desire a more fundamental understanding of the changes induced by different organic spacers on the structure and optoelectronic properties of 2D and quasi-2D perovskites, we refer to a broad review that was recently published by Kanatzidis' group.[17] Apart from molecular changes in the spacer structure, the field of RPPs has also experienced an extensive use of additives to induce modifications in film morphology, crystal orientation, or overall crystallization process.

In this section, we analyze some successful examples of molecular and additive engineering in high efficiency RPP solar cells, where chemical changes at the molecular level and induced changes of the film properties have led to enhanced photovoltaic performances (*i.e.,* PCE >14%).

2.2.1 FLUORINATED SPACERS

The use of fluorinated functional groups has been successfully applied to organic solar cells with improvements in both film morphology and device efficiency.[63] Likewise, as RPPs might benefit from the tunability of spacers' chemical structure, multiple groups synthesized and used fluorinated organic spacers in quasi-2D perovskite solar cells (Table 2.2). Such spacers possess different dipole moments, molecular size, and solubility compared to non-fluorinated ones, leading to differences in phase distribution that can be exploited to achieve high efficiency devices.

Wang *et al.* studied a series of halogenated PEAs and thoroughly characterized both the surface of the films and their distribution of phases.[47] Fluorination of PEA (4FPEA) (**Figure 2.6**a) was found to increase crystallinity and grain size and to suppress the formation of $n = 1$ phases, as observed from the absence of a short-lived $n = 1$ bleaching signal in the ultrafast transient absorption (TA) spectra when 4FPEA is used instead of PEA (Figure 2.6c). Such $n = 1$ phases which are usually detrimental for device performance because of its parallel orientation that inhibits charge transport along the vertical direction.[34] Furthermore, while they still exhibited a 2D-3D gradient with small-n phases at the bottom, 4FPEA-based films possessed a higher content of large-n phases compared to PEA-based films, which is instead favorable for the cells' performance. In contrast, due to the lower solubility of 4BrPEA and 4ClPEA, small-n phases nucleated at an early stage of film formation when using such spacers, leading to a phase distribution drastically shifted towards 2D and, as a result, to low PCE. By using 4FPEA ($<n> = 4$) in combination with MACl and $PbCl_2$ as additives, the authors reported a PCE of 18.1% with open-circuit voltage (V_{OC}) of 1.21 V and short-circuit current density (J_{SC}) higher than 19 mA cm^{-2}. On another note, Shi *et. al.* linked the increased dipole moment of 4FPEA compared to PEA (1.98 *vs* 1.26 D) with reduced dielectric confinement and exciton binding energy.[48] This, in combination with better intermolecular packing of the organic spacers, provided a basis for an efficient charge transport that pushed the PCE of $(4FPEA)_2MA_4Pb_5I_{16}$ to 17.3% with V_{OC} of 1.16 V and J_{SC} of 19 mA cm^{-2}. Overall, PCEs higher than 14% have been reached also by other groups by using the same organic spacer, usually in combination with additives, such as NH_4SCN.[64,65]
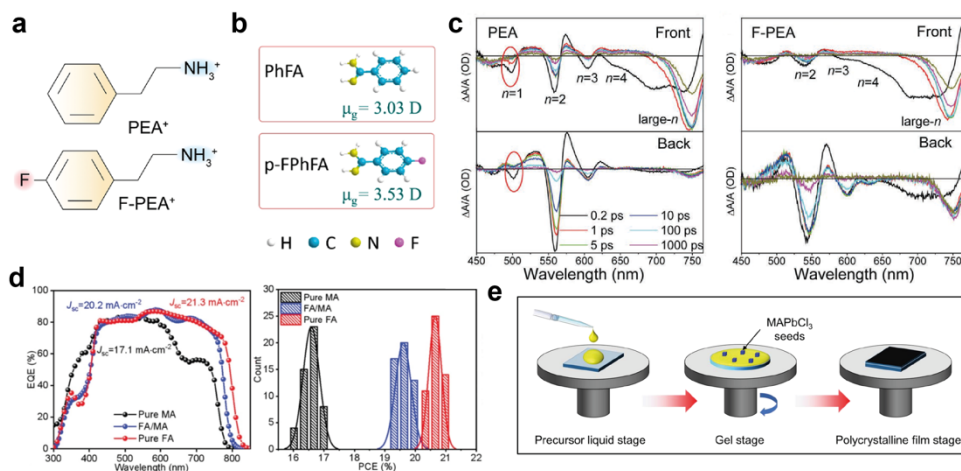
Figure 2.6. (a) Chemical structure of PEA+ and 4FPEA+. Reprinted with permission from [47]. Copyright 2021 Wiley VCH. (b) Chemical structure of PhFA and 4FPhFA with corresponding dipole moment. Reprinted with permission from [54]. Copyright 2021 American Chemical

Society (c) Ultrafast transient absorption of PEA- and 4FPEA-based RPPs. Circled area (left plot) represents the ground state bleaching of $n = 1$, which is suppressed in 4FPEA. Reprinted with permission from [47]. Copyright 2021 Wiley VCH. (d) External quantum efficiency (EQE) spectra and PCE statistical distribution of pure MA, FA-MA, and pure FA RPP based on 4FPEA. Reprinted with permission from [43]. Copyright 2021 Wiley VCH (e) Schematic representation of the spin-coating process where MAPbCl$_3$ seeds are formed during the gel stage. Reprinted with permission from [43]. Copyright 2021 Wiley VCH.

As explained above, 4FPEA possesses a higher dipole moment compared to PEA, which is important for decreasing the exciton binding energy. A way to increase even further such dipole moment is to functionalize a FA cation with a bulky functional group, such as a fluorinated phenyl group. This strategy was first adopted by Dong *et al.,* who functionalized FA with a thiophene group, and recently by another group who used a chlorinated phenyl group.[49,66] Li *et al.* reported the use of PhFA (Ph = phenyl) and 4FPhFA (Figure 2.6b) for MA-based RPPs and achieved efficiencies up to 17.37%.[54] Interestingly, they also associated the enhanced hydrogen bonding between the fluorinated spacer and the [PbX$_6$]$^{4-}$ framework with increased stability of the perovskite layer, showing that FA spacers are a suitable way to both decrease the PCE gap between 3D and RPPs and to further enhance their stability. It is useful to notice, however, that stability was measured in very mild conditions, namely room-temperature and N$_2$ atmosphere. By now, many different fluorinated cations have been developed and used for passivation. We refer to an excellent review on this topic and literature cited therein for further information.[17]

Table 2.2. Solar cell parameters for high-efficiency RPPs fabricated with fluorinated organic spacer cations.

RPP	Method*	J_{SC} (mA cm^{-2})	V_{OC} (V)	FF (-)	PCE (%)	Ref.
(4FPEA)$_2$MA$_3$Pb$_4$I$_{13}$	H.C., Add.	19.04	1.21	0.78	18.10	[47]
(4FPEA)$_2$MA$_4$Pb$_5$I$_{16}$	Add.	19.00	1.16	0.79	17.34	[48]
(4FPEA)$_2$MA$_3$Pb$_4$I$_{13}$	H.C.	17.50	1.08	0.8	15.2	[64]
(4FPEA)$_2$MA$_4$Pb$_5$I$_{16}$	Add.	18.00	1.06	0.76	14.5	[65]
(4FPhFA)$_2$MA$_4$Pb$_5$I$_{16}$	Add., A.S.	20.54	1.13	0.74	17.37	[54]
(4FPEA)$_2$FA$_4$Pb$_5$I$_{16}$	H.C., Add.	22.45	1.18	0.79	21.07	[43]
(4FPEA)$_2$MA$_3$Pb$_4$I$_{13}$	H.C., Add.	18.75	1.20	0.83	18.67	[45]
(4FBZA)$_2$MA$_3$Pb$_4$I$_{13}$	H.C., Add.	17.14	1.23	0.80	16.82	[52]

* H.C. = hot casting, Add. = additives are used in the precursor solution, A.S. = antisolvent, FF = fill factor

The use of FAPbI$_3$ in the 3D perovskites field has led solar cells to new highs in efficiency, because of its lower bandgap energy and less significant voltage losses. Although the use of FA in RPPs has been limited to a handful of studies, it has shown great promise in enhancing photovoltaic performances.[67] A recent study has reported a record efficiency of 21.07% by using 4FPEA as organic spacer in an FA-based RPP.[43] Shao and co-workers used a combination of 4FPEA and FA as A cation to push the efficiency from 17% (pure MA) to 21% (pure FA) (Figure 2.6d). To ensure the formation of α-phase, MACl and PbCl$_2$ were used as additives in a 1:1 ratio. By varying the concentrations, it was found that the presence of Cl induces the formation of MAPbCl$_3$ seeds during spin-coating (Figure 2.6e), which act as nucleation points to assist the crystallization of 3D-like perovskite phases, thus suppressing the formation of $n = 2$ and facilitating charge transport. Even though no comparisons with non-fluorinated spacers were shown, this study currently presents the highest recorded PCE for an RPP and directs the research field towards FA-based perovskites for further improvements.

2.2.2 MULTI-SPACER RP PEROVSKITES

Tuning the interlayers' interaction can be achieved *via* engineering size, chemical structure, and functional groups of the organic spacer, but also by mixing multiple spacers. These different cations can act as co-spacers and create layered perovskites with a crystalline structure that, for example, differs in lattice spacing compared to the one-spacer RPP.[68] In 2019, Lian *et al.* introduced the use of a second spacer in an RPP solar cell by mixing BA and PEA.[69] To achieve good device performance, namely a PCE of 14.09% in a *p-i-n* device with poly(3,4-ethylenedioxythiophene) polystyrene sulfonate (PEDOT:PSS) as hole transport layer (HTL) and phenyl-C$_{61}$-butyric acid methyl ester (PCBM) as electron transport layer (ETL), the authors indicated a stronger aggregation of the precursors in solution, measured via DLS, as a pre-requisite to achieve high-quality films with large crystal grains (**Figure 2.7**). This condition was successfully met when mixing two spacers, no matter their size or molecular shape, but efficiencies >14% were reached only with BA and PEA. More recently, a mixture of BA and PEA as organic spacers with the addition of a sulfobetaine zwitterionic additive has been successfully used to fabricate a solar cell with PCE of 17.04% [70] The addition of this S=O containing additive has led to a more homogeneous phase distribution and an alleviated competition between MA and BA during the crystallization process because of its interaction with the perovskite precursors, proving that additive engineering to tune the colloidal properties of the precursor solution is a suitable strategy to improve solar cell performances.

Liu *et al.* mixed BAI with bulky 1-naphthalenemethylammonium (NMA), showing the existence of a delicate equilibrium between enhanced interlayer interaction and vertical orientation, poor morphology, and formation of low-*n* phases.[71] Only after optimization of its concentration, an optimum was found with PCE of 14.21%. Another notable example of multiple spacers is provided by Long *et al.*, who fabricated $(BA_{0.775}GA_{0.225})_2MA_2Pb_3I_{10}$ by mixing BA and guanidinium (GA).[72] Interestingly, not only it did not change the phase distribution of the resulting RPP, but the addition of GA displayed accelerated energy transfer from $n = 3$ to $n = 4$ and 5 phases, which was shown to be beneficial for exciton dissociation and charge extraction, and enhanced crystallinity and crystal orientation. In an *n-i-p* configuration, the authors reported a high V_{OC} of 1.25 V and PCE of 14.47%. Similarly, an inverted device published elsewhere and based on $(PEA_{0.8}GA_{0.2})_2MA_4Pb_5I_{16}$ reached 15.27% efficiency.[73]
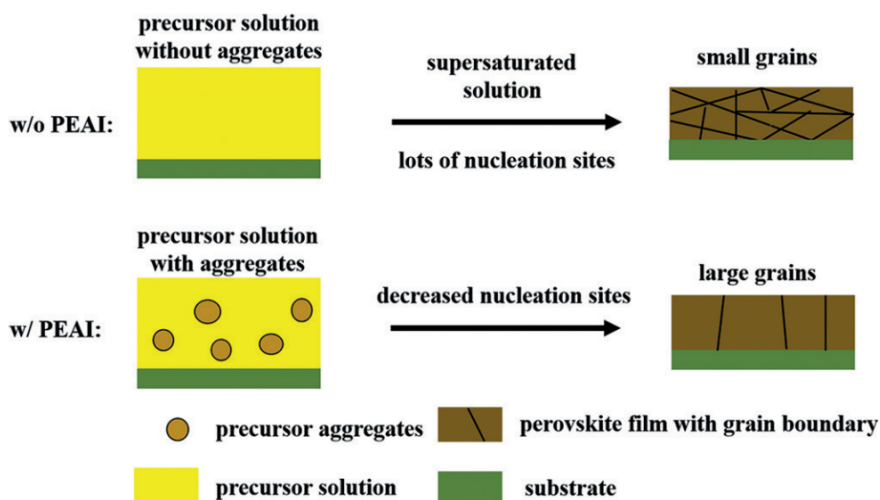
Figure 2.7. The use of multiple spacers induces aggregation in the precursor solution, which results in decreased nucleation sites and larger grains. Reprinted with permission from [69]. Copyright 2021 Wiley VCH.

Overall, the use of multiple spacers is a facile way to improve the quasi-2D perovskite film quality and solar cell efficiency. PCEs obtained through such method are in the range of ≈14% with improvements to ≈17% achieved with the use of additives (**Table 2.3**). Furthermore, despite having investigated the impact of a second spacer on the crystalline structure of an RPP, the underlying mechanisms behind the improvement in efficiency still need to be understood and require further study.

Table 2.3. Solar cell parameters for high-efficiency multi-spacer RPPs.

RPP	Method*	J_{SC} (mA cm^{-2})	V_{OC} (V)	FF (-)	PCE (%)	Ref
$(PEA_{0.8}GA_{0.2})_2MA_4Pb_5I_{13}$	H.C., Add.	17.24	1.17	0.75	15.27	[73]
$(BA_{0.77}GA_{0.22})_2MA_2Pb_3I_{10}$	A.S.	16.20	1.25	0.71	14.47	[72]
$(BA_{0.9}NMA_{0.1})_2MA_3Pb_4I_{13}$	H.C.	17.54	1.12	0.72	14.21	[71]
$(BA_{0.9}PEA_{0.1})_2MA_4Pb_5I_{16}$	H.C.	16.74	1.10	0.77	14.09	[69]
$(BA_{0.9}PEA_{0.1})_2MA_3Pb_4I_{13}$	H.C., Add.	18.88	1.19	0.75	17.04	[70]

* H.C. = hot casting, Add. = additives are used in the precursor solution, A.S. = antisolvent

2.2.3 ADDITIVE ENGINEERING

Methylammonium chloride (MACl) is extensively used both in RP and 3D perovskite film fabrication as a valuable salt to improve device performances.[74] As such, this additive has become part of the toolbox of the 2D perovskite researcher to optimize film deposition (**Table 2.4**). In fact, apart from the examples described below, which focus specifically on the use of MACl, numerous other works referenced in this review make use of this additive in their baseline spin-coating recipe. While MACl acts as stabilizer of the α-phase and as crystallization rate modifier in FAPbI$_3$ perovskites,[60,75] it also has a large impact on the vertical orientation and the distribution of RPP phases with different n-values. Zheng *et al.* investigated these effects by fabricating BA$_2$MA$_4$Pb$_5$I$_{16}$ films via drop-casting (see Section 2.3.2 for more information about this fabrication method) and calculated specific changes in n-values when doping the perovskite with MACl.[76] They found that MACl facilitates the formation of small-n perovskites and, as a result, increases the n-value of the 3D-like phases that are inevitably formed during crystallization (**Figure 2.8**a). Tuning the amount of MACl is important to find an optimal spot where the small-n phases provide a passivation effect without aggregating and forming quasi-2D domains with limited charge transport. Overall, by adding 6% MACl, solar cells fabricated in the *p-i-n* configuration reached 14.6% PCE. Apart from being used as additive, MACl has been also employed as the main precursor instead of or with MAI. For instance, Lai *et al.* introduced 2-thiophenemethylammonium (TMA) as organic spacer in an <n> = 3 RPP and found a higher degree of vertical orientation (Figure 2.8c), suppressed formation of n = 2 and parallel oriented small-n phases (Figure 2.8b), and overall higher performance (15.42% PCE) when using a mixture of MACl/MAI (0.5/0.5) as perovskite precursor.[50] A similar suppression of n = 2 phases was reported also by using PbCl$_2$, another Cl source, leading to a

15.08% *p-i-n* BA-based solar cell.[77] MACl was additionally used as the only MA source by Yang *et al.*, who found that the *n*-value needed to be optimized in the range of non-integer values to achieve the right balance between the precursors, in this case PbI_2, MACl, and 3-bromobenzylammonium iodide (3BrBZAI).[62] Additionally, this work displayed that also small-*n* phases can orient vertically, thus favorably for charge transport, under the right conditions of film fabrication (in this article, hot casting). The peak efficiency for solar cells based on this material was 18.2%, with an impressive V_{OC} of 1.23 V.

Thiocyanate salts, usually NH_4SCN, have also been used as additives for RPPs to induce vertical orientation in the films, usually in combination with chlorides (NH_4Cl, MACl, etc.).[65,80–82] Just as MACl is a volatile species that leaves the film during thermal annealing,[83] also SCN^- forms volatile HSCN and is not expected to remain in the film after thermal treatment. Recently, the use of NH_4SCN and HCl as co-additives led to an improvement of optoelectronic properties of $(BA)_2(FAMA)_3Pb_4I_{13}$ that resulted in a PCE of 16.45%.[38] $Pb(SCN)_2$ has also shown promise in enhancing film morphology and charge carrier mobility while reducing non-radiative recombination. The use of this additive has been reported to push the PCE of a solar cell based on propargylamine spacer to 15.20%, whereas the pristine film stopped at 12.15%.[84]
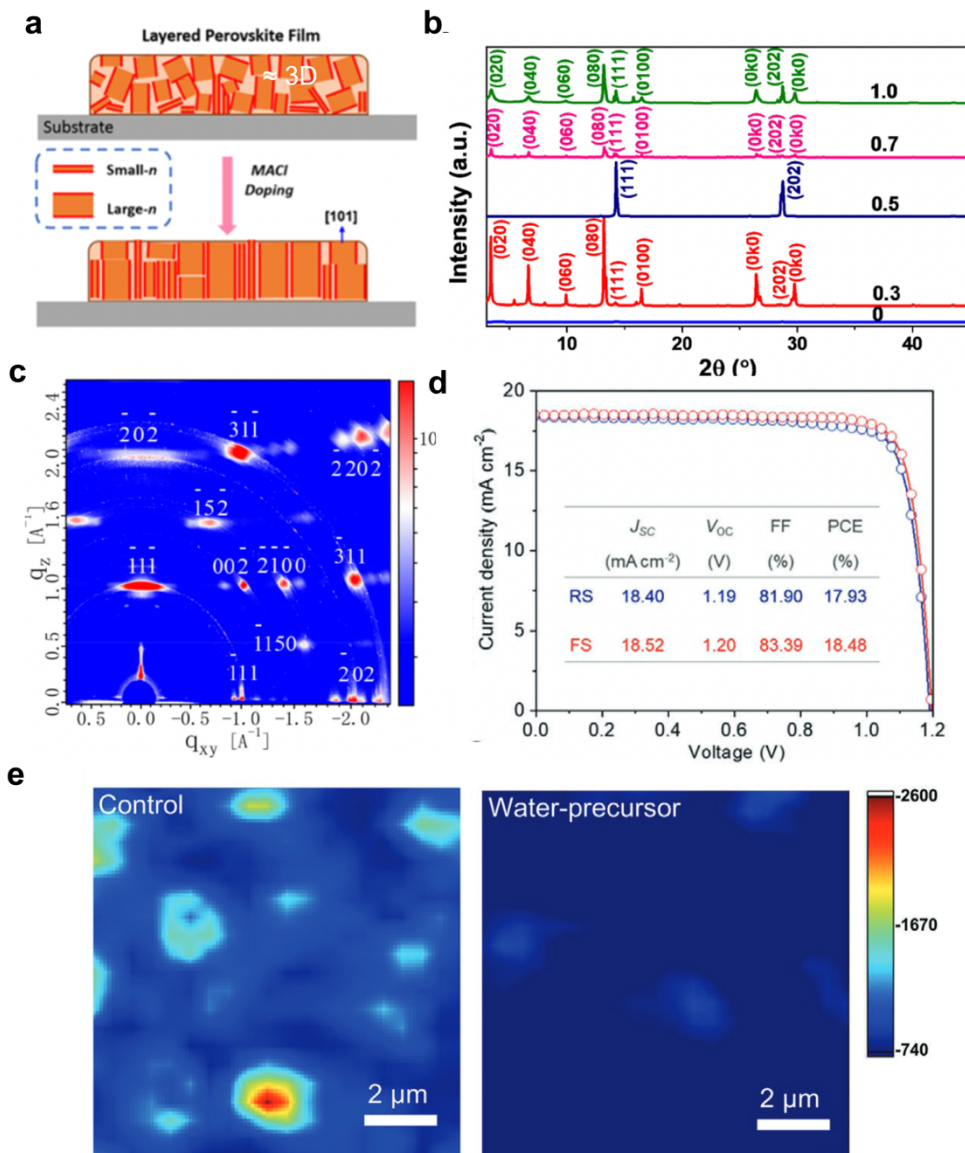
Figure 2.8. (a) Schematic representation of the effect of MACl on the crystalline structure of RPPs. Reprinted with permission from [76]. Copyright 2020 American Chemical Society (b) X-ray diffractograms of $(TMA)_2MA_2Pb_3I_{10}$ with different MACl/MAI ratios. Reprinted with permission from [50]. Copyright 2018 American Chemical Society (c) GIWAXS pattern for the same RPP as (b) with MACl/MAI ratio = 0.5. VCH Copyright 2020 Wiley VCH. (d) Current-density *vs* Voltage (*JV*) plot for $PEA_2MA_3Pb_4I_{13}$ solar cell processed with $NH_4I_{0.2}Cl_{0.8}$ additive. Reprinted with permission from [79]. (e) Confocal PL intensity maps (650-850 nm) for $BA_2MA_4Pb_5I_{16}$ processed with and without H_2O additive: a more homogeneous phase distribution is obtained in the latter. Reprinted with permission from [78]. Copyright 2020 Wiley

Additives have also been used in antisolvents in a process called precursor organic salt-assisted crystal growth (PACG).[49] Among the highest efficiencies in RPPs, we mention a study on $(TMA)_2FA_4Pb_5I_{16}$ based solar cells by Lai *et al*. that makes use of such method to achieve 19.06% PCE with an outstanding J_{SC} of 23.39 mA cm^{-2}.[44] This method consists of using an antisolvent solution containing an organic spacer, 4-(trifluoromethyl)benzylammonium iodide in the case mentioned above, that is poured onto the spinning substrate during spin-coating. The fluorinated spacer is incorporated in the crystal lattice and induces changes in the film properties, resulting in a higher degree of vertical orientation, reduced trap density, faster charge collection, and enhanced hydrophobicity. Interestingly, this is one of the few examples of FA-based RPPs, which confirms the advantage when shifting to FA to achieve lower bandgaps and higher PCEs, as mentioned already in Section 2.2.1. Finally, among the plethora of additives used, the usually undesired water has also played a role in increasing RPP efficiency. The addition of 2 vol%. of H_2O was found to benefit the performances of both MA-based and CsFAMA-based RPP with BA as organic spacer ($<n>$ = 5), which reached PCEs of 16.52 and 18.04%, respectively.[78] This provides a good example of how additive-precursors interactions might tune the perovskite crystallization and its phase distribution. In fact, the authors found that the formation of MAI·H_2O hydrate in the presence of water, as demonstrated by nuclear magnetic resonance (NMR) measurements and DFT, effectively inhibits the formation of MAPbI$_3$. This alleviates the competition between the crystallization of 2D and 3D phases, making a more uniform energetic landscape, as indicated in the confocal PL mappings that visualize the spatial distribution of n-values (Figure 2.8e), and increasing J_{SC} compared to the control devices. Similarly, in work published by our group, it was shown that co-solvents impact the availability of perovskite precursors to react, leading to drastic changes in phase distribution.[29] As a result, it seems that the discovery and development of new additives or co-solvents might be a key factor in controlling the crystallization kinetics to achieve films with an optimized distribution of n-values or with phase purity.

Table 2.4. Solar cell parameters for high-efficiency RPPs fabricated with additives.

RPP	Method*	J_{SC} (mA cm^{-2})	V_{OC} (V)	FF (-)	PCE (%)	Ref.
$(BA)_2MA_4Pb_5I_{16}$	D.C., Add.	19.00	1.11	0.64	14.60	[76]
$(TMA)_2MA_2Pb_3I_9$	A.S., Add.	18.89	1.07	0.76	15.42	[50]
$(BA)_2MA_3Pb_4I_{13}$	H.C., Add.	20.24	0.99	0.75	15.08	[77]
$(3BrBZA)_2MA_3Pb_4I_{13}$	H.C., Add.	18.22	1.23	0.81	18.20	[62]
$(BA)_2(FAMA)_3Pb_4I_{13}$	A.S., Add.	19.34	1.11	0.77	16.45	[38]
$(PPA)_2MA_2Pb_3I_{10}$	Add.	17.60	1.20	0.72	15.20	[84]
$(TMA)_2FA_4Pb_5I_{16}$	PACG	23.39	1.07	0.76	19.06	[44]
$(TMA)_2FA_2Pb_3I_{10}$	PACG	20.17	1.05	0.79	16.72	[49]
$(BA)_2MA_3Pb_4I_{13}$	H.C., Add.	21.38	1.12	0.75	18.04	[78]
$(BA)_2MA_3Pb_4I_{13}$	H.C., Add.	18.52	1.20	0.83	18.48	[79]
$(BA)_2MA_3Pb_4I_{13}$	Add., S.A.	18.67	1.18	0.75	16.48	[87]

* D.C. = drop casting, H.C. = hot casting, Add. = additives are used in the precursor solution, A.S. = antisolvent, PACG = precursor organic salts-assisted crystal growth, S.A. = solvent vapor annealing. PPA = propargylammonium,

Water seems to also have a role in determining the efficacy of other additives, such as NH_4Cl, as it facilitates the deprotonation of NH_4^+ and its release from the film when fabricated in air. Yang and co-workers studied the use of some ammonium additives: NH_4Cl, NH_4I, and $NH_4I_xCl_{1-x}$.[79] They found that NH_4Cl prefers to adsorb on vertical-oriented (202) planes, meaning that during crystallization the (111) planes are exposed for secondary nucleation and grow faster. On the contrary, NH_4I adsorbs on (111), facilitating the crystallization of (202) planes that are favorably oriented. However, this positive effect is hindered by the slow deprotonation rate of NH_4I by atmospheric H_2O (because of the low vapor pressure of HI compared to HCl) that allows crystallization to be completed only during thermal annealing, leaving space to homogeneous nucleation and disruption of the vertical crystal growth of the film. The authors found a solution by using a mixed I and Cl additive, $NH_4I_{0.2}Cl_{0.8}$, which led to enhanced vertical orientation, crystallinity, and reduction of defects. By fabricating in air a device based on $(PEA)_2MA_3Pb_4I_{13}$, a resulting PCE of 18.48% was obtained, with a V_{OC} of 1.20 V and an outstanding FF of 83.39% (Figure 2.8d). Overall, while the fabrication of 3D perovskites usually takes place in N_2-filled

gloveboxes to avoid the presence of water and oxygen, RPPs have shown potential with regards to being fabricated in ambient air, with important consequences for upscaling.[70,85,86]

2.2.4 PHASE PURE RP PEROVSKITES VIA ACETATE SALTS

Although previous works described here have reached high efficiencies in solar cells, all these studies failed in making a phase pure RPP. High-efficiency devices often consist of both quasi-2D and 3D perovskite phases, with small-n values being avoided to favor charge transport along the vertical direction and large-n being mostly the cause of enhanced efficiency. In a recent article, Liang *et al.* reported the formation of phase pure RPPs by using an ionic liquid precursor, namely butylammonium acetate (BAAc) (**Figure 2.9**a).[32] As proof of phase purity, the PL spectra of the films fabricated with BAAc display an emission peak precisely around the bandgap energy of the corresponding n-phase (Figure 2.9c), whereas the films fabricated with BAI as precursor consist of emission from multiple phases (Figure 2.9b,d). The perovskite precursor solution plays an important role in determining the phase purity of the corresponding film. In fact, this solution is often a complex mixture of colloidal particles with sizes ranging from nanometers to micrometers. In this regard, the use of acetate creates a solution with a narrow size distribution, around 0.6 nm, because of the interaction between Pb^{2+} and Ac^- (Figure 2.9e). Overall, it seems that in presence of BAAc there is gelation of a uniformly distributed intermediate phase and subsequent crystallization of a phase pure quantum well with the evaporation of solvents and methylammonium acetate (MAAc). Apart from describing its formation mechanism, the authors fabricated an n-i-p device with SnO_2 as ETL, $BA_2MA_3Pb_4I_{13}$ as active layer, and Spiro-OMeTAD as HTL, and achieved 16.25% PCE and a record-V_{OC} of 1.31 V. The external quantum efficiency (EQE) spectrum also shows an impressive phase purity with a steep onset at ≈660 nm (Figure 2.9f). Surprisingly, such a high efficiency was obtained even though the phase pure films displayed a high degree of parallel orientation with respect to the substrate. Phase-pure devices have also shown enhanced stability in the dark, under illumination, and at elevated temperature compared to the ones containing multiple phases.[32]

Several reports have shown the use of another ionic liquid, methylammonium acetate (MAAc), as solvent for perovskite precursors, including an 18.06% PCE solar cell fabricated with a RPP based on 2-(methylthio)ethylamine hydrochloride and a 3D $MAPbI_3$.[51,88] With regards to the RPP, however, the focus was set mainly on the enhanced interaction between the organic spacers due to S-S bonds, which enabled good charge transport and high stability, and not on the use of MAAc as

solvent. Nevertheless, the study represents an important milestone in high efficiency RPPs.
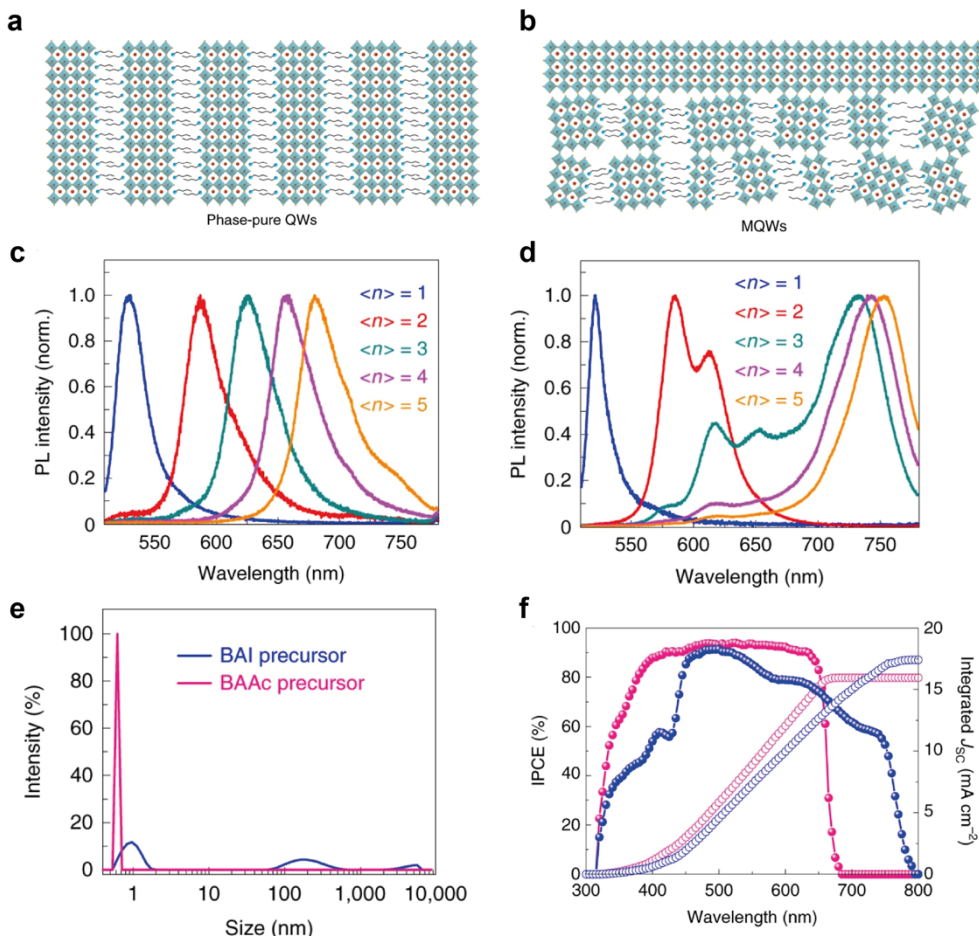
Figure 2.9. (a,b) Schematic illustration of (a) phase pure and (b) phase impure RPP. (c,d) PL spectra for BA-based RPPs with different $<n>$ when processed from (c) BAAc and (d) BAI. (e) Particle size distribution of precursor solution obtained by dynamic light scattering (DLS). (f) EQE of phase pure (pink) and impure (blue) RPP solar cells. Note that the onset for the phase pure is located at the bandgap, whereas for the film with phase distribution the onset corresponds to a 3D perovskite. Reprinted with permission from [32]. Copyright 2021 Springer Nature.

Phase pure RPPs have been up to now the holy grail of lower-dimensional perovskites. If reproduced by multiple labs, among other applications, these materials could be integrated into tandem solar cells, where bandgap tuning without the use of high amounts of bromide ions is highly needed to avoid halide phase segregation.[89,90] More about phase purity will be discussed in Section 2.4.

2.3 FABRICATION METHODS

Apart from the numerous organic spacers or additives that can be synthesized for RPPs, various fabrication methods have been used over time to reach higher PCEs. In this section, we aim to describe some successful examples. However, we will not consider routine changes in the deposition technique as a different fabrication method. For instance, differences between room-temperature spin-coating, hot casting, and use of antisolvents will not be treated in detail, even though they have been shown to change device performance considerably. Such techniques have now become routine methods to optimize the deposition of high-quality perovskite layers. Instead, we will highlight a few more remarkable changes in the fabrication method, such as the use of single crystal precursors, drop casting, or even thermal treatment of complete devices.

2.3.1 RP PEROVSKITES FROM SINGLE CRYSTAL PRECURSORS

In 2016, Kanatzidis' group published an extensive work on the synthesis and characterization of phase pure RP single-crystals based on the BA spacer.[12] This method makes use of the different solubilities of RP with different n-values to achieve selective crystallization of a specific phase. For example, in a HI/H$_3$PO$_2$ solvent mix, larger-n phases are more soluble than small-n phases. As a result, BA is always used as a limiting reagent and in sub-stoichiometric amounts to achieve the desired phase. This method has been used extensively in the literature to form RP crystals with a reasonably high phase purity (**Figure 2.10**a). The next step to make RPP films is to dissolve the crystals in a solvent, usually DMF, and then proceed with spin-coating and thermal annealing. This was firstly reported by Tsai *et al.*, who hot-casted a BA $<n>$ = 4 layer and achieved a PCE of around 12% for a *p-i-n* device.[37] The main issue with this process is that usually the phase purity of RPs is lost once the crystals are dissolved, meaning that when probing the phase distribution in the resulting film, multiple quantum well structures are found instead of a uniform distribution around a specific n-value.
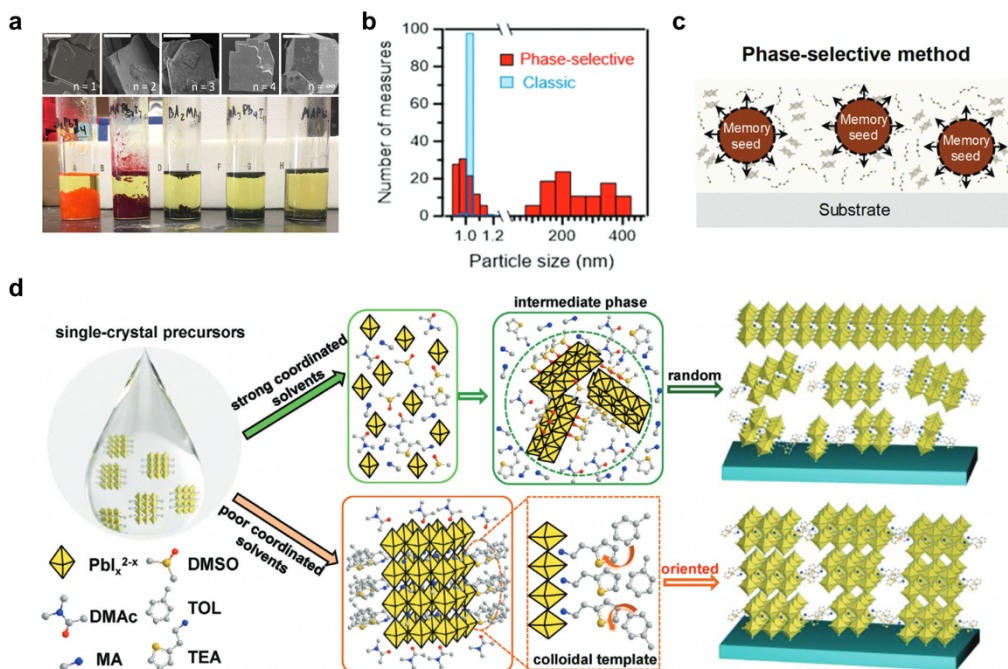
Figure 2.10. (a) Scanning electron microscope (SEM) images (top) and photographs (bottom) of RPP single crystals synthesized from HI/H_3PO_2 solvent mix. Reprinted with permission from [12]. Copyright 2016 American Chemical Society. (b) Dynamic light scattering (DLS) measurement displays the presence of "memory seeds" with phase-selective method. Reprinted with permission from [91]. Copyright 2021 Wiley VCH. (c) Memory seeds act as nucleation points for perovskite crystallization. Reprinted with permission from [91]. Copyright 2021 Wiley VCH. (d) Non-coordinating solvents are used to create a colloidal template to produce phase-pure, vertical oriented RPPs. Reprinted with permission from [92]. Copyright 2020 Wiley VCH.

In a recent work, Sidhik *et al.* investigated how to exploit single crystals to retain phase purity in quasi-2D perovskite films, and by using optimized and relatively phase pure $BA_2MA_2Pb_3I_{10}$ they achieved a PCE of 17.1% and a V_{OC} of 1.20 V.[91] Their method consisted of dissolving single-crystals in DMF, with the addition of a small amount of MACl. The authors found striking differences between the crystallization of perovskites when powder precursors are dissolved in solution or when "parent" crystals are used. In the latter, the precursor solution contains particles of 200 nm average size (Figure 2.10b) that effectively act as memory seeds and around which nucleation takes place (Figure 2.10c), whereas in the former only particles <1 nm were observed and the nucleation appeared to start at the liquid-air interface. Even though with single crystals dissolution higher phase purity is achieved, the resulting films still contain phase impurities. While particle sizes were determined via DLS,

crystallization was investigated via in-situ high-resolution microscopy, a technique barely used to explore perovskites. Nevertheless, the use of relatively phase pure films is not enough to achieve high efficiency. The same perovskite only reached an efficiency of 12.6% when using PEDOT:PSS as HTL, whereas NiO_x improved its efficiency to the abovementioned value of 17.1%. This confirms the importance of HTL and ETL design; for which we refer the reader to extensive works published elsewhere.[93–95]

On a similar note, Qin *et al.* proposed that the use of a non-coordinating co-solvent, such as toluene, in conjunction with HI can dissolve the single crystals but retain particles of ≈1500 nm in solution, which act as a colloidal template for crystallization of relatively phase pure RPPs (Figure 2.10d).[92] On the contrary, a strong coordinating co-solvent decreases the distribution of colloidal particle size to 600 nm, because it coordinates with Pb^{2+} and forms intermediate phases that are not beneficial for phase purity. By using and optimizing this method, they fabricated an RPP based on 2-thiopheneethylammonium iodide (TEAI) and achieved a PCE of 14.68% with a V_{OC} of 1.23 V.

Table 2.5. Solar cell parameters for high-efficiency RPPs fabricated by using several fabrication methods.

RPP	Method*	J_{SC} (mA cm^{-2})	V_{OC} (V)	FF (-)	PCE (%)	Ref.
$(BA)_2MA_2Pb_3I_{10}$	S.C. (R.T., Add.)	17.56	1.20	0.81	17.1	[91]
$(BA)_2MA_3Pb_4I_{13}$	S.C. (H.C., Add.)	19.23	1.14	0.68	14.9	[96]
$(TEA)_2MA_2Pb_3I_{10}$	S.C. (H.C., Add.)	15.85	1.23	0.72	14.68	[92]
$(TMA)_2MA_2Pb_3I_9$	S.C. (A.S.)	18.89	1.07	0.76	15.42	[50]
$(BA)_2MA_4Pb_5I_{16}$	D.C. (Add.)	19.0	1.11	0.64	14.6	[97]
$(BA)_2MA_3Pb_4I_{13}$	D.C.	18.8	1.14	0.69	14.9	[98]
$(iBA)_2MA_4Pb_5I_{16}$	D.C. (N$_2$)	18.3	1.15	0.77	16.0	[99]
$(BA)_2MA_3Pb_4I_{13}$	SPA (H.C.)	19.89	1.24	0.70	17.26	[100]
$(AA)_2MA_3Pb_4I_{13}$	SPA (H.C.)	18.57	1.24	0.80	18.42	[101]
$(AA)_2MA_4Pb_5I_{16}$	SPA (H.C.)	18.69	1.24	0.80	18.68	[102]

* S.C. = single crystal precursors, D.C. = drop casting, SPA = slow post annealing, R.T. = room-temperature spin-coating, H.C. = hot casting, Add. = additives are used in the precursor solution., A.S. = antisolvent, N$_2$ = blow drying. AA = *n*-amylammonium, iBA = isobutylammonium

Single crystals have become a widespread technique to fabricate RPPs, although there is still a lack of consensus on how to achieve phase purity in films even when starting from phase pure single crystals. Regarding phase purity, in-depth studies on the precursor solution are still needed to reach a comprehensive understanding of the topic. As multiple reports have shown, however, relatively high efficiencies (**Table 2.5**) by starting with crystal precursors and applying different strategies to improve the resulting RPP film, this field is promising for further developments of high-efficiency devices.

2.3.2 DROP CASTING

Up to date, most of the processing methods for RPPs include spin-coating, which is known not to be suitable for upscaling. There are, however, some notable examples of active layers fabricated via drop casting method (Table 2.4). This process consists of dropping a small volume of precursor solution onto a preheated substrate (usually at 50 or 60 °C) and is followed by diffusion, solvent evaporation, and crystallization (**Figure 2.11**a). Advantages of drop casting include easy up-scaling, via doctor blading to slot-die coating, and little to no waste of precursor solution.
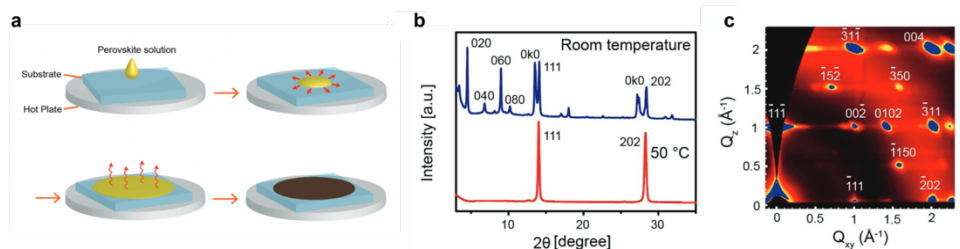
Figure 2.11. (a) Illustration of drop casting fabrication method. (b) XRD patterns of $BA_2MA_3Pb_4I_{13}$ drop casted at room temperature and 50° C (c) GIWAXS pattern of the same film as (b) drop casted at 50°C. Reprinted with permission from [98]. Copyright 2018 Wiley VCH.

In 2019, Zuo *et al.* fabricated $BA_2MA_3Pb_4I_{13}$ via drop casting in air and achieved a 14.9% PCE.[98] The study highlighted the importance of substrate pre-heating to achieve vertical-oriented films with enhanced charge transport (Figure 2.11b,c) and the possibility of easily changing film thickness by simply varying the volume of the precursor solution used in the process. Later, the same group specialized in drop-casting and published a series of articles, in one of which they achieved a 16% solar cell by applying an N_2 blow-drying process to $(iBA)_2MA_3Pb_4I_{13}$ RPPs.[76,97] Such process controlled the film thickness, increased the nucleation rate, and led to smoother films with smaller grains, which improved the morphology. The authors

additionally fabricated solar cells via a roll-to-roll (R2R) processing on a flexible ITO/PET substrate, reaching 9.3% efficiency. This demonstrates that drop casting is a promising method to prepare for upscaling, even though more optimization is highly needed especially in terms of reduction of roughness, sheet resistance, or hydrophobicity of the PET/ITO flexible substrate.[103]

2.3.3 POST-ANNEALING TREATMENTS

The control of phase distribution and crystal alignment of quasi-2D perovskite phases is known to be crucial to fabricate high efficiency devices and avoid the detrimental effect of quantum wells on charge collection. While numerous studies tried to achieve such control *via* rapid-crystallization techniques, such as hot-casting or N_2-quenching, thus focusing on the fabrication of the perovskite layer, several studies have investigated the impact of post-annealing treatments on complete devices (Table 2.5). In 2019, Wu *et al.* introduced for the first time a slow post-annealing (SPA) process, where the complete devices are kept at 60°C for 60 h in an N_2-filled glovebox.[104] The SPA treatment introduced changes in the phase distribution gradient along the thickness of the film, introducing a finer alignment compared to the non-uniform gradient formed just during hot-casting (**Figure 2.12**). By applying this technique to hot-casted $BA_2MA_3Pb_4I_{13}$ in a *p-i-n* solar cell, the authors achieved 17.26% PCE with J_{SC} of almost 20 mA cm^{-2} and an impressive V_{OC} of 1.24 V. Interestingly, applying SPA only on the perovskite layer did not enhance PCE as much as when treating the complete device, possibly because the slow annealing also promotes surface trap passivation by C_{60}, used as ETL. In later studies, the same group pushed the PCE to 18.42%[101] (15.78% before SPA treatment) and 18.68%[102] by using *n*-amylammonium (AA) iodide as organic spacer, which has a C5 chain compared to C4 for butylammonium. In both papers, differences in colloidal aggregation after thermal aging of the precursor solutions and strengthened self-assembly properties due to increased van der Waals interactions were thought to be behind the increase in efficiency. The SPA treatment was used to further enhance the PCE of their best devices.
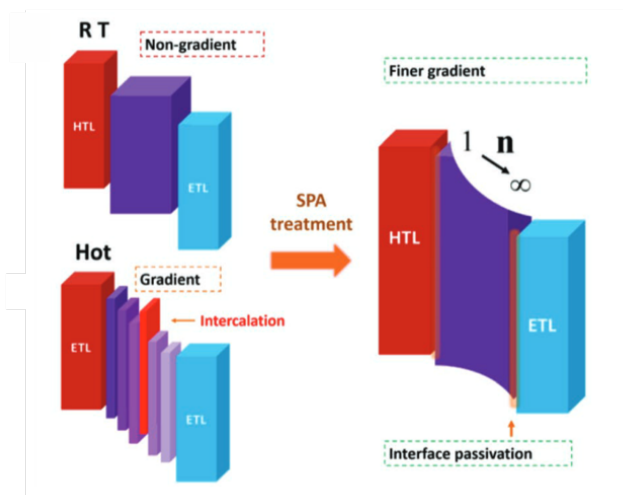
Figure 2.12. SPA process induces a finer gradient along the film thickness and provides interface passivation for improved PCE. Reprinted with permission from [104]. Copyright 2019 Wiley VCH.

Post-annealing methods can be an almost effortless way to push the PCE of RPPs closer to their 3D counterpart. Nevertheless, a careful reader must have now noticed that research on RPPs often leads to groups specializing in one specific technique or method. These methods are rarely directly reproduced by other groups in the community, leaving the question of whether their application is generalizable to other systems. More specifically, questions remain open for the SPA method, such as whether it is dependent on the choice of materials (electron/hole transport layer, electrodes) and perovskite composition. By including methods such as drop-casting and post-annealing treatment in this review, we encourage researchers in the field to evaluate their validity in a variety of systems.

2.4 IMPLICATIONS ON PHASE PURITY AND MULTI-JUNCTION SOLAR CELLS

Despite the high efficiency reached by many RPP-based solar cells, there are important considerations to make regarding the lower dimensional nature of such films. As mentioned before, phase purity has been a long-hunted objective in the RPP field and is a challenging task where both kinetics and thermodynamics aspects need to be tackled. A phase pure device would possess high bandgap and, consequently, V_{OC}. In fact, polydispersity has been previously linked to voltage losses.[34] Solar cells based on phase pure $BA_2MA_3Pb_4I_{13}$ published by Liang *et al.* possess a V_{OC} of 1.31 V, which is the highest value published in the literature.[32] Similarly, Sidikh *et al.* reported a V_{OC} of 1.20 V for relatively phase pure $BA_2MA_2Pb_3I_{10}$, still quite high compared to other cells published in the literature, but lower than the

abovementioned study and with a loss >800 mV considering the bandgap of 2.1 eV associated with the pursued n = 3 perovskite, simply because of the presence of phase impurities with larger n-value.[91,105] Whether or not phase pure quasi-2D perovskites are needed will depend on their application. For example, in light-emitting diodes (LEDs) it is necessary to avoid emission at higher wavelengths from impurities, hence the optimization of phase pure RPPs will be crucial and has already seen promising developments.[106]
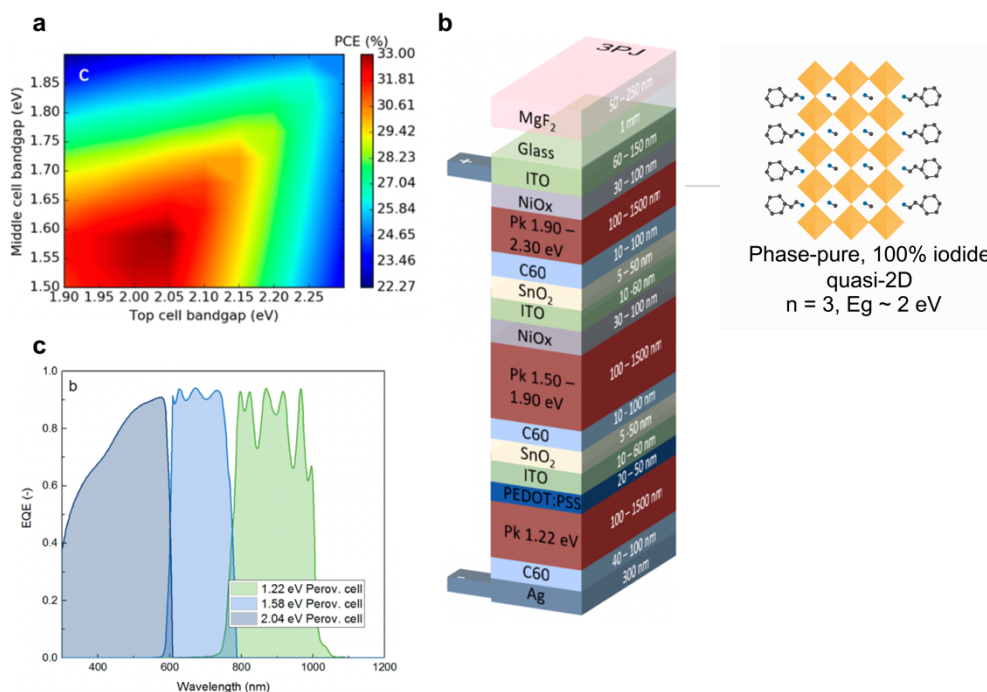
Figure 2.13. (a) Theoretical PCE for a triple-junction all-perovskite solar cell with fixed 1.22 eV narrow bandgap bottom cell. A combination of 1.6 eV middle cell and 2 eV top cell would lead to >30% PCE. (b) Schematic representation of a triple-junction all-perovskite solar cell. A phase pure n = 3 quasi-2D perovskite would be suitable as top cell. (c) Calculated EQE for a triple-junction solar cell. The area highlighted represents the EQE onset of the top cell, which should be sharp enough not to reduce the bandgap and the V_{OC} associated with the top cell. Reprinted with permission from [107]. Copyright 2017 American Chemical Society.

Multijunction solar cells require the use of wide-bandgap perovskite sub-cells with high V_{OC}, which might be quasi-2D in nature if phase purity is reproducibly achieved. Most work on wide-bandgap sub-cells in multi-junction devices, however, is currently based on traditional 3D mixed-halide perovskites, which undergo phase segregation under illumination, meaning that low-energy iodide-rich phases are formed once the solar cell is illuminated, providing a significant shift in bandgap

energy and loss in photovoltaic performances. RPPs could provide the optimal bandgaps for such application; an n = 3 phase-pure iodide-based RPP would possess an optical bandgap of about 2 eV, which is ideal for a triple-junction perovskite solar cells with estimated maximum efficiency >30%,[107–109] without the need of mixed-halide compositions (**Figure 2.13**a,b). Once control of phase purity becomes an option, we anticipate broad use of RPPs for multi-junction solar cells. Presently, high-efficiency RPPs lack the high V_{OC} required for this application because their dominant 3D (or large-n) nature leads to a decrease of E_g. In the case of a triple-junction solar cell, phase impurities in quasi-2D perovskite with reduced bandgap reduce the V_{OC} (Figure 2.13c). Interestingly, this draws a parallel between the phase segregation issue in 3D mixed-halide perovskites and phase distribution in quasi-2D RPPs, which both potentially impact the field of multi-junction devices.

For applications in single-junction PV devices, however, phase purity seems not to be a pressing concern, and stability could become the key issue that RPPs try to improve. An example is the use of precursor organic salts-assisted crystal growth method (PACG) mentioned earlier to achieve high efficiency RPPs. In that study by Lai *et al.*, the bandgap energy was calculated as 1.50 eV, which is comparable to the one of FAPbI$_3$, and the EQE spectrum displayed a large contribution at ≈800 nm. As the films were prepared with a nominal stoichiometry of $<n>$ = 5, this suggests that the solar cell performances were dominated by 3D phases more than quasi-2D ones, which should instead have higher bandgap energy.[44] Nevertheless, the authors demonstrated significantly enhanced environmental and thermal stability of the RPPs compared to FAPbI$_3$. As a result, further efforts to bring the PCEs of RPP-based solar cells close to the 3D counterpart, despite the presence of phase impurities, might lead to an easier path to commercialization because of their enhanced stability. In our view, such studies should put more focus on stability, apart from solar cell performances, which could eventually be the main reason why RPPs will be preferred over the (until now) more efficient 3D perovskites. Such focus should result in a deeper understanding of the degradation paths of RPPs and, additionally, in uniform testing conditions, so that it becomes easier to draw comparisons between different studies, as is well explained in the consensus statement for stability assessment that was recently published and signed by many researchers of the field.[46]

Overall, a reproducible method to fabricate phase pure RPPs will be a breakthrough that will pave the way to numerous applications that expand well beyond photovoltaics. As a result, the research community is dedicating time and effort to accomplish this task via a variety of methods that include the use of solvents,[29,110] additives,[106] new spacers,[27], and new fabrication methods.[111] In

addition, as phase pure RPPs also display enhanced stability compared to ones containing a mixture of phases, such a breakthrough would be impactful also for long-term stability of devices such as multi-junction solar cells, which currently suffer from instabilities from Br-containing wide-bandgap perovskites.

2.5 OUTLOOK

As more knowledge of Ruddlesden-Popper perovskites is developed, their efficiency in solar cell devices is slowly approaching the one of the 3D counterparts, although still lagging behind $FAPbI_3$-based solar cells.[59,60] In this work, we discussed several studies where multiple strategies have been used to achieve efficiencies above ~14%. Most of the high-efficiency solar cells rely on the use of additives that have an impact on morphology, crystallinity, vertical orientation, phase distribution, and charge transport. The additives used are usually chlorides, such as MACl or NH_4Cl, or thiocyanates, such as NH_4SCN. In some works, an additional organic spacer is used as an additive to improve the abovementioned properties, either in the perovskite layer or even in the antisolvent solution. Interestingly, even for the less-common fabrication methods, such as drop casting or slow post-annealing of complete devices, the use of such additives was often a prerequisite. Additive engineering is clearly an effective tool to achieve higher efficiencies, even though the mechanism behind the enhancement in efficiency is often not studied or explained. Just like using hot-casting and anti-solvents have become a routine optimization path for developing RPPs, it seems that the use of such additives is also approaching the same route. As such, in our view, more studies are needed to evaluate the generalizability of such systems and more importantly the unravelling underlying mechanisms.

Apart from additive engineering, tuning the interlayer interaction and the dielectric confinement has also proved to be an effective way to increase the PCE of RPPs. Fluorination is by far the most successful strategy described in the literature. Given the enormous structural variety that is achievable with RPPs, functionalization of organic spacers is still an unexplored territory that needs further developments. For a more thorough study of the impact of spacers on RPPs, we refer to the extensive review recently published by Li *et al.*[17]

The study of precursor solution will also be crucial in developing a reproducible method to form efficient, phase pure RPPs. Up to now, there are conflicting reports on the impact of colloidal particles size distribution. For example, when phase pure RPPs were obtained by dissolving previously synthesized single-crystals in a solvent, Sidhik *et al.* highlighted the importance of having particles of around 200 nm, or seeds, in solution.[91] Qin *et al.* improved phase purity by using toluene and

HI as co-solvent and additive, respectively, to boost the colloidal particles size up to 1500 nm.[92] On the contrary, phase pure perovskites fabricated with acetate salts were spin-coated from a solution with an average particle size of 0.6 nm, which in that case was attributed to the interaction of Pb^{2+} and Ac^- and was reported to be an important requirement to crystallize a single n-phase.[32] Overall, a more comprehensive study on the role of colloidal particle size is needed, as it seems that the precursor solution plays an even more major role in RPPs than in 3D perovskites.

Finally, there is a general difficulty in evaluating the phase purity of RPPs. For this purpose, more efforts are needed to characterize the phase distribution of high-efficiency RPPs and to find ways to effectively fabricate films with narrow phase distribution. As we have described above, high PCEs can result also from a large contribution from 3D perovskite phases, which are usually responsible for lower V_{OC} and higher J_{SC}. For some applications, such as tandem solar cells, phase purity is a crucial concern, and improving it would definitely lead to breakthroughs in multi-junction photovoltaic devices. Single-junction solar cells, on the contrary, seem to show enhanced stability for highly efficient devices, even in the presence of phase impurities, hence a deeper understanding of the degradation paths of RPPs, together with further enhancements of PCEs, might be the key to lead perovskite solar cells closer to commercialization.

Overall, Ruddlesden-Popper perovskites have shown enormous potential and in just a few years a great amount of expertise has developed. Despite RPPs being often described as "more stable but less efficient" compared to traditional 3Ds, with this work we show that there is plenty of potential and room for further improvements of this fascinating class of materials.

2.6 REFERENCES

[1]   National Renewable Energy Laboratory (NREL), "Best Research-Cell Efficiencies," can be found under https://www.nrel.gov/pv/cell-efficiency.html.
[2]   M. Saliba, J.-P. Correa-Baena, M. Grätzel, A. Hagfeldt, A. Abate, *Angew. Chem., Int. Ed.* **2018**, *57*, 2554.
[3]   X. Wu, B. Li, Z. Zhu, C.-C. Chueh, A. K. Y. Jen, *Chem. Soc. Rev.* **2021**, *50*, 13090.
[4]   P. Gao, A. R. bin Mohd Yusoff, M. K. Nazeeruddin, *Nat. Commun.* **2018**, *9*, 5028.
[5]   G. Grancini, M. K. Nazeeruddin, *Nat. Rev. Mater.* **2019**, *4*, 4.
[6]   Y. Zheng, T. Niu, X. Ran, J. Qiu, B. Li, Y. Xia, Y. Chen, W. Huang, *J. Mater. Chem. A* **2019**, *7*, 13860.
[7]   C. Ortiz-Cervantes, P. Carmona-Monroy, D. Solis-Ibarra, *ChemSusChem* **2019**, *12*, 1560.
[8]   Y. Chen, Y. Sun, J. Peng, J. Tang, K. Zheng, Z. Liang, *Adv. Mater.* **2018**, *30*, 1703487.
[9]   X. Gao, X. Zhang, W. Yin, H. Wang, Y. Hu, Q. Zhang, Z. Shi, V. L. Colvin, W. W. Yu, Y. Zhang, *Adv. Sci.* **2019**, *6*, 1900941.
[10] C. C. Stoumpos, C. M. M. Soe, H. Tsai, W. Nie, J. C. Blancon, D. H. Cao, F. Liu, B. Traoré, C. Katan, J. Even, A. D. Mohite, M. G. Kanatzidis, *Chem* **2017**, *2*, 427.
[11] T. Niu, H. Ren, B. Wu, Y. Xia, X. Xie, Y. Yang, X. Gao, Y. Chen, W. Huang, *J. Phys. Chem.* **2019**, *10*, 2349.

[12] C. C. Stoumpos, D. H. Cao, D. J. Clark, J. Young, J. M. Rondinelli, J. I. Jang, J. T. Hupp, M. G. Kanatzidis, *Chem. Mater.* **2016**, *28*, 2852.

[13] P. Huang, S. Kazim, M. Wang, S. Ahmad, *ACS Energy Lett.* **2019**, *4*, 2960.

[14] M. C. Gélvez-Rueda, E. M. Hutter, D. H. Cao, N. Renaud, C. C. Stoumpos, J. T. Hupp, T. J. Savenije, M. G. Kanatzidis, F. C. Grozema, *J. Phys. Chem. C* **2017**, *121*, 26566.

[15] F. Zhang, S. Y. Park, C. Yao, H. Lu, S. P. Dunfield, C. Xiao, S. Uličná, X. Zhao, L. du Hill, X. Chen, X. Wang, L. E. Mundt, K. H. Stone, L. T. Schelhas, G. Teeter, S. Parkin, E. L. Ratcliff, Y.-L. Loo, J. J. Berry, M. C. Beard, Y. Yan, B. W. Larson, K. Zhu, *Science* **2022**, *375*, 71.

[16] H. Chen, S. Teale, B. Chen, Y. Hou, L. Grater, T. Zhu, K. Bertens, S. M. Park, H. R. Atapattu, Y. Gao, M. Wei, A. K. Johnston, Q. Zhou, K. Xu, D. Yu, C. Han, T. Cui, E. H. Jung, C. Zhou, W. Zhou, A. H. Proppe, S. Hoogland, F. Laquai, T. Filleter, K. R. Graham, Z. Ning, E. H. Sargent, *Nat. Photonics* **2022**, *16*, 352.

[17] X. Li, J. M. Hoffman, M. G. Kanatzidis, *Chem. Rev.* **2021**, *121*, 2230.

[18] W. Guo, Z. Yang, J. Dang, M. Wang, *Nano Energy* **2021**, *86*, 106129.

[19] T. Niu, Q. Xue, H. L. Yip, *Nanophotonics* **2021**, *10*, 2069.

[20] H. Fu, *J. Mater. Chem. C* **2021**, *9*, 6378.

[21] E. S. Vasileiadou, B. Wang, I. Spanopoulos, I. Hadar, A. Navrotsky, M. G. Kanatzidis, *J. Am. Chem. Soc.* **2021**, *143*, 2523.

[22] J. M. Hoffman, J. Strzalka, N. C. Flanders, I. Hadar, S. A. Cuthriell, Q. Zhang, R. D. Schaller, W. R. Dichtel, L. X. Chen, M. G. Kanatzidis, *Adv. Mater.* **2020**, *32*, 2002812.

[23] A. Z. Chen, M. Shiu, J. H. Ma, M. R. Alpert, D. Zhang, B. J. Foley, D. M. Smilgies, S. H. Lee, J. J. Choi, *Nat. Commun.* **2018**, *9*, 1336.

[24] T. Liu, Y. Jiang, M. Qin, J. Liu, L. Sun, F. Qin, L. Hu, S. Xiong, X. Jiang, F. Jiang, P. Peng, S. Jin, X. Lu, Y. Zhou, *Nat. Commun.* **2019**, *10*, 878.

[25] N. Liu, P. Liu, H. Ren, H. Xie, N. Zhou, Y. Gao, Y. Li, H. Zhou, Y. Bai, Q. Chen, *ACS Appl. Mater. Interfaces* **2020**, *12*, 3127.

[26] F. Zheng, C. R. Hall, D. Angmo, C. Zuo, S. Rubanov, Z. Wen, S. J. Bradley, X.-T. Hao, M. Gao, T. A. Smith, K. P. Ghiggino, *J. Mater. Chem. C* **2021**, *9*, 5362.

[27] A. H. Proppe, R. Quintero-Bermudez, H. Tan, O. Voznyy, S. O. Kelley, E. H. Sargent, *J. Am. Chem. Soc.* **2018**, *140*, 2890.

[28] A. Z. Chen, J. J. Choi, *J. Vac. Sci. Technol. A* **2020**, *38*, 010801.

[29] A. Caiazzo, K. Datta, J. Jiang, M. C. Gélvez-Rueda, J. Li, R. Ollearo, J. M. Vicent-Luna, S. Tao, F. C. Grozema, M. M. Wienk, R. A. J. Janssen, *Adv. Energy Mater.* **2021**, *11*, 2102144.

[30] L. Liu, Y. Bai, X. Zhang, Y. Shang, C. Wang, H. Wang, C. Zhu, C. Hu, J. Wu, H. Zhou, Y. Li, S. Yang, Z. Ning, Q. Chen, *Angew. Chem., Int. Ed.* **2020**, *59*, 5979.

[31] Y. Wei, H. Chu, Y. Tian, B. Chen, K. Wu, J. Wang, X. Yang, B. Cai, Y. Zhang, J. Zhao, *Adv. Energy Mater.* **2019**, *9*, 1900612.

[32] C. Liang, H. Gu, Y. Xia, Z. Wang, X. Liu, J. Xia, S. Zuo, Y. Hu, X. Gao, W. Hui, L. Chao, T. Niu, M. Fang, H. Lu, H. Dong, H. Yu, S. Chen, X. Ran, L. Song, B. Li, J. Zhang, Y. Peng, G. Shao, J. Wang, Y. Chen, G. Xing, W. Huang, *Nat. Energy* **2021**, *6*, 38.

[33] S. Y. Leblebici, L. Leppert, Y. Li, S. E. Reyes-Lillo, S. Wickenburg, E. Wong, J. Lee, M. Melli, D. Ziegler, D. K. Angell, D. F. Ogletree, P. D. Ashby, F. M. Toma, J. B. Neaton, I. D. Sharp, A. Weber-Bargioni, *Nat. Energy* **2016**, *1*, 16093.

[34] R. Quintero-Bermudez, A. Gold-Parker, A. H. Proppe, R. Munir, Z. Yang, S. O. Kelley, A. Amassian, M. F. Toney, E. H. Sargent, *Nat. Mater.* **2018**, *17*, 900.

[35] W. L. Tan, Y.-B. Cheng, C. R. McNeill, *J. Mater. Chem. A* **2020**, *8*, 12790.

[36] A. Z. Chen, M. Shiu, X. Deng, M. Mahmoud, D. Zhang, B. J. Foley, S.-H. Lee, G. Giri, J. J. Choi, *Chem. Mater.* **2019**, *31*, 1336.

[37] H. Tsai, W. Nie, J.-C. Blancon, C. C. Stoumpos, R. Asadpour, B. Harutyunyan, A. J. Neukirch, R. Verduzco, J. J. Crochet, S. Tretiak, L. Pedesseau, J. Even, M. A. Alam, G. Gupta, J. Lou, P. M. Ajayan, M. J. Bedzyk, M. G. Kanatzidis, A. D. Mohite, *Nature* **2016**, *536*, 312.

[38] M. D. Malouangou, J. T. Matondo, L. Bai, M. Mbumba, Y. Yang, M. W. Akram, M. Guli, *ACS Appl. Energy Mater.* **2021**, *4*, 13216.

[39] C. M. M. Soe, W. Nie, C. C. Stoumpos, H. Tsai, J. C. Blancon, F. Liu, J. Even, T. J. Marks, A. D. Mohite, M. G. Kanatzidis, *Adv. Energy Mater.* **2018**, *8*, 2.

[40] F. Zhu, G. Lian, B. Yu, T. Zhang, L. Zhang, H. Yu, D. Cui, Q. Wang, H. Zhang, Q. Meng, C.-P. Wong, *ACS Applied Materials & Interfaces* **2022**, *14*, 1526.

[41] I. C. Smith, E. T. Hoke, D. Solis-Ibarra, M. D. McGehee, H. I. Karunadasa, *Angew. Chem., Int. Ed.* **2014**, *53*, 11232.

[42] L. N. Quan, M. Yuan, R. Comin, O. Voznyy, E. M. Beauregard, S. Hoogland, A. Buin, A. R. Kirmani, K. Zhao, A. Amassian, D. H. Kim, E. H. Sargent, *J. Am. Chem. Soc.* **2016**, *138*, 2649.

[43] M. Shao, T. Bie, L. Yang, Y. Gao, X. Jin, F. He, N. Zheng, Y. Yu, X. Zhang, *Adv. Mater.* **2022**, *34*, 2107211.

[44] H. Lai, D. Lu, Z. Xu, N. Zheng, Z. Xie, Y. Liu, *Adv. Mater.* **2020**, *32*, 2001470.

[45] Z. Wang, L. Liu, X. Liu, D. Song, D. Shi, S. Wu, Y. Tong, H. Ren, M. Li, Y. Zheng, D. Zhao, *Chem. Eng. J.* **2022**, *432*, 134367.

[46] M. v Khenkin, E. A. Katz, A. Abate, G. Bardizza, J. J. Berry, C. Brabec, F. Brunetti, V. Bulović, Q. Burlingame, A. di Carlo, R. Cheacharoen, Y.-B. Cheng, A. Colsmann, S. Cros, K. Domanski, M. Dusza, C. J. Fell, S. R. Forrest, Y. Galagan, D. di Girolamo, M. Grätzel, A. Hagfeldt, E. von Hauff, H. Hoppe, J. Kettle, H. Köbler, M. S. Leite, S. Liu, Y.-L. Loo, J. M. Luther, C.-Q. Ma, M. Madsen, M. Manceau, M. Matheron, M. McGehee, R. Meitzner, M. K. Nazeeruddin, A. F. Nogueira, Ç. Odabaşı, A. Osherov, N.-G. Park, M. O. Reese, F. de Rossi, M. Saliba, U. S. Schubert, H. J. Snaith, S. D. Stranks, W. Tress, P. A. Troshin, V. Turkovic, S. Veenstra, I. Visoly-Fisher, A. Walsh, T. Watson, H. Xie, R. Yıldırım, S. M. Zakeeruddin, K. Zhu, M. Lira-Cantu, *Nat. Energy* **2020**, *5*, 35.

[47] Z. Wang, Q. Wei, X. Liu, L. Liu, X. Tang, J. Guo, S. Ren, G. Xing, D. Zhao, Y. Zheng, *Adv. Funct. Mater.* **2021**, *31*, 2008404.

[48] J. Shi, Y. Gao, X. Gao, Y. Zhang, J. Zhang, X. Jing, M. Shao, *Adv. Mater.* **2019**, *31*, 1901673.

[49] Y. Dong, D. Lu, Z. Xu, H. Lai, Y. Liu, *Adv. Energy Mater.* **2020**, *10*, 2000694.

[50] H. Lai, B. Kan, T. Liu, N. Zheng, Z. Xie, T. Zhou, X. Wan, X. Zhang, Y. Liu, Y. Chen, *J. Am. Chem. Soc.* **2018**, *140*, 11639.

[51] H. Ren, S. Yu, L. Chao, Y. Xia, Y. Sun, S. Zuo, F. Li, T. Niu, Y. Yang, H. Ju, B. Li, H. Du, X. Gao, J. Zhang, J. Wang, L. Zhang, Y. Chen, W. Huang, *Nat. Photonics* **2020**, *14*, 154.

[52] Z. Wang, X. Liu, H. Ren, L. Liu, X. Tang, X. Yao, Z. Su, X. Gao, Q. Wei, H. Xie, Y. Zheng, M. Li, *ACS Appl. Mater. Interfaces* **2022**, *14*, 7917.

[53] F. Zhang, D. H. Kim, H. Lu, J.-S. Park, B. W. Larson, J. Hu, L. Gao, C. Xiao, O. G. Reid, X. Chen, Q. Zhao, P. F. Ndione, J. J. Berry, W. You, A. Walsh, M. C. Beard, K. Zhu, *J. Am. Chem. Soc.* **2019**, *141*, 5972.

[54] Q. Li, Y. Dong, G. Lv, T. Liu, D. Lu, N. Zheng, X. Dong, Z. Xu, Z. Xie, Y. Liu, *ACS Energy Lett.* **2021**, *6*, 2072.

[55] Y. Lin, Y. Bai, Y. Fang, Q. Wang, Y. Deng, J. Huang, *ACS Energy Lett.* **2017**, *2*, 1571.

[56] Z. Huang, A. H. Proppe, H. Tan, M. I. Saidaminov, F. Tan, A. Mei, C.-S. Tan, M. Wei, Y. Hou, H. Han, S. O. Kelley, E. H. Sargent, *ACS Energy Lett.* **2019**, *4*, 1521.

[57] J. Cho, P. S. Mathew, J. T. DuBose, P. v. Kamat, *Adv. Mater.* **2021**, *33*, 2105585.

[58] J. J. Yoo, G. Seo, M. R. Chua, T. G. Park, Y. Lu, F. Rotermund, Y. Kim, C. S. Moon, N. J. Jeon, J.-P. Correa-Baena, V. Bulović, S. S. Shin, M. G. Bawendi, J. Seo, *Nature* **2021**, *590*, 587.

[59] J. Jeong, M. Kim, J. Seo, H. Lu, P. Ahlawat, A. Mishra, Y. Yang, M. A. Hope, F. T. Eickemeyer, M. Kim, Y. J. Yoon, I. W. Choi, B. P. Darwich, S. J. Choi, Y. Jo, J. H. Lee, B. Walker, S. M. Zakeeruddin, L. Emsley, U. Rothlisberger, A. Hagfeldt, D. S. Kim, M. Grätzel, J. Y. Kim, *Nature* **2021**, *592*, 381.

[60] H. Min, D. Y. Lee, J. Kim, G. Kim, K. S. Lee, J. Kim, M. J. Paik, Y. K. Kim, K. S. Kim, M. G. Kim, T. J. Shin, S. il Seok, *Nature* **2021**, *598*, 444.

[61] X. Zhang, X. Ren, B. Liu, R. Munir, X. Zhu, D. Yang, J. Li, Y. Liu, D.-M. Smilgies, R. Li, Z. Yang, T. Niu, X. Wang, A. Amassian, K. Zhao, S. (Frank) Liu, *Energy Environ. Sci.* **2017**, *10*, 2095.

[62] R. Yang, R. Li, Y. Cao, Y. Wei, Y. Miao, W. L. Tan, X. Jiao, H. Chen, L. Zhang, Q. Chen, H. Zhang, W. Zou, Y. Wang, M. Yang, C. Yi, N. Wang, F. Gao, C. R. McNeill, T. Qin, J. Wang, W. Huang, *Adv. Mater.* **2018**, *30*, 1804771.

[63] D. Deng, Y. Zhang, J. Zhang, Z. Wang, L. Zhu, J. Fang, B. Xia, Z. Wang, K. Lu, W. Ma, Z. Wei, *Nat. Commun.* **2016**, *7*, 13740.

[64] J. Liang, Z. Zhang, Y. Zheng, X. Wu, J. Wang, Z. Zhou, Y. Yang, Y. Huang, Z. Chen, C. C. Chen, *J. Mater. Chem. A* **2021**, *9*, 11741.

[65] W. Fu, H. Liu, X. Shi, L. Zuo, X. Li, A. K. Y. Jen, *Adv. Funct. Mater.* **2019**, *29*, 1900221.

[66] X. Li, W. Hu, Y. Shang, X. Yu, X. Wang, W. Zhou, M. Wang, Q. Luo, C. Q. Ma, Y. Lu, S. Yang, *J. Energy Chem.* **2022**, *66*, 680.

[67] J. v. Milić, S. M. Zakeeruddin, M. Grätzel, *Acc. Chem. Res.* **2021**, *54*, 2729.

[68] J. Qing, S. Ramesh, Q. Xu, X. Liu, H. Wang, Z. Yuan, Z. Chen, L. Hou, T. C. Sum, F. Gao, *Adv. Mater.* **2021**, *33*, 2104381.

[69] X. Lian, J. Chen, M. Qin, Y. Zhang, S. Tian, X. Lu, G. Wu, H. Chen, *Angew. Chem., Int. Ed.* **2019**, *58*, 9409.

[70] H. Zheng, T. Zhang, Y. Wang, C. Li, Z. Su, Z. Wang, H. Chen, S. Yuan, Y. Gu, L. Ji, J. Li, S. Li, *ACS Appl. Mater. Interfaces* **2022**, *14*, 814.

[71] C. Liu, R. Liu, Z. Bi, Y. Yu, G. Xu, H. Hou, Q. Wu, H. Yu, X. Xu, *Solar RRL* **2021**, *5*, 2100495.

[72] M. Long, T. Zhang, D. Chen, M. Qin, Z. Chen, L. Gong, X. Lu, F. Xie, W. Xie, J. Chen, J. Xu, *ACS Energy Lett.* **2019**, *4*, 1025.

[73] J. Shi, X. Jin, Y. Wu, M. Shao, *APL Mater.* **2020**, *8*, 101102.

[74] K. Odysseas Kosmatos, L. Theofylaktos, E. Giannakaki, D. Deligiannis, M. Konstantakou, T. Stergiopoulos, *Energy Environ. Mater.* **2019**, *2*, 79.

[75] M. Jeong, I. W. Choi, E. M. Go, Y. Cho, M. Kim, B. Lee, S. Jeong, Y. Jo, H. W. Choi, J. Lee, J.-H. Bae, S. K. Kwak, D. S. Kim, C. Yang, *Science* **2020**, *369*, 1615.

[76] F. Zheng, C. Zuo, M. Niu, C. Zhou, S. J. Bradley, C. R. Hall, W. Xu, X. Wen, X. Hao, M. Gao, T. A. Smith, K. P. Ghiggino, *ACS Appl. Mater. Interfaces* **2020**, *12*, 25980.

[77] Y. Xie, H. Yu, J. Duan, L. Xu, B. Hu, *ACS Appl. Mater. Interfaces* **2020**, *12*, 11190.

[78] X. Li, G. Wu, M. Wang, B. Yu, J. Zhou, B. Wang, X. Zhang, H. Xia, S. Yue, K. Wang, C. Zhang, J. Zhang, H. Zhou, Y. Zhang, *Adv. Energy Mater.* **2020**, *10*, 2001832.

[79] Y. Yang, C. Liu, O. A. Syzgantseva, M. A. Syzgantseva, S. Ma, Y. Ding, M. Cai, X. Liu, S. Dai, M. K. Nazeeruddin, *Adv. Energy Mater.* **2021**, *11*, 2002966.

[80] W. Fu, J. Wang, L. Zuo, K. Gao, F. Liu, D. S. Ginger, *ACS Energy Lett.* **2018**, *3*, 2086.

[81] Z. Han, W. Fu, Y. Zou, Y. Gu, J. Liu, B. Huang, D. Yu, F. Cao, X. Li, X. Xu, H. Zeng, *Adv. Mater.* **2021**, *33*, 2003852.

[82] X. Zhang, G. Wu, S. Yang, W. Fu, Z. Zhang, C. Chen, W. Liu, J. Yan, W. Yang, H. Chen, *Small* **2017**, *13*, 1700611.

[83] Z. Wang, Y. Zhou, S. Pang, Z. Xiao, J. Zhang, W. Chai, H. Xu, Z. Liu, N. P. Padture, G. Cui, *Chem. Mater.* **2015**, *27*, 7149.

[84] T. Zhu, Y. Yang, K. Gu, C. Liu, J. Zheng, X. Gong, *ACS Appl. Mater. Interfaces* **2020**, *12*, 51744.

[85] L. Chao, T. Niu, Y. Xia, X. Ran, Y. Chen, W. Huang, *J. Phys. Chem.* **2019**, *10*, 1173.

[86] J. Qing, C. Kuang, H. Wang, Y. Wang, X. Liu, S. Bai, M. Li, T. C. Sum, Z. Hu, W. Zhang, F. Gao, *Adv. Mater.* **2019**, *31*, 1904243.

[87] J. Song, G. Zhou, W. Chen, Q. Zhang, J. Ali, Q. Hu, J. Wang, C. Wang, W. Feng, A. B. Djurišić, H. Zhu, Y. Zhang, T. Russell, F. Liu, *Adv. Mater.* **2020**, *32*, 2002784.

[88] L. Chao, Y. Xia, B. Li, G. Xing, Y. Chen, W. Huang, *Chem* **2019**, *5*, 995.

[89] K. Datta, B. T. van Gorkom, Z. Chen, M. J. Dyson, T. P. A. van der Pol, S. C. J. Meskers, S. Tao, P. A. Bobbert, M. M. Wienk, R. A. J. Janssen, *ACS Appl. Energy Mater.* **2021**, *4*, 6650.

[90] J. Xu, C. C. Boyd, Z. J. Yu, A. F. Palmstrom, D. J. Witter, B. W. Larson, R. M. France, J. Werner, S. P. Harvey, E. J. Wolf, W. Weigand, S. Manzoor, M. F. A. M. van Hest, J. J. Berry, J. M. Luther, Z. C. Holman, M. D. McGehee, *Science* **2020**, *367*, 1097.

[91] S. Sidhik, W. Li, M. H. K. Samani, H. Zhang, Y. Wang, J. Hoffman, A. K. Fehr, M. S. Wong, C. Katan, J. Even, A. B. Marciel, M. G. Kanatzidis, J. Blancon, A. D. Mohite, *Adv. Mater.* **2021**, *33*, 2007176.

[92] Y. Qin, H. Zhong, J. J. Intemann, S. Leng, M. Cui, C. Qin, M. Xiong, F. Liu, A. K. -Y. Jen, K. Yao, *Adv. Energy Mater.* **2020**, *10*, 1904050.

[93] V. M. le Corre, M. Stolterfoht, L. Perdigón Toro, M. Feuerstein, C. Wolff, L. Gil-Escrig, H. J. Bolink, D. Neher, L. J. A. Koster, *ACS Appl. Energy Mater.* **2019**, *2*, 6280.

[94] G. M. Arumugam, S. K. Karunakaran, C. Liu, C. Zhang, F. Guo, S. Wu, Y. Mai, *Nano Select* **2021**, *2*, 1081.

[95] S. Sidhik, Y. Wang, W. Li, H. Zhang, X. Zhong, A. Agrawal, I. Hadar, I. Spanopoulos, A. Mishra, B. Traoré, M. H. K. Samani, C. Katan, A. B. Marciel, J.-C. Blancon, J. Even, A. Kahn, M. G. Kanatzidis, A. D. Mohite, *Cell Rep.* **2021**, *2*, 100601.

[96] H. Li, X. Wang, T. Zhang, X. Gong, Q. Sun, H. Pan, Y. Shen, S. Ahmad, M. Wang, *Adv. Funct. Mater.* **2019**, *29*, 1903296.

[97] C. Zuo, A. D. Scully, W. L. Tan, F. Zheng, K. P. Ghiggino, D. Vak, H. Weerasinghe, C. R. McNeill, D. Angmo, A. S. R. Chesman, M. Gao, *Commun. Mater.* **2020**, *1*, 33.

[98] C. Zuo, A. D. Scully, D. Vak, W. Tan, X. Jiao, C. R. McNeill, D. Angmo, L. Ding, M. Gao, *Adv. Energy Mater.* **2019**, *9*, 1803258.

[99] F. Zheng, C. Zuo, M. Niu, C. Zhou, S. J. Bradley, C. R. Hall, W. Xu, X. Wen, X. Hao, M. Gao, T. A. Smith, K. P. Ghiggino, *ACS Appl. Mater. Interfaces* **2020**, *12*, 25980.

[100] G. Wu, X. Li, J. Zhou, J. Zhang, X. Zhang, X. Leng, P. Wang, M. Chen, D. Zhang, K. Zhao, S. Liu, H. Zhou, Y. Zhang, *Adv. Mater.* **2019**, *31*, 1903889.

[101] G. Wu, T. Yang, X. Li, N. Ahmad, X. Zhang, S. Yue, J. Zhou, Y. Li, H. Wang, X. Shi, S. (Frank) Liu, K. Zhao, H. Zhou, Y. Zhang, *Matter* **2021**, *4*, 582.

[102] X. Li, K. Li, B. Wang, X. Zhang, S. Yue, Y. Li, Q. Chen, S. Li, T. Yue, H. Zhou, Y. Zhang, *Adv. Funct. Mater.* **2021**, *31*, 2107675.

[103] C. Zuo, A. D. Scully, M. Gao, *ACS Appl. Mater. Interfaces* **2021**, *13*, 56217.

[104] G. Wu, X. Li, J. Zhou, J. Zhang, X. Zhang, X. Leng, P. Wang, M. Chen, D. Zhang, K. Zhao, S. (Frank) Liu, H. Zhou, Y. Zhang, *Adv. Mater.* **2019**, *31*, 1903889.

[105] Y. Lin, Y. Fang, J. Zhao, Y. Shao, S. J. Stuard, M. M. Nahid, H. Ade, Q. Wang, J. E. Shield, N. Zhou, A. M. Moran, J. Huang, *Nat. Commun.* **2019**, *10*, 1008.

[106] D. Ma, K. Lin, Y. Dong, H. Choubisa, A. H. Proppe, D. Wu, Y.-K. Wang, B. Chen, P. Li, J. Z. Fan, F. Yuan, A. Johnston, Y. Liu, Y. Kang, Z.-H. Lu, Z. Wei, E. H. Sargent, *Nature* **2021**, *599*, 594.

[107] M. T. Hörantner, T. Leijtens, M. E. Ziffer, G. E. Eperon, M. G. Christoforo, M. D. McGehee, H. J. Snaith, *ACS Energy Lett.* **2017**, *2*, 2506.

[108] J. Wang, V. Zardetto, K. Datta, D. Zhang, M. M. Wienk, R. A. J. Janssen, *Nat. Commun.* **2020**, *11*, 5254.

[109] K. Xiao, J. Wen, Q. Han, R. Lin, Y. Gao, S. Gu, Y. Zang, Y. Nie, J. Zhu, J. Xu, H. Tan, *ACS Energy Lett.* **2020**, *5*, 2819.

[110] Y. Han, S. Park, J. Wang, S. Jariwala, K. Lee, C. G. Bischak, S. Kim, J. Hong, S. Kim, M. J. Lee, D. S. Ginger, I. Hwang, *Adv. Mater. Interfaces* **2019**, *7*, 1901860.

[111] S. Shao, H. Duim, Q. Wang, B. Xu, J. Dong, S. Adjokatse, G. R. Blake, L. Protesescu, G. Portale, J. Hou, M. Saba, M. A. Loi, *ACS Energy Lett.* **2020**, *5*, 39.

3

Effect of Co-solvents on the Crystallization and Phase Distribution of Quasi-2D Perovskites

Abstract

Changing the number of inorganic layers (n) sandwiched between the organic spacers allows for bandgap tuning of quasi-2D perovskites. However, narrowing the phase distribution around a specific n-value is a challenge. Here, in-situ UV–vis–NIR absorption spectroscopy is used to time-resolve the crystallization dynamics of quasi-2D butylammonium-based (BA) perovskites with $<n>$ = 4, processed from N,N-dimethylformamide (DMF) in the presence of different co-solvents. By combining with photoluminescence, transient absorption, and X-ray characterization, the crystallization is correlated to the distribution of phases with different n-values. Infrared spectroscopy and density functional theory reveal that the phase distribution correlates with perovskite precursor—co-solvent interaction energies and that stronger interactions shift the phase distribution towards smaller n-values. Careful tuning of the solvent/co-solvent ratio provides a more homogeneous phase distribution, providing a power conversion efficiency for $BA_2MA_3Pb_4I_{13}$ solar cells that increases from 3.5% when processed from DMF to over 11% and 10% when processed from DMF/co-solvent mixtures.

3.1 INTRODUCTION

2D and quasi-2D perovskites possess high versatility compared to 3D perovskites. One way to vary the properties of the perovskite film is given by the possibility of changing the organic spacers, which allows tuning of the interlayer interaction in the crystal structure and changing the electronic properties.[1] In addition, another means to tweak the 2D perovskite structure is the variation of n, which represents the number of inorganic layers sandwiched between the bulky organic molecules. As widely reported in the literature, tuning n leads to a change in the optoelectronic properties of the material, such as bandgap energy and exciton binding energy.[2,3] For solar cell applications, quasi-2D perovskites with n-values between 3 and 5 are generally used to achieve a relatively small bandgap, a vertical orientation of the inorganic slabs, which provides a good basis for efficient charge transport, and a smaller exciton binding energy that allows direct generation of free charge carriers instead of excitons, as in the strongly confined (dimensionally and dielectrically) $n = 1$.[4,5]

The formation of phase-pure quasi-2D perovskites with a specific n-value, however, is an ongoing challenge. Usually, a variety of structural phases with different n-values are obtained during film formation, meaning that exploiting the tunability of quasi-2D perovskite properties (such as bandgap energy tuning) is still not possible.[6] Lately, different processing techniques have been explored to improve the phase purity and solve this issue: among others, solvent engineering has been shown to be a very promising approach.[7–10] Typical solvents for perovskite precursors are N,N–dimethylformamide (DMF) and dimethyl sulfoxide (DMSO). The latter is commonly used to improve film morphology *via* the so-called adduct approach.[11] These polar, aprotic solvents are Lewis bases that form a coordinative bond with Pb^{2+}, which behaves as a Lewis acid.[12] The interactions between solvents and precursors in solution have a strong influence on the crystallization rate and film morphology obtained after spin-coating.[13] As a result, the presence of a new organic cation in the perovskite precursor solution, such as provided by the widely used butylammonium iodide (BAI) or phenethylammonium iodide (PEAI) precursors, introduces a new degree of complexity during film formation because the organic spacer ammonium iodides have different interactions with the solvent and PbI_2 than methylammonium iodide (MAI) and thereby influences the crystallization process. This might explain why it is commonly reported in the literature that during the processing of quasi-2D perovskites, many different perovskite structures are formed.[14,15] Even though the stoichiometry of the precursor solution is centered around a specific n-value, the resulting perovskite film

usually consists of a broad distribution of n-values, which may be caused by the different crystallization rates of such perovskite structures.[16]

Several studies have investigated the crystallization of quasi-2D perovskites and current consensus is that nucleation starts at the liquid-air interface.[17–19] Moreover, by using in-situ techniques, it has been recently found that the crystallization is likely to start as a 3D-like perovskite.[18] However, a link between crystallization mechanism and phase distribution in quasi-2D perovskites films has yet to be found. In 2018, a pioneering study about quantum wells distribution in quasi-2D perovskites highlighted the importance of solvent engineering to tune the phase distribution and crystallinity of such materials.[20] Since then, many reports have studied the effect of solvent mixtures on the composition of quasi-2D perovskites.[19,21–23] In an effort to explain the mechanism behind vertical 2D-3D phase separation in quasi-2D perovskites, Mao *et al.* studied the effect of DMSO in the precursor solution, finding that a narrower phase distribution with suppression of small-n perovskites can be obtained by using 5% DMSO.[24] An intermediate phase derived from the coordination of DMSO with Pb^{2+} was found to be responsible for the suppressed formation of small-n phases, as the intermediate was thought to form large-n RPPs more easily. On a similar note, Cheng *et al.* described precursor–solvent interactions as a key factor in determining the phase purity, crystal orientation, and optoelectronic properties, resulting in a power conversion efficiency (PCE) >10% for a propylammonium-based quasi-2D perovskite by tuning the DMF/DMSO ratio in solution.[25] Despite the wide use of DMSO and other co-solvents to enhance the quality of perovskite films, fundamental understanding of how the co-solvents affect the phase distribution is still lacking. Moreover, co-solvents are often assessed by their donor number (D_N) and their coordination ability with Pb^{2+}, without considering their interactions with organic spacers which might be crucially important in explaining phase distribution issues in quasi-2D perovskites. In fact, the aggregation of perovskite precursors, dictated by the formation of an intermediate phase with the co-solvent, might act as a nucleation site and alter the crystallization process drastically.[16] Recently, a large variety of new organic spacers for 2D perovskites are being used to further exploit the potential of this material.[26] Thus, to tune phase purity and enhance device efficiency, it is crucial to study the general principles of how these cations interact with solvents in the precursor solution and how such interactions impact the distribution of the n-values in resulting films.

In this chapter, we investigate the crystallization mechanism of quasi-2D perovskite films in the presence of co-solvents and analyze the molecular interactions between different perovskite precursors (MAI, BAI, PbI_2) and solvents (DMF, *N,N*-dimethylacetamide (DMAc), *N*-methyl-2-pyrrolidone (NMP), and DMSO)

to correlate such interactions with the resulting phase distribution obtained after film deposition. Additionally, we show that careful tuning of the solvent mixture induces a narrower phase distribution and a less pronounced 2D-3D gradient throughout the thickness of the film, with important implications for the external quantum efficiency and performance of solar cells based on quasi-2D perovskites.

3.2 CRYSTALLIZATION OF QUASI-2D PEROVSKITES

Previous studies in the literature have suggested that crystallization of Ruddlesden-Popper perovskites starts from the liquid-air interface as a 3D-like perovskite.[17,18] Interested in the impact of co-solvents on the crystallization mechanism and phase distribution, we first investigated the kinetics of film formation of quasi-2D perovskite $BA_2MA_3Pb_4I_{13}$ processed from DMF/co-solvent mixtures using in-situ UV-vis-NIR absorption measurements conducted during spin-coating or thermal annealing.
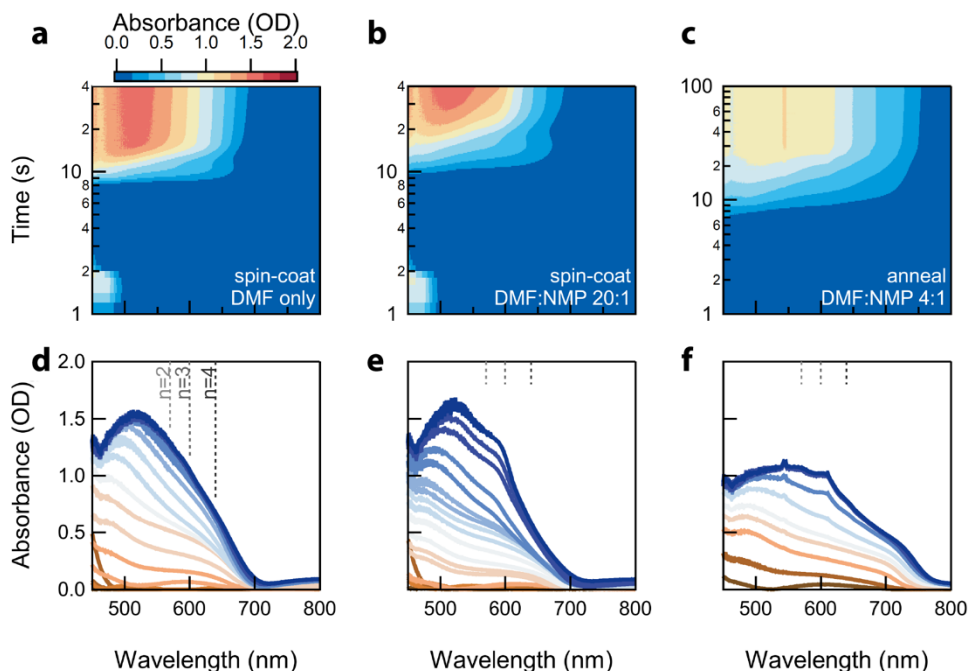

Figure 3.1. In-situ UV-vis-NIR absorption spectra recorded in reflection mode during spin-coating for $BA_2MA_3Pb_4I_{13}$ ($<n>$ = 4). (a, d) Processed from DMF. (b, e) Processed from DMF/NMP (20:1). (c, f) In-situ UV-vis-NIR absorption spectra recorded during thermal annealing for $BA_2MA_3Pb_4I_{13}$ ($<n>$ = 4) processed from DMF/NMP (4:1). This film did not show any absorption peaks during spin-coating, because of the slow crystallization that takes place only during annealing.

The perovskite film was processed *via* room-temperature spin-coating, followed by thermal annealing at 100 °C. The $BA_2MA_3Pb_4I_{13}$ composition corresponds to a 2D RPP with an expected *n*-value of $<n> = 4$. We selected two high boiling point co-solvents, namely NMP (b.p. 202 °C) and DMSO (b.p. 189 °C), as they effectively slow down the drying rate of the film and allow for a reorganization of the 2D/3D phases in the film. As a comparison, we used DMF (b.p. 153 °C) as pure solvent and a relatively low boiling point co-solvent, such as DMAc (b.p. 165 °C). The perovskite precursors coordinate with the solvents *via* Lewis acid-base interactions, which in conjunction with different evaporation rates will likely impact the crystallization process, as explained later.

The perovskite film turns dark during spin-coating only when processed from pure DMF or from a mixture of DMF/DMAc, which have similar boiling points and evaporation rates. **Figure 3.1**a and 3.1d show that an absorption onset appears after about 8 s in the 700 nm region when processing the $<n> = 4$ perovskite precursor from DMF, indicating formation of a quasi-3D perovskite phase soon after spin-coating has started. After 35 s, the UV-vis-NIR absorption spectra do not show any additional changes, suggesting completed crystallization during spinning. Interestingly, during spin-coating we observe a slight redshift in the absorption onset, which may be representative of perovskite crystal growth to larger *n*-values. Distinct absorption features corresponding to smaller *n*-values are not observed as the film crystallizes. In contrast, when processed from a DMF/NMP 20:1 solvent mixture, the spectrum of a quasi-3D perovskite film develops slightly slower (by ~2 s) (Figure 3.1b and 3.1e). In this case, after the formation of a quasi-3D perovskite, an excitonic peak at 600 nm, representative of an $n = 3$ phase,[27] begins to appear at 12-13 s. This indicates that the crystallization starts with a quasi-3D phase and is followed by the formation of quasi-2D perovskites, which form slower due to the weak van der Waals interactions between the butyl chains. Similar to the previous case, the absorption onset slightly redshifts with time during spin-coating. In an NMP-richer solvent mixture (DMF/NMP 4:1), the film does not turn dark during spin-coating, indicating that drying and crystallization of the film is retarded due to the high boiling point of NMP. In this case, a quasi-3D onset at around 720 nm appears during the first seconds of annealing the film at 100 °C, followed by $n = 2$ (570 nm) and $n = 3$ (600 nm) excitonic peaks (Figure 3.1c and 3.1f).[27] Interestingly, even though the initial quasi-3D onset is observed at 720 nm, the same onset shifts to >750 nm when the quasi-2D perovskite phases are formed. This indicates that the quasi-3D phase at the end of the annealing has become very similar to a $MAPbI_3$ perovskite.[28]

Overall, it seems that also under these conditions, the crystallization of a 3D perovskite is kinetically more favorable and implies that the formation of a phase-pure quasi-2D perovskite is challenging because the presence of MA inevitably leads to a fast crystallization of quasi-3D perovskites. Similar behavior is observed when using DMSO as a co-solvent. The addition of high boiling point co-solvents therefore effectively slows down the crystallization of the perovskite film. Moreover, slow crystallization influences the phase distribution of the resulting film: when pure DMF is used, mostly a quasi-3D perovskite with undefined n-value is formed, because the 2D perovskite phase crystalizes too slow to form a distinct 2D-3D gradient. When using high boiling point co-solvents, instead, distinct 2D and 3D phases are formed. Notably, we also find that such 3D-like perovskite seems to form larger n-values over time, indicating that the top part of the film might still be influenced by the ongoing crystallization of the small-n phases at the bottom.

3.3 PHASE DISTRIBUTION AND COMPOSITION ANALYSIS

To investigate changes in the formation of different structural phases and their distribution across the thickness of the film the perovskite films processed from DMF/co-solvent mixtures were characterized by optical spectroscopy. **Figure 3.2**a shows the UV-vis-NIR absorption spectra of quasi-2D $BA_2MA_3Pb_4I_{14}$ ($<n>$ = 4) perovskite films processed from precursor solutions containing pure DMF or DMF/co-solvent mixtures. The films processed from DMF/NMP and DMF/DMSO display more clear signals of 2D phases, and distinct, redshifted absorption onsets for the 3D perovskite compared to the spectra of layers processed from DMF/DMAc or pure DMF. With a bandgap of about 1.63 eV, the quasi-2D perovskites processed from DMF/NMP and DMF/DMSO seem to induce the formation of an almost pure 3D perovskite phase in parts of the film, compared to the formation of quasi-3D perovskite phases with higher bandgap in the films processed from DMF and DMF/DMAc (1.72 and 1.77 eV, respectively).
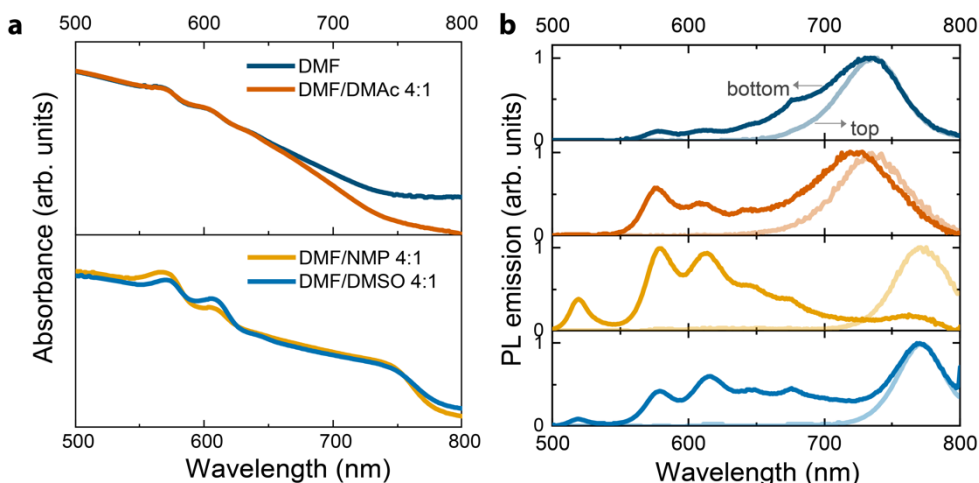
Figure 3.2. Optical characterization of $BA_2MA_3Pb_4I_{13}$ ($<n>$ = 4) quasi 2D-perovskite layers on glass substrates. (a) UV-vis-NIR spectra of films processed from DMF/co-solvent 4:1 (v/v). (b) Normalized steady-state PL spectra of the same films as (a) with excitation at 405 nm from the air/perovskite (top) and substrate/perovskite (bottom) interface side.

In the 500-650 nm region of the UV-vis-NIR spectra, the films processed with all solvent mixtures display excitonic absorption peaks associated with (quasi-) 2D perovskite structures with different n-values.[27] The absorption spectra indicate that the co-solvent has an impact on the phase distribution of the small-n phases, because the quasi-2D perovskite film processed from DMF/NMP shows a strong excitonic peak for the $n = 2$ phase at 570 nm, with relatively smaller peaks for $n = 1$ at 515 nm and $n = 3$ at 610 nm, whereas the perovskite processed from DMF/DMSO display a strong excitonic peak for $n = 3$ and low intensity for $n = 2$ and $n = 4$ (640 nm). UV-vis-NIR spectra of films processed with DMF only and DMF/DMAc are relatively similar with a shallow absorption onset for the 3D perovskite phase and weak excitonic peaks. A sharper 3D perovskite absorption onset, as seen with NMP and DMSO as co-solvents, is therefore associated with higher intensities for the excitonic peaks of the small-n perovskites. Once a 3D perovskite is formed, the excess BA^+ cations will lead to the formation of quasi-2D perovskites with smaller n-values.

While photoluminescence (PL) spectra cannot be used to quantify the different phases because energy transfer occurs, it can be used to identify phases that are present. The steady-state PL spectra reveal that a 3D perovskite phase is present as they show one main 3D emission peak when films are excited at 405 nm from the perovskite (top) side (Figure 3.2b). The PL maximum is shifted to longer wavelengths in case of DMF/NMP and DMF/DMSO. The difference in the bandgaps can be also

determined from the PL maxima, which are found at about 1.68 eV for DMF and DMF/DMAc compared to 1.61 eV for DMF/NMP and DMF/DMSO. As mentioned before, the latter values are similar to the emission of MAPbI$_3$.[28] As commonly reported in the literature, quasi-2D perovskite films show different PL spectra when excited from the air/perovskite (top) or substate/perovskite (bottom) interfaces, because of a vertical 2D-3D phase distribution in the film. The normalized PL spectra of the quasi-2D perovskite films confirm this vertical phase separation. The film processed from DMF exhibits weak PL peaks at 560, 605, 640, and 680 nm, corresponding to 2D phases with $n = 2$, 3, 4, and 5[29] when excited from substrate (bottom) side but no sign of 2D phase emission when excited from the air (top) side. This indicates that the 3D phase is confined at the top of the film and the 2D phases at the bottom. The co-solvents strongly influence the phase distribution of 2D phases at the substrate side. Compared to pure DMF, films processed from DMF/DMAc result in an enhanced emission for the 2D phases with $n = 2$ to 4 with bottom excitation. The film processed from DMF/NMP shows peaks at 520, 580, 615, 645, and 675 nm, corresponding to quasi-2D phases with $n = 1$ to 5.[29] The most intense PL peak is found for the 2D phase with $n = 2$ and there is only a small peak for the 3D phase. Finally, the film processed from DMF/DMSO also displays the PL emissions for $n = 1$ to 5, but the phase distribution is shifted towards larger n-values compared to NMP, and the 3D phase PL peak has the highest intensity. While these largely different PL spectra certainly point towards different phase distributions for different co-solvents, a quantitative analysis of the phase distribution is hampered by the several unknown factors, such as the absorption coefficient and PL quantum yields of different phases, and the extent to which emission occurs after migration of charge carriers to low-bandgap regions.

The presence of a vertical 2D-3D phase separation is confirmed by angle-dependent grazing-incidence wide-angle X-ray scattering (GIWAXS) measurements (**Figure 3.3**) The angle of incidence a was varied from 0.1° to 0.5° to gain depth sensitive information about the film. At angles below 0.2°, only the top 10-20 nm of the film are analyzed, while the X-rays penetrate the full thickness of the film at higher angles.[30] Because the PL spectra indicate that the 2D phases are most prominent in films processed from DMF/NMP, we investigated the vertical phase distribution of these films. With $a = 0.2°$, the quasi-2D perovskite film processed from DMF/NMP 4:1 resembles a well oriented 3D perovskite, while with $a > 0.2°$ new Bragg spots appear in the out-of-plane direction at 0.2 Å^{-1} and 0.3 Å^{-1}, which are associated with the $n = 3$ and $n = 2$ (020) planes.[31] These results confirm that small-n phases are formed mainly at the bottom of the film, as also observed *via* PL spectroscopy, when processed with relatively high amount of NMP in the precursor solution.
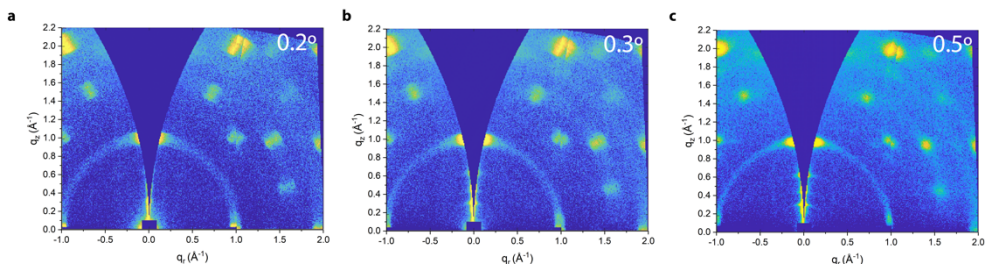
Figure 3.3. Incident angle dependent GIWAXS measurements of $BA_2MA_3Pb_4I_{13}$ ($<n>$ = 4) films processed from DMF/NMP 4:1. The angle of incidence α is indicated in each panel.

Based on the optical characterization and GIWAXS, we can conclude that our in-situ UV-vis-NIR absorption measurements are in good agreement with previous reports and confirm that the crystallization starts from the liquid/air interface as a 3D-like perovskite, even with the presence of a high boiling point co-solvent. In fact, in-situ UV-vis-NIR absorption measurements during spin-coating or annealing indicated that the perovskite crystallization starts as a quasi-3D perovskite, while PL and angle-dependent GIWAXS located such phases at the top of the film, suggesting that the crystallization starts from the top.

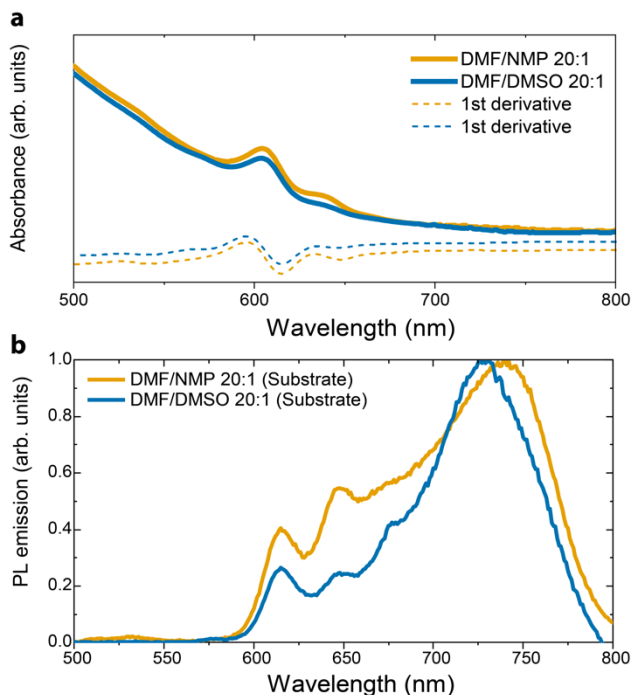**Figure 3.4**. (a) UV-vis-NIR spectra of $BA_2MA_3Pb_4I_{13}$ films processed from DMF/co-solvent 20:1 (v/v) (b) Normalized steady-state PL spectra of the same films as (a) with excitation at 405 nm from the substrate/perovskite (bottom) interface side.

To investigate if the optical quality of the films can be improved and scattering of light can be reduced, lower amounts of NMP and DMSO in DMF were used, which enhanced the drying rate. The UV-vis-NIR spectrum of $BA_2MA_3Pb_4I_{13}$ ($<n>$ = 4) films processed from DMF/NMP 20:1 and DMF/DMSO 20:1 reveal that the use of NMP and DMSO in smaller amounts with DMF is efficient in producing a more phase-pure film that shows only excitonic peaks for n = 3 and 4, no pronounced 3D onset, and much less scattering (**Figure 3.4**a). This solvent/co-solvent ratio provides an optimal crystallization rate where the arrangement of 2D-3D phases is neither absent, as in the case of the 1:0 ratio, nor as distinct as observed in the 4:1. As a result, the crystallization kinetics is driven to the formation of a relatively phase-pure quasi-2D perovskite. However, while the stoichiometry of the precursor solution was selected to make an n = 4 quasi-2D perovskite, the phase distribution for these films seem to be centered around n = 3 with a prominent peak at 605 nm. The PL spectra from substrate side of these films still show emission peaks corresponding to 2D phases with n = 3 and 4 but are dominated by the 730 nm peak related to a quasi-3D perovskite phase (**Figure 3.4**b). Peaks that are due to n = 1 and 2 are largely absent. This result suggests that a more phase-pure 2D might have been formed but that a certain amount of quasi-3D perovskites is still present. The strong PL emission in the 700-800 nm region might originate from efficient charge transport from small-n phases to the quasi-3D phase, which might lead to a dominant PL emission arising from a quasi-3D phase with lower bandgap energy, even if the latter is present only in small amounts in the film. Because of this, it is not possible to use the PL spectra to quantitatively determine the amounts of different phases in the film. Instead, we rely on UV-vis-NIR spectra and determine that the quasi-3D perovskite phase must be present in small concentrations as indicated by the very shallow onset in the 700 nm region and that we are able to fabricate a reasonably phase-pure quasi-2D perovskite by carefully tuning the DMF/co-solvent ratio.

3.4 DYNAMICS OF CHARGE CARRIERS IN QUASI-2D PEROVSKITE FILMS

To gain more understanding of the dynamics of charge carriers and to quantitatively investigate the phase distribution in the films with optimized n-value distribution, we measured ultrafast transient absorption (TA) for $BA_2MA_3Pb_4I_{13}$ ($<n>$ = 4) perovskite films processed from DMF and DMF/NMP 20:1 with excitation at 400 nm and a density of 7.2×10^{12} photons/cm² per pulse (180 fs). **Figures 3.5**a-b display the TA spectra at different decay times after top and bottom excitation, respectively, for the reference film processed from pure DMF. After excitation from the perovskite (top) side, the TA spectrum displays ground state bleaching (GSB) of n = 2 to 4 and quasi-3D perovskites, followed by an ultrafast bleach recovery for the small-n

phases and a concomitant rise of the GSB peak for quasi-3D perovskite at 720 nm. This indicates fast (<1 ps timescale) and efficient carrier migration from the quasi-2D perovskites phases to the quasi-3D phase. As also suggested by the PL spectra, a 2D-3D vertical phase separation is observed in the TA spectra, where excitation from the substrate (bottom) side leads to much more intense GSB peaks for $n = 2$ (570 nm), $n = 3$ (605 nm), $n = 4$ (640 nm), and $n = 5$ (665 nm), with no bleaching in the 700 nm region.
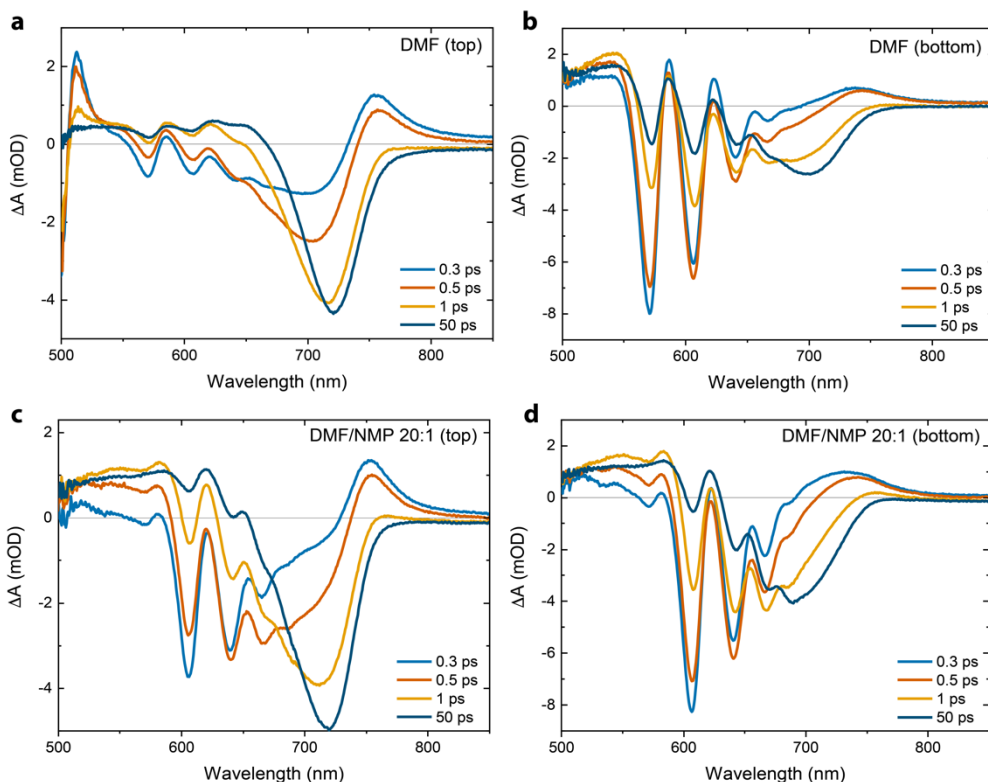

Figure 3.5. Ultrafast transient absorption (TA) spectra of $BA_2MA_3Pb_4I_{13}$ ($<n>$ = 4). (a-b) Films processed from DMF and excited from air/perovskite (top) and substrate/perovskite (bottom) side, respectively. (c-d) Films processed from DMF/NMP 20:1 and excited from top and bottom side, respectively.

In a timescale of less than 1 ps, we observe a sequential bleaching and recovery for $n > 2$ perovskites, suggesting carrier migration from small-n to large-n perovskites,[32] as indicated by a GSB peak at 700 nm, which reaches its maximum at around 50 ps. This peak is found at shorter wavelength compared to the quasi-3D GSB peak observed after top illumination, thus it is related to a perovskite phase with a lower, unidentified large n-value. After 50 ps, decay from all perovskite phases is observed, although it is worth to note that the charge carrier transfer does not

seem complete, as GSB peaks are still observed for n = 2 to 4 at 50 ps and they simply decay together with the larger-n peak. The TA spectra of the $BA_2MA_3Pb_4I_{13}$ film processed from DMF/NMP (20:1) display n = 3 to 6 and quasi-3D GSB peaks (Figure 3.5c-d), confirming that n = 1 and 2 phases are not formed in agreement with the UV-vis and PL spectra. Moreover, top- and bottom-excitation TA spectra seem to indicate a more homogeneous phase distribution where n = 3 to 6 quasi-2D perovskites are located throughout the whole thickness of the film. This suggests that by optimizing the DMF/co-solvent ratio it is possible to avoid a strong 2D-3D vertical phase separation, even though it seems that a certain degree of such separation is inevitable. The TA spectrum from bottom excitation, in fact, displays only n = 3 to 6 GSB peaks, located at 605, 640, 665, and 690 nm, and no clear quasi-3D perovskite absorption at 0.3 ps delay time. In contrast, top excitation shows slightly higher absorption in the quasi-3D region at 720 nm, which suggests formation of quasi-3D phases preferentially at the top of the film and a narrower phase distribution at the bottom. This might explain the ultrafast charge carrier migration from quasi-2D to quasi-3D in the top excitation TA spectrum, which shows an ultrafast rise of the quasi-3D bleach peak that dominates the spectrum after just 1 ps. From bottom excitation, we again observe a sequential bleach and recovery for the quasi-2D phases, although on a longer timescale, as can be seen from the n = 3 to 6 peaks still present at 50 ps. We speculate that the slower carrier transfer after bottom excitation might be related to the fact that less or no quasi-3D phases are present at the bottom of the perovskite film, thus leaving no space for an ultrafast carrier transfer that is instead observed after top excitation.

3.5 CRYSTALLINITY AND VERTICAL ORIENTATION

We further investigated the crystal structure and orientation of the quasi-2D perovskite films with X-ray diffraction (XRD) and GIWAXS.

Figure 3.6a shows the XRD diffraction patterns of $BA_2MA_3Pb_4I_{13}$ ($<n>$ = 4) films processed from DMF/co-solvent 4:1. DMSO and NMP are effective in improving the orientation and crystallinity of the film in the out-of-plane direction, as indicated by the drastic enhancement in intensity of the peaks at 14° and 28°, assigned to (111) and (202) planes of RPP or (quasi-)3D perovskites,[33] and by the full width at half maximum (FWHM) of the (111) peak decreasing from 0.56° and 0.26° for DMF and DMF/DMAc, respectively, to 0.12° and 0.16° for DMF/NMP and DMF/DMSO. In addition, a set of (0k0) peaks in the 3–10° region is observed in the diffraction patterns of the films processed with NMP and DMSO, which indicates the formation of parallel-oriented small-n quasi-2D phases. For instance, the peaks at 3.4° and 4.4° are assigned to n = 3 and n = 2 quasi-2D perovskite (020) planes, respectively.

The XRD diffraction patterns confirm the prevalence of *n* = 3 phases in the DMF/DMSO-processed films and of *n* = 2 phases in the DMF/NMP-processed samples, in agreement with the optical characterization. Some (0*k*0) peaks are also found in the DMF and DMF/DMAc films, although the peaks are not sharp and of low intensity. Interestingly, while the perovskite processed with DMF and DMF/DMAc retain such parallel oriented RPPs even when using the optimized 20:1 ratio (Figure 3.6b-inset), films processed with DMF/NMP (20:1) and DMF/DMSO (20:1) do not show any (0*k*0) peaks if the co-solvent is present in small amounts in the precursor mixture. Remarkably, the addition of NMP is found to drastically increase (~30×) the intensity of the (202) peak, compared to the diffraction pattern of the film processed in DMF only. In addition, the ratio $I_{(202)}/I_{(111)}$ increases from 0.61 and 0.81 for DMF and DMF/DMAc to 2.36 and 1.39 for DMF/NMP and DMF/DMSO, thus indicating a preferential out-of-plane crystal growth with the use of the latter co-solvents.[34]
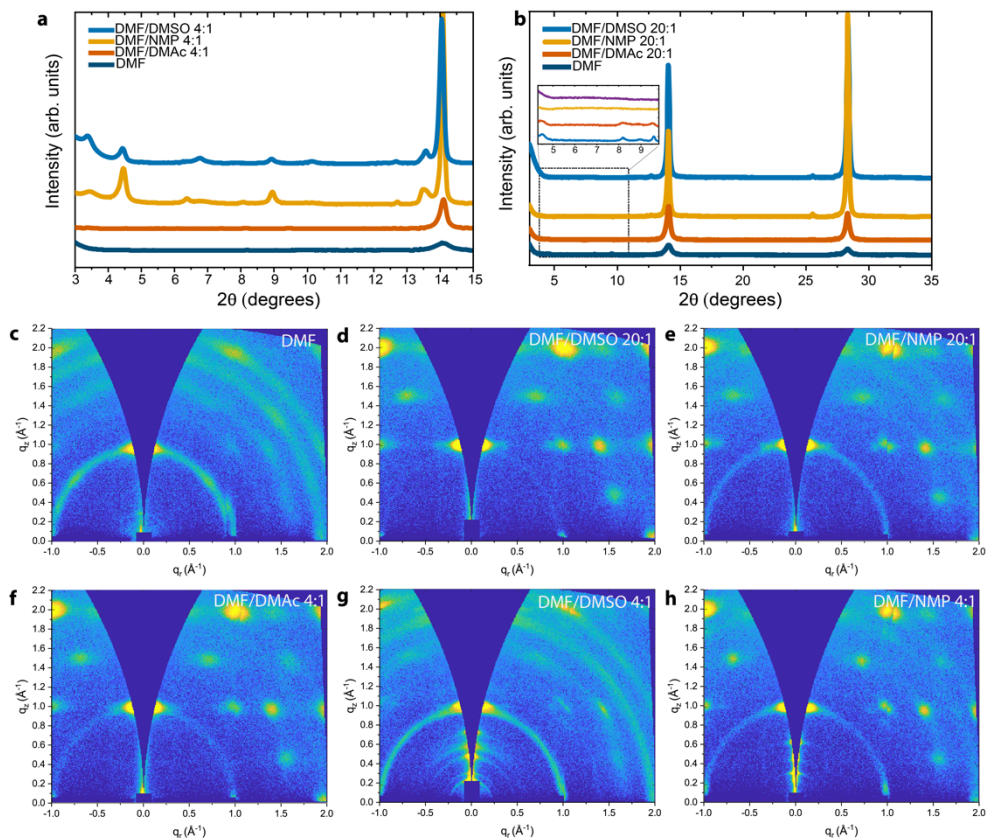
Figure 3.6. (a-b) XRD diffraction patterns for $BA_2MA_3Pb_4I_{13}$ (<*n*> = 4) films processed in DMF/co-solvent 4:1 and DMF/co-solvent 20:1 mixture, respectively. (c-h) GIWAXS patterns for $BA_2MA_3Pb_4I_{13}$ (<*n*> = 4) films processed in a variety of solvent mixtures, as indicated on top of each plot.

Figure 3.6c-h display the GIWAXS measurements for the quasi-2D perovskite films processed from DMF and DMF/co-solvent combinations with 4:1 and 20:1 volume ratios. The film processed from pure DMF exhibits scattered rings (Figure 3.6c), which suggests a random orientation of the crystals. Moreover, a weak Bragg spot at $q_z = 0.3$ Å^{-1} (020) indicates the presence of an $n = 2$ phase oriented parallel with respect to the substrate. In contrast, films processed with small amounts (20:1 ratio) of NMP and DMSO display discrete Bragg spots (Figure 3.6d,e), indicating an enhanced crystal orientation in the out-of-plane direction, as also inferred from XRD, that might be beneficial for charge transport, and no spots associated to parallel-oriented small-n quasi-2D phases.[35,36] As the insulating large organic spacers do not allow for charge carriers to be transported, a favorable orientation of the crystals in quasi-2D perovskites is thought to be beneficial for charge collection and device efficiency. As mentioned above, addition of co-solvents in larger amounts (DMF/co-solvent ratio 4:1) induces a strong 2D-3D phase separation. The film processed in DMF/DMSO 4:1 shows again azimuthal spreading of the diffracted intensity at $q = 1$ Å^{-1} (Figure 3.6g), thus indicating that a larger amount of DMSO, compared to the ratio DMF/DMSO 20:1, is not beneficial anymore in enhancing the crystal orientation. In addition, the small-angle region exhibits many Bragg spots related to small n-values quasi-2D perovskites. Such small-n phases are oriented parallel to substrate and inhibit charge transport. Interestingly, the $n = 3$ phase ($q = 0.2$ Å^{-1}) shows a noticeable ring apart from an intense Bragg spot along the out-of-plane direction, which denotes the tendency of phases with $n > 2$ to orient also in non-parallel directions with respect to the substrate. Moreover, in agreement with XRD, the out-of-plane cut (**Figure 3.7**) shows a peak at $q_z = 0.24$ Å^{-1}, which is–as mentioned above–indicative of an $n = 3$ quasi-2D perovskite phase, that is drastically more intense than the $n = 2$ phase, indicating prevalence of perovskites with such n-value. On the contrary, perovskite films processed from DMF/NMP 4:1 (Figure 3.6h) and DMF/DMAc 4:1 (Figure 3.6f) retain enhanced crystal orientation, even though small-n peaks are clearly visible for films processed with NMP, in agreement with optical characterization. In the latter case, the out-of-plane cut displays both peaks related to $n = 2$ and $n = 3$, with the former being more intense. Overall, the use of any co-solvent seems to induce vertical orientation in the films, possibly because the interaction of the co-solvents with the perovskite precursors does not allow the formation of a monolayer of butylammonium molecules at the liquid-air interface, which would lead to parallel orientation.
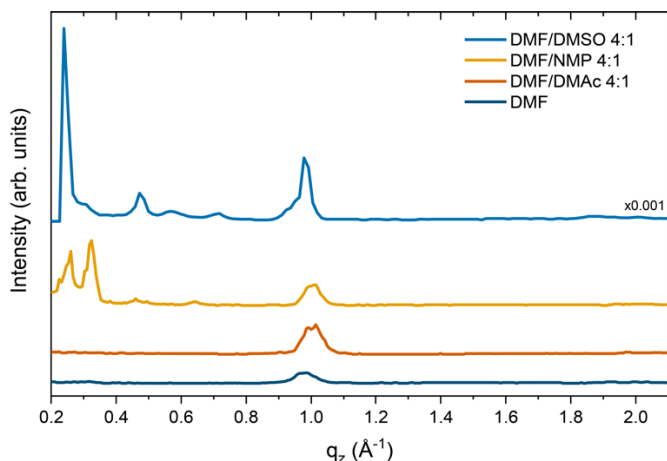
Figure 3.7. Out-of-plane cuts (GIWAXS) for $BA_2MA_3Pb_4I_{13}$ ($<n>$ = 4) processed in DMF/co-solvent 4:1. The perovskite processed from DMF/DMSO has its phase distribution centered around n = 3, as indicated by the intense peak at 0.24 Å^{-1}, whereas the film processed from DMF/NMP possesses both n = 2 and n = 3, with higher intensity for the n = 2 peak.

3.6 INTERACTION BETWEEN PEROVSKITE PRECURSORS

The analysis of the phase distribution obtained *via* optical and X-ray characterization reveals that by using different high boiling point co-solvents, the distribution of n-values is shifted. More specifically, we have observed that by using NMP or DMSO as a co-solvent with DMF in a 1:20 ratio, a more phase-pure quasi-2D perovskite film can be fabricated, whereas by using a 1:4 ratio, the phase distribution is centered around n = 2 and n = 3, respectively. Understanding why some co-solvents lead to different phase distributions is important to make new design rules for the choice of solvent mixtures in quasi-2D perovskites processing. A recent study has identified the perovskite precursor phases that are present in the sol-gel state before crystallization and by mapping the possible reaction pathways, the authors proposed a mechanism where the precursor phases likely react with free BAI or MAI molecules to form the perovskite. When a co-solvent is present in the solvent mixture, however, the availability of MAI and BAI in solution might be different. In fact, MAI or BAI might interact differently in the solvent–PbI_2–MAI(BAI) complexes that are likely present in solution and be more or less bound to them. The different interactions of BAI and MAI with PbI_2 and solvents in solution might explain the change in phase distribution, as this would influence how easy it is for a BAI or MAI molecule to react with the precursor phase to form a perovskite.
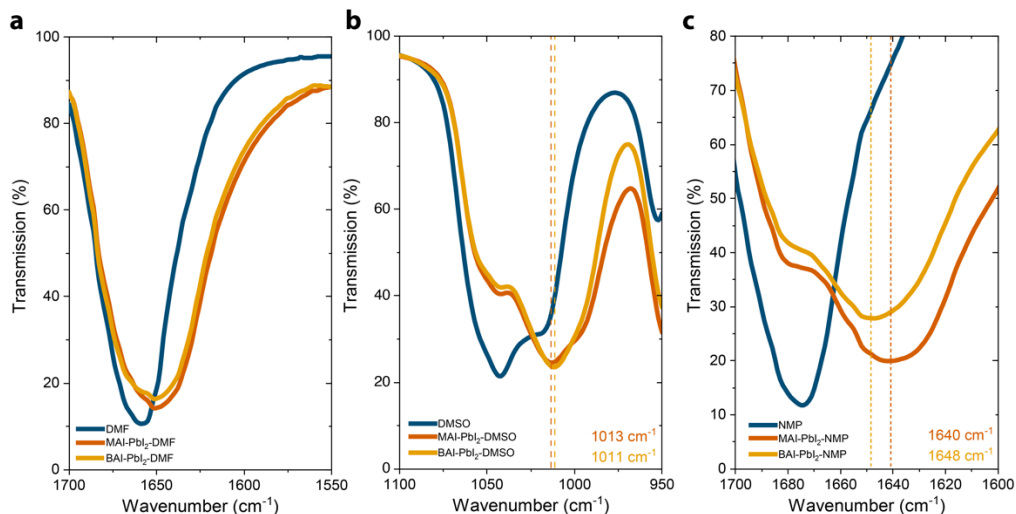
Figure 3.8. FTIR spectra of perovskite precursor solutions composed of BAI (MAI), PbI$_2$, and solvents. The reference spectrum for the pure solvent is displayed in each plot, respectively.

To verify whether this hypothesis is valid, we analyzed the interaction of ternary complexes MAI(BAI)–PbI$_2$–solvent (DMF, NMP, DMSO) by measuring the Fourier transform infrared (FTIR) spectra (**Figure 3.8**). In the case of DMF, the C=O stretching peak broadens and its maximum shifts from 1659 cm^{-1} for pure DMF to 1651 cm^{-1} after addition of PbI$_2$ and MAI or PbI$_2$ and BAI. The shift indicates that the C=O bond weakens by the interaction with the perovskite precursors.[37,38] The broadening can be due to the coalescence of the peaks of pure DMF at 1659 cm^{-1} and one at lower wavenumbers for the DMF-PbI$_2$-MAI and DMF-PbI$_2$-BAI complexes. The C=O peak shifts by the same amount (8 cm^{-1}) when using MAI and BAI, indicating that there is no significant difference for these organic ions. The C=O stretch vibration of NMP undergoes a similar change, but in this case two separate signals are observed in the mixtures, one for pure NMP at 1679 cm^{-1} and one at lower wavenumbers for the NMP–PbI$_2$–MAI and NMP–PbI$_2$–BAI complexes. Interestingly, the MAI complex shifts the C=O peak to 1640 cm^{-1}, whereas the BAI complex to 1648 cm^{-1}. This suggests that the C=O bond from NMP is more weakened when it interacts with MAI–PbI$_2$ compared to BAI–PbI$_2$, indicating that NMP interacts more strongly with MAI–PbI$_2$. Finally, in the case of DMSO, the S=O stretching peak shifts from 1043 cm^{-1} for bare DMSO to 1013 cm^{-1} and 1011 cm^{-1} after addition of MAI–PbI$_2$ and BAI–PbI$_2$, indicating that a slightly stronger interaction might be found with the BAI complex, contrarily to what observed with NMP. As a result, when using NMP as a co-solvent it seems that MAI is stronger bound in the MAI–PbI$_2$–NMP complex, thus making it easier for the precursors in the sol-gel state

to react with BAI and to shift the phase distribution towards small-n phases. On the other hand, when using DMSO the picture tends to a certain extent to be reversed, and a broader phase distribution might be facilitated.
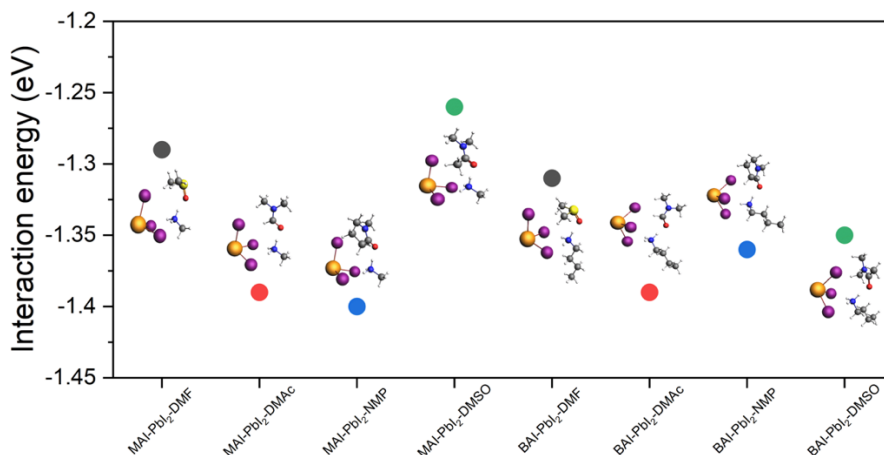

Figure 3.9. Molecular interaction of MAI or BAI ternary complexes formed with PbI$_2$ and solvents and calculated *via* DFT.

Furthermore, we calculated the interaction energies of PbI$_2$, MAI, and BAI with the three solvents (DMF, NMP, and DMSO) (**Figure 3.9**) *via* density functional theory (DFT) calculations. We adopted the molecular structure of [MA$^+$(BA$^+$)–PbI$_3$$^-$– solvent]. The configuration is one of the most favorable out of 1000s tested by using the combination of Monte Carlo and density functional theory (MC–DFT) scheme. This structure has been successfully applied in a previous study to evaluate the interaction strength of FA$^+$–PbI$_3$$^-$– solvent. The interaction energies of MAI (BAI)– PbI$_2$–DMSO are E_{inter} = −1.26 and −1.35 eV, respectively, indicating that MAI interacts more weakly in a complex with DMSO and PbI$_2$ compared to BAI. On the contrary, the complex formed by MAI, PbI$_2$, and NMP has a slightly stronger interaction energy compared to the BAI complex (−1.40 *vs* −1.36 eV).

Overall, to explain all the results described above, we propose a mechanism where the crystallization of the quasi-2D perovskite film starts at the liquid/air interface as a quasi-3D perovskite. Depending on the content of DMSO or NMP, such crystallization starts during spin-coating or during annealing. While the crystallization proceeds, BAI and MAI molecules react to keep forming a perovskite layer. However, the availability of BAI and MAI molecules in the wet film is not the same, as they might interact differently with the co-solvent that has yet to evaporate. This affects the n-values distribution that is found at the bottom of the film, in the way described *via* optical and X-ray characterization. The use of NMP allows a phase distribution more shifted to small n-values, such as n = 2, because BAI interacts less

in solution and is more available to react, whereas the use of DMSO shifts the distribution to slightly larger *n*-values.

3.7 SOLAR CELLS

Finally, using the new insights obtained by tuning the DMF/DMSO and DMF/NMP ratios to achieve relatively phase-pure quasi-2D perovskites, we fabricated planar *p-i-n* solar cell devices. The quasi-2D $BA_2MA_3Pb_4I_{13}$ ($<n>$ = 4) perovskite was processed on a glass substrate covered with a patterned transparent indium tin oxide (ITO) electrode and a poly[bis(4-phenyl)(2,4,6-trimethylphenyl)amine] (PTAA) hole-transport layer, and then sandwiched by thermally-evaporated C_{60} and bathocuproine (BCP) electron-transport layers and an Al back electrode (glass/ITO/PTAA/quasi-2D $BA_2MA_3Pb_4I_{13}$ ($<n>$ = 4)/C_{60}/BCP/Al).
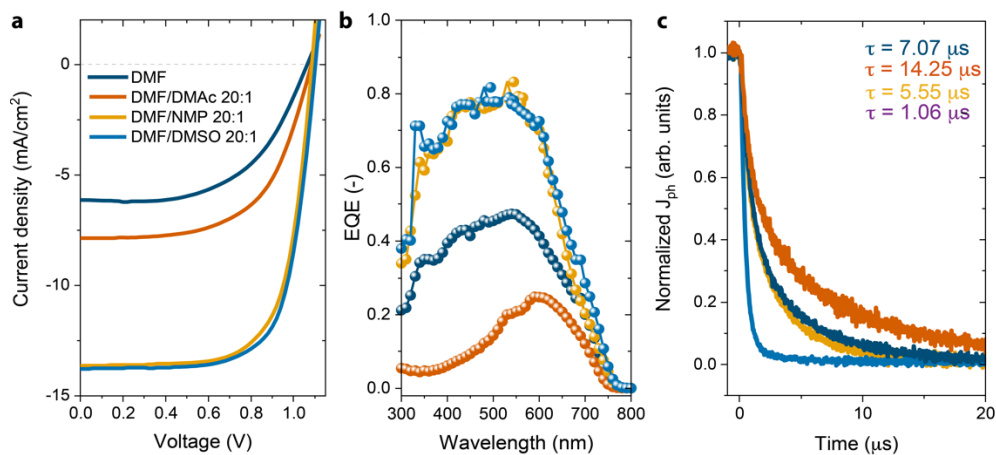
Figure 3.10. (a) *J–V* characteristics for solar cells based on $BA_2MA_3Pb_4I_{13}$ ($<n>$ = 4) active layer and processed from DMF/co-solvent mix 20:1, recorded with simulated AM1.5G (100 mW cm^{-2}) light. (b–c) EQE spectra and TPC measurements for the abovementioned solar cell devices.

Figure 3.10a–b displays the current density – voltage (*J–V*) characteristics recorded with AM1.5G (100 mW cm^{-2}) illumination and the external quantum efficiency (EQE) spectra of the $BA_2MA_3Pb_4I_{13}$ ($<n>$ = 4) based devices, while **Table 3.1** summarizes the relevant solar cell parameters. The quasi-2D perovskites processed only in DMF and in DMF/DMAc 20:1 lead to poor photovoltaic devices with PCEs of 3.5% and 5.2%, respectively. Optimized devices processed from DMF/NMP and DMF/DMSO with ratio 20:1 display dramatically enhanced solar cell parameters, reaching efficiencies of 10.2% and 11.1%, respectively. Moreover, the hysteresis index (HI) of the solar cells fabricated with optimized quasi-2D films is

calculated as 0.07, much lower than the HI of the cells with active layer processed from DMF and DMF/DMAc solvent mix (0.19 and 0.15, respectively). The most prominent increase in the solar cells is reported for the short-circuit current density, which is more than doubled after addition of NMP and DMSO in the solvent mixture, even though this is also accompanied by an increase in both open-circuit voltage (V_{OC}) and fill factor (FF).

Table 3.1. Solar cell parameters for $BA_2MA_3Pb_4I_{13}$ ($<n>$ = 4) active layers processed from DMF/co-solvent (20:1) mixtures. The thickness of the active layers is comparable (±15 nm)

	$J_{SC,EQE}$ (mA cm^{-2})	V_{OC} (V)	FF (-)	PCE (%)	Hysteresis index (-)
DMF	6.0	1.06	0.56	3.5	0.19
DMF/DMAc 20:1	8.1	1.08	0.60	5.2	0.15
DMF/NMP 20:1	13.5	1.09	0.70	10.2	0.07
DMF/DMSO 20:1	14.2	1.10	0.71	11.1	0.07

We attribute the increase in solar cell performances to the absence of n = 1 and 2 phases in the optimized films, which are usually oriented parallel to the substrate and inhibit charge transport, and by the enhanced crystallinity and more favorable crystal orientation. *Via* solvent engineering, we show that it is possible to have a certain degree of control over these important parameters in quasi-2D perovskites, as schematically represented in **Figure 3.11**.
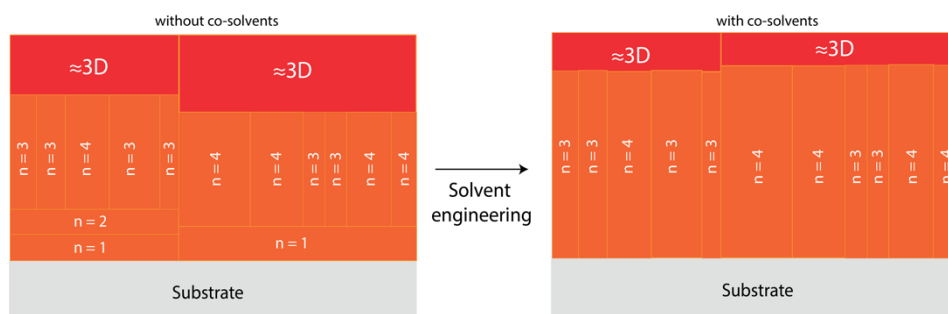

Figure 3.11. Schematic illustration quasi-2D perovskite film composition before and after tuning of the DMF/co-solvent ratio

To support this, we measured transient photocurrent (TPC) on devices with active layers processed from all solvent mixtures, as shown in Figure 3.10c. As expected, devices processed with DMF or DMF/DMAc, which display a less

homogeneous phase distribution, show a longer decay time (τ) of the photocurrent equal to 7 and 14 µs, respectively, possibly because 2D crystallites are orientated parallel to the surface and because phase impurity leads to difficulties in extracting charge carriers. On the other hand, the optimized devices processed with DMF/NMP or DMF/DMSO display a shorter decay time, with τ reaching 5 and 1 µs, respectively. This is in line with the better crystal orientation and more homogeneous phase distribution, which makes charge carriers extraction easier. A more pronounced vertical orientation in the films processed with DMF/DMSO, as indicated by the less noticeable ring at 1 Å^{-1} in Figure 3.6d, is consistent with the shorter decay time for such devices, compared to the ones processed in DMF/NMP. The external quantum efficiency (EQE) spectra, displayed in Figure 3.10b, show a drastic enhancement in quantum efficiency for devices processed with DMF/NMP and DMF/DMSO, reaching 80% in the 400-600 nm range, while much poorer performances are observed for other devices. In addition, we observe an onset at 750 nm for all devices, which is an indication of the formation of a quasi-3D perovskite phase. This onset clearly shows that even though phase purity is better for optimized films, in terms of vertical phase separation and absence of small-n structures, there is always the formation of a certain amount of 3D-like perovskite. Very commonly in the literature, such onset in the EQE spectra is not considered as evidence of impurity in what are often wrongly considered phase-pure quasi-2D perovskite devices. Finally, in agreement with the analysis of the interaction energies of the precursor intermediates, we observe that perovskites processed from DMF/DMSO 20:1 display a slightly broader shoulder in the 700 nm region, which seems to confirm the assumption that DMSO leads more easily to the formation of quasi-3D perovskites compared to NMP.

3.8 CONCLUSIONS

In summary, we have demonstrated that the perovskite precursor solution plays an important role in determining the phase distribution in quasi-2D perovskite films and that solvent engineering is a viable strategy to improve phase purity and device efficiency. Carefully tuning the solvent mixture led to an improvement in the efficiency of solar cells using a BA <n=4> perovskite active layer from 3.5% when using no co-solvent to 11.1% and 10.2% when processed from DMF/DMSO and DMF/NMP mixtures, respectively. We noticed an enhancement in crystallinity and crystal orientation, together with a narrower 2D-3D phase distribution, which is beneficial for charge carrier extraction. Moreover, we confirmed that the crystallization of quasi-2D perovskite films starts from the liquid/air interface as a quasi-3D perovskite, even in the presence of high boiling point co-solvents, and

proceeds to form quasi-2D perovskite phases on the bottom of the film. Each co-solvent, however, influences the distribution of n-values differently. By investigating the solvent-precursors interaction energies *via* FTIR and DFT, we confirmed that the phase distribution is indeed influenced by the co-solvents due to a difference between the interaction of MA (or BA) and PbI_2 with the co-solvents. As the perovskite crystallization proceeds, the availability of MA and BA to react is different because the organic ions interact more or less strongly with the co-solvents, which leads to a shift of the phase distribution towards small n-values in the case of NMP and to a broader distribution of structural phases when using DMSO. Our results indicate that a careful analysis of the precursor solution is a good starting point to tune the phase distribution of quasi-2D perovskites. In particular, new organic spacers might interact in a different manner with PbI_2 and the solvents, compared to MAI; thus, the use of new solvent mixtures or additives might be crucial to develop an efficient and phase-pure quasi-2D perovskite with unconventional spacers.

3.9 METHODS

Solution preparation. All materials were purchased from commercial sources and used as received. To prepare the $BA_2MA_3Pb_4I_{13}$ precursor solution, a PbI_2-based 1.5 M solution was prepared by mixing BAI (>99%, Greatcell Solar Materials), MAI (>99.99%, Greatcell Solar Materials), and PbI_2 (99.99%, TCI Chemicals) in a molar ratio of 2:3:4 and dissolving in DMF (99.8%, Sigma Aldrich) with overnight stirring at 60 °C. The stock solution was diluted to reach 1 M concentration based on PbI_2 and by using the correct amounts of solvents to reach the desired DMF/co-solvent ratio. Poly[bis(4-phenyl)(2,4,6-trimethylphenyl)amine] (PTAA) (M_w = 14.5 kg mol^{-1}, EM Index Co. Ltd) (3 mg) was dissolved in anhydrous toluene (99.5%, TCI Chemicals) (1 mL). For FTIR measurements, equimolar amounts of MAI or BAI and PbI_2 were dissolved in the corresponding solvent to reach a molar ratio of 1:1:9. All materials and solvents, except PTAA, were stored in an N_2-filled glovebox. Solutions were prepared in an N_2-filled glovebox.

Device fabrication. Pre-patterned ITO glass substrates (Naranjo, 17 Ω sq^{-1}) were cleaned by sonication in acetone (15 min.) and sodium dodecyl sulfate (99%, Acros) soapy water (15 min.), rinsed with deionized water, and then sonicated in isopropanol (15 min.). Before spin-coating, substrates were treated with UV-ozone for 30 min. PTAA layer was spin-coated at 5700 rpm for 30 s, then annealed at 100 °C for 10 min. 60 µL of perovskite precursor solution was spin-coated at 5000 rpm for 45 s, then annealed at 100 °C for 10 min. For the electron transport layer and metal electrode, of C_{60} (SES Research, 99.95%) (20 nm), bathocuproine (BCP, 99%, Lumtec) (8 nm), and Al (100 nm) were thermally evaporated in ultrahigh vacuum at rates of 0.5 Å s^{-1}, 0.5 Å s^{-1}, and 2-5 Å s^{-1}, respectively.

Device characterization. A tungsten-halogen lamp combined with a daylight filter (Hoya LB120) and a UV-filter (Schott GG385) were used to simulate the solar spectrum. The light intensity was calibrated *via* a Si photodiode. The solar cell area was defined by a black shadow mask with an aperture of 0.0676 cm² or 0.1296 cm². Fast J–V measurements were

performed with a Keithley 2400 source meter to sweep the voltage from –0.5 V (1.5 V) to 1.5 V (–0.5 V) at a scan rate of 0.25 V s^{-1} in both reverse and forward scan. The hysteresis index was calculated as the difference between current density in reverse and forward sweep at 0.8·V_{OC} divided by the current density at 0.8·V_{OC} in reverse sweep. For the slow J–V measurements, the V_{OC} was tracked for 5 min. and then a reverse voltage sweep was performed from (V_{OC} + 0.02 V) to –0.02 V with a step size of 0.02 V and by measuring the current density for 5 s at each step. For EQE measurements, a modulated (Oriel, Cornerstone 130) tungsten-halogen lamp (Philips Focusline, 50 W) was used light source. The signal was amplified *via* a current preamplifier (Stanford Research, SR 570) and measured by a lock-in amplifier (Stanford Research, SR 830). Based on a calibrated silicon reference cell, the EQE is then calculated from the spectral response signal. An additional 530 nm LED (Thorlabs) was used to generate a photocurrent in the solar cell during the EQE measurement, which is close to the current measured during J–V measurements, to mimic 1-sun condition. Transient photocurrent (TPC) was measured using a custom-made setup. Light pulses were generated by a green LED (515 nm) connected to a wave-function generator (Agilent 33250A) and focused through optical focal lenses (Thorlabs) towards the device. For this measurement, a circular aperture size of 1 mm of diameter was used to define the active area. The substrates were kept sealed in a N$_2$-filled box equipped with a quartz window. Light intensity was calibrated using a reference silicon photodiode (Thorlabs FDS100), while the response signal from the solar cell was read by a digital oscilloscope (Tektronix TDS5052B).

Film characterization. UV-vis-NIR spectra were recorded by using a PerkinElmer Lambda 1050 UV-vis-NIR spectrophotometer. PL spectra were recorded by using an Edinburgh Instruments FLSP920 double-monochromator luminescence spectrophotometer. XRD patterns were recorded by using a Bruker 2D phaser (Cu Kα radiation, λ = 1.5406 Å): measurements were performed in the range 3-40° with a step size 0.02° and collection time of 1 s. 2D GIWAXS and GIMAXS measurements were performed with a Ganesha 300XL+ system from JJ X-ray equipped with a Pilatus 300K detector (pixel side 172 µm x 172 µm). The X-ray source was a Genix 3D Microfocus sealed tube X-ray Cu-source with integrated monochromator. The wavelength used was 1.5408 Å. The detector moves in a vacuum chamber with sample-to-detector distance (SDD) varied between 0.115 m and 1.47 m depending on the configuration used, as calibrated using silver behenate (d$_{001}$ = 58.380 Å). For GIWAXS, the SDD was 115.4 mm and for GIMAXS the SDD was 515.4 mm. The angle dependent 2D GIWAXS and GIMAXS were conducted *via* controlling incident angle from 0.1-0.5° with 0.1° interval.

Ultrafast transient absorption. Pump–probe transient absorption measurements were performed using a tunable laser system comprising a Yb:KGW laser source (1028 nm) operating at 5 kHz (2.5 kHz repetition rate) with a pulse duration of 180 fs (PHAROS-SP-06-200, Light Conversion) and an optical parametric amplifier (ORPHEUS- PO15F5HNP1, light conversion). The 2D data were acquired with a transient absorption spectrometer (HELIOS, Ultrafast Systems). The thin films were excited at 400 nm with a light intensity of 0.6 mW cm^{-2} and excitation density of 7.4E+12 photons/cm^2. With this wavelength, only about 25% of the film thickness is illuminated from top or bottom. The changes in the absorption spectra due

to photoexcitation were monitored using short, broadband pulses that are obtained from continuum generation in a CaF_2 crystal (340 to 900 nm). The system is in quasi parallel pump–probe geometry with a 200 μm probe spot size.

In-situ UV-vis-NIR absorption spectroscopy. White paint was applied on the back of a glass substrate, then the substrate was placed on the spin coater or on the hot plate in a N_2-filled glovebox and illuminated by focused light from a halogen lamp. A fiber optical cable was placed at an off-specular angle and collected the light that was scattered by the white paint and transmitted through the perovskite layer. The fiber was connected to a spectrophotometer that analyzed the raw photon counts. The absorption was calculated according to the following equation:

$$A(\lambda) = -log_{10}(\frac{I_m(\lambda) - I_{m,dark}(\lambda)}{I_{m,blank}(\lambda) - I_{m,dark}(\lambda)})$$

where $I_m(\lambda)$ represents the photon counts at a specific wavelength, $I_{m,dark}$ and $I_{m,blank}$ represent a dark and blank reference, respectively, on the same substrate before the spin-coating process started or on a similar substrate in case of annealing experiment.

Fourier transform infrared spectroscopy (FT-IR). ATR-FTIR spectra were recorded by using a PerkinElmer Spectrum Two FT-IR spectrometer. Solutions were made by dissolving MAI (or BAI) and PbI_2 in DMF, DMSO or NMP, with the following molar ratios: 9:1:1 (MA or BA: PbI_2 : solvent) for DMF and DMSO, 5:1:1 for NMP.

MC-DFT simulations. A MC-DFT scheme was performed to study the configurations of ternary components [MAI (BAI) – PbI_2 – solvent] and select a reasonable structure for further investigations including interaction energy and frequency. The DMF is used to execute the MC-DFT calculations and 2000 configurations of the MAI-PbI_2-DMF and BAI-PbI_2-DMF systems created with Monte Carlo (MC) insertion moves using the RASPA code.[39] A PbI_3 molecular cluster is fixed in the origin of the cell, and one MA (or BA) cation and one DMF molecule are randomly placed within a cubic box of 8 Å side length. Then DFT single-point calculations were carried out to obtain the energy of each configuration.

DFT calculations. All DFT calculations were carried out in the Kohn–Sham framework, using the Amsterdam Density Functional package (version ADF 2019.302).[40] Geometry optimizations were done using the Perdew-Burke-Ernzerhof (PBE) functional,[41] and Slater-type triple-zeta (TZP) basis sets for all the atoms (the cores 1s–2s, 1s–4p and 1s–4d were kept frozen, respectively, for S, I, and Pb) in combination with large core effective potentials were used. Scalar relativistic effects are accounted, by using the zeroth-order regular approximation (ZORA) Hamiltonian.[42–44] Geometry convergence is achieved to 10^{-4} Å and energy convergence to 10^{-5} Eh. Frequency calculations are done at the harmonic level approximation without correction to ensure that the optimized structures are located at global or local minima on the potential energy surface.[45–47]

3.10 REFERENCES

[1]   H. Ren, S. Yu, L. Chao, Y. Xia, Y. Sun, S. Zuo, F. Li, T. Niu, Y. Yang, H. Ju, B. Li, H. Du, X. Gao, J. Zhang, J. Wang, L. Zhang, Y. Chen, W. Huang, *Nat. Photonics* **2020**, *14*, 154.
[2]   G. Grancini, M. K. Nazeeruddin, *Nat. Rev. Mater.* **2019**, *4*, 4.
[3]   C. Ortiz-Cervantes, P. Carmona-Monroy, D. Solis-Ibarra, *ChemSusChem* **2019**, *12*, 1560.

[4]   D. Thrithamarassery Gangadharan, D. Ma, *Energy Environ. Sci.* **2019**, *12*, 2860.

[5]   M. C. Gélvez-Rueda, E. M. Hutter, D. H. Cao, N. Renaud, C. C. Stoumpos, J. T. Hupp, T. J. Savenije, M. G. Kanatzidis, F. C. Grozema, *J. Phys. Chem. C* **2017**, *121*, 26566.

[6]   M. C. Gélvez-Rueda, P. Ahlawat, L. Merten, F. Jahanbakhshi, M. Mladenović, A. Hinderhofer, M. I. Dar, Y. Li, A. Dučinskas, B. Carlsen, W. Tress, A. Ummadisingu, S. M. Zakeeruddin, F. Schreiber, A. Hagfeldt, U. Rothlisberger, F. C. Grozema, J. V. Milić, M. Graetzel, *Adv. Funct. Mater.* **2020**, *30*, 2003428.

[7]   A. Z. Chen, J. J. Choi, *J. Vac. Sci. Technol. A* **2020**, *38*, 010801.

[8]   Y. Qin, H. Zhong, J. J. Intemann, S. Leng, M. Cui, C. Qin, M. Xiong, F. Liu, A. K. -Y. Jen, K. Yao, *Adv. Energy Mater.* **2020**, *10*, 1904050.

[9]   J. Dong, S. Shao, S. Kahmann, A. J. Rommens, D. Hermida-Merino, G. H. ten Brink, M. A. Loi, G. Portale, *Adv. Funct. Mater.* **2020**, *30*, 2001294.

[10] C. M. M. Soe, G. P. Nagabhushana, R. Shivaramaiah, H. Tsai, W. Nie, J.-C. Blancon, F. Melkonyan, D. H. Cao, B. Traoré, L. Pedesseau, M. Kepenekian, C. Katan, J. Even, T. J. Marks, A. Navrotsky, A. D. Mohite, C. C. Stoumpos, M. G. Kanatzidis, *Proc. Natl. Acad. Sci.* **2019**, *116*, 58.

[11] J.-W. Lee, H.-S. Kim, N.-G. Park, *Acc. Chem. Res.* **2016**, *49*, 311.

[12] B. Li, D. Binks, G. Cao, J. Tian, *Small* **2019**, *15*, 1903613.

[13] J.-W. Lee, Z. Dai, C. Lee, H. M. Lee, T.-H. Han, N. De Marco, O. Lin, C. S. Choi, B. Dunn, J. Koh, D. Di Carlo, J. H. Ko, H. D. Maynard, Y. Yang, *J. Am. Chem. Soc.* **2018**, *140*, 6317.

[14] S. Shao, H. Duim, Q. Wang, B. Xu, J. Dong, S. Adjokatse, G. R. Blake, L. Protesescu, G. Portale, J. Hou, M. Saba, M. A. Loi, *ACS Energy Lett.* **2020**, *5*, 39.

[15] N. Liu, P. Liu, H. Ren, H. Xie, N. Zhou, Y. Gao, Y. Li, H. Zhou, Y. Bai, Q. Chen, *ACS Appl. Mater. Interfaces* **2020**, *12*, 3127.

[16] Y. Xu, M. Wang, Y. Lei, Z. Ci, Z. Jin, *Adv. Energy Mater.* **2020**, *10*, 2002558.

[17] A. Z. Chen, M. Shiu, J. H. Ma, M. R. Alpert, D. Zhang, B. J. Foley, D. M. Smilgies, S. H. Lee, J. J. Choi, *Nat. Commun.* **2018**, *9*, 1.

[18] J. M. Hoffman, J. Strzalka, N. C. Flanders, I. Hadar, S. A. Cuthriell, Q. Zhang, R. D. Schaller, W. R. Dichtel, L. X. Chen, M. G. Kanatzidis, *Adv. Mater.* **2020**, *2002812*, 1.

[19] C. M. M. Soe, W. Nie, C. C. Stoumpos, H. Tsai, J. C. Blancon, F. Liu, J. Even, T. J. Marks, A. D. Mohite, M. G. Kanatzidis, *Adv. Energy Mater.* **2018**, *8*, 2.

[20] R. Quintero-Bermudez, A. Gold-Parker, A. H. Proppe, R. Munir, Z. Yang, S. O. Kelley, A. Amassian, M. F. Toney, E. H. Sargent, *Nat. Mater.* **2018**, *17*, 900.

[21] A. Z. Chen, M. Shiu, X. Deng, M. Mahmoud, D. Zhang, B. J. Foley, S.-H. Lee, G. Giri, J. J. Choi, *Chem. Mater.* **2019**, *31*, 1336.

[22] C. J. Dahlman, R. A. DeCrescent, N. R. Venkatesan, R. M. Kennard, G. Wu, M. A. Everest, J. A. Schuller, M. L. Chabinyc, *Chem. Mater.* **2019**, *31*, 5832.

[23] Y. Hu, L. M. Spies, D. Alonso-Álvarez, P. Mocherla, H. Jones, J. Hanisch, T. Bein, P. R. F. Barnes, P. Docampo, *J. Mater. Chem. A* **2018**, *6*, 22215.

[24] P. Mao, J. Zhuang, Y. Wei, N. Chen, Y. Luan, J. Wang, *Sol. RRL* **2019**, *3*, 1800357.

[25] P. Cheng, Z. Xu, J. Li, Y. Liu, Y. Fan, L. Yu, D.-M. Smilgies, C. Müller, K. Zhao, S. F. Liu, *ACS Energy Lett.* **2018**, *3*, 1975.

[26] X. Li, J. M. Hoffman, M. G. Kanatzidis, *Chem. Rev.* **2021**, *121*, 2230.

[27] J. Liu, J. Leng, K. Wu, J. Zhang, S. Jin, *J. Am. Chem. Soc.* **2017**, *139*, 1432.

[28] P. Cheng, P. Wang, Z. Xu, X. Jia, Q. Wei, N. Yuan, J. Ding, R. Li, G. Zhao, Y. Cheng, K. Zhao, S. F. Liu, *ACS Energy Lett.* **2019**, *4*, 1830.

[29] C. C. Stoumpos, D. H. Cao, D. J. Clark, J. Young, J. M. Rondinelli, J. I. Jang, J. T. Hupp, M. G. Kanatzidis, *Chem. Mater.* **2016**, *28*, 2852.

[30] R. Yang, R. Li, Y. Cao, Y. Wei, Y. Miao, W. L. Tan, X. Jiao, H. Chen, L. Zhang, Q. Chen, H. Zhang, W. Zou, Y. Wang, M. Yang, C. Yi, N. Wang, F. Gao, C. R. McNeill, T. Qin, J. Wang, W. Huang, *Adv. Mater.* **2018**, *30*, 1804771.

[31] W. L. Tan, Y.-B. Cheng, C. R. McNeill, *J. Mater. Chem. A* **2020**, *8*, 12790.

[32] J. Song, G. Zhou, W. Chen, Q. Zhang, J. Ali, Q. Hu, J. Wang, C. Wang, W. Feng, A. B. Djurišić, H. Zhu, Y. Zhang, T. Russell, F. Liu, *Adv. Mater.* **2020**, *32*, 2002784.

[33] H. Tsai, W. Nie, J.-C. Blancon, C. C. Stoumpos, R. Asadpour, B. Harutyunyan, A. J. Neukirch, R. Verduzco, J. J. Crochet, S. Tretiak, L. Pedesseau, J. Even, M. A. Alam, G. Gupta, J. Lou, P. M. Ajayan, M. J. Bedzyk, M. G. Kanatzidis, A. D. Mohite, *Nature* **2016**, *536*, 312.

[34] J. Shi, Y. Gao, X. Gao, Y. Zhang, J. Zhang, X. Jing, M. Shao, *Adv. Mater.* **2019**, *31*, 1901673.

[35] X. Li, G. Wu, M. Wang, B. Yu, J. Zhou, B. Wang, X. Zhang, H. Xia, S. Yue, K. Wang, C. Zhang, J. Zhang, H. Zhou, Y. Zhang, *Adv. Energy Mater.* **2020**, *10*, 2001832.

[36] C. Zuo, A. D. Scully, W. L. Tan, F. Zheng, K. P. Ghiggino, D. Vak, H. Weerasinghe, C. R. McNeill, D. Angmo, A. S. R. Chesman, M. Gao, *Commun. Mater.* **2020**, *1*, 33.

[37] L. Li, Y. Chen, Z. Liu, Q. Chen, X. Wang, H. Zhou, *Adv. Mater.* **2016**, *28*, 9862.

[38] Y. Han, S. Park, J. Wang, S. Jariwala, K. Lee, C. G. Bischak, S. Kim, J. Hong, S. Kim, M. J. Lee, D. S. Ginger, I. Hwang, *Adv. Mater. Interfaces* **2020**, *7*, 1901860.

[39] D. Dubbeldam, S. Calero, D. E. Ellis, R. Q. Snurr, *Mol. Simul.* **2016**, *42*, 81.

[40] G. te Velde, F. M. Bickelhaupt, E. J. Baerends, C. Fonseca Guerra, S. J. A. van Gisbergen, J. G. Snijders, T. Ziegler, *J. Comput. Chem.* **2001**, *22*, 931.

[41] J. P. Perdew, K. Burke, M. Ernzerhof, *Phys. Rev. Lett.* **1996**, *77*, 3865.

[42] E. van Lenthe, E. J. Baerends, J. G. Snijders, *J. Chem. Phys.* **1993**, *99*, 4597.

[43] E. van Lenthe, E. J. Baerends, J. G. Snijders, *J. Chem. Phys.* **1994**, *101*, 9783.

[44] E. van Lenthe, A. Ehlers, E.-J. Baerends, *J. Chem. Phys.* **1999**, *110*, 8943.

[45] H. Jacobsen, A. Bérces, D. P. Swerhone, T. Ziegler, *Comput. Phys. Commun.* **1997**, *100*, 263.

[46] A. Bérces, R. M. Dickson, L. Fan, H. Jacobsen, D. Swerhone, T. Ziegler, *Comput. Phys. Commun.* **1997**, *100*, 247.

[47] S. K. Wolff, *Int. J. Quantum Chem.* **2005**, *104*, 645.

4

Impact of Alkyl Chain Length on the Formation of Regular- and Reverse-Graded Quasi-2D Perovskites

Abstract

Crystallization of quasi-2D perovskites is a complex process that leads to multidimensional films consisting of 2D, quasi-2D, and 3D phases. Most quasi-2D perovskite films possess a regular-gradient, with low-dimensional phases located at the bottom of the film and 3D phases at the top. Recently, multiple studies have reported reverse-graded perovskite films, where the location of 2D and 3D structures is inverted. The underlying reasons of such peculiar phase distribution are unclear. Here, we examine the impact of the alkyl chain length on the formation of regular- and reverse-graded perovskites using n-alkylammonium ions. We find that long alkyl chains reverse the phase distribution gradient, and we demonstrate that crystallization starts at the liquid–N_2 interface, though as 3D phases for short spacers, and as quasi-2D phases for long spacers. We link this behavior to enhanced van-der-Waals interactions between long alkylammonium ions in polar solvents and their tendency to accumulate at the liquid–N_2 interface, creating a concentration gradient along the film thickness.

4.1 INTRODUCTION

Quasi-two-dimensional (quasi-2D) metal-halide perovskites are promising candidates for a variety of optoelectronic devices, such as solar cells, light-emitting diodes, and photodetectors.[1–3] Conventional three-dimensional (3D) metal-halide perovskites possess an ABX_3 structure, where A is a small monovalent cation, such as methylammonium (MA) or formamidinium (FA), B is usually divalent lead (Pb) or tin (Sn) ion, and X is a halide anion, usually iodide (I) or bromide (Br).[4] These perovskites consist of metal-halide octahedra intercalated by small cations. Ruddlesden-Popper 2D and quasi-2D perovskites share a similar inorganic part, but with a large ammonium spacer cation, such as butylammonium (BA) or phenethylammonium (PEA), cutting the octahedra along the <100> direction to form a layered crystal structure.[5] 2D perovskites (R_2BX_4, where R is an ammonium spacer cation) possess a single layer of BX_6^{4-} octahedra sandwiched between ammonium spacer cations ($n = 1$), whereas quasi-2D perovskites ($R_2A_{n-1}B_nX_{3n+1}$) have more layer of BX_6^{4-} octahedra in between ($n = 2 – 5$).[1,6]

The crystallization of quasi-2D perovskites is more complex than for pure 3D or 2D. For instance, for $BA_2MA_3Pb_4I_{13}$ the precursor solution contains BAI, MAI, and PbI_2, which compete to crystallize 2D, quasi-2D with different n value, and 3D perovskites.[7] The overall result is a mixed-phase quasi-2D perovskite film with an average $<n>$ value. Quasi-2D perovskites largely show a phase distribution gradient with (quasi-)2D phases at the bottom of the film and 3D phases at the top (regular-graded).[8–12] Phase distribution can be tuned via solvent and additive engineering,[9,13–15] although modifying the substrate surface or varying processing conditions has also been shown to have an impact.[16–18] Of course, the ammonium spacer cation also has a profound effect on which phases are formed during crystallization. Its chemical structure will influence inter-spacer interactions and, as a result, the phase distribution of the quasi-2D perovskite film.[19] For example, fluorination of PEA reduces the formation of $n = 1$, which is usually detrimental for photovoltaic performances, and allows a more efficient charge transport because of a different molecular stacking.[12,20] Recently, so-called reverse-graded quasi-2D perovskites have been reported, where 3D phases are at the bottom and (quasi-)2D phases at the top of the film. The first studies to show this peculiar behavior employed cyclohexylmethylammonium iodide (CMAI) as spacer.[21,22] Both Type I (i.e., nested) and Type II (i.e., cascading) alignments of the valence and conduction bands have been reported for graded quasi-2D films.[22–26] A Type II phase distribution of regular-graded quasi-2D films is suitable for solar cells in a *p-i-n* configuration because it facilitates hole and electron collection and has provided

power conversion efficiencies (PCEs) up to ~21%.[27–29] Conversely, for reverse-graded quasi-2D perovskites, the Type II band alignment is better adapt for *n-i-p* devices and highest reported PCEs are ~20%.[22,24,30]

Although regular- and reverse-graded quasi-2D perovskites have been reported before, their crystallization mechanism and the underlying reasons behind this peculiar distribution are still unclear. Mao et al. claimed that BA ions prefer to stay in solution, while MA ions stay at the surface, thus explaining the 2D-3D gradient that is often observed.[31] However, no proof of concentration gradient in the wet film was shown. Liu et al. employed a cation diffusion model to explain phase distribution in quasi-2D perovskite films and found large differences in diffusivity between cations based on their mass and molecular volume.[32] They mostly attributed differences in cation diffusivity as the main reason behind the formation of a 2D-3D graded film. However, they only investigated *n*-alkylammonium ions containing 3 and 4 carbon atoms (propylammonium, PA, and BA) and no reverse-graded films. Jang et al. studied the formation mechanism of multiphase Ruddlesden-Popper perovskites for isobutylammonium (isoBA) using cold- and ambient-antisolvent bathing after spin coating, prior to annealing.[30] They found that cold-bathing results in low-*n* phase formation at the top of the film and considered that at low temperature delayed sequential nucleation occurs, where the lower solubility of the small (MA) compared to the bulky (isoBA) organic cations favors formation of 3D phases as the substrate-liquid interface.

In this work, we analyze a series of quasi-2D perovskite films for *n*-alkylammonium ions with increasing chain length, going from C4 to C12. We observe that from C8 onwards a reversal of the phase distribution gradient is obtained, hinting that the length and apolar nature of the alkyl chains have a profound impact on the crystallization of the film. Correlating photoluminescence (PL) spectra with in-situ UV-vis-NIR absorption spectroscopy during thermal annealing to reveal the temporal evolution of the crystallization of quasi-2D perovskites, we find that the liquid–N_2 interface is the location where crystallization takes place for both regular- and reverse-graded perovskites, although the crystallization starts as quasi-3D for short *n*-alkylammonium ions, and as quasi-2D perovskites for long *n*-alkylammonium ions. By using a mixture of short and long *n*-alkylammonium ions we add a degree of tunability to quasi-2D perovskite films that enables improving the film morphology and stratification of 2D and 3D phases.

4.2 QUASI-2D PEROVSKITES WITH N-ALKYLAMMONIUM SPACERS

We fabricated quasi-2D perovskite films with formula $(R)_2MA_3Pb_4I_{13}$, where R = *n*-butylammonium (C4), *n*-pentylammonium (C5), *n*-hexylammonium (C6), *n*-

octylammonium (C8), and *n*-dodecylammonium (C12) iodide (**Figure 4.1**a). Based on our previous work, we optimized the solvent/co-solvent (DMF/DMSO) ratio to 4:1 such that large amounts of small-*n* phases (*n* = 1, 2, 3, etc.) are formed.[9] Although the presence of these phases has been shown to be detrimental for photovoltaic performances, because of poor orientation and consequently poor charge transport,[33] we opted for this phase distribution to more easily observe differences between 3D and 2D, or quasi-2D phases and their distribution.
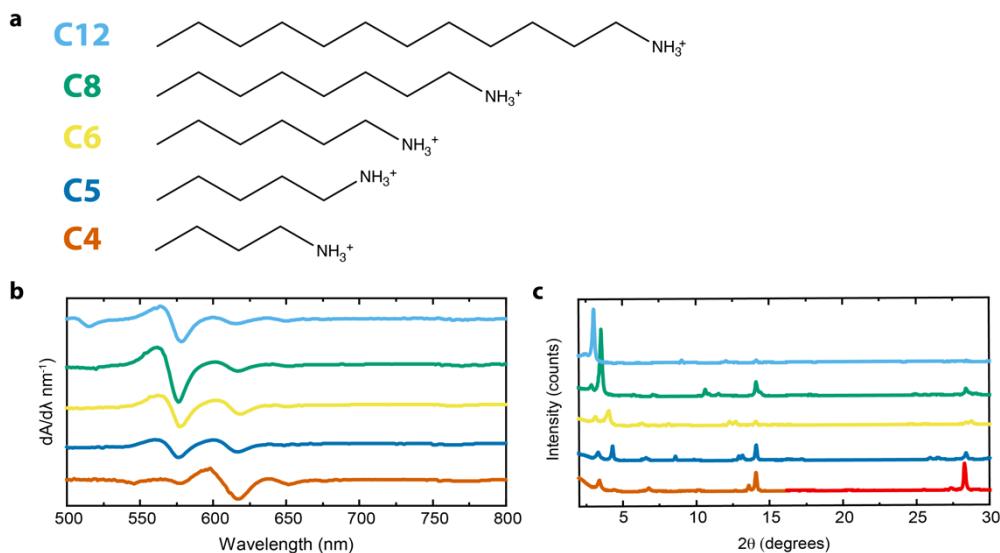

Figure 4.1. (a) Chemical structures of butylammonium (C4), pentylammonium (C5), hexylammonium (C6), octylammonium (C8), dodecylammonium (C12) spacers. (b) Derivative of UV-vis-NIR absorption spectra for $R_2MA_3Pb_4I_{13}$ films, where R = C4–C12. (c) XRD patterns for the same films as in (b).

Figure 4.1b displays the first derivative of the UV-vis-NIR absorption spectra of such films. Structural phases such as *n* = 1–5 are usually observed as shoulders in the absorption spectra, thus the first derivative will highlight such peaks. All films display a negligible peak at >750 nm, which represents a very shallow onset for the absorption of 3D perovskite phases. With increasing length of the *n*-alkylammonium ion, the phase distribution shifts towards smaller-*n* phases as can be seen from the blue shift of the spectral signatures. For instance, C4 shows prevalently *n* = 3 (~600 nm) and small amounts of *n* = 2 (~570 nm) and *n* = 4 (~640 nm), whereas the amount of *n* = 2 is enhanced from C5 onwards. C8 forms mostly *n* = 2, whereas C12 is the only spacer that also forms *n* = 1 (~520 nm). The formation of smaller-*n* phases with longer alkyl chains can be attributed to their enhanced van-der-Waals interactions, which facilitate the formation of small-*n* phases because the assembly of alkyl chains

becomes more energetically favored. This scenario is comparable to the use of aromatic spacers; these molecules, such as PEA, can form π–π stacking and such an additional interaction leads to smaller-n phases being more easily formed.

X-ray diffraction (XRD) confirms the trend observed with UV-vis-NIR absorption spectroscopy (Figure 4.1c). Parallel-oriented 2D and quasi-2D phases display diffraction peaks at 2θ angles below 10°. C4 shows the formation of $n = 3$ (3.4°) and $n = 2$ (4.4°). These two diffraction peaks are visible for all the films, but $n = 3$ steadily decreases while $n = 2$ becomes dominant in the XRD pattern with increasing alkyl spacer length.[9] The diffraction angles for both quasi-2D phases decrease from C4 to C12, in line with an increase of lattice spacing because of the presence of a larger organic cation. The 3D perovskite peaks at 14° and 28° are observed for all films. However, in line with the observation that longer alkylammonium ions form more 2D and quasi-2D phases, C4 shows the strongest diffraction at the abovementioned angles, and C12 the weakest.

4.3 REGULAR- AND REVERSE-GRADED QUASI-2D PEROVSKITES

To investigate the impact of alkyl chain lengths on the phase distribution gradient, we analyzed the location of 2D and 3D phases via PL spectroscopy (**Figure 4.2**).
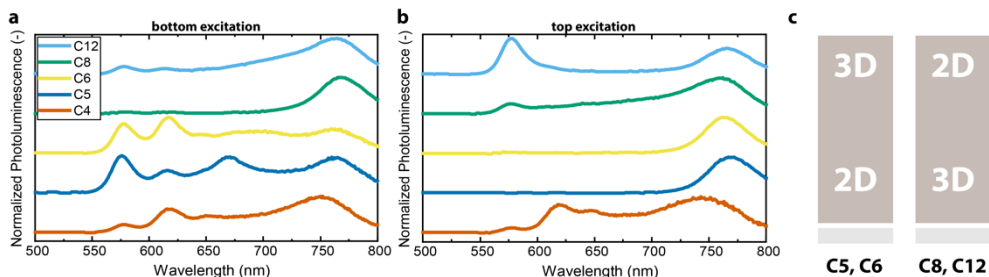

Figure 4.2. (a-b) Photoluminescence spectra of $R_2MA_3Pb_4I_{13}$ films, where R = C4–C12 from bottom (a) and top (b) 405 nm excitation. (c) Illustration of regular (left) and reversed (right) phase distribution gradient.

C4 displays relatively small differences between top and bottom excitation. C5 and C6 exhibit the characteristic features of a 2D-3D, regular-graded perovskite, where quasi-2D phases are at the bottom of the film and 3D phases at the top. A variety of n-phases can be identified, ranging from $n = 2$ to 4 from peaks at 575, 615, and 650 nm, when exciting the film from the bottom (glass) side. On the contrary, when exciting from the top (N_2 ambient atmosphere) side, mainly 3D perovskites are emitting at ~750 nm. An opposite observation is made starting from C8, where it seems that the overall phase distribution shifts and becomes 3D-2D, reverse-graded. In this case, $n = 2$ phases (570 nm) emit mostly from the top side of the film, whereas 3D phases are prevalent at the bottom. This behavior is even

more apparent for C12 where the PL of the $n = 2$ phase at 570 nm remains higher than from the 3D phase at 765 nm under top illumination. These results demonstrate that the gradient of 2D and 3D phases can be tuned by increasing the length of the alkyl spacer (Figure 4.2c). This is possibly linked to the surfactant properties of long n-alkylammonium ions, that preferentially locate at the liquid-N_2 interface.[34] In addition, the reduced solubility of long n-alkylammonium ions in the polar DMF/DMSO solvent mixture can enhance nucleation of low-n phases compared to the 3D phase. These mechanisms can explain why, for C8 and C12, the 2D phases crystallize mostly at the liquid-N_2 interface.

We performed X-ray photoelectron spectroscopy (XPS) on C4 and C12 films to further analyze the gradient distribution of 2D and 3D phases. By analyzing the C 1s spectra (**Figure 4.3**), we observe that C4 displays two features attributed to carbon atoms binding to carbon (285 eV) and nitrogen (286 eV). For C12, the same features are observed but the 285 eV signal is, expectedly, more intense. With argon ion sputtering we performed a depth-profiling measurement, where XPS scans are performed after each etching cycle. Figure 4.3b displays the atomic concentration of C as function of sputtering time. With the settings used for sputtering (500 eV ion energy), 1000 s are enough to etch the entire film thickness. In the case of C12, the C concentration decreases with sputtering time and stabilizes at about 45%, in agreement with a reverse-graded film. In the case of C4, the carbon amount is more stable along the whole range and is only slightly higher at the bottom than the top, in line with a relatively uniform film.
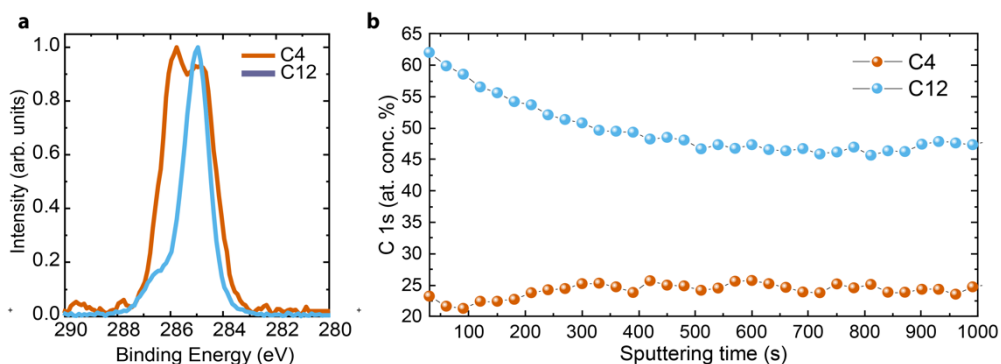
Figure 4.3. (a) C 1s XPS spectra for $(C4)_2MA_3Pb_4I_{13}$ and $(C12)_2MA_3Pb_4I_{13}$ films. (b) Atomic concentration of carbon for the same films as (a) as function of sputtering time. After 1000 s, the entire film is etched.

4.4 CRYSTALLIZATION KINETICS

Crystallization of quasi-2D perovskites has been shown to start from the liquid–air interface as a 3D perovskite phase, and to form at a later stage 2D or quasi-2D

phases towards the bottom.[7,9,35,36] All previous studies were performed on short *n*-alkylammonium ions, meaning that these possessed a 2D-3D gradient. Once shown that long *n*-alkylammonium ions form reverse-graded Ruddlesden-Popper films, we investigated the crystallization mechanism focusing on the nucleation. To answer such a question, we performed in-situ UV-vis-NIR absorption during thermal annealing of wet films. As displayed in **Figure 4.4**a, C4 starts to crystallize as quasi-3D (unidentified large-*n* value) perovskites, with an onset at ~750 nm appearing after about 4 s. After 10 s, an excitonic peak related to *n* = 3 appears, indicating that the quasi-2D perovskite phases are formed after the 3D perovskite already begun crystallizing. C5 follows the same mechanism. After 1 s, C6 starts crystallizing as *n* = 4 and 5 phases with peaks at ~640 and ~660 nm (Figure 4.4b); shortly afterwards (~5 s) it develops into a quasi-3D perovskite, with an onset at ~770 nm, and finally it develops *n* = 2 and 3 features. In contrast, C8 and C12 start crystallizing after 5 s mainly as *n* = 2 (~570 nm), developing 3D-like features only long after annealing (~30 s) has started (Figure 4.4c,d Interestingly, this phenomenon is also visible by naked eye. During annealing, C8 and C12 films turn from yellow (wet film) to red (wide bandgap material), and then to a darker color, indicating the formation of lower bandgap phases (3D). By comparison, the films turn immediately darker in the case of C4. There is a striking trend with regard to which phases are formed first. By increasing the alkyl length, the crystallization shifts from starting as a higher-dimensional perovskite to starting as a quasi-2D. With the location of 3D phases being the top of the film, as demonstrated by PL spectroscopy, C4–C6 confirm that the perovskite films crystallize as quasi-3D (or large-*n*) at the liquid-air interface. In the case of C6, we also expect *n* = 4 and 5 phases at the surface of the film, which might not be visible in PL because of efficient carrier transfer from high to low bandgap phases. For C8 and C12, crystallization starts as quasi-2D, again at the liquid–N_2 interface. Irrespective of the perovskite phases formed, crystallization begins at the liquid–N_2 interface. The experiments show that with long alkyl chains, crystallization of the 3D phase is significantly delayed (to ~30 s) compared to short alkyl chains (at ~5 s). Interestingly, the cation diffusivity model proposed by Liu et al. does not seem to be valid in our experiments.[32] In fact, the diffusivity of cations with larger mass, such as C5–C12, should decrease even further compared to C4 and MA and the 2D-3D phase distribution gradient should be more evident. The diffusivity model does also not predict reverse-graded phase distribution. Also the model of Jang et al. cannot explain the results obtained here because crystallization of the 3D phase is retarded compared to the low-*n* quasi-2D perovskite in the reverse-graded perovskite films obtained with C8 and C12.[30]
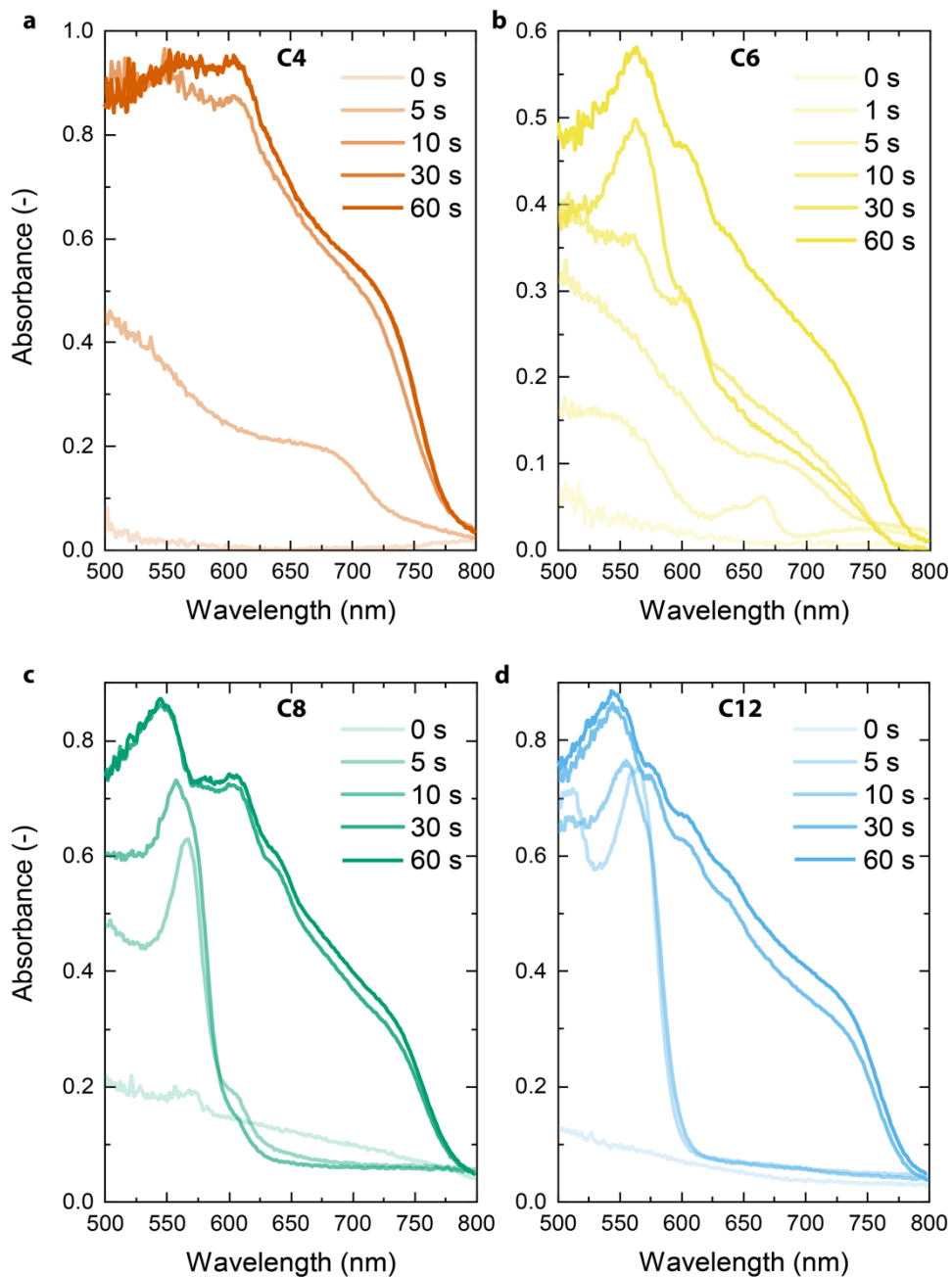
Figure 4.4. In-situ UV-vis-NIR absorption during thermal annealing of $(R)_2MA_3Pb_4I_{13}$. (a) R = C4. (b) R = C6. (c) R = C8. (d) R = C12.

Based on our experimental results, we postulate the following crystallization mechanism. We consider that crystallization starts at the liquid–N_2 interface where the solids concentration increases as a result of solvent evaporation.
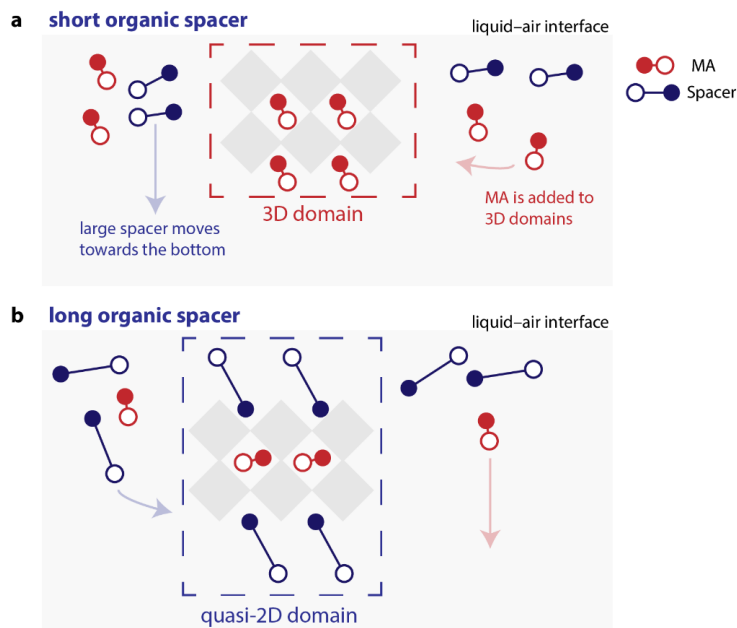

Figure 4.5. Illustration of the proposed crystallization mechanism for (a) short organic spacers (C4, C5) and long organic spacers (C8, C12).

With regard to C4, the similarity with MA is high. The concentration of MA at the liquid–N_2 interface is high enough to enable crystallization of 3D perovskites, followed shortly afterwards by quasi-2D phases. In this case, the phase distribution gradient is minimal. C5 falls in a similar category as C4, meaning that the crystallization will start as 3D. However, with increasing length, the alkylammonium ions will assemble more at the polar liquid–N_2 interface and the increased van-der-Waals interaction between the alkyl chains favors formation quasi-2D crystalline nuclei. The C6 molecules are concentrated enough at the liquid–N_2 interface to enable a crystallization of larger-n quasi-2D phases, namely $n = 4$ and 5. For, C8 and C12 molecules this tendency is further enhanced such that crystallization at the liquid–N_2 interface starts a as quasi-2D perovskite. More specifically, as the crystallization for C12 starts as $n = 2$, we expect a ratio of C12:MA of 2:1. The concentration of MA increases towards the bottom of the film, forming 3D perovskites at the interface with the substrate. This is schematically illustrated in **Figure 4.5**.

4.5 MULTISPACER QUASI-2D PEROVSKITE FILMS

We confirmed the abovementioned crystallization mechanism by mixing C4 and C12 in a 9:1 ratio to form a $(C4_{0.9}C12_{0.1})_2MA_3Pb_4I_{13}$ Ruddlesden-Popper perovskite film. As mentioned, C12 molecules will locate at the liquid–N_2 interface and the crystallization of a mixed *n*-alkylammonium ion film is expected to be intermediate between the one of the individual C4 and C12 components.
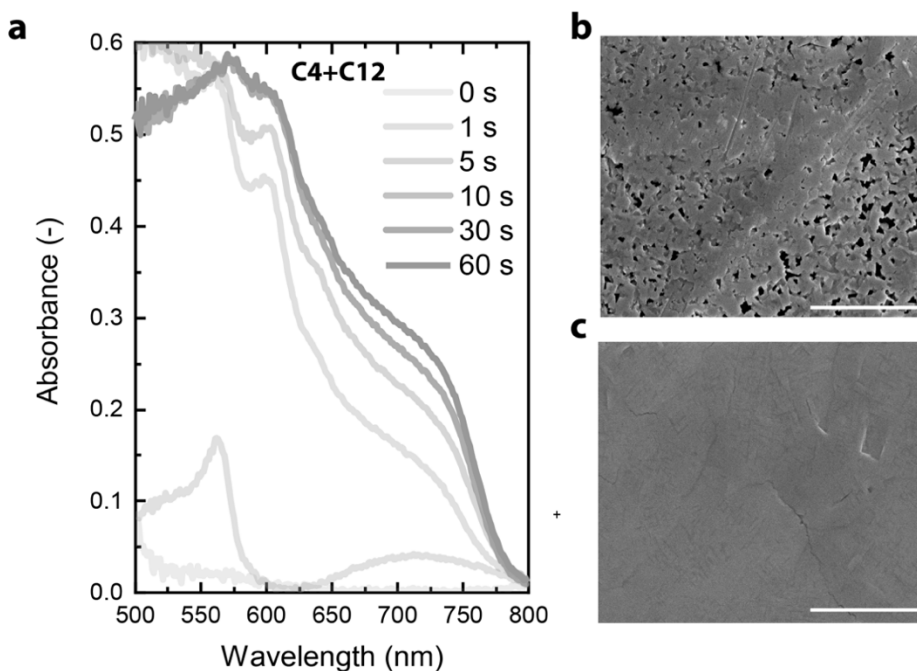

Figure 4.6. (a) In-situ UV-vis-NIR absorption during thermal annealing of $(C4_{0.9}C12_{0.1})_2MA_3Pb_4I_{13}$. (b–c) Top-view SEM images of $(C4)_2MA_3Pb_4I_{13}$ (b) and $(C4_{0.9}C12_{0.1})_2MA_3Pb_4I_{13}$ (c). Scalebar is 4 µm.

In-situ UV-vis-NIR during thermal annealing (**Figure 4.6**a) shows that the small amount of C12 present in the solution (10% compared to C4) is enough to lead the crystallization to start as a C12-based $n = 2$ (~570 nm) in the first few seconds of annealing. After 5 s, the perovskite film already shows quasi-3D and quasi-2D phases and such features develop further during annealing. Changes in crystallization rate are usually effective in changing the morphology of the resulting film. Scanning-electron microscope (SEM) images show that the pristine C4 Ruddlesden-Popper perovskite film is not uniform but contains pinholes (Figure 4.6b). The multispacer film, however, displays a uniform and pinhole-free film (Figure 4.6c) due to a slower crystallization. The presence of cracks is attributed to grain

boundaries, which become more visible in the SEM image during electron-beam exposure.

The use of mixed n-alkylammonium ions could prove itself useful to control crystallization rate and the phase distribution gradient. Theoretically, an optimized multispacer system could pave the way for a non-phase-distributed system, which has been a difficult task to achieve in quasi-2D perovskites. Changes in the spacers' molecular structure could also induce different phase distribution gradients. Multispacer systems have been used before in quasi-2D perovskites optoelectronic devices, although mostly by trial-and-error.[37] With more understanding of the crystallization mechanism of quasi-2D perovskites based on multiple spacers, a new degree of tunability of Ruddlesden-Popper perovskites can be added, possibly leading to a new class of perovskite films containing spacers with a variety of chemical properties.

4.6 CONCLUSIONS

We demonstrated that the length of n-alkylammonium ions in quasi-2D perovskites determines the phase distribution gradient with short alkyl chains favoring regular-graded films (i.e., 3D at top and quasi-2D at bottom) and long alkyl chains resulting in reverse-graded films (i.e., quasi-2D at top and 3D at bottom). In-situ UV-vis-NIR spectroscopy during thermal annealing showed that crystallization starts with the 3D phase for short alkyl chains, but with the quasi-2D phases and for long alkyl chains. This implies that in each case crystallization starts at the linquid–N_2 interfaces where the solids concentration increases when solvent evaporates. We attribute the different behavior of short and long n-alkylammonium ions to the tendency of long apolar alkyl chains to accumulate at the liquid– N_2 interface and the increasing van-der-Waals interactions between chains when their length increases.

4.7 METHODS

Materials. PbI_2 was purchased from TCI Chemicals (99.99%) and the alkylammonium iodides from GreatCell Solar. Solvents were purchased from Sigma Aldrich. All materials were used as received. To prepare $R_2MA_3Pb_4I_{13}$ solutions, a PbI_2-based 1 M solution was prepared by mixing alkylammonium iodide (RAI), methylammonium iodide (MAI), and PbI_2 in the ratio 2:3:4 in *N-N*-dimethylformamide/dimethyl sulfoxide (DMF/DMSO) 4:1 (v/v solvent mixture). RAI corresponds to n-butylammonium (C4), n-pentylammonium (C5), n-hexylammonium (C6), n-octylammonium (C8), and n-dodecylammonium (C12) iodide.

Perovskite deposition. 60 µL of precursor solution was dropped onto a glass substrate (previously cleaned by sonication in isopropanol and by UV-ozone treatment for 30 min). Spin coating was performed at 5000 rpm for 45 s and followed by thermal annealing at 100 °C for 10 min. All fabrication was performed in an N_2-filled glovebox.

Film characterization. UV-vis-NIR spectra were recorded by using a PerkinElmer Lambda 1050 UV-vis-NIR spectrophotometer. Photoluminescence spectra were recorded by using an Edinburgh Instruments FLSP920 double-monochromator luminescence spectrophotometer. X-ray diffractograms were recorded by using a Bruker 2D phaser (Cu Kα radiation, $\lambda = 1.5406\,\text{Å}$): measurements were performed in the range 3-40° with a step size 0.02° and collection time of 0.5 s. XPS measurements were performed using a Thermo Scientific K-Alpha with a 180° double focusing hemispherical analyzer and a 128-channel detector. Monochromatic Al Kα (1486.6 eV) radiation was used, and the X-ray spot size was 400 μm. For the surface analysis, a survey spectrum was first measured for 12 scans with a pass energy of 200 eV. High-resolution scan (20 times) of each element was conducted with a pass energy of 50 eV. During the sputtering experiment, the sample was removed layer-by-layer by argon ion etching operated at low current and low ion energy (500 eV). The crater region generated by argon ions is $\sim 2 \times 4$ mm^2 . For the depth profiles, snapshot mode was used for each element, and the number of frames was 5×1 s. SEM images were collected with a FEI Quanta 3D FEG microscope (5 keV electron beam, secondary electron detector). Films were sputtered with Au beforehand to improve the surface conductivity.

In-situ UV-vis-NIR absorption. White paint was applied on the back of a glass substrate, then the substrate was placed on the hot plate in a N$_2$-filled glovebox and illuminated by focused light from a halogen lamp. A fiber optical cable was placed at an off-specular angle and collected the light that was scattered by the white paint and transmitted through the perovskite layer. The fiber was connected to a spectrophotometer that analyzed the raw photon counts. The absorbance was calculated according to the following equation:

$$A(\lambda) = -log_{10}\left(\frac{I_m(\lambda) - I_{m,dark}(\lambda)}{I_{m,blank}(\lambda) - I_{m,dark}(\lambda)}\right)$$

where $I_m(\lambda)$ represents the photon counts at a specific wavelength, $I_{m,dark}$ and $I_{m,blank}$ represent a dark and blank reference, respectively, on a similar substrate on the hot plate.

4.8 REFERENCES

[1]   A. Caiazzo, R. A. J. Janssen, *Adv. Energy Mater.* **2022**, 2202830.
[2]   Y. Chen, Y. Sun, J. Peng, J. Tang, K. Zheng, Z. Liang, *Adv. Mater.* **2018**, *30*, 1703487.
[3]   C. Ortiz-Cervantes, P. Carmona-Monroy, D. Solis-Ibarra, *ChemSusChem* **2019**, *12*, 1560.
[4]   M. Saliba, J.-P. Correa-Baena, M. Grätzel, A. Hagfeldt, A. Abate, *Angew. Chem. Int. Ed.* **2018**, *57*, 2554.
[5]   L. Mao, C. C. Stoumpos, M. G. Kanatzidis, *J. Am. Chem. Soc.* **2019**, *141*, 1171.
[6]   G. Grancini, M. K. Nazeeruddin, *Nat. Rev. Mater.* **2019**, *4*, 4.
[7]   J. M. Hoffman, J. Strzalka, N. C. Flanders, I. Hadar, S. A. Cuthriell, Q. Zhang, R. D. Schaller, W. R. Dichtel, L. X. Chen, M. G. Kanatzidis, *Adv. Mater.* **2020**, *32*, 2002812.
[8]   T. Zhu, Y. Yang, K. Gu, C. Liu, J. Zheng, X. Gong, *ACS Appl. Mater. Interfaces* **2020**, *12*, 51744.
[9]   A. Caiazzo, K. Datta, J. Jiang, M. C. Gélvez-Rueda, J. Li, R. Olleard, J. M. Vicent-Luna, S. Tao, F. C. Grozema, M. M. Wienk, R. A. J. Janssen, *Adv. Energy Mater.* **2021**, *11*, 2102144.
[10] C. Zuo, A. D. Scully, W. L. Tan, F. Zheng, K. P. Ghiggino, D. Vak, H. Weerasinghe, C. R. McNeill, D. Angmo, A. S. R. Chesman, M. Gao, *Commun. Mater.* **2020**, *1*, 33.
[11] Y. Yang, C. Liu, O. A. Syzgantseva, M. A. Syzgantseva, S. Ma, Y. Ding, M. Cai, X. Liu, S. Dai, M. K. Nazeeruddin, *Adv. Energy Mater.* **2021**, *11*, 2002966.

[12] Z. Wang, Q. Wei, X. Liu, L. Liu, X. Tang, J. Guo, S. Ren, G. Xing, D. Zhao, Y. Zheng, *Adv. Funct. Mater.* **2021**, *31*, 2008404.
[13] Y. Han, S. Park, J. Wang, S. Jariwala, K. Lee, C. G. Bischak, S. Kim, J. Hong, S. Kim, M. J. Lee, D. S. Ginger, I. Hwang, *Adv. Mater. Interfaces* **2019**, *1901860*, 1.
[14] J. Zhang, L. Zhang, X. Li, X. Zhu, J. Yu, K. Fan, *ACS Sustain. Chem. Eng.* **2019**, *7*, 3487.
[15] L. Meng, Q. Wei, Z. Yang, D. Yang, J. Feng, X. Ren, Y. Liu, S. (Frank) Liu, *J. Energy Chem.* **2020**, *41*, 43.
[16] S. Tian, J. Chen, X. Lian, Y. Wang, Y. Zhang, W. Yang, G. Wu, W. Qiu, H. Chen, *J. Mater. Chem. A* **2019**, *7*, 14027.
[17] T. Liu, Y. Jiang, M. Qin, J. Liu, L. Sun, F. Qin, L. Hu, S. Xiong, X. Jiang, F. Jiang, P. Peng, S. Jin, X. Lu, Y. Zhou, *Nat. Commun.* **2019**, *10*, 1.
[18] S. Shao, H. Duim, Q. Wang, B. Xu, J. Dong, S. Adjokatse, G. R. Blake, L. Protesescu, G. Portale, J. Hou, M. Saba, M. A. Loi, *ACS Energy Lett.* **2020**, *5*, 39.
[19] R. Vázquez-Cárdenas, J. Rodríguez-Romero, C. Echeverría-Arrondo, J. Sanchez-Diaz, V. S. Chirvony, J. P. Martínez-Pastor, P. Díaz-Leyva, J. Reyes-Gómez, I. Zarazua, I. Mora-Seró, *Chem. Mater.* **2022**, *34*, 3076.
[20] F. Zhang, D. H. Kim, H. Lu, J.-S. Park, B. W. Larson, J. Hu, L. Gao, C. Xiao, O. G. Reid, X. Chen, Q. Zhao, P. F. Ndione, J. J. Berry, W. You, A. Walsh, M. C. Beard, K. Zhu, *J. Am. Chem. Soc.* **2019**, *141*, 5972.
[21] Y. Wei, H. Chu, B. Chen, Y. Tian, X. Yang, B. Cai, Y. Zhang, J. Zhao, *Sol. Energy* **2020**, *201*, 13.
[22] Y. Wei, H. Chu, Y. Tian, B. Chen, K. Wu, J. Wang, X. Yang, B. Cai, Y. Zhang, J. Zhao, *Adv. Energy Mater.* **2019**, *9*, 1900612.
[23] X. Zhong, X. Ni, S. Sidhik, H. Li, A. D. Mohite, J. Brédas, A. Kahn, *Adv. Energy Mater.* **2022**, 2202333.
[24] J. Liang, Z. Zhang, Q. Xue, Y. Zheng, X. Wu, Y. Huang, X. Wang, C. Qin, Z. Chen, C.-C. Chen, *Energy Environ. Sci.* **2022**, *15*, 296.
[25] D. H. Cao, C. C. Stoumpos, O. K. Farha, J. T. Hupp, M. G. Kanatzidis, *J. Am. Chem. Soc.* **2015**, *137*, 7843.
[26] M. Yuan, L. N. Quan, R. Comin, G. Walters, R. Sabatini, O. Voznyy, S. Hoogland, Y. Zhao, E. M. Beauregard, P. Kanjanaboos, Z. Lu, D. H. Kim, E. H. Sargent, *Nat. Nanotechnol.* **2016**, *11*, 872.
[27] Z. Wang, L. Liu, X. Liu, D. Song, D. Shi, S. Wu, Y. Tong, H. Ren, M. Li, Y. Zheng, D. Zhao, *Chem. Eng. J.* **2022**, *432*, 134367.
[28] J. Shi, Y. Gao, X. Gao, Y. Zhang, J. Zhang, X. Jing, M. Shao, *Adv. Mater.* **2019**, *31*, 1901673.
[29] M. Shao, T. Bie, L. Yang, Y. Gao, X. Jin, F. He, N. Zheng, Y. Yu, X. Zhang, *Adv. Mater.* **2022**, *34*, 2107211.
[30] G. Jang, S. Ma, H. C. Kwon, S. Goh, H. Ban, J. S. Kim, J. H. Kim, J. Moon, *ACS Energy Lett.* **2021**, *6*, 249.
[31] P. Mao, J. Zhuang, Y. Wei, N. Chen, Y. Luan, J. Wang, *Sol. RRL* **2019**, *3*, 1800357.
[32] L. Liu, Y. Bai, X. Zhang, Y. Shang, C. Wang, H. Wang, C. Zhu, C. Hu, J. Wu, H. Zhou, Y. Li, S. Yang, Z. Ning, Q. Chen, *Angew. Chem. Int. Ed.* **2020**, *59*, 5979.
[33] R. Quintero-Bermudez, A. Gold-Parker, A. H. Proppe, R. Munir, Z. Yang, S. O. Kelley, A. Amassian, M. F. Toney, E. H. Sargent, *Nat. Mater.* **2018**, *17*, 900.
[34] R. Perea-Cárpio, F. González-Caballero, J. M. Bruque, C. F. González-Fernández, *J. Colloid Interface Sci.* **1986**, *110*, 96.
[35] A. Z. Chen, M. Shiu, J. H. Ma, M. R. Alpert, D. Zhang, B. J. Foley, D.-M. Smilgies, S.-H. Lee, J. J. Choi, *Nat. Commun.* **2018**, *9*, 1336.
[36] J. Dong, S. Shao, S. Kahmann, A. J. Rommens, D. Hermida-Merino, G. H. ten Brink, M. A. Loi, G. Portale, *Adv. Funct. Mater.* **2020**, *30*, 2001294.
[37] X. Lian, J. Chen, M. Qin, Y. Zhang, S. Tian, X. Lu, G. Wu, H. Chen, *Angew. Chem. Int. Ed.* **2019**, *58*, 9409.

5

Multidimensional Perovskites for High Detectivity Photodiodes

Abstract

Low-dimensional perovskites attract increasing interest due to tunable optoelectronic properties and high stability. Here, it is shown that perovskite thin films with a vertical gradient in dimensionality result in graded electronic bandgap structures that are ideal for photodiode applications. Positioning low-dimensional, vertically-oriented perovskite phases at the interface with the electron blocking layer increases the activation energy for thermal charge generation and thereby effectively lowers the dark current density to a record-low value of 5 × 10^{-9} mA cm^{-2} without compromising responsivity, resulting in a noise-current-based specific detectivity exceeding 7 × 10^{12} Jones at 600 nm. These multidimensional perovskite photodiodes show promising air stability and a dynamic range over ten orders of magnitude, and thus represent a new generation of high-performance low-cost photodiodes.

5.1 INTRODUCTION

2D and quasi-2D perovskites have been widely employed for a variety of optoelectronic devices, such as solar cells, light-emitting diodes, and photodiodes.[1–3] As described previously in this work, while 3D hybrid perovskites adopt a cubic structure consisting of $[BX_6]^{4-}$ corner-sharing octahedra, with the organic cation fitting in the voids between the inorganic units, 2D or quasi-2D perovskites consist of a number (n) of inorganic sheets sandwiched between organic spacers, such as butylammonium (BA) or phenethylammonium (PEA). Such cations are too bulky to fit in the octahedral voids, so they effectively slice the perovskite framework and form quantum-well structures with a bandgap and exciton binding energy that depends on the value of n.[4] Small n-values correspond to 2D ($n = 1$) or quasi-2D ($n \leq 5$) perovskites with a bandgap energy inversely proportional to n, while large n-values approaching infinity describe a quasi-3D or 3D perovskite with the conventional optoelectronic properties widely described in the literature.[5] When solution-processing quasi-2D perovskites, typically a range of structural phases with different n-values are formed in the films while drying. Consequently, these films often display a 2D-3D gradient, with 2D or quasi-2D phases located at the bottom and 3D phases at the top air interface, resulting in a complex, multidimensional material.[6,7] As n is coupled with the energy bandgap, a 2D-3D gradient results in a bandgap gradient that can be used beneficially to increase the detectivity of perovskite photodiodes (PPDs), as will be shown below.

To develop PPDs with high specific detectivity (D^*), low noise current (i_n) should be combined with high photosensitivity.[8] In previous work from our group, we have shown that high-detectivity photodiodes can be achieved by minimizing the dark current density (J_D), and thus i_n, of 3D PPDs by using appropriate blocking layers.[9] When charge injection is suppressed, J_D and i_n are determined by thermal charge generation at the interface between the electron-blocking layer (EBL)–also defined as hole-transport layer (HTL) in previous chapters–and the perovskite layer, and exponentially depends on the energy offset between the highest occupied molecular orbital (HOMO) of the EBL ($E_{HOMO, EBL}$) and the conduction band minimum (CBM) of perovskite ($E_{C, PVK}$), $i.e.$, $\Phi = E_{C, PVK} - E_{HOMO, EBL}$. Increasing Φ reduces J_D and i_n, and thus improves D^*. 3D perovskites, however, offer limited solutions in controlling energy levels to maximize Φ. A wide bandgap perovskite could potentially increase Φ, but at the cost of a narrower spectral response window and higher instability under illumination.[10] On the contrary, multidimensional perovskites are a versatile candidate material that allows tuning of energy levels at the interface with the transport layers by optimizing their 2D-3D gradient composition. Their

bandgap gradient along the thickness of such films enables an upshift of the CBM at the interface with the EBL, yielding an increased energy offset between the HOMO of the EBL and the conduction band of the perovskite, de facto increasing Φ. As a result, such perovskites could be exploited to achieve higher D^* compared to 3D perovskite devices. The absorption profile and thus spectral response would remain relatively unaltered, with only a slight blueshift.

Although quasi-2D perovskites have been broadly employed in solar cells and light-emitting diodes,[11–15] their use for photodiode applications has been seldom investigated.[16–20] Moreover, a comprehensive study correlating the design of low-dimensional phases with the device characteristics both in dark and light is lacking.

In this chapter, we investigate several quasi-2D perovskite compositions in PPDs. We outline the key conditions to maximize the photodiode performance. By means of composition and spacer engineering, we control the 2D-3D gradient and demonstrate that multidimensional perovskite films can effectively reduce J_D. By analyzing the temperature-dependence of J_D, we confirmed that J_D is the result of thermal charge generation process at the EBL interface with a wide-bandgap 2D or quasi-2D phase. We find that vertical-oriented perovskites are necessary to obtain an external quantum efficiency (EQE) >80% and fast response times. Employing the quasi-2D perovskites with proper gradient direction and crystal orientation in combination with deep-HOMO EBL, we fabricate PPDs with record-low J_D of 5×10^{-9} mA cm^{-2}, noise-current based specific detectivity exceeding 7×10^{12} Jones, fast microsecond response times, and a linear photo-response over more than 8 orders of magnitude of light intensity. Hence, interface engineering with low-dimensional perovskites leads to photodiodes with performance that is on par with traditional inorganic semiconductors.

5.2 2D-3D GRADED PEROVSKITE PHOTODIODES

In a previous work, our group demonstrated that in 3D PPDs the interface with the EBL is very critical.[9] J_D decreases exponentially with Φ, i.e., the energy offset between the 3D perovskite CBM and the HOMO of the EBL. With the aim to increase Φ even further, we investigated 2D-3D graded perovskites as active layers in PPDs. In **Figure 5.1**a, a multidimensional perovskite device is shown, consisting prevalently of 2D ($n = 1$) and quasi-2D ($n \leq 5$) at the bottom of the film, and 3D phases ($n \approx \infty$) at the top. This material possesses a bandgap (E_g) gradient along the thickness of the film, with higher E_g and CBM at the bottom.[21] The introduction of 2D phases at the EBL interface thus results in a potential increase of Φ (Figure 5.1b).
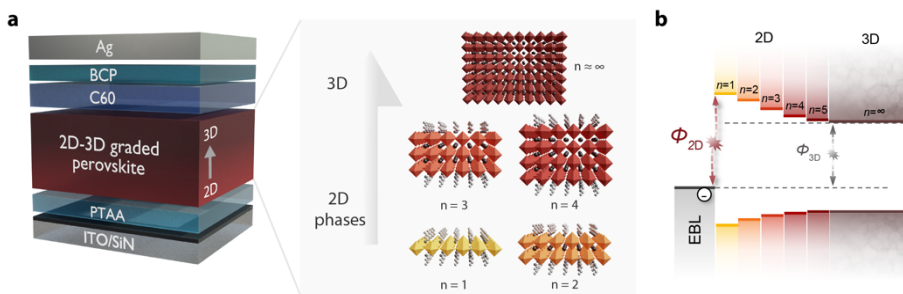
Figure 5.1. (a) Device schematics of a multidimensional perovskite photodiode with focus on the 2D-3D graded perovskite active layer. (b) Schematic energy band diagram for a 2D–3D graded perovskite layer considering a Type I alignment between low-dimensional phases. The difference between conduction band and HOMO level of EBL corresponds to the energy barrier Φ for thermal charge generation.

The formation of a 2D-3D gradient is controlled by the perovskite fabrication method. As widely explained in Chapter 3, solvent-precursors interactions are crucial in determining the phase distribution of a quasi-2D perovskite film.[22] By following a similar solvent engineering approach, we fabricated 2D-3D graded perovskite films in which we deliberately controlled the distribution of structural phases and their crystal orientation, to obtain n-values ranging from 1 to 5 and either parallel or perpendicular crystals. We used two largely studied organic spacers, *i.e.*, butylammonium (BA) and phenethylammonium (PEA). The stoichiometry of the precursor solutions was set to form $BA_2MA_3Pb_4I_{13}$ ($<n>$ = 4) and $BA_2MA_4Pb_5I_{16}$ ($<n>$ = 5), in the case of BA, and $PEA_2MA_3Pb_4I_{13}$ ($<n>$ = 4) for PEA. The choice of such a value of n, and not for example smaller n-values that could further increase Φ, was dictated by considerations about the narrowing of spectral response for the wider optical bandgap associated with the smaller n and about crystal orientation, as will be discussed below. In addition, two 3D perovskites with comparable bandgap, *i.e.*, $FA_{0.66}MA_{0.34}PbI_3$ (FAMA) and $Cs_{0.05}(FA_{0.83}MA_{0.17})_{0.95}Pb(I_{0.83}Br_{0.17})_3$ (CsFAMA), were also investigated. All perovskite films were spin-coated on an ITO-patterned glass substrate covered with an edge cover layer (SiN) and poly[bis(4-phenyl)(2,4,6-trimethylphenyl)amine] (PTAA) as EBL. On top of the perovskite layer, a bilayer of thermally-evaporated C_{60} and bathocuproine (BCP) acts as HBL, while Ag is the back electrode (Figure 5.1a).

The composition and phase distribution of the perovskite films was characterized using photoluminescence (PL) measurements (**Figure 5.2**). The 3D perovskites have similar PL spectra with an emission peak at 1.55 and 1.63 eV for FAMA and CsFAMA, respectively. All quasi-2D perovskite films display a dimensionality gradient. When exciting the film with light of 405 nm (penetrating only

the first ~40 nm out of ~200 nm layer thickness) and detecting PL from the top side, the films emit at ~1.7 eV, indicating the presence of a 3D perovskite. Upon exciting and detecting at the bottom side, additional emission peaks, indicative of structural phases with different *n*-values and of the presence of a 2D-3D gradient, are observed. It is worth mentioning, however, that the 3D emission peak at 1.7 eV that dominates the spectrum even when exciting at the bottom side, is due to ultrafast carrier migration from quasi-2D to 3D phase, as commonly reported in the literature.[23]
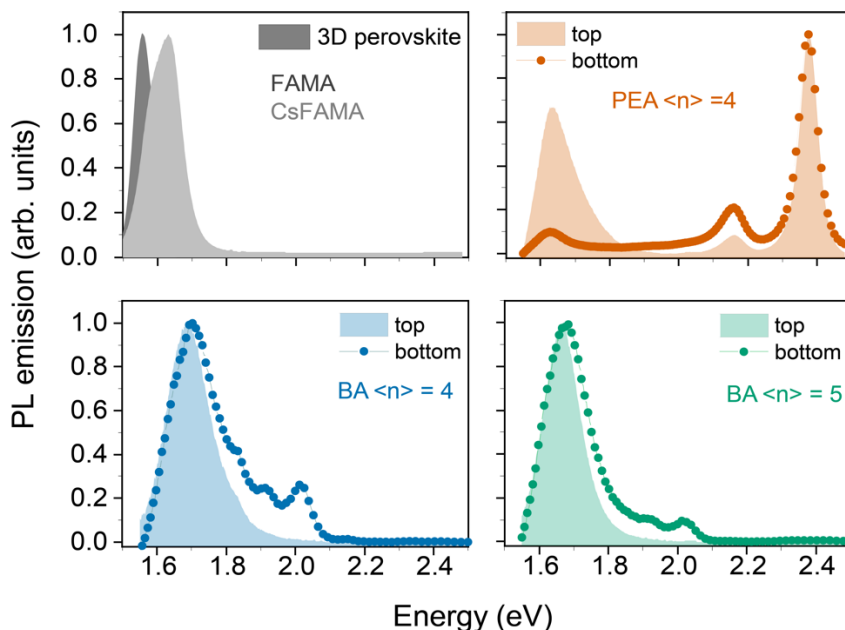

Figure 5.2. Normalized steady-state PL spectra of the 3D and quasi-2D perovskite films recorded with excitation (405 nm) and detection at the top (perovskite/air) and bottom (substrate/perovskite) sides. 3D perovskites are measured only from the top interface.

In the case of BA, we observe the formation of structural phases with *n* between 3 and 5 (for BA <*n*> = 4) and between 3 and 4 (for BA <*n*> = 5) at the bottom of the film. The emission peaks of these quasi-2D phases are found at 2.02, 1.91, and 1.82 eV for *n* = 3, 4, and 5, respectively. The different $BAI:MAI:PbI_2$ precursor ratios between <*n*> = 4 and <*n*> = 5 cause a change in crystallization kinetics and are likely behind these differences in phase distribution. On the contrary, PEA-based perovskite films possess a large amount of *n* = 1 (2.37 eV) and 2 (2.16 eV) at the bottom, and a 3D perovskite mixed with the same low-dimensional phases at the top. Although PL spectroscopy is not a quantitative technique, we emphasize that the absence (or minor presence) of a 3D emission peak in the bottom-excitation PL

spectrum of PEA $<n>$ = 4, indicates a drastic majority of small-n phases, which are unable to transfer charges to 3D phases.
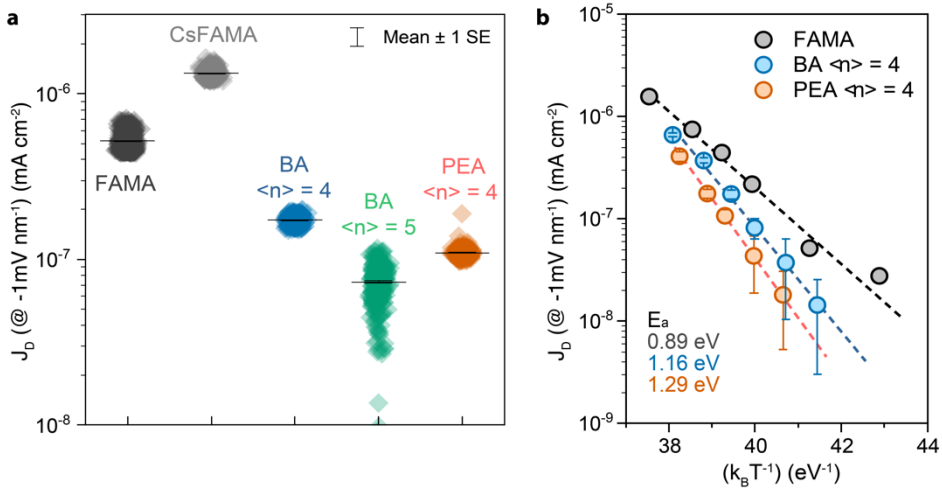

Figure 5.3. (a) Variation of the dark current density during 300 s, measured under a constant electric field of -1 mV nm^{-1} for the different perovskite photodiodes. (b) Temperature dependence of J_D measured at an electric field of -1 mV nm^{-1} versus the reciprocal temperature in an Arrhenius plot for FAMA, BA $<n>$ = 4, and PEA $<n>$ = 4 perovskites. Dashed lines are linear fits of J_D to $\exp(-E_a/k_B T)$, open symbols represent the experimental mean values of J_D, and whiskers represent standard deviation. The fitted thermal activation energies (E_a) are shown in the inset.

We next measured the reverse dark current of the quasi-2D PPDs and compared it with that of 3D PPDs (**Figure 5.3**a). The J_D was measured over time (300 s) by applying a constant electric field of -1 mV nm^{-1}. In the case of BA $<n>$ = 4, $<n>$ = 5 and PEA $<n>$ = 4, the time-averaged mean J_D is 2×10^{-7}, 6×10^{-8} and 1×10^{-7} mA cm^{-2}, respectively. Notably, BA and PEA $<n>$ = 4 display a negligible spread of current densities with time, whereas it is larger for BA $<n>$ = 5 for reasons that we have yet to identify. The mean J_D values are reproducible over several devices. These values are almost one order of magnitude lower than the ones measured for 3D perovskites CsFAMA and FAMA (1×10^{-6} and 6×10^{-7} mA cm^{-2}, respectively) and are ranked among the lowest reported in the literature for quasi-2D and 3D PPDs.[8,9,17,24] We additionally investigated the energetic correlation of quasi-2D phases with Φ by analyzing the thermal activation energy (E_a) of J_D for three PPDs (FAMA, BA $<n>$ = 4 and PEA $<n>$ = 4). E_a was determined by using temperature-dependent J_D measurements (Figure 5.3b). For all devices, J_D shows an Arrhenius-type behavior, with E_a increasing from 0.87 eV (3D FAMA) to 1.16 eV (BA $<n>$ = 4, with n = 3, 4, 5) and 1.29 eV (PEA $<n>$ = 4, with n = 1, 2). The highest temperature

activation is thus observed in the PPD with the lowest dark current. Quasi-2D perovskites exhibit a significantly higher E_a, *i.e.*, by 0.3 – 0.4 eV, compared to that of the 3D perovskite, which is consistent with an increase of Φ caused by the wide-bandgap low-dimensional phases at the EBL interface, in line with Figure 5.1b. Determining E_a for BA $<n>$ = 5 turned out to be difficult due to the low current level ($J_D < 10^{-7}$ mA cm^{-2}).

5.3 IMPORTANCE OF GRADIENT DIRECTION

To further investigate the influence of low-dimensional phases at the EBL interface on Φ, we fabricated a multidimensional PPD with reverse 3D-2D graded perovskite ($<n>$ = 4). Here, by using cyclohexylmethylammonium (CMA) as organic spacer,[25] we promote the formation of 2D phases on the top of the film, and 3D ones at the bottom (**Figure 5.4**a). X-ray diffraction (XRD) displays a peak at 3.87° corresponding to the (020) plane of n = 2 (Figure 5.4b).[26] PL emission spectra confirm the reversed dimensionality gradient, showing a 3D emission peak at 1.62 eV with excitation from the bottom side, whereas multiple emission peaks related to quasi-2D phases are observed with excitation from the top side (Figure 5.4c). The main emission peak from the top side is found at 2.1 eV, suggesting the dominant presence of an n = 2 phase in agreement with XRD. Additionally, we employed angle-dependent grazing-incidence wide-angle X-ray scattering (GIWAXS) to gain depth-sensitive information on the 3D-2D graded perovskite crystalline structure.
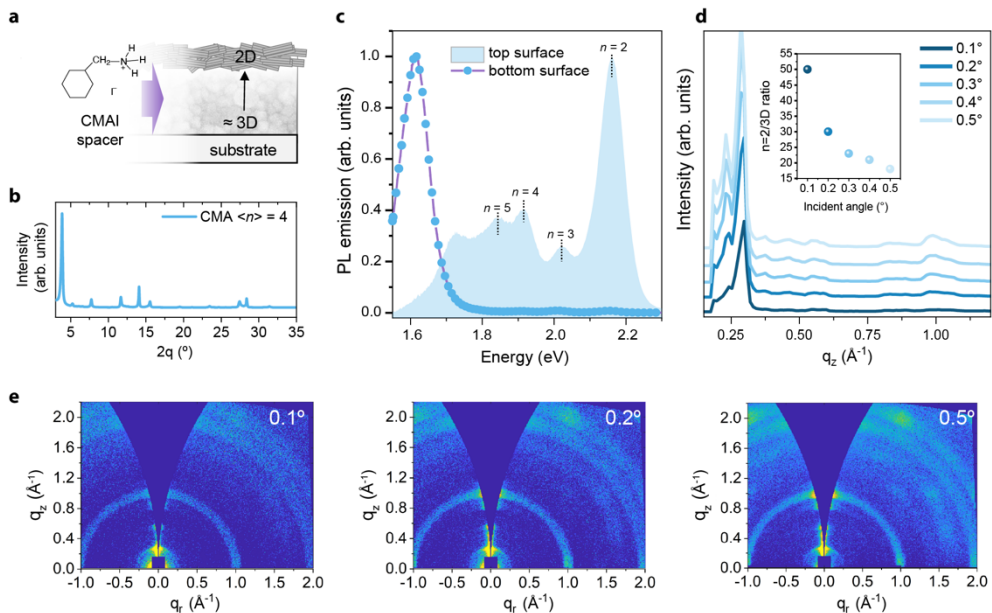

Figure 5.4. (a) Schematic illustration of the 3D-2D gradient obtained by using cyclohexylmethylammonium iodide as organic spacer. (b) XRD pattern for (CMA)$_2$MA$_3$Pb$_4$I$_{13}$

($<n>$ = 4). (c) Normalized steady-state PL spectra of the same film as in (b) measured with excitation (405 nm) and detection at the top (perovskite/air) and bottom (substrate/perovskite) sides. (d) Out-of-plane (q_z) cuts of GIWAXS patterns for CMA $<n>$ = 4. Inset: intensity ratio between n = 2 and 3D peaks q_z at 0.29 and ~1 Å^{-1}. (e) Angle-dependent 2D GIWAXS patterns for (CMA)$_2$MA$_3$Pb$_4$I$_{13}$ ($<n>$ = 4) recorded with incidence angles of 0.1, 0.2, and 0.5°.

When using a 0.1° or 0.2° incidence angle, the X-rays penetrate only the top surface of the film, whereas at larger angles (0.5°) the whole film thickness is probed. The top surface (measured with 0.1° incidence angle) of the perovskite film exhibits an intense Bragg spot at q_z = 0.29 Å^{-1} and a weak scattered ring at 1 Å^{-1} (Figure 5.4e). The peak at 0.29 Å^{-1} corresponds to the abovementioned (020) plane of an n = 2 phase oriented parallel to the substrate. The weak ring at 1 Å^{-1} results from the (111) plane of a Ruddlesden-Popper phase. At higher incidence angles (0.2° and 0.5°), the ring becomes more intense, because of the contribution of the (100) plane of the 3D phases, and a Bragg spot in the out-of-plane direction appears, indicating preferential crystal orientation. Moreover, the out-of-plane cuts display peaks at q_z = 0.23 and 0.18 Å^{-1}, corresponding to an interplane spacing of 27 and 36 Å, consistent with n = 3 and 4 phases,[27] respectively, which become more intense with increasing incident angle, indicating the appearance of larger-n phases moving towards the bottom of the film (Figure 5.4d).
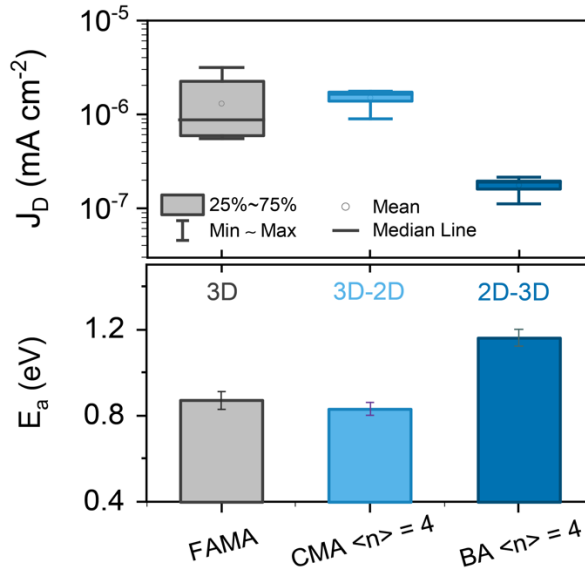

Figure 5.5. Statistical distribution of J_0 (top) and measured activation energy E_a (bottom, whiskers are standard error) for bulk 3D, 3D-2D graded and 2D-3D graded perovskite photodiodes. J_0 is measured at –1 mV nm^{-1}.

By integrating the CMA $<n>$ = 4 reverse graded perovskite as active layer in a photodiode with the same p-i-n device stack as before, we found J_0 to be 2 × 10^{-6} mA cm^{-2} (**Figure 5.5**) at room-temperature, with an E_a of 0.87 eV. These numbers are close to the values of J_0 of 6 × 10^{-7} mA cm^{-2} and E_a of 0.83 eV of 3D FAMA and differ significantly from those of 2D-3D bottom-side graded perovskites, *i.e.,* 1.16 and 1.29 eV. These results suggest that the EBL-perovskite interface in a 3D-2D top-side graded perovskite is by all means similar to 3D FAMA and CsFAMA. Low-dimensional phases are thus less effective in decreasing J_0 when located at the HBL interface.

5.4 EFFECT OF CRYSTAL ORIENTATION ON LIGHT RESPONSE

In multidimensional perovskites, the response of the material to light is strongly affected by the crystal orientation of the films, minimizing thermal charge generation.[12] Previous studies have reported that small-n phases such as n = 1 or 2 preferentially orient horizontally, *i.e.*, parallel to the substrate.[28] Larger-n phases (n = 3–5) tend to orient vertically, *i.e.*, perpendicular to the substrate. Through GIWAXS measurements, we determined the crystal orientation of the 2D-3D graded perovskites, and we compared them to 3D FAMA, which only exhibits a scattered ring at 1 $Å^{-1}$, consistent with a randomly oriented crystalline structure (**Figure 5.6**a). BA-templated perovskites with $<n>$ = 4 or 5 display vertical orientation of the crystals (Figure 5.6b), as confirmed by the intense Bragg spot at 1 $Å^{-1}$ that corresponds to the (111) plane of Ruddlesden-Popper or (110) of 3D perovskites. This is in line with the PL characterization results described above, where only phases with n = 3, 4, and 5 appeared together with a bulk 3D perovskite, and with XRD patterns, which show diffraction peaks only for the abovementioned planes (as shown in Chapter 3). In the GIWAXS pattern of PEA $<n>$ = 4, we observe Bragg spots at 0.28 $Å^{-1}$ and 0.38 $Å^{-1}$ along the q_z direction, which are assigned to n = 1 and 2 phases parallel-oriented to substrate, and overall, a lower degree of vertical orientation (Figure 5.6c). By using GIWAXS, we can therefore distinguish between perpendicular-oriented and parallel-oriented films that are schematically illustrated in Figure 5.6d. BA-based perovskites with $<n>$ = 4 and 5 are perpendicular-oriented, while PEA $<n>$ = 4 is parallel oriented.

We measured both EQE (Figure 5.6e) and response speed (Figure 5.6f) of the photodiodes described above. Light is incident from the bottom side. The randomly oriented bulk 3D shows a sharp onset at the bandgap above 800 nm, and a maximum EQE approaching 80%. The perpendicular-oriented 2D-3D graded perovskites possess a favorable crystal orientation for charge transport, and this is reflected in the EQE >80% in the visible region of the EQE spectrum. The onset,

however, is shallower because of low volumetric amounts of pure 3D perovskite phases. The parallel-oriented perovskite displays a sharper 3D onset because of higher amounts of 3D perovskites. The values of EQE, nonetheless, are halved to 40% (with few peaks at 50%), due to unfavorable crystal orientation for charge transport and possibly poor film morphology.
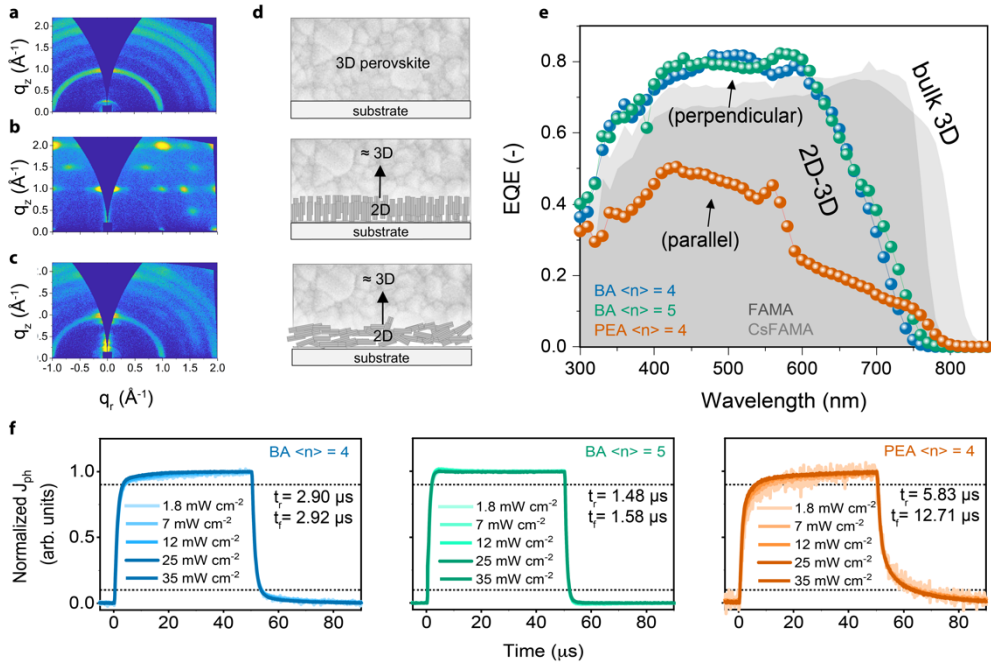

Figure 5.6. (a–c) GIWAXS pattern for FAMA (a), BA $<n>$ = 4 (b), PEA $<n>$ = 4 (c). (d) Schematic illustration of random oriented 3D (top) and perpendicular- (middle) or parallel- (bottom) oriented 2D-3D graded perovskite films. (e) EQE spectra for 3D, perpendicular-, and parallel-oriented 2D-3D graded PPDs. (f) Normalized transient photocurrent response upon light pulses (50 μs duration, 540 nm) with different light intensities for BA $<n>$ = 4, BA $<n>$ = 5, and PEA $<n>$ = 4. Rise (and fall) time, *i.e.*, time for response vary from 10% (90%) to 90% (10%), are also reported.

The PPD response times, measured using 50 µs wide light pulses at 540 nm wavelength for various intensities, are shown in Figure 5.6f. The response speed was found to be independent of light intensity in the perpendicular-oriented perovskites, with microsecond rise and decay times (*i.e.,* 2.9 and 1.5 µs for BA $<n>$ = 4 and 5, respectively). A longer decay time ($\approx$ 12 µs) is observed instead for parallel-oriented PEA $<n>$ = 4, together with a light intensity dependent rise time that varies between ~6 and 10 µs, as an indication of sub-optimal charge transport. Together with changes in EQE, these findings outline the importance of crystal orientation in 2D-3D graded perovskites for fast and efficient collection of

photogenerated charges, while having negligible impact on J_D (Figure 5.3). Perovskite films with vertical-oriented crystals and, more importantly, without parallel-oriented small-n phases are therefore preferred as they suppress J_D while retaining high and fast responsivity.

5.5 ELECTRON-BLOCKING LAYER ENGINEERING

To improve PPD performance, we combined the multidimensional 2D-3D graded perovskites with vertical-oriented crystals, *i.e.*, BA $<n>$ = 4 and 5, with a deep HOMO EBL, *i.e.*, a mixed PTAA:poly-TPD layer. The interfacial energy Φ of such combinations is in fact maximized beyond that of PPDs employing only 2D-3D perovskites due to deep EBL HOMO energy (ca. –5.45 eV for PTAA:poly-TPD compared to –5.2 eV for PTAA) and the J_D is suppressed to extremely low values. A reproducible J_D of 1×10^{-8} mA cm^{-2} and $\sim 5 \times 10^{-9}$ mA cm^{-2} at –0.2 V was measured for BA $<n>$ = 4 and 5, respectively (**Figure 5.7**a). Such J_D values are amongst the lowest dark current densities reported for a PPD. Compared to other photodiodes, J_D is more than 10 times lower than that of most commercial Si and at least more than five times lower than the best performing organic PDs.[29–31] The noise current i_n, measured at –0.2 V in the frequency interval f = 1 – 100 Hz is shown in Figure 5.7b. We observe a frequency-independent i_n behavior (with no evidence of 1/f dependence) with outstanding values of current noise spectral density of 5.5 and 6.5×10^{-15} A Hz$^{-1/2}$ for BA $<n>$ = 5 and 4, respectively. Combined with the high EQE at 600 nm, this results in a maximum noise-current based specific detectivity D^* of the photodiodes, *i.e.*, derived using $D^* = SR\,(AB)^{1/2}\,i_n^{-1}$ with A = 0.01 cm^2 and B = 1 Hz of $\sim 7.5 \times 10^{12}$ (BA $<n>$ = 5) and 6×10^{12} (BA $<n>$ = 4) Jones (Figure 5.7c).
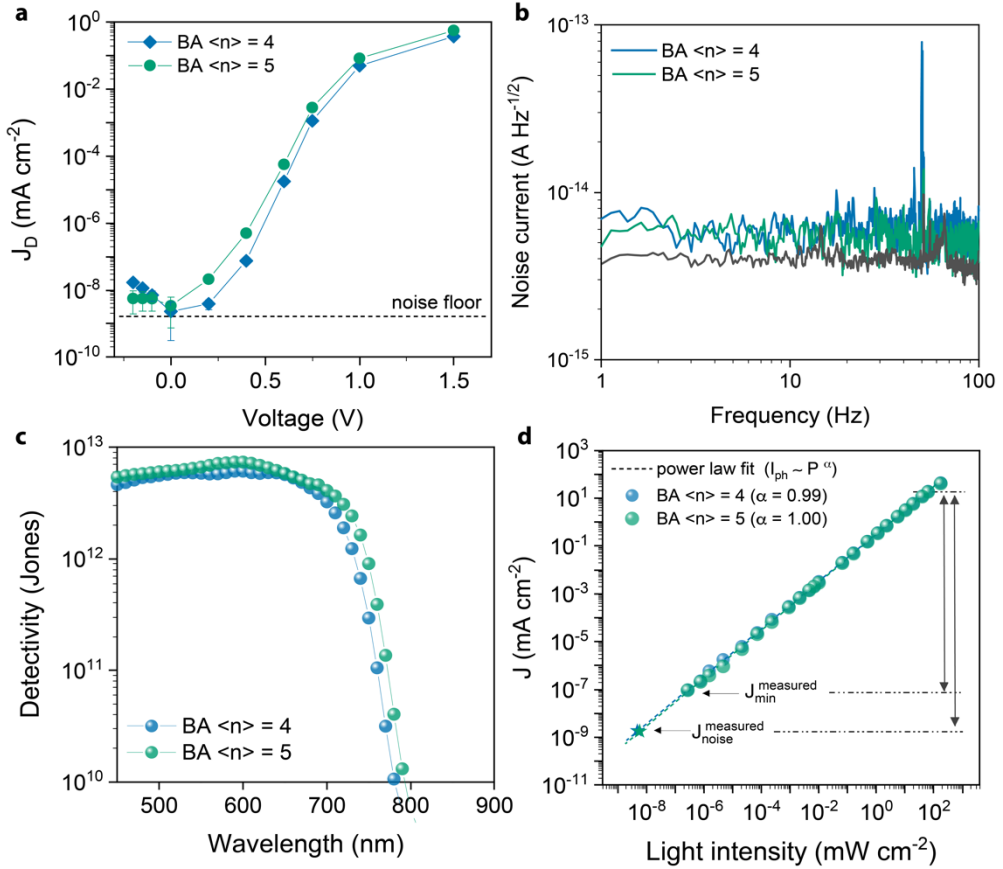
Figure 5.7. (a) J-V characteristics in dark; from −0.2 V to +0.6 V, J-V have been reconstructed from constant voltage measurements over time at discrete biases. Whiskers represent standard deviation. (b) Noise current spectral density as a function of frequency measured at −0.2 V for the best devices. Each spectrum is obtained with an average of 15 measurements. Harmonics with large amplitude in the spectrum are due to powerline interference. Black line represents the noise floor of the setup (~ 4 × 10^{-15} A Hz$^{-1/2}$). (c) Specific detectivity of the photodiodes *vs.* wavelength under reverse bias (−0.2 V). (d) Photocurrent, J_{ph}, measured at −0.2 V for a broad range of light intensities (540 nm). Lines denote a linear fit, with α the power law exponent equal to unity.

The shot noise-limited specific detectivity (D^*_{shot}), *i.e.*, under the assumption of predominating and limiting shot noise, of these PPDs amounts to ~2 × 10^{14} Jones, calculated as $D^*_{shot} = SR/(2qJ_D)^{1/2}$. The photocurrent ($J_{ph}$) as function of light intensity (I_{light}) of both devices is shown in Figure 5.7d. J_{ph} increases linearly over nine orders of light intensity, with a slope of α = 0.99 and 1.00 for BA $<n>$ = 4 and $<n>$ = 5, respectively. This corresponds to a linear dynamic range (LDR= 20 log ($J_{ph,upper}/J_{ph,lower}$)) of the photodiodes, *i.e.*, the span of the light intensity range within

which the device output is linear to the incident light intensity, of ~169 dB. At a light intensity of 175 mW cm^{-2}, the photocurrent does not scale linearly with I_{light} anymore. The value of J_{ph} at I_{light} = 175 mW cm^{-2} is therefore taken as $J_{ph,upper}$. The lower limit of LDR is governed by the minimum light intensity that could be produced repeatedly and constantly by our equipment. When considering the measured $J^{measured}_{noise}$ resulting from i_n as $J_{ph,lower}$,[24,32,33] linearity range extends to more than ten orders of magnitude, corresponding to LDR >200 dB.

5.6 STABILITY OF 2D-3D GRADED PHOTODIODES

We performed preliminary stability tests by exposing the BA $<n>$ = 4 PPD, to ambient air (with RH = 40% and T = 295 K). We tested its environmental stability without intentional encapsulation or protection layers. As shown in **Figure 5.8**a,c, the photodiode maintained its low J_D value of ~1 × 10^{-8} mA cm^{-2} and high EQE (~80%) for 400 h with no appreciable decay (< 4% for EQE). The J_{ph}/J_D ratio remained therefore high, ca. 10^9. Approaching 500 h, the EQE decreases to 60%, indicating device degradation. As only the device area covered with the electrode shows a change of color (turning yellow) in the film, whereas the perovskite layer remains brown in the uncovered areas, we believe that degradation is caused by interaction between the electrode material (Ag) and the perovskite layer. Proper encapsulation will likely lead to even longer device stability.

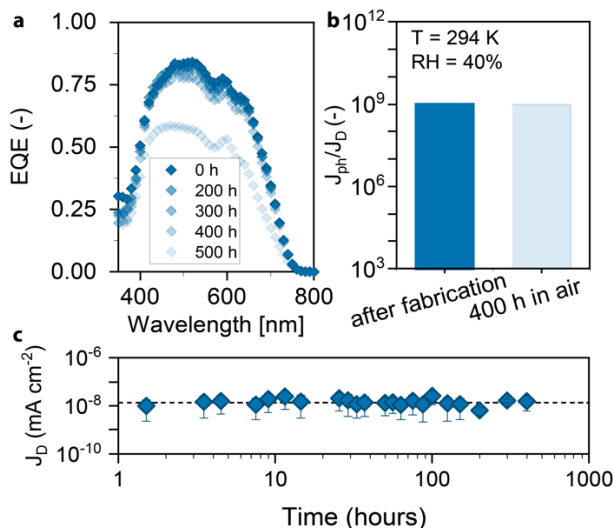**Figure 5.8**. Stability in air (RH 40%) of BA $<n>$ = 4 PPD after > 400 hours, expressed in terms of EQE (a), J_{ph}/J_D ratio (b), and J_D over time (c). J_{ph} is integrated from the EQE spectrum at V =0 V, J_D is measured at constant voltage measurements over time at discrete biases (symbols and whiskers represent mean values and standard deviation.

5.7 CONCLUSIONS

We outlined key requirements for the design and integration of multidimensional perovskites in photodiodes for record-low dark current density, broad sensitivity to light intensity, and high specific detectivity. Through the study of several quasi-2D perovskites, we demonstrated how the distribution of low-dimensional structural phases, gradient direction, and crystal orientation impact the main figures of merit of a photodiode. Overall, we found that while the formation of a 2D-3D gradient and its direction help to minimize dark current, vertical orientation of quasi-2D perovskite films is also crucial to achieve high performance PPDs. Our work provides a comprehensive study of low-dimensional perovskites in PPDs and shows that multidimensional structuring is an accessible route to fabricate high detectivity and stable photodiodes.

5.8 METHODS

Materials. All materials were purchased from commercial sources and used without further purification unless otherwise mentioned. PbI_2 (99.99%) was purchased from TCI Chemicals, all the organic salts for perovskites were purchased from GreatCell Solar, all the solvents were bought from Sigma Aldrich.

Perovskite deposition. Solution preparation and device fabrication were performed in an N_2-filled glovebox. $FA_{0.66}MA_{0.34}PbI_3$ (FAMA) was prepared via two-step spin-coating according to a previous publication from our group.[34] First, a 1.2 M PbI_2 solution was spin-coated on the EBL at 3000 rpm for 30 s. Then, the organic solution made of 0.31 M FAI and 0.16 M MAI in isopropanol was spin-coated at 3000 rpm for 60 s. The perovskite films were thermally annealed at 100 °C for 30 min. $Cs_{0.05}(FA_{0.83}MA_{0.17})_{0.95}Pb(I_{0.83}Br_{0.17})_3$ (CsFAMA) was prepared via one-step spin-coating according to previously published research.[35] First, PbI_2 and $PbBr_2$ are dissolved in separate vials in DMF/DMSO 4:1 (concentration is 1.5 M). Then, solutions of $FAPbI_3$ and $MAPbBr_3$ are prepared by mixing the lead solutions described above with FAI and MABr in equimolar ratio. Finally, $FAPbI_3$ and $MAPbBr_3$ are mixed in the ratio 5:1, followed by addition of 5% (by volume) CsI (1.5 M in DMSO). The perovskite precursor was spin-coated at 1000 rpm for 10 s, followed by 6000 rpm for 20 s; 200 µL of chlorobenzene were poured onto the spinning substrate 5 s before the end of the spin-coating process. The perovskite films were annealed at 100 °C for 45 min. Quasi-2D perovskites with nominal formula $R_2MA_{n-1}Pb_nI_{3n+1}$ were prepared by mixing the organic spacer (BAI or PEAI), MAI, and PbI_2 in the ratio 2 : n–1 : n in DMF:DMSO mixtures, with the concentration of PbI_2 set at 1 M. BA- and CMA-based perovskites were processed from a DMF:DMSO 20:1 solvent mixture, whereas the PEA-based perovskite was processed from DMF:DMSO 4:1 The precursor solutions were spin-coated at 5000 rpm for 45 s, followed by thermal annealing at 100 °C for 10 min.

Device fabrication. Indium tin oxide (ITO) (135 nm) was sputtered on glass and structured to form a bottom electrode via photolithography. SiN (50 nm) was deposited and patterned via dry etch to cover the perimeter of the ITO electrodes to reduce undesirable leakage paths.[36]

Prior to deposition of the EBLs, a 30 min UV-ozone treatment was performed on the substrates. PTAA (3 mg mL^{-1} in toluene) was spin-coated at 5700 rpm for 30 s, followed by thermal annealing at 100 °C for 10 min. PTAA:polyTPD (10 mg PTAA, 10 mg polyTPD in 1 mL o-dichlorobenzene) was spin-coated at 2500 rpm for 40 s, followed by thermal annealing at 135 °C for 35 min. C_{60} (20 nm, SES Research), BCP (8 nm, Lumtec), and the Ag top electrode (100 nm) were thermally evaporated under high vacuum ($\approx 10^{-7}$ mbar).

Material characterization. PL spectra were measured by using an Edinburgh Instruments FLSP920 double-monochromator luminescence spectrophotometer. UV-vis-NIR spectra were measured by using a PerkinElmer Lambda 1050 UV-vis-NIR spectrophotometer. XRD patterns were measured by using a Bruker 2D phases (Cu Kα, $\lambda = 1.5406$ Å) in the range 3-35° with a step size of 0.02° and collection time of 1 s. 2D GIWAXS measurements were performed with a Ganesha 300XL+ system from JJ X-Ray equipped with a Pilatus 300K detector (pixel side 172 μm × 172 μm). The X-ray source was a Genix 3D Microfocus sealed tube X-ray Cu-source with integrated monochromator. The wavelength used was 1.5408 Å, the sample-to-detector distance was set to 115.4 mm.

Device characterization. Room temperature dark current density was measured in an N_2-filled glovebox through manual probes connected to an Agilent 4155C semiconductor parameter analyzer. For an accurate determination of J_D, a constant reverse voltage bias was applied over time to eliminate unwanted charging effects. For temperature dependent J_D measurements, the device was placed under vacuum (10^{-4} mbar) in a cryostat chamber and connected to a Keithley (2636A) source meter, while temperature was controlled using liquid nitrogen and a LakeShore 336 temperature controller. The transient photocurrent (TPC) was measured using a digital oscilloscope (Tektronix TDS5052B) and green light pulses (540 nm) generated by a LED driven by a wave-function generator (Agilent 33250A). Optical focal lens and a circular aperture (1 mm in diameter) by Thorlabs were used to guide the light signal. Within the same setup, the photocurrent response of the PPD was measured employing two different green LEDs to emit at high and low light intensity regions that were calibrated with a reference silicon photodiode (Thorlabs FDS100). The custom-made setup for EQE measurements consisted of a tungsten-halogen lamp, a monochromator (Oriel, Cornerstone 130), a chopper, a pre-amplifier (Stanford Research Systems SR570), and a lock-in amplifier (Stanford Research Systems SR830 DSP). The devices were transferred in the setup through a N_2-filled box equipped with a quartz window, on which a circular aperture (1 mm diameter) was applied. EQE signal was calibrated with a reference silicon solar cell. The standard deviation of this setup is less than 0.005 electron/photon (in the range 350-1050 nm of wavelengths). Noise measurements were performed in a battery-powered current to voltage conversion readout circuit developed with off-the-shelf components. The setup is arranged in a metal enclosure to shield the device from electromagnetic interference and keep it in dark conditions. The photodiode (active area of 1 mm^2) was connected by means of two probes and triaxial cables to a trans-impedance amplifier (TIA) implemented with the operation amplifier Analog Devices (ADA4530). The device was biased by applying an adjustable DC voltage source to the non-inverting terminal of the TIA. The output of the TIA is fed to an active

bandpass amplifier (building using Analog Devices AD8065 operational amplifier) and finally read out by a dynamic signal analyzer (HP35670A).

5.9 REFERENCES

[1]   X. Li, J. M. Hoffman, M. G. Kanatzidis, *Chem. Rev.* **2021**, *121*, 2230.
[2]   F. Zhang, H. Lu, J. Tong, J. J. Berry, M. C. Beard, K. Zhu, *Energy Environ. Sci.* **2020**, *13*, 1154.
[3]   G. Grancini, M. K. Nazeeruddin, *Nat. Rev. Mater.* **2019**, *4*, 4.
[4]   C. C. Stoumpos, D. H. Cao, D. J. Clark, J. Young, J. M. Rondinelli, J. I. Jang, J. T. Hupp, M. G. Kanatzidis, *Chem. Mater.* **2016**, *28*, 2852.
[5]   M. Saliba, J.-P. Correa-Baena, M. Grätzel, A. Hagfeldt, A. Abate, *Angew. Chem. Int. Ed.* **2018**, *57*, 2554.
[6]   L. Liu, Y. Bai, X. Zhang, Y. Shang, C. Wang, H. Wang, C. Zhu, C. Hu, J. Wu, H. Zhou, Y. Li, S. Yang, Z. Ning, Q. Chen, *Angew. Chem. Int. Ed.* **2020**, *59*, 5979.
[7]   N. Liu, P. Liu, H. Ren, H. Xie, N. Zhou, Y. Gao, Y. Li, H. Zhou, Y. Bai, Q. Chen, *ACS Appl. Mater. Interfaces* **2020**, *12*, 3127.
[8]   Y. Wang, Y. Liu, S. Cao, J. Wang, *J. Mater. Chem. C* **2021**, *9*, 5302.
[9]   R. Ollearo, J. Wang, M. J. Dyson, C. H. L. Weijtens, M. Fattori, B. T. van Gorkom, A. J. J. M. van Breemen, S. C. J. Meskers, R. A. J. Janssen, G. H. Gelinck, *Nat. Commun.* **2021**, *12*, 7277.
[10]   J. Tong, Q. Jiang, F. Zhang, S. B. Kang, D. H. Kim, K. Zhu, *ACS Energy Lett.* **2021**, *6*, 232.
[11]   D. Ma, K. Lin, Y. Dong, H. Choubisa, A. H. Proppe, D. Wu, Y.-K. Wang, B. Chen, P. Li, J. Z. Fan, F. Yuan, A. Johnston, Y. Liu, Y. Kang, Z.-H. Lu, Z. Wei, E. H. Sargent, *Nature* **2021**, *599*, 594.
[12]   H. Tsai, W. Nie, J.-C. Blancon, C. C. Stoumpos, R. Asadpour, B. Harutyunyan, A. J. Neukirch, R. Verduzco, J. J. Crochet, S. Tretiak, L. Pedesseau, J. Even, M. A. Alam, G. Gupta, J. Lou, P. M. Ajayan, M. J. Bedzyk, M. G. Kanatzidis, A. D. Mohite, *Nature* **2016**, *536*, 312.
[13]   M. Shao, T. Bie, L. Yang, Y. Gao, X. Jin, F. He, N. Zheng, Y. Yu, X. Zhang, *Adv. Mater.* **2022**, *34*, 2107211.
[14]   Y. Yang, C. Liu, O. A. Syzgantseva, M. A. Syzgantseva, S. Ma, Y. Ding, M. Cai, X. Liu, S. Dai, M. K. Nazeeruddin, *Adv. Energy Mater.* **2021**, *11*, 2002966.
[15]   H. Lai, D. Lu, Z. Xu, N. Zheng, Z. Xie, Y. Liu, *Adv. Mater.* **2020**, *32*, 2001470.
[16]   F. Zhu, G. Lian, B. Yu, T. Zhang, L. Zhang, H. Yu, D. Cui, Q. Wang, H. Zhang, Q. Meng, C.-P. Wong, *ACS Appl. Mater. Interfaces* **2022**, *14*, 1526.
[17]   Z. Han, W. Fu, Y. Zou, Y. Gu, J. Liu, B. Huang, D. Yu, F. Cao, X. Li, X. Xu, H. Zeng, *Adv. Mater.* **2021**, *33*, 2003852.
[18]   J. Kim, W. Lee, K. Cho, H. Ahn, J. Lee, K.-Y. Baek, J.-K. Kim, K. Kang, T. Lee, *Nanotechnology* **2021**, *32*, 185203.
[19]   H. L. Loi, J. Cao, X. Guo, C. K. Liu, N. Wang, J. Song, G. Tang, Y. Zhu, F. Yan, *Adv. Sci.* **2020**, *7*, 1.
[20]   H. Xu, Y. Jiang, T. He, S. Li, H. Wang, Y. Chen, M. Yuan, J. Chen, *Adv. Funct. Mater.* **2019**, *29*, 1.
[21]   R. Quintero-Bermudez, A. H. Proppe, A. Mahata, P. Todorović, S. O. Kelley, F. De Angelis, E. H. Sargent, *J. Am. Chem. Soc.* **2019**, *141*, 13459.
[22]   A. Caiazzo, K. Datta, J. Jiang, M. C. Gélvez-Rueda, J. Li, R. Ollearo, J. M. Vicent-Luna, S. Tao, F. C. Grozema, M. M. Wienk, R. A. J. Janssen, *Adv. Energy Mater.* **2021**, *11*, 2102144.
[23]   R. Quintero-Bermudez, A. Gold-Parker, A. H. Proppe, R. Munir, Z. Yang, S. O. Kelley, A. Amassian, M. F. Toney, E. H. Sargent, *Nat. Mater.* **2018**, *17*, 900.
[24]   L. Min, W. Tian, F. Cao, J. Guo, L. Li, *Adv. Mater.* **2021**, *33*, 2101714.
[25]   Y. Wei, H. Chu, Y. Tian, B. Chen, K. Wu, J. Wang, X. Yang, B. Cai, Y. Zhang, J. Zhao, *Adv. Energy Mater.* **2019**, *9*, 1900612.

[26] Y. Wei, H. Chu, B. Chen, Y. Tian, X. Yang, B. Cai, Y. Zhang, J. Zhao, *Sol. Energy* **2020**, *201*, 13.
[27] C. M. M. Soe, G. P. Nagabhushana, R. Shivaramaiah, H. Tsai, W. Nie, J.-C. Blancon, F. Melkonyan, D. H. Cao, B. Traoré, L. Pedesseau, M. Kepenekian, C. Katan, J. Even, T. J. Marks, A. Navrotsky, A. D. Mohite, C. C. Stoumpos, M. G. Kanatzidis, *Proc. Natl. Acad. Sci.* **2019**, *116*, 58.
[28] Y. Chen, Y. Sun, J. Peng, J. Tang, K. Zheng, Z. Liang, *Adv. Mater.* **2018**, *30*, 1703487.
[29] C. Fuentes-Hernandez, W. F. Chou, T. M. Khan, L. Diniz, J. Lukens, F. A. Larrain, V. A. Rodriguez-Toro, B. Kippelen, *Science* **2020**, *370*, 698.
[30] A. J. J. M. van Breemen, M. Simon, O. Tousignant, S. Shanmugam, J. L. van der Steen, H. B. Akkerman, A. Kronemeijer, W. Ruetten, R. Raaijmakers, L. Alving, J. Jacobs, P. E. Malinowski, F. De Roose, G. H. Gelinck, *Npj Flex. Electron.* **2020**, *4*, 1.
[31] M. Kielar, O. Dhez, G. Pecastaings, A. Curutchet, L. Hirsch, *Sci. Rep.* **2016**, *6*, 1.
[32] Q. Lin, A. Armin, D. M. Lyons, P. L. Burn, P. Meredith, *Adv. Mater.* **2015**, *27*, 2060.
[33] Y. Fang, J. Huang, *Adv. Mater.* **2015**, *27*, 2804.
[34] J. Wang, K. Datta, J. Li, M. A. Verheijen, D. Zhang, M. M. Wienk, R. A. J. Janssen, *Adv. Energy Mater.* **2020**, *10*, 2000566.
[35] M. Saliba, J.-P. Correa-Baena, C. M. Wolff, M. Stolterfoht, N. Phung, S. Albrecht, D. Neher, A. Abate, *Chem. Mater.* **2018**, *30*, 4193.
[36] A. J. J. M. van Breemen, R. Ollearo, S. Shanmugam, B. Peeters, L. C. J. M. Peters, R. L. van de Ketterij, I. Katsouras, H. B. Akkerman, C. H. Frijters, F. Di Giacomo, S. Veenstra, R. Andriessen, R. A. J. Janssen, E. A. Meulenkamp, G. H. Gelinck, *Nat. Electron.* **2021**, *4*, 818.

6

Light-Induced Halide Segregation in 2D and Quasi-2D Mixed-Halide Perovskites

Abstract

Photo-induced halide segregation hinders wide-spread application of three-dimensional (3D) mixed-halide perovskites, but much less is known for corresponding low-dimensional systems. Studying photo-induced halide segregation in low-dimensional mixed iodide–bromide perovskites $(PEA)_2MA_{n-1}Pb_n(Br_xI_{1-x})_{3n+1}$, with PEA^+: phenethylammonium and MA^+: methylammonium, through time-dependent photoluminescence spectroscopy, reveals that layered two-dimensional (2D) structures render additional stability against the de-mixing of halide phases under illumination. The dimensionality of the 2D phase is, however, critical in regulating this behavior. The development of iodide-rich domains upon light illumination of mixed-halide perovskites is largely suppressed in pure-2D ($n = 1$) layered phases, but the behavior of mixed-halide quasi-2D ($n = 2$) phases is intermediate to that of 2D and 3D phases.

6.1 INTRODUCTION

Wide-bandgap mixed-halide perovskite absorbers find application in efficient multijunction solar cells where their tunable bandgap allows them to be combined with a variety of narrow-bandgap semiconductors (c-Si, CIGS, perovskite, organic) to increase the conversion efficiency.[1–4] However, conventional three-dimensional (3D) perovskite systems are vulnerable to environmental factors, such as oxygen and moisture, which can compromise long-term stability.[5,6] In addition, photo-induced halide segregation occurs in mixed-halide compositions due to the thermodynamically favorable formation of low-energy iodide-rich regions under illumination, aided by defect migration processes that can further exacerbate device instability.[7,8]

In recent years, layered Ruddlesden–Popper (RP) perovskites have shown promise as a potentially stable alternative to conventional 3D perovskite-based solar cells, light emitting diodes, and photodetectors.[9–11] Such lower-dimensional RP systems can be visualized as a 3D perovskite sliced along its (100)-oriented crystallographic planes to form structures where a large organic spacer molecule (for example, BA+, butylammonium, or PEA+, phenethylammonium) separates slabs of conjoined lead halide octahedral sheets, intercalated with smaller monovalent organic cations (for example MA+, methylammonium, FA+, formamidinium, or Cs+, cesium).[12] These lower-dimensional perovskite phases are labelled by an n-value, defined by the number of conjoined lead halide octahedral sheets that form each slab; $n = 1$ refers to a two-dimensional (2D) phase with independent sheets of lead halide octahedra separated by the organic spacer, $n = 2$ refers to a quasi-2D phase consisting of two conjoined octahedral sheets in each slab, and so on. By engineering the crystallization of different structural phases, the physical properties of perovskite thin films, such as the absorption spectrum, phase purity, or defect concentration, can be tuned and therefore used to modulate optoelectronic properties and material stability.[13]

In previous studies, pure-iodide or pure-bromide lower-dimensional perovskites have been successfully used to limit charge-carrier recombination at interfaces of the 3D perovskite with charge-transport layers.[14–18] In contrast, the use of lower-dimensional mixed-halide perovskites remains a largely unexplored area.[19] Among the studies published on such materials, it has been shown that the spacer cation may determine ion migration characteristics in mixed-halide compositions, with BA-based perovskites being more prone to halide de-mixing than PEA-based analogues.[20] Furthermore, a reduced perovskite dimensionality has been correlated to suppressed ion migration, indicating the potential of 2D perovskites to

prevent photo-induced instability.[21–23] Nevertheless, the direct effect of perovskite dimensionality on instabilities inherent to mixed-halide 3D perovskite compositions in not yet firmly established.

Herein, the photostability of mixed-halide 2D perovskite ($n = 1$) systems is studied using time-dependent photoluminescence (PL) spectroscopy to identify their susceptibility to light-induced halide segregation. The photostability is then correlated with the non-binomial halide distribution determined by ^{207}Pb NMR. Thereafter, this behavior is studied in mixed-halide, quasi-2D perovskite thin films where the distribution between different structural phases ($n = 1$, 2, etc.) is controlled by a solvent engineering approach. This allows to correlate the tendency to undergo light-induced halide segregation with the dimensionality of the perovskite phase. The same structural properties are also found to influence halide redistribution in the dark, thereby modulating the reversibility of light-induced segregation.

6.2 FABRICATION OF PEA-BASED 2D PEROVSKITE

2D ($n = 1$) PEA lead halide perovskites were prepared on glass substrates *via* one-step room-temperature spin-coating from a *N,N*-dimethylformamide (DMF)-based precursor solution, leading to a film with a nominal composition $PEA_2Pb(Br_xI_{1-x})_4$. Details regarding the layer deposition can be found in Methods. Partial substitution of iodide with bromide yields a blueshift in the absorption onset and in the PL spectrum (**Figure 6.1**a,b). X-ray diffraction (XRD) confirms the structural change, as the diffraction peak at 5.4°, corresponding to the (002) plane of PEA_2PbI_4, shifts to lower angles upon addition of Br (Figure 6.1c).[24]
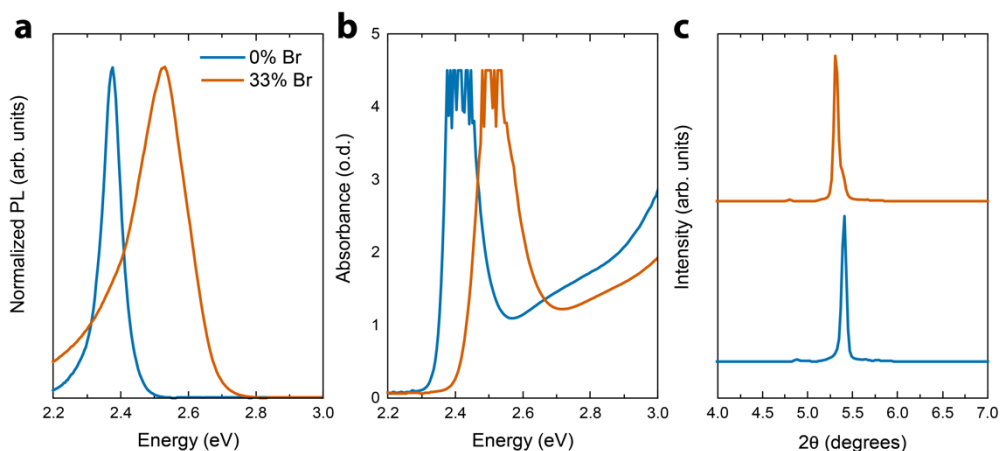

Figure 6.1. (a) Steady-state photoluminescence spectra, (b) UV-vis-NIR absorption spectra, and (c) XRD pattern of $PEA_2Pb(Br_xI_{1-x})_4$ with $x = 0$ and $x = 0.33$. The noisy features at the top of the excitonic absorption band are an artefact and caused by the high (>4) optical density in that spectral region.

Solid-state ^{207}Pb nuclear magnetic resonance (ssNMR) was performed to examine the halide distribution in $PEA_2Pb(Br_xI_{1-x})_4$ films. Solid-state NMR has been used to study a wide variety of phenomena in halide perovskites.[25,26] Previously, it has been shown that ^{207}Pb ssNMR is sensitive to the halide ion in 3D perovskite materials and to the local configuration of the lead halide octahedra in mixed-halide perovskites.[25,27–31] ^{207}Pb ssNMR has also been performed for 2D and quasi-2D perovskites $BA_2MA_{n-1}Pb_nI_{3n+1}$, showing that the ^{207}Pb shift is sensitive to n.[32] However, mixed-halide 2D or quasi-2D compositions have not yet been investigated.
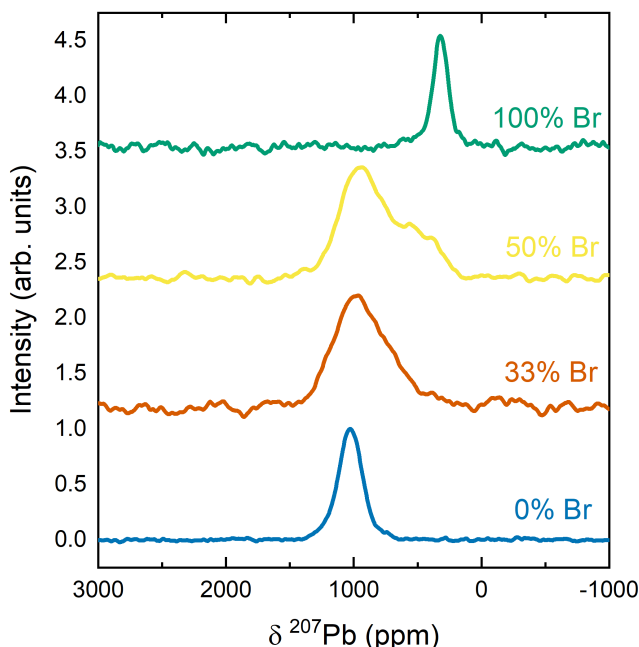

Figure 6.2. Isotropic ^{207}Pb NMR spectra of $PEA_2Pb(Br_xI_{1-x})_4$ for different halide compositions, obtained by summation of the corresponding phase-adjusted spinning sidebands (PASS) spectra.

Figure 6.2 shows the isotropic ^{207}Pb NMR spectra for $PEA_2Pb(Br_xI_{1-x})_4$ with different bromide/iodide contents (x = 1, 0.50, 0.33, and 0). The isotropic chemical shift for the pure iodide PEA_2PbI_4 system is 1030 ppm, which is similar to the previously reported shift of BA_2PbI_4 (1084 ppm),[32] but significantly lower than the shift for 3D perovskites (1265, 1445, and 1515 ppm for Cs^+, MA^+, and FA^+ cations, respectively).[28,33] Pure bromide PEA_2PbBr_4 possesses a lower chemical shift of 325 ppm, consistent with the trend for 3D perovskites. Unlike the pure iodide, the pure bromide n = 1 2D perovskite is within the range of observed ^{207}Pb shifts for 3D

bromide-perovskites (262, 365, and 515 ppm for Cs^+, MA^+, and FA^+ cations, respectively).[28]

For mixed-halide 3D perovskites, different individual configurations of the lead iodide octahedra are possible, *e.g.*, $[PbI_aBr_{6-a}]^{4-}$ with $a = 0 - 6$, and the isotropic [207]Pb chemical shift for each configuration depends approximately linearly on a.[27,30] Mixed-halide 3D compositions with a 1:1 halide ratio exhibit a broad [207]Pb resonance approximately midway between those of the corresponding pure halides, which suggests a random halide occupancy and a binomial distribution of the individual local configurations.[27,29,30,34] Here, it can be seen that the isotropic [207]Pb spectrum of $PEA_2PbBr_2I_2$ (*i.e.*, $x = 0.50$) is broader than that of the pure iodide and pure bromide perovskites, indicating a distribution of individual configurations rather than a single ordered arrangement (Figure 6.2). The peak in the spectrum is significantly skewed to higher chemical shift (corresponding to iodide-rich octahedra, $a \geq 4$), but with a clear shoulder at lower chemical shift (that match bromide-rich octahedra, $a \leq 2$). This indicates the presence of different (not fully random) distributions of bromide and iodide across the octahedra in the sample. The $n = 1$, $x = 0.33$ sample exhibits a similar isotropic [207]Pb spectrum, but with the center of mass shifted further to higher frequency, as expected given the higher iodide concentration. Again, the center of mass of the spectrum is at a higher frequency than what would be expected for a simple random bromide–iodide distribution over the octahedra. The observed spectra thus suggest the presence of both iodide-rich and bromide-rich octahedra in the samples. Halide heterogeneity has previously been identified in solution-processed 3D mixed-halide perovskites.[35–37]

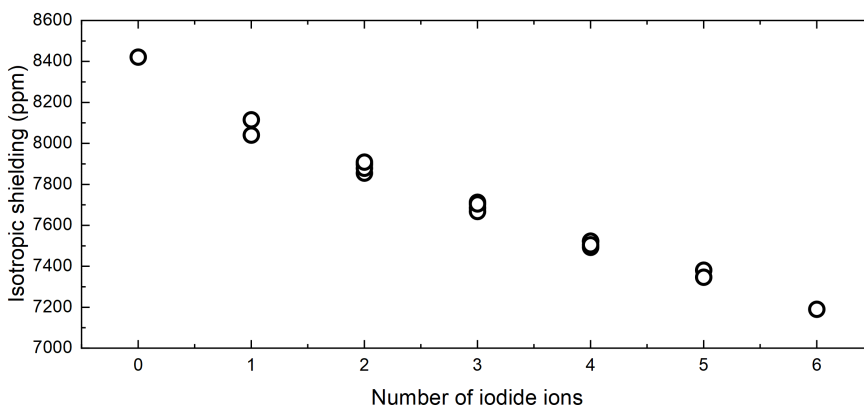**Figure 6.3**. Calculated isotropic shielding for different $[PbI_aBr_{6-a}]^{4-}$ configurations as function of the number of iodine atoms, a.

To test this hypothesis, the isotropic chemical shielding for all 18 possible individual configurations for $[PbI_aBr_{6-a}]^{4-}$ (with $a = 0 - 6$) was calculated (see

Methods). The shielding again depends approximately linearly on a (**Figure 6.3**), as observed for the 3D perovskites. These computed shieldings were then used to simulate spectra for both random and non-random halide distributions (**Figure 6.4**)
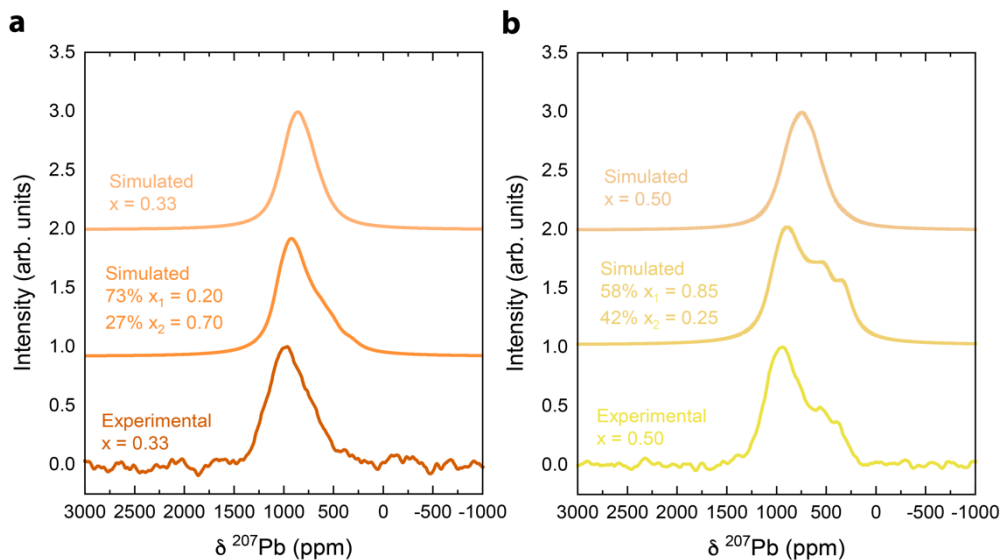

Figure 6.4. Experimental and simulated isotropic ^{207}Pb spectra of PEA$_2$Pb(Br$_x$I$_{1-x}$)$_4$ for (a) $x =$ 0.33 and (b) $x = 0.50$. The simulated spectra are obtained by summation of gaussians centered at the calculated isotropic shifts for each configuration (see Methods), each with a full-width-at-half-maximum of 220 ppm taken from the experimental spectrum of PEA$_2$PbI$_4$. In the bottom spectra, the weights of each configuration are given by a single binomial distribution of halides within the nominal composition of the sample (x). The middle spectra represent a model, where the sample is assumed to comprise two different effective compositions (x_1, x_2) in different proportions, that averaged together give the nominal sample composition (for (a), $x = 73\% \times 0.20 + 27\% \times 0.70 = 0.33$; for (b), $x = 58\% \times 0.25 + 42\% \times 0.85 = 0.5$). The weights of each configuration are calculated from the binomial distribution for the two regions then combined *via* the relative proportions. The experimental spectra are as in Figure 6.2. Although this simple model does not exactly match experiment, which could also result from limitations in the chemical shift calculations, it nevertheless supports the hypothesis of halide clustering. Importantly, the simulated spectra with a random halide distribution are not consistent with the experimental results.

As expected, a random binomial halide distribution results in an approximately symmetric spectrum that does not match the experimental spectrum. In contrast, a model in which both iodide-rich and bromide-rich compositions are present, affords simulated spectra that reproduce the general features of the experimental spectra. A single phase (one peak) was observed for the $x = 0.5$ sample from XRD, rather than segregated into iodide-rich and bromine-rich phases. Therefore, the

preference for iodide-rich and bromide-rich octahedra must occur within nanoscale clusters, or even at the scale of single octahedra. Non-random distribution of halides at the level of single octahedra has been demonstrated in recent studies, which have shown preferential occupation of equatorial sites for bromide ions and axial for iodides.[37–39] With ssNMR, we find a non-random halide distribution, which may also include axial/equatorial preference within a single octahedron.

6.3 HALIDE SEGREGATION IN 2D PEROVSKITES

The photostability of the mixed-halide ($x = 0.33$) film was studied by continuously illuminating the film with blue (405 nm) light and tracking the evolution of the PL spectrum over time (**Figures 6.5**a,b). For details of the experiment, see Methods (Section 6.8). Firstly, the PL spectrum is asymmetrical, which is likely due to slight compositional inhomogeneity, as observed *via* ssNMR. Secondly, the spectral centroid, during 10,000 s (approx. 3 h) of illumination at approximately 3 Sun equivalent intensity, exhibits only a marginal redshift from 2.46 to 2.41 eV. Such redshift has been extensively studied in 3D perovskites and is related to the light-induced formation of iodide-rich domains which provide low-energy sites for charge-carrier recombination.[7] However, since the PL energy never approaches that of a pure iodide phase (2.37 eV), it can be argued that a small proportion of low-bandgap iodide-rich phase forms in the system over time. This is in stark contrast to observations made in methylammonium-based 3D perovskites, in which a nearly pure iodide-rich phase is formed leading to a large red-shift of the emission spectrum.[7]

After 10,000 s of illumination, the film was stored in the dark and, intermittently, PL spectra were recorded (light exposure for 500 ms during excitation). Under similar conditions, segregated 3D perovskites typically undergo an entropically driven redistribution of halide ions that restores the statistically mixed-halide phase leading to a blueshift of the PL spectrum.[8] In contrast, after storage in dark conditions for approx. 25 h, the spectrum of segregated $PEA_2Pb(Br_{0.33}I_{0.67})_4$ remained steady with a maximum at 2.41 eV (Figure 6.5b) implying the absence of any halide redistribution.

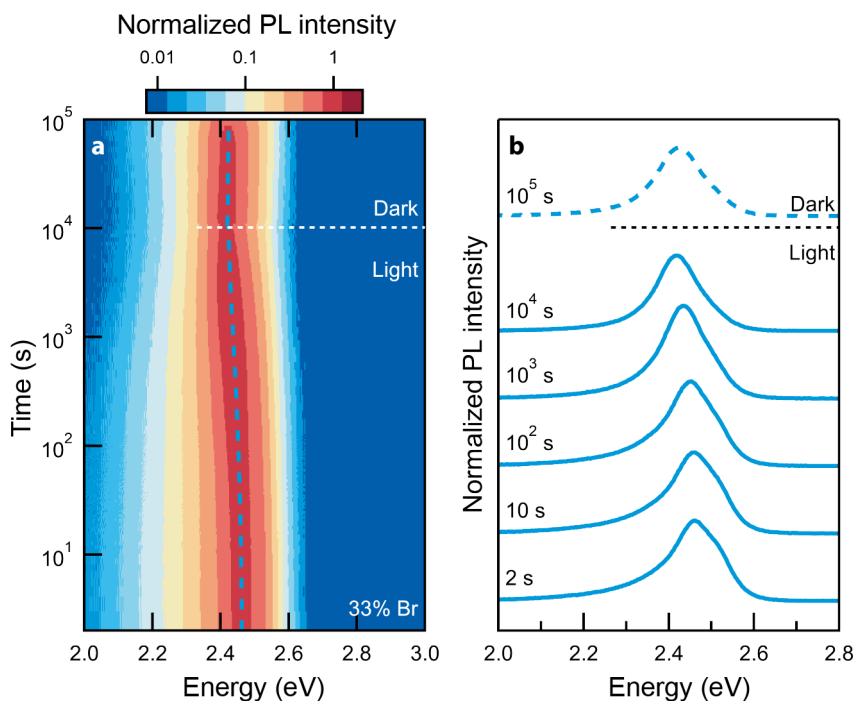**Figure 6.5.** (a) Normalized PL spectra as a function of time for PEA$_2$Pb(Br$_{0.33}$I$_{0.67}$)$_4$ film. The film is illuminated by a 405 nm LED source at ~3 Sun equivalent intensity for 10,000 s (~3 h) followed by storage in the dark for 90,000 s (~25 h) with spectra recorded intermittently. Note the logarithmic intensity and time axes. (b) Normalized photoluminescence spectra at selected times. The spectra are offset vertically for clarity but have the same vertical scale.

The absence of halide segregation in the 2D perovskite can be tentatively ascribed to the non-binomial halide distribution determined by [207]Pb NMR. The spectra indicate a preference for iodide-rich and bromide-rich octahedra, implying an additional energy barrier for bromide ions to move into the iodide-rich octahedra, and vice versa. This barrier to halide migration would suppress the segregation under light illumination, as well as the recovery in the dark.

6.4 MIXED-HALIDE MULTIDIMENSIONAL PEROVSKITES

The very wide bandgap of 2D ($n = 1$) perovskites leads to a poor overlap of their absorption spectrum with the solar irradiance and makes them less relevant for integration in solar cells. Instead, quasi-2D perovskite ($2 \leq n \leq 5$) systems are becoming increasingly common to balance the stability and efficiency of solar cells by combining a broad absorption profile with the stability afforded by layered structures.[9]
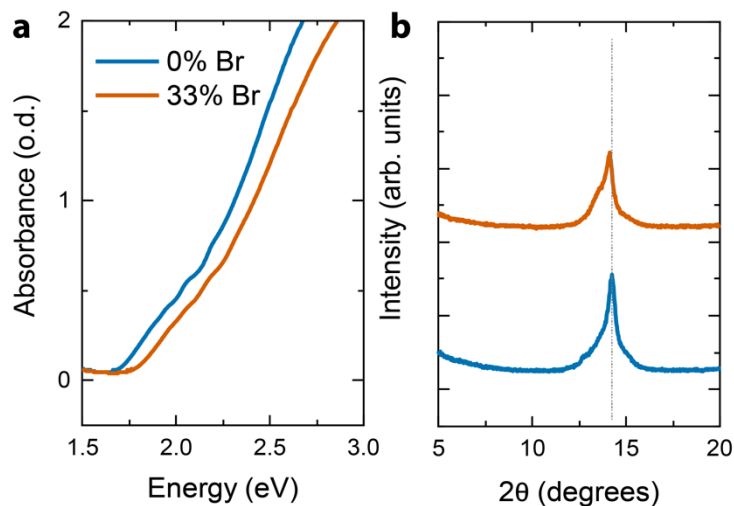
Figure 6.6. (a) UV-vis-NIR absorption of $PEA_2MA_3Pb_4(Br_xI_{1-x})_{13}$ perovskite thin films with $x = 0$ and $x = 0.33$ prepared from a pure DMF precursor solution. (b) Corresponding X-ray diffractograms

Mixed-halide quasi-2D (nominal $n = 4$) perovskite films were prepared using PEA as the bulky spacer and MA as the organic cationic component of the $n > 1$ phases (nominal composition $PEA_2MA_3Pb_4(Br_xI_{1-x})_{13}$). By incorporating bromide ($x = 0.33$), the onset of optical absorption blueshifts compared to the corresponding pure iodide ($x = 0$) quasi-2D ($n = 4$) perovskite (**Figure 6.6**) along with a shift of the Bragg peaks to larger diffraction angles, confirming the successful bromide incorporation and resulting widening of the optical bandgap.

During solution-based fabrication of quasi-2D perovskites with nominal $n > 1$, it is often the case that a distribution of structural phases with different n-values is obtained in the perovskite film. In most cases, quasi-2D phases with lower n-values crystallize at the interface with the substrate whereas quasi-3D phases with higher n-values form at the interface with air. The introduction of a co-solvent (dimethyl sulfoxide, DMSO) to the DMF-based perovskite precursor solution predictably changes this structural distribution, which allows inducing stratification of the quasi-2D and quasi-3D-phases over the film thickness.[40,41]

Figure 6.7a shows a schematic of this dimensional stratification because of co-solvent addition. For example, in films prepared from a pure DMF solvent (0% DMSO), a gradual onset of the UV-vis-NIR absorption spectrum is observed, indicating the formation of a quasi-3D perovskite phase, *i.e.*, $PEA_2MA_{n-1}Pb_n(Br_xI_{1-x})_{3n+1}$ with high n-values (Figure 6.7b). By increasing the DMSO fraction in the DMF precursor solution, excitonic absorption features corresponding

to lower-dimensional phases appears in films at ~2.5 eV ($n = 1$) and at ~2.3 eV ($n = 2$). At the same time, the onset of higher-dimensional perovskite phases redshifts with the addition of more co-solvent, leading to the formation of a 3D phase with a steep absorption onset at ~1.78 eV when the DMSO volume concentration exceeds 10%. PL spectra (Figure 6.7b) of films prepared from a DMSO-containing DMF precursor solution exhibit high-energy emissions from $n = 1$ and $n = 2$ phases when excited from the substrate side, while excitation from the film side results in a spectrum dominated by low-energy emission corresponding to an increased contribution from the 3D perovskite phases. This confirms the presence of a structural stratification, with 2D ($n = 1$) and quasi-2D ($n = 2$) phases located at the interface with the substrate and quasi-3D or 3D phases organized on top at the interface with air.[42]
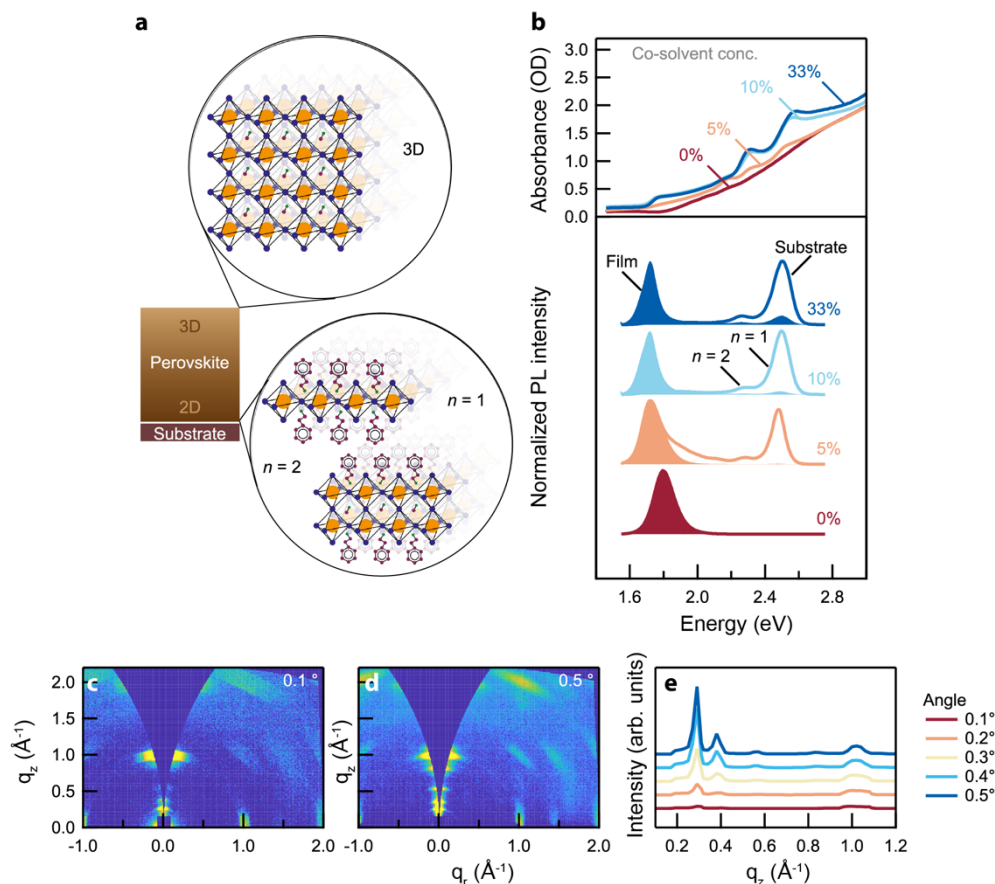

Figure 6.7. (a) Schematic of different dimensional phases ($n = 1$, $n = 2$, and 3D) formed in quasi-2D perovskite thin films by solvent engineering. (b) UV-vis-NIR absorption spectra (top panel), and photoluminescence spectra (bottom panel) using excitation from the substrate

side (solid lines) and film side (shaded) of perovskite films prepared using different concentrations of DMSO in the DMF precursor solutions. (c, d) Angle-resolved GIWAXS patterns of perovskite films prepared from a DMF precursor solution containing 20% DMSO, measured at incidence angles of (c) 0.1° and (d) 0.5°. (e) Out-of-plane (q_z) cuts of angle-resolved GIWAXS measurements collected at incident angles of 0.1° – 0.5°.

The stratification of 2D–3D phases is further corroborated using angle-resolved grazing-incidence wide-angle X-ray scattering (AR-GIWAXS) (Figures 6.7c and 6.7d). When probing $PEA_2MA_3Pb_4(Br_{0.33}I_{0.67})_{13}$, raising the angle of incidence from 0.1° to 0.5° increases the penetration depth of the X-rays and therefore allows the characterization of the perovskite structure as a function of depth in the film. At all incident angles, the GIWAXS patterns indicate well-oriented perovskite phases with Bragg spots at $q_z = 1$ Å^{-1}, corresponding to (100) planes of a quasi-3D perovskite, and at $q_z = 0.28$ and 0.38 Å^{-1}, representative of (002) planes of $n = 2$ and $n = 1$ perovskites, respectively.[25,43] At higher incident angles, the Bragg spots associated with small n-value perovskites increase in intensity. Analyzing the out-of-plane line cuts of the AR-GIWAXS patterns (Figure 6.7e) shows that these lower-dimensional phases are mostly localized at the substrate interface. In fact, the ratio ($I_{n=2}/I_{3D}$) increases from 1.1 to 8.1 when going from 0.1° to 0.5° incidence angle, confirming the 2D–3D stratification.

6.5 HALIDE SEGREGATION IN QUASI-2D PEROVSKITES

The evolution of the PL spectrum of $PEA_2MA_3Pb_4(I_{0.67}Br_{0.33})_{13}$ films under continuous illumination to characterize photo-induced halide segregation in this system is shown in **Figure 6.8**a. Similar to the experiment shown in Figure 6.5, the measurement consisted of two phases, the first phase (approx. 3 h) characterizing photo-induced PL behavior changes, and the second phase (approx. 14 h) tracking the reversal of these changes in dark conditions. In order to better observe the different structural phases, films were probed from the substrate side where a higher proportion of the lower-dimensional phases are formed. To ensure that the broad distribution of different dimensional phases is excited a combination of blue (405 nm) and green (530 nm) light was used (Figure 6.8a).
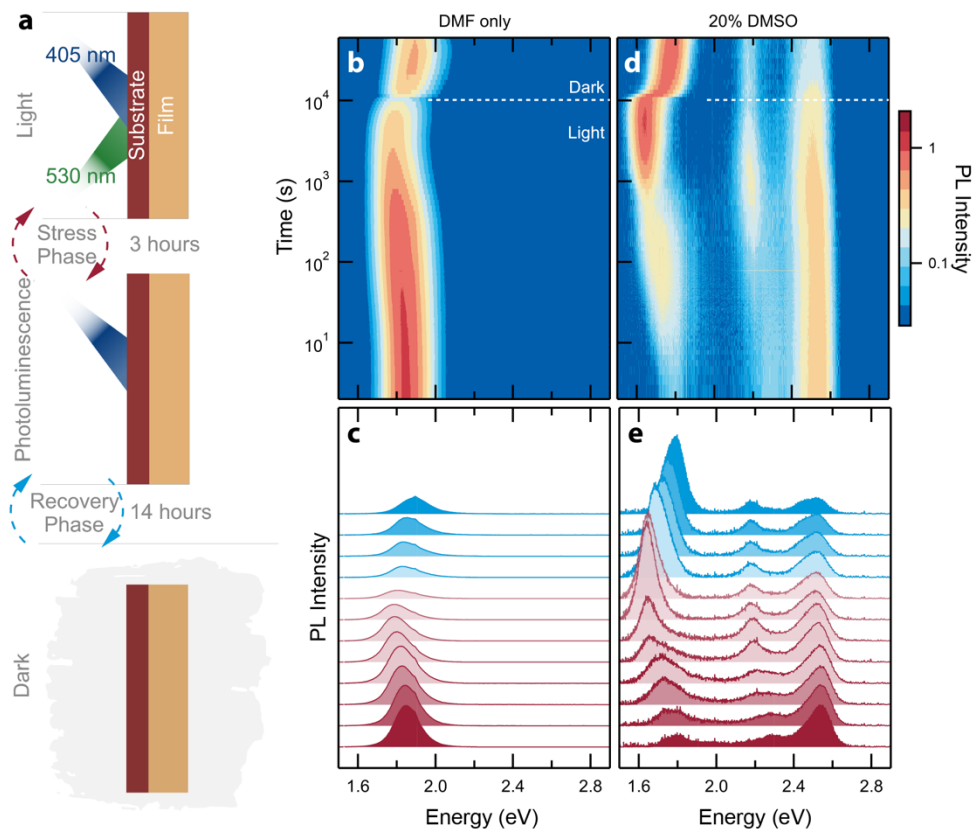
Figure 6.8. (a) Schematic describing the measurement protocol to characterize light-induced halide segregation and dark relaxation in mixed-halide perovskite thin films. (b-e) Normalized 2D plots of the photoluminescence intensity (b,d) and photoluminescence spectra (c,e) versus photon energy recorded over time under 10,000 s of continuous green (530 nm) and blue (405 nm) excitation, followed by 50,000 s of storage in the dark with intermittent photoluminescence measurements. Perovskite films were prepared from (b,c) DMF-only, and (d,e) 20% DMSO-containing DMF precursor solutions. Note the logarithmic intensity and time axes in panels (b) and (d).

Firstly, it was found that in an unstratified film prepared from a pure DMF solvent system, the PL spectrum corresponding to a quasi-3D perovskite appears at ~1.84 eV and under illumination shows a mild redshift after 1,000 s of illumination. The PL intensity is also found to decrease as the film is illuminated for ~3 h indicating increased non-radiative recombination of photogenerated charge carriers. This behavior may result from an ion migration-related increase in local strain which has been shown to increase non-radiative recombination.[44] In contrast, a film prepared with 20% DMSO in the DMF precursor solution shows PL signals corresponding to lower-dimensional phases at ~2.5 eV ($n = 1$) and ~2.3 eV ($n = 2$), and an emission

from the 3D phase at ~1.78 eV. Under continuous illumination, the signal corresponding to the $n = 1$ phase shows only a minor redshift accompanied by a reduction in intensity, consistent with observations reported in Figure 6.5. The PL signal related to the $n = 2$ phase, which first appears as a shoulder at ~2.3 eV, splits to form a distinct peak at ~2.18 eV, thus indicating the formation of an iodide-rich $n = 2$ phase within ~100 s of illumination. Similar to observations made with 3D perovskites,[8] the redshifted peak progressively brightens, indicating a higher radiative yield of the emission.

Lastly, the peak corresponding to a 3D phase at ~1.78 eV also shows a redshift and concurrent brightening within 10 s of illumination, stabilizing at ~1.63 eV after ~1,000 s. The PL of the unstratified (nominally $n = 4$) perovskite (Figure 6.8b,c) is noticeably more stable with time than that of the 3D phase in a stratified film (Figure 6.8d,e).

6.6 HALIDE REDISTRIBUTION IN SEGREGATED QUASI-2D PEROVSKITES

When a segregated system is stored in the dark after being illuminated, the effects of halide de-mixing are typically reversed in 3D perovskites due to the entropy-driven restoration of the statistical composition as halide ions remix. Consequently, the PL blueshifts to the original emission energy. For lower-dimensional systems, the structural nature of the perovskite was found to influence this behavior. For instance, in the case of a perovskite film prepared from DMF only (Figures 6.8b,c), the redshifted emission reversed in the dark and the PL peak approached the emission energy of the pristine film prior to illumination. The same behavior was observed in the 3D phase of a stratified quasi-2D perovskite (Figure 6.8d,e), where the PL peak blueshifted from 1.63 eV to 1.78 eV over 14 h of storage in dark.

Remarkably, the peak assigned to the segregated $n = 2$ layered phases did not recover but rather remained at ~2.18 eV throughout dark storage (Figures 6.8d,e). The same was the case for the segregated $n = 1$ phase, where the mildly redshifted PL peak remained constant at the low emission energy. This observation indicates the absence of remixing of halides in $n = 2$ phases at room temperature, as observed for the $n = 1$ system. Perovskite films developed using other co-solvent compositions showed similar behavior, where the segregated 3D phase shows the typical signs of halide redistribution in the dark, whereas the $n = 2$ and $n = 1$ phases do not.
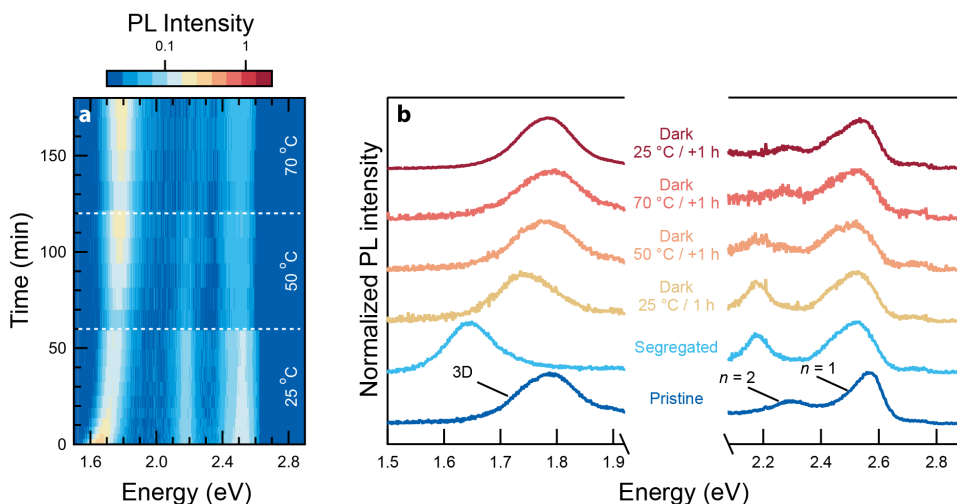
Figure 6.9. (a) Normalized 2D plot of photoluminescence intensity versus photon energy recorded over time for a $PEA_2MA_3Pb_4(Br_{0.33}I_{0.67})_{13}$ film during the dark recovery at different film temperatures after illumination for 2 h. (b) Photoluminescence spectra of 3D (left) and 2D (right) phases, normalized to the maximum peak intensity, at the start of the illumination (pristine), after 2 h of illumination (segregated), and after dark recovery at sequentially elevated temperatures (25, 50, and 70 °C) for 1 h each, followed by cooling to 25 °C for 1 h.

To induce a remixing of halide ions in lower-dimensional phases, the dark recovery of the PL of a halide-segregated film was tracked at elevated temperatures (**Figure 6.9**). Like the observations reported in Figure 6.8d, the peak corresponding to the 3D phase showed a blueshift at room temperature, whereas the peaks for lower-dimensional phases did not. However, when maintained at 50 °C for 60 min., the PL peak related to a segregated $n = 2$ phase starts to decrease in intensity and thereafter, at a temperature of 70 °C, blueshifts to develop the shoulder originally observed in pristine films. Interestingly, the PL peak corresponding to the $n = 1$ phase remains at a lower energy even at elevated temperatures, which indicates the absence of recovery.

In conclusion, the dimensionality of perovskites in thin films plays an important role in their tendency to undergo light-induced halide segregation and, correspondingly, for halide ions to remix in the dark. Layered perovskites containing single lead halide octahedra sheets ($n = 1$) show limited signs of photo-induced halide segregation. The small redshift observed in PL under illumination nevertheless shows that 2D systems are not completely immune to these processes. In a quasi-2D system with two conjoined octahedral sheets ($n = 2$), the experiments confirm the occurrence of halide segregation. However, the entropically-driven

redistribution of halides in the dark is still restricted and only occurs at elevated temperatures. Lastly, higher-n perovskites, for instance the quasi-3D perovskites prepared from a DMF-pure solution or the 3D phase when prepared from a DMF solution containing 20% DMSO, show the characteristic behavior of halide segregation under illumination and the subsequent recovery in the dark owing. However, a quasi-3D perovskite system still demonstrates higher photostability than a 3D perovskite formed in the stratified film.

6.7 CONCLUSIONS

Mixed-halide $PEA_2MA_{n-1}Pb_n(Br_xI_{1-x})_{3n+1}$ 2D perovskites demonstrate superior photostability when compared to 3D perovskites. This is, however, contingent on their structural properties and distribution of different layered phases in the film. Pure 2D layered systems containing a single sheet of lead halide octahedra ($n = 1$) are largely stable against photo-induced segregation of iodide and bromide ions. This is tentatively explained by the non-binomial halide-distribution revealed by [207]Pb NMR, which increases the barrier to halide diffusion. Quasi-2D phases ($n > 1$), however, are more susceptible to light-induced halide de-mixing. When halide-segregated films are stored in dark, halide redistribution occurs in quasi-3D and 3D perovskites, signaled by a blueshift in the PL spectrum. However, in layers containing fewer conjoined sheets ($n = 2$ or $n = 1$) halide redistribution is arrested because of higher ion migration energy barriers, leading to a segregated phase that remains de-mixed over time.

6.8 METHODS

Solution preparation and film fabrication. The precursor solutions were prepared by dissolving PEAI, MAI, PbI_2 in the ratio 2:n–1:n in DMF for n = 1 and in DMF/DMSO (0, 5%, 10%, 20%, or 33%) for $<n>$ = 4, with overnight stirring at 60 °C. The concentration of the precursor solutions was 1 M in PbI_2. Glass substrates were cleaned by sonicating in acetone, scrubbing and sonicating in soap solution, rinsing in demineralized water, sonicating in 2-propanol, followed by 30 min UV-ozone treatment. 60 µL of the perovskite precursor solution was spin-coated at room-temperature at 5000 rpm for 45 s, followed by thermal annealing at 100 °C for 10 min. *Film characterization.* UV-vis-NIR absorption spectra were recorded by using a PerkinElmer Lambda 1050 UV-vis-NIR spectrophotometer. Photoluminescence spectra were recorded by using an Edinburgh Instruments FLSP920 double-monochromator luminescence spectrophotometer. XRD patterns were recorded by using a Bruker 2D phaser (Cu Kα radiation, $\lambda = 1.5406\,\text{Å}$): measurements were performed in the range 3-40° with a step size 0.02° and collection time of 1 s. 2D GIWAXS measurements were performed with a Ganesha 300XL+ system from JJ X-ray equipped with a Pilatus 300K detector (pixel side 172 µm × 172 µm). The X-ray source was a Genix 3D Microfocus sealed tube X-ray Cu-source with integrated monochromator. The wavelength used was 1.5406 Å. The detector moves in a

vacuum chamber with sample-to-detector distance (SDD) varied between 0.115 m and 1.47 m depending on the configuration used, as calibrated using silver behenate (d_{001} = 58.380 Å). For GIWAXS, the SDD was 115.4 mm. The angle dependent 2D GIWAXS were conducted *via* controlling incident angle from 0.1-0.5° with a 0.1° interval. For time- and illumination-dependent photoluminescence measurements, the samples were mounted into a custom-built sealed holder to maintain an inert atmosphere.

Halide segregation. To induce halide segregation, samples were illuminated with blue (Thorlabs M405L4, 405 nm), and where mentioned green (Thorlabs M530L3, 530 nm), light-emitting diodes. The green light was filtered by a 600 nm short-pass filter and the LEDs were driven by a Thorlabs DC4104 driver. During spectrum acquisition, the blue LED was used as the excitation source for photoluminescence measurements and the green LED was switched off. To track the photoluminescence behavior when the sample was stored in the dark, the blue LED was used intermittently (exposure time ~500 ms) as the excitation source and was otherwise switched off. The photoluminescent light, filtered by a 645 nm long-pass filter, was focused onto an optical fiber connected to the spectrometer (Avantes Avaspec-2048x14) operated on a custom-built code in the LabVIEW environment. To measure photoluminescence behavior at elevated temperatures, the sample was loaded onto a heating stage (Linkam THMS 600) continuously flushed with nitrogen gas.

Solid-state NMR. Solid-state NMR experiments were performed at room temperature on an 11.7 T Bruker Advance III spectrometer using 1.3 mm outer-diameter rotors. Isotropic [207]Pb spectra were obtained by summing the rows of sheared 2D PASS spectra, which separate the isotropic and anisotropic [207]Pb chemical shifts in a two-dimensional experiment. Five-pulse PASS spectra were acquired at 24 kHz MAS,[45] with a single rotor period for the PASS block, a radiofrequency amplitude of 250 kHz, eight increments in the indirect dimension, and a recycle delay of 0.1 s. Between 48,000 and 186,000 scans were acquired per increment, depending on the sample. Spectra were referenced to $Pb(NO_3)_2$ with an isotropic shift of −3490 ppm at room temperature. The chemical shielding calculations were performed on $[PbX_6]^{4-}$ octahedral clusters using the Amsterdam Density Functional (ADF) 2017 package, as previously reported for 3D perovskites.[28,31,46] The atomic positions were extracted for different local configurations from periodic DFT calculations, as reported in Ref.[38]. Relativistic effects were included through the zero-order regular approximation (ZORA) method at the spin–orbit level.[47–49] The BP86 functional with Grimme DFT-D3 dispersion correction and Becke and Johnson (BJ) damping was used along with ZORA/QZ4P all-electron basis sets.[50–53] Chemical shieldings were computed using the Gauge-including atomic orbital (GIAO) formalism.[54–57]

6.9 APPENDIX

Table A1. The 18 possible configurations of $[PbI_aBr_{6-a}]$ octahedra for n = 1 layered mixed-halide $PEA_2Pb(Br_xI_{1-x})_3$ perovskites, assuming the two axial sites are equivalent, the four equatorial sites are equivalent, but the axial and equatorial sites are inequivalent.

Iodines	Axial Iodines	Equatorial Iodines		Degeneracy	Probability ($x = 0.5$)	Shielding σ/ppm	Shift δ /ppm
0	0	0		1	1.6%	8421	325
1	1	0		2	3.1%	8041	543
1	0	1		4	6.3%	8115	500
2	2	0		1	1.6%	7855	649
2	1	1		8	12.5%	7879	636
2	0	2	cis	4	6.3%	7909	618
2	0	2	trans	2	3.1%	7897	625
3	2	1		4	6.3%	7667	757
3	0	3		4	6.3%	7713	731
3	1	2	cis	8	12.5%	7705	735
3	1	2	trans	4	6.3%	7685	746
4	0	4		1	1.6%	7522	840
4	1	3		8	12.5%	7522	840
4	2	2	cis	4	6.3%	7505	850
4	2	2	trans	2	3.1%	7493	857
5	1	4		2	3.1%	7380	921
5	2	3		4	6.3%	7347	940
6	2	4		1	1.6%	7190	1030

The probability of each configuration for an $x = 0.5$ sample with a random binomial distribution is shown. The calculated isotropic shieldings are converted to isotropic chemical shifts by interpolating between the experimental shifts of the pure bromide and pure iodide samples ($\delta = 5147.4 - 0.57266\sigma$).

6.10 REFERENCES

[1] A. Al-Ashouri, E. Köhnen, B. Li, A. Magomedov, H. Hempel, P. Caprioglio, J. A. Márquez, A. B. Morales Vilches, E. Kasparavicius, J. A. Smith, N. Phung, D. Menzel, M. Grischek, L. Kegelmann, D. Skroblin, C. Gollwitzer, T. Malinauskas, M. Jošt, G. Matič, B. Rech, R. Schlatmann, M. Topič, L. Korte, A. Abate, B. Stannowski, D. Neher, M. Stolterfoht, T. Unold, V. Getautis, S. Albrecht, *Science* **2020**, *370*, 1300.
[2] M. Jošt, E. Köhnen, A. Al-Ashouri, T. Bertram, Š. Tomšič, A. Magomedov, E. Kasparavicius, T. Kodalle, B. Lipovšek, V. Getautis, R. Schlatmann, C. A. Kaufmann, S. Albrecht, M. Topič, *ACS Energy Lett.* **2022**, *7*, 1298.
[3] R. Lin, J. Xu, M. Wei, Y. Wang, Z. Qin, Z. Liu, J. Wu, K. Xiao, B. Chen, S. M. Park, G. Chen, H. R. Atapattu, K. R. Graham, J. Xu, J. Zhu, L. Li, C. Zhang, E. H. Sargent, H. Tan, *Nature* **2022**, *603*, 73.
[4] K. O. Brinkmann, T. Becker, F. Zimmermann, C. Kreusel, T. Gahlmann, M. Theisen, T. Haeger, S. Olthof, C. Tückmantel, M. Günster, T. Maschwitz, F. Göbelsmann, C. Koch, D. Hertel, P. Caprioglio, F. Peña-Camargo, L. Perdigón-Toro, A. Al-Ashouri, L. Merten, A. Hinderhofer, L. Gomell, S. Zhang, F. Schreiber, S. Albrecht, K. Meerholz, D. Neher, M. Stolterfoht, T. Riedl, *Nature* **2022**, *604*, 280.
[5] D. Bryant, N. Aristidou, S. Pont, I. Sanchez-Molina, T. Chotchunangatchaval, S. Wheeler, J. R. Durrant, S. A. Haque, *Energy Environ. Sci.* **2016**, *9*, 1655.

[6]   J. S. Yun, J. Kim, T. Young, R. J. Patterson, D. Kim, J. Seidel, S. Lim, M. A. Green, S. Huang, A. Ho-Baillie, *Adv. Funct. Mater.* **2018**, *28*, 1705363.

[7]   E. T. Hoke, D. J. Slotcavage, E. R. Dohner, A. R. Bowring, H. I. Karunadasa, M. D. McGehee, *Chem. Sci.* **2015**, *6*, 613.

[8]   K. Datta, B. T. van Gorkom, Z. Chen, M. J. Dyson, T. P. A. V. D. Pol, S. C. J. Meskers, S. Tao, P. A. Bobbert, M. M. Wienk, R. A. J. Janssen, *Appl. Energy Mater.* **2021**, *4*, 6650.

[9]   C. Liang, H. Gu, Y. Xia, Z. Wang, X. Liu, J. Xia, S. Zuo, Y. Hu, X. Gao, W. Hui, L. Chao, T. Niu, M. Fang, H. Lu, H. Dong, H. Yu, S. Chen, X. Ran, L. Song, B. Li, J. Zhang, Y. Peng, G. Shao, J. Wang, Y. Chen, G. Xing, W. Huang, *Nat. Energy* **2021**, *6*, 38.

[10] G. Grancini, C. Roldán-Carmona, I. Zimmermann, E. Mosconi, X. Lee, D. Martineau, S. Narbey, F. Oswald, F. De Angelis, M. Graetzel, M. K. Nazeeruddin, *Nat. Commun.* **2017**, *8*, 15684.

[11] L. N. Quan, F. P. García de Arquer, R. P. Sabatini, E. H. Sargent, *Adv. Mater.* **2018**, *30*, 1801996.

[12] G. Grancini, M. K. Nazeeruddin, *Nat. Rev. Mater.* **2019**, *4*, 4.

[13] Y. Xu, M. Wang, Y. Lei, Z. Ci, Z. Jin, *Adv. Energy Mater.* **2020**, *10*, 2002558.

[14] T. Duong, H. Pham, T. C. Kho, P. Phang, K. C. Fong, D. Yan, J. Yin, J. Peng, M. A. Mahmud, S. Gharibzadeh, B. A. Nejand, I. M. Hossain, M. R. Khan, N. Mozaffari, Y. Wu, H. Shen, J. Zheng, H. Mai, W. Liang, C. Samundsett, M. Stocks, K. McIntosh, G. G. Andersson, U. Lemmer, B. S. Richards, U. W. Paetzold, A. Ho-Ballie, Y. Liu, D. Macdonald, A. Blakers, J. Wong-Leung, T. White, K. Weber, K. Catchpole, *Adv. Energy Mater.* **2020**, *10*, 1903553.

[15] S. Gharibzadeh, B. Abdollahi Nejand, M. Jakoby, T. Abzieher, D. Hauschild, S. Moghadamzadeh, J. A. Schwenzer, P. Brenner, R. Schmager, A. A. Haghighirad, L. Weinhardt, U. Lemmer, B. S. Richards, I. A. Howard, U. W. Paetzold, *Adv. Energy Mater.* **2019**, *9*, 1803699.

[16] S. Gharibzadeh, I. M. Hossain, P. Fassl, B. A. Nejand, T. Abzieher, M. Schultes, E. Ahlswede, P. Jackson, M. Powalla, S. Schäfer, M. Rienäcker, T. Wietler, R. Peibst, U. Lemmer, B. S. Richards, U. W. Paetzold, *Adv. Funct. Mater.* **2020**, *30*, 1909919.

[17] C. Chen, Z. Song, C. Xiao, R. A. Awni, C. Yao, N. Shrestha, C. Li, S. S. Bista, Y. Zhang, L. Chen, R. J. Ellingson, C.-S. Jiang, M. Al-Jassim, G. Fang, Y. Yan, *ACS Energy Lett.* **2020**, *5*, 2560.

[18] S. Yang, J. Dai, Z. Yu, Y. Shao, Y. Zhou, X. Xiao, X. C. Zeng, J. Huang, *J. Am. Chem. Soc.* **2019**, *141*, 5781.

[19] A. Rajagopal, R. J. Stoddard, S. B. Jo, H. W. Hillhouse, A. K.-Y. Jen, *Nano Lett.* **2018**, *18*, 3985.

[20] P. S. Mathew, J. T. DuBose, J. Cho, P. V. Kamat, *ACS Energy Lett.* **2021**, *6*, 2499.

[21] J. Cho, P. S. Mathew, J. T. DuBose, P. V. Kamat, *Adv. Mater.* **2021**, *33*, 2105585.

[22] Y. Lin, Y. Bai, Y. Fang, Q. Wang, Y. Deng, J. Huang, *ACS Energy Lett.* **2017**, *2*, 1571.

[23] X. Xiao, J. Dai, Y. Fang, J. Zhao, X. Zheng, S. Tang, P. N. Rudd, X. C. Zeng, J. Huang, *ACS Energy Lett.* **2018**, *3*, 684.

[24] T. L. Leung, Z. Ren, A. A. Syed, L. Grisanti, A. B. Djurišić, J. Popović, *ACS Energy Lett.* **2022**, *7*, 3500.

[25] K. Du, Q. Tu, X. Zhang, Q. Han, J. Liu, S. Zauscher, D. B. Mitzi, *Inorg. Chem.* **2017**, *56*, 9291.

[26] D. J. Kubicki, S. D. Stranks, C. P. Grey, L. Emsley, *Nat. Rev. Chem.* **2021**, *5*, 624.

[27] W. M. J. Franssen, A. P. M. Kentgens, *Solid State Nucl. Magn. Reson.* **2019**, *100*, 36.

[28] A. Karmakar, A. M. Askar, G. M. Bernard, V. V. Terskikh, M. Ha, S. Patel, K. Shankar, V. K. Michaelis, *Chem. Mater.* **2018**, *30*, 2309.

[29] M. Aebli, L. Piveteau, O. Nazarenko, B. M. Benin, F. Krieg, R. Verel, M. V. Kovalenko, *Sci. Rep.* **2020**, *10*, 8229.

[30] B. A. Rosales, L. Men, S. D. Cady, M. P. Hanrahan, A. J. Rossini, J. Vela, *Chem. Mater.* **2016**, *28*, 6848.

[31] A. M. Askar, A. Karmakar, G. M. Bernard, M. Ha, V. V. Terskikh, B. D. Wiltshire, S. Patel, J. Fleet, K. Shankar, V. K. Michaelis, *J. Phys. Chem. Lett.* **2018**, *9*, 2671.

[32] C. Roiland, G. Trippé-Allard, K. Jemli, B. Alonso, J.-C. Ameline, R. Gautier, T. Bataille, L. Le Pollès, E. Deleporte, J. Even, C. Katan, *Phys. Chem. Chem. Phys.* **2016**, *18*, 27133.

[33] J. Lee, W. Lee, K. Kang, T. Lee, S. K. Lee, *Chem. Mater.* **2021**, *33*, 370.

[34] A. Karmakar, M. S. Dodd, X. Zhang, M. S. Oakley, M. Klobukowski, V. K. Michaelis, *Chem. Commun.* **2019**, *55*, 5079.

[35] C. Quarti, E. Furet, C. Katan, *Helv. Chim. Acta* **2021**, *104*, e2000231.

[36] J.-P. Correa-Baena, Y. Luo, T. M. Brenner, J. Snaider, S. Sun, X. Li, M. A. Jensen, N. T. P. Hartono, L. Nienhaus, S. Wieghold, J. R. Poindexter, S. Wang, Y. S. Meng, T. Wang, B. Lai, M. V. Holt, Z. Cai, M. G. Bawendi, L. Huang, T. Buonassisi, D. P. Fenning, *Science* **2019**, *363*, 627.

[37] P. Gratia, G. Grancini, J.-N. Audinot, X. Jeanbourquin, E. Mosconi, I. Zimmermann, D. Dowsett, Y. Lee, M. Grätzel, F. De Angelis, K. Sivula, T. Wirtz, M. K. Nazeeruddin, *J. Am. Chem. Soc.* **2016**, *138*, 15821.

[38] Z. Chen, H. Xue, G. Brocks, P. A. Bobbert, S. Tao, *ACS Energy Lett.* **2023**, *8*, 943.

[39] N. E. Wright, X. Qin, J. Xu, L. L. Kelly, S. P. Harvey, M. F. Toney, V. Blum, A. D. Stiff-Roberts, *Chem. Mater.* **2022**, *34*, 3109.

[40] A. Caiazzo, K. Datta, J. Jiang, M. C. Gélvez-Rueda, J. Li, R. Ollearo, J. M. Vicent-Luna, S. Tao, F. C. Grozema, M. M. Wienk, R. A. J. Janssen, *Adv. Energy Mater.* **2021**, *11*, 2102144.

[41] J. Zhang, L. Zhang, X. Li, X. Zhu, J. Yu, K. Fan, *ACS Sustain. Chem. Eng.* **2019**, *7*, 3487.

[42] A. Z. Chen, M. Shiu, J. H. Ma, M. R. Alpert, D. Zhang, B. J. Foley, D. M. Smilgies, S. H. Lee, J. J. Choi, *Nat. Commun.* **2018**, *9*, 1336.

[43] R. Vázquez-Cárdenas, J. Rodríguez-Romero, C. Echeverría-Arrondo, J. Sanchez-Diaz, V. S. Chirvony, J. P. Martínez-Pastor, P. Díaz-Leyva, J. Reyes-Gómez, I. Zarazua, I. Mora-Seró, *Chem. Mater.* **2022**, *34*, 3076.

[44] T. W. Jones, A. Osherov, M. Alsari, M. Sponseller, B. C. Duck, Y.-K. Jung, C. Settens, F. Niroui, R. Brenes, C. V. Stan, Y. Li, M. Abdi-Jalebi, N. Tamura, J. E. Macdonald, M. Burghammer, R. H. Friend, V. Bulović, A. Walsh, G. J. Wilson, S. Lilliu, S. D. Stranks, *Energy Environ. Sci.* **2019**, *12*, 596.

[45] O. N. Antzutkin, S. C. Shekar, M. H. Levitt, *J. Magn. Reson. A* **1995**, *115*, 7.

[46] G. te Velde, F. M. Bickelhaupt, E. J. Baerends, C. Fonseca Guerra, S. J. A. van Gisbergen, J. G. Snijders, T. Ziegler, *J. Comput. Chem.* **2001**, *22*, 931.

[47] E. van Lenthe, E. J. Baerends, J. G. Snijders, *J. Chem. Phys.* **1994**, *101*, 9783.

[48] E. van Lenthe, A. Ehlers, E.-J. Baerends, *J. Chem. Phys.* **1999**, *110*, 8943.

[49] E. van Lenthe, E. J. Baerends, J. G. Snijders, *J. Chem. Phys.* **1993**, *99*, 4597.

[50] J. P. Perdew, *Phys. Rev. B* **1986**, *33*, 8822.

[51] A. D. Becke, *Phys. Rev. A* **1988**, *38*, 3098.

[52] S. Grimme, S. Ehrlich, L. Goerigk, *J. Comput. Chem.* **2011**, *32*, 1456.

[53] E. Van Lenthe, E. J. Baerends, *J. Comput. Chem.* **2003**, *24*, 1142.

[54] G. Schreckenbach, T. Ziegler, *Int. J. Quantum Chem.* **1996**, *60*, 753.

[55] S. K. Wolff, T. Ziegler, *J. Chem. Phys.* **1998**, *109*, 895.

[56] S. K. Wolff, T. Ziegler, E. van Lenthe, E. J. Baerends, *J. Chem. Phys.* **1999**, *110*, 7689.

[57] G. Schreckenbach, T. Ziegler, *Int. J. Quantum Chem.* **1997**, *61*, 899.

7

3D Perovskite Passivation with a Benzotriazole-based 2D Interlayer for High-Efficiency Solar Cells

Abstract

2-Benzotriazol-2-yl-ethylammonium bromide and iodide and its difluorinated derivatives are synthesized and employed as novel interlayers for passivation of formamidinium lead triiodide (FAPbI$_3$) solar cells. These benzotriazole derivatives form two-dimensional (2D) Ruddlesden-Popper perovskites (RPP), as evidenced by their crystal structures and thin film characteristics. When used to passivate *n-i-p* FAPbI$_3$ solar cells, the power conversion efficiency improves from 20% to close to 22% by enhancing the open-circuit voltage. Quasi-Fermi level splitting experiments and scanning-electron microscopy cathodoluminescence reveal that passivation provides a reduced non-radiative recombination at the interface between the perovskite and hole transport layer. Photoluminescence spectroscopy, angle-resolved grazing-incidence wide-angle X-ray scattering, and depth profiling X-ray photoelectron spectroscopy studies of the 2D/3D interface between the benzotriazole RPP and FAPbI$_3$ show that a non-uniform layer of 2D perovskite is enough to passivate defects, enhance charge extraction, and decrease non-radiative recombination.

7.1 INTRODUCTION

Perovskite solar cells based on formamidinium lead iodide (FAPbI$_3$) as active layer have recently become a standard baseline to reach a high power conversion efficiency (PCE).[1] This material introduces new challenges in processing, mainly related to stabilizing the photoactive α-phase at room temperature, as the photoinactive δ-phase is thermodynamically more stable.[2,3] Careful use of additive engineering and various processing methods help stabilize 3D perovskite FAPbI$_3$ in a tetragonal phase with slight octahedral tilting,[4] paving the way for solar cells with narrower bandgap compared to MAPbI$_3$ and with extremely low voltage losses.[5–8] Currently, state-of-the-art FAPbI$_3$ films make use of methylammonium chloride (MACl) as an additive, with other notable cases using methylene diammonium dichloride.[1,9–12] Such additives induce octahedral tilting, which inhibits the transformation to photoinactive δ-phase.[4] Additionally, these compounds are volatile, thus they do not remain in the film after thermal annealing and do not impact the optical bandgap with the presence of methylammonium (MA) or chloride (Cl) ions.

As widely mentioned in the literature, the interface between the perovskite and charge transport layers is of crucial importance to reduce non-radiative recombination losses and achieve high open-circuit voltage (V_{OC}) with respect to the radiative limit.[13,14] More specifically, in solar cells with *n-i-p* configurations it has been shown that the interface between the perovskite and the 2,2',7,7'-tetrakis[*N,N*-di(4-methoxyphenyl)amino]-9,9'-spirobifluorene (Spiro-OMeTAD) hole transporting layer can be passivated with organic spacers that are able to form 2D or quasi-2D perovskites.[15–19] These lower dimensional perovskites consist of inorganic layers of lead halide octahedra sandwiched between large organic spacers, which are too bulky to fit into octahedral voids to form a 3D perovskite.[20] Despite the large number of studies published on this topic, no consensus has been reached on the nature of the 2D interlayer found at the perovskite/Spiro-OMeTAD interface, its uniformity, and the mechanism behind commonly-reported performance enhancement. Moreover, one of the main advantages of employing 2D perovskites is their chemical variability, since they can be formed ideally with many bulky organic cations leading to different material properties.[21] Despite this, most studies focus only on a handful of spacers, often based on butylammonium (BA), octylammonium (OA), and phenethylammonium (PEA). Functionalization of PEA with fluorine atoms and subsequent passivation of 3D perovskites has also been shown to improve solar cell power conversion efficiency (PCE) and stability towards humidity, mostly by making the film surface more hydrophobic and less subject to the impact of moisture.[22]

Exploration of new spacers is however limited, even though it can potentially lead to impactful discoveries.

In this chapter, we explore the use of benzotriazole derivatives as new spacers to form 2D perovskites and we employ them as interlayers in solar cells with $FAPbI_3$-rich perovskite films as active layer. A novel, easy-to-synthesize, and easy-to-functionalize benzotriazole derivative is proposed as an organic cation to form Ruddlesden-Popper perovskites (RPP) and to passivate 3D perovskites. With a simple passivation strategy, the PCE of solar cells improved from about 20% to almost 22% by enhancing the V_{OC}. Furthermore, by characterizing the 3D/2D heterostructure, we elucidated the formation mechanism of the benzotriazole-based RPP and found that a non-uniform layer of 2D perovskite is enough to passivate defects, enhance charge extraction, and decrease non-radiative recombination at the hole-transport layer interface.

7.2 SYNTHESIS OF BENZOTRIAZOLE DERIVATIVES

Benzotriazole (BTa) is a versatile aromatic building block that allows for a facile derivatization for application in perovskite-based solar cells. It is a weak electron acceptor that has already featured in donor-acceptor type conjugated polymers for organic photovoltaics in the past.[23,24] The benzotriazole unit can be synthesized conveniently from an *o*-phenylenediamine and sodium nitrite and, since many of these diamines are commercially available, it is straightforward to introduce substituents. For this work, we targeted both pristine benzotriazole and a difluorinated derivative. Through a Mitsunobu reaction, both units were functionalized with a two-carbon alkyl chain containing a tert-butyloxycarbonyl (Boc)-protected amino group. Finally, by using either HBr or HI the amine was deprotected and converted into an ammonium bromide or iodide respectively. This reaction yields BTaBr and BTaI out of the pristine unit, and F_2BTaBr and F_2BTaI out of the fluorinated unit (**Figure 7.1**). Details on the synthesis procedures and characterization can be found in the Methods. This straightforward three-step process, consisting of core formation, alkylation, and salt formation can be applied to various *o*-phenylenediamine derivatives and any alkyl tail lengths, and hence a multitude of tailored benzotriazole salts can be synthesized. This opens the possibility for benzotriazole derivatives to be used as novel versatile building blocks for (quasi-) 2D perovskites.
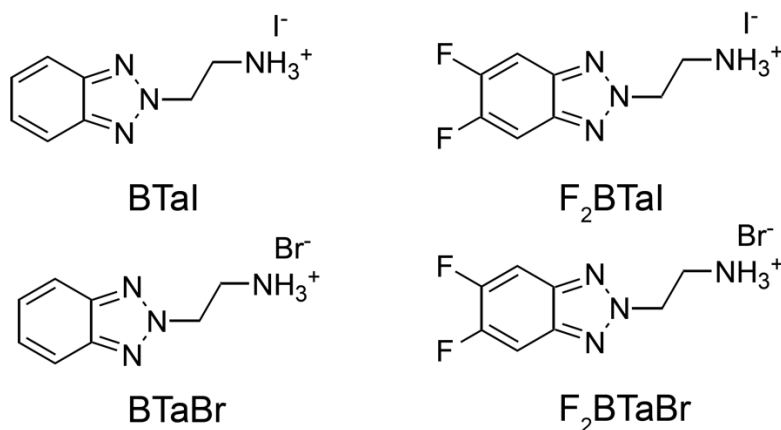
Figure 7.1. Chemical structure of benzotriazole derivatives used in this study.

To verify whether these synthesized benzotriazole salts can be used as organic cations to obtain 2D perovskites, we spin-coated thin films from precursor solutions containing a benzotriazole salt and PbI_2 or $PbBr_2$ in a 2:1 molar ratio. **Figure 7.2**a summarizes the optical properties of lead-based 2D perovskite thin films of two of the benzotriazole salts. Excitonic absorption peaks are located at 523 nm and 395 nm for $(BTa)_2PbI_4$ and $(BTa)_2PbBr_4$, respectively. Similar absorption peaks are reported for the fluorinated derivatives of the salts. These wavelengths match with typical literature values for 2D lead iodide and lead bromide perovskites,[25–27] which indicates that 2D perovskite self-assembly was successful with all salts. The UV-vis absorption spectra of $(BTa)_2PbI_4$ also clearly show excitations to higher Rydberg states at about 350 nm and 400 nm.[28] Additionally, below 320 nm the organic layer (benzotriazole unit) contributes to the absorption spectrum. The excitonic photoluminescence (PL) peaks are Stokes-shifted with respect to their corresponding absorption peaks, as expected.[24]

The PL spectra of $(BTa)_2PbI_4$ perovskite also shows a shoulder at longer wavelengths. The appearance of dual emission peaks for films of hybrid perovskites can arise from self-absorption effects and thin-film cavity effects *via* interference.[29,30] Following the work of Van der Pol *et al.*,[30] we investigated the influence of the perovskite film thickness by varying the spin coating speed, and found that the intensity ratio of the emission peaks indeed depends on the film thickness, with the long-wavelength shoulder becoming more pronounced for thicker films. This is a strong indication for cavity effects as the origin of the shoulder.[30]

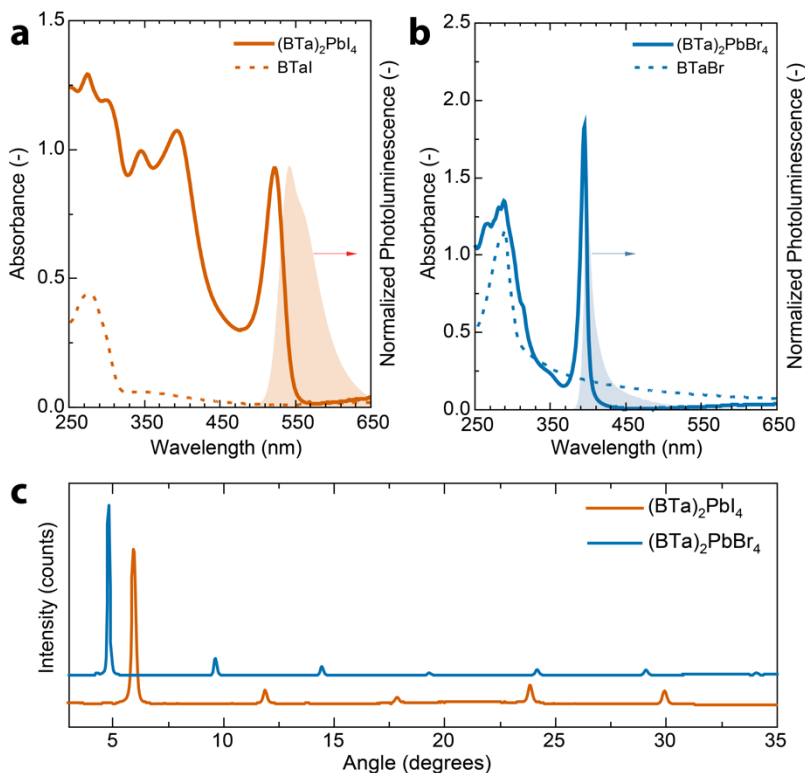**Figure 7.2.** (a) UV-vis absorption (solid line) and PL emission spectra (shaded area) of $(BTa)_2PbI_4$ (left) and $(BTa)_2PbBr_4$ (right). Dashed lines represent absorption spectra of BTaI and BTaBr salts. The PL emission spectra of $(BTa)_2PbI_4$ and $(BTa)_2PbBr_4$ were obtained with excitation at 430 nm and 300 nm, respectively. (b) XRD patterns of the same perovskites as in (a).

The phase purity of the perovskite thin films was studied by X-ray diffraction (XRD), which clearly shows the (00$2l$) reflections (l = 1–5 and 1–7) characteristic for a 2D perovskite grown with a preferential orientation of PbX_6 sheets parallel to the surface (Figure 7.2b).[31,32] By using Bragg's law and the position of the first-order reflections, a d-spacing between the sheets of 14.9 Å and 18.4 Å was calculated for $(BTa)_2PbI_4$ and $(BTa)_2PbBr_4$. Similar spacings of 15.0 Å and 18.7 Å were found for the 2D perovskites containing the fluorinated salts. To further elucidate the perovskite crystal structure, single crystals of all four perovskites were grown. Single crystals were obtained *via* an optimized solvent conversion-induced rapid crystallization method reported in the literature.[33] Single crystal structures are shown in **Figure 7.3**. Interestingly, the crystal structure of $(BTa)_2PbI_4$ (and $(F_2BTa)_2PbI_4$) contains organic bilayers of interdigitating benzotriazole cores, whereas $(BTa)_2PbBr_4$ (and $(F_2BTa)_2PbBr_4$) has an organic bilayer where the

benzotriazole cores of each part of the bilayer do not interdigitate, as is more frequently encountered in the literature for large organic cations.[25,27,34] In each case the d-spacing found in the thin-film XRD matches with the spacing between the PbX_6 sheets inferred from the single-crystal structure. For $(BTa)_2PbI_4$ and $(F_2BTa)_2PbI_4$ that both crystalize in the same orthorhombic space group, $d = b/2$, while for $(BTa)_2PbBr_4$ and $(F_2BTa)_2PbBr_4$ that crystallize in different monoclinic space groups, $d = a/2$ and $d = a$, respectively. This shows that crystal structure in the spin-coated films matches with that of the solution-grown single crystals. We hypothesize that the smaller size of the $PbBr_6$ octahedrons compared to PbI_6 precludes the interdigitation of the BTa and F_2BTa units in the unit cell.[27] A separate detailed structural study combined with computational modeling is ongoing to fully elucidate these aspects.
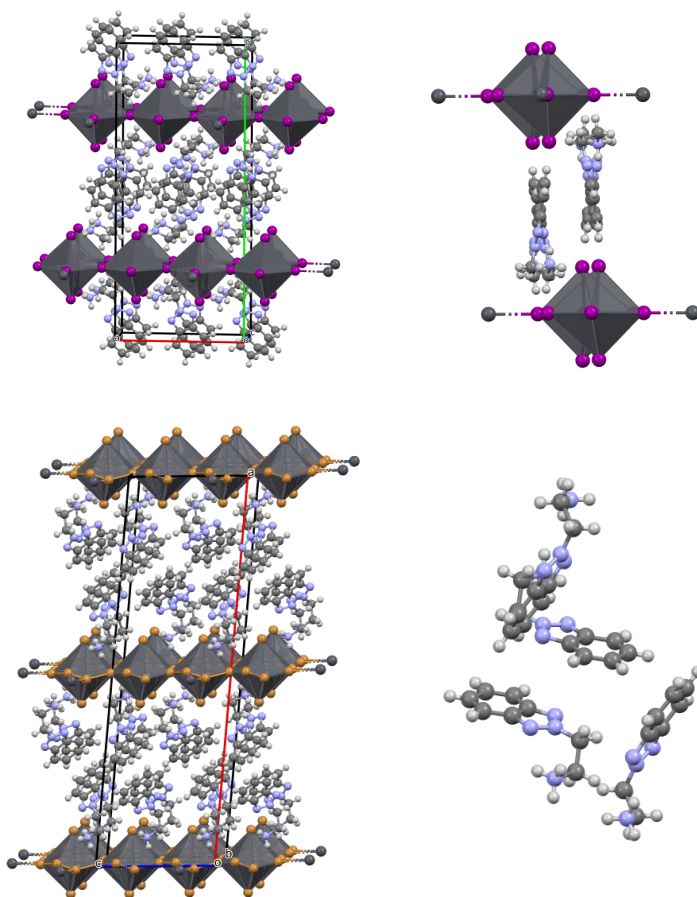

Figure 7.3. Packing arrangements of benzotriazole-based single crystals. The images on the left contain the unit cell of each arrangement; the images on the right show a detail of the packing of the organic layers. (top) $(BTa)_2PbI_4$ and (bottom) $(BTa)_2PbBr_4$. Color codes: black (Pb), purple (I), brown (Br), grey (C), white (H), blue (N), and yellow (F). Spacings (d) are:

$(BTa)_2PbI_4$ $b/2$ = 14.8 Å and $(BTa)_2PbBr_4$ $a/2$ = 18.6 Å. The fluorinated derivatives are almost equivalent to the correspondent non-fluorinated ones and not reported here.

7.3 PASSIVATION OF FAPbI₃ 3D PEROVSKITE

Once confirmed that the benzotriazole derivatives are suitable to form 2D perovskites, we employed these molecules as interlayers in solar cells in the *n-i-p* configuration with $FAPbI_3$ 3D perovskites as active layer. 2D perovskites at the perovskite/hole transport layer (HTL) interface should provide a passivation effect and lead to optimized band alignment, according to previous reports.[18] The device stack is illustrated in **Figure 7.4**a. On top of indium tin oxide (ITO) as transparent conductive oxide, a SnO_2 layer passivated by a monolayer of [6,6]-phenyl-C_{61}-butyric acid (PCBA) is used as electron-transport layer (ETL),[35] Spiro-OMeTAD is used as hole-transport layer (HTL), and a bilayer of MoO_3/Au as top contact. $FAPbI_3$ was processed according to a two-step spin coating procedure, where the deposition of a first layer of PbI_2 is followed by the organic components (formamidinium iodide (FAI) and methylammonium chloride (MACl)) and thermal annealing in air. The detailed procedures are described in the Methods section. Benzotriazole salts were spin-coated from solutions of 1 mg mL^{-1} and 10 mg mL^{-1} in 2-propanol, *i.e.*, concentrations commonly reported in the literature, onto $FAPbI_3$. All four benzotriazole derivatives (fluorinated, non-fluorinated, iodide or bromide anion) were used as passivation layer, with the BTaBr providing the best results in terms of solar cell performance and reproducibility. As a result, we decided to employ BTaBr for the rest of the study.
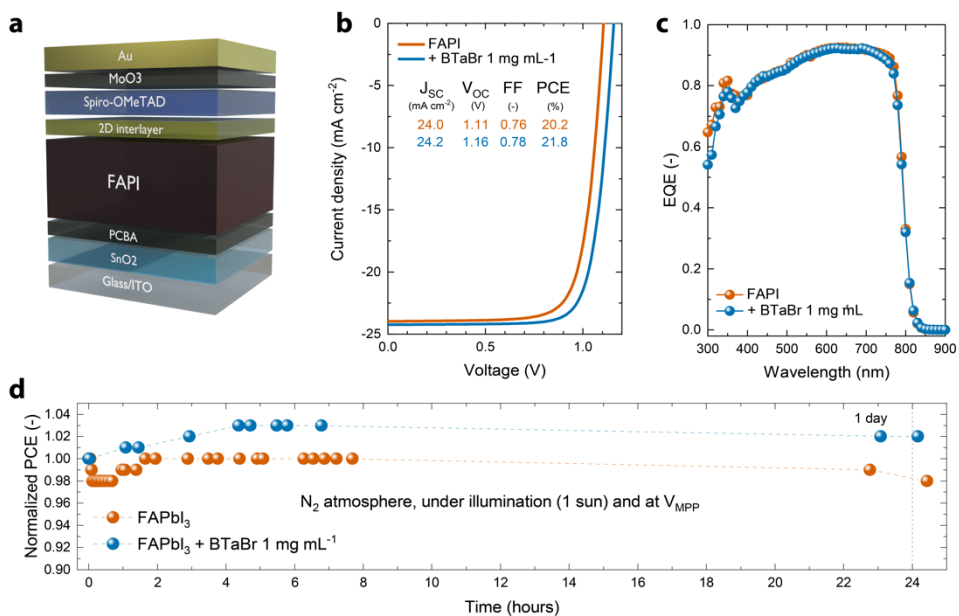
Figure 7.4. (a) Device stack for *n-i-p* perovskite solar cells used in this study. (b) *J-V* curves for FAPbI₃ solar cells without and with BTaBr (1 mg mL⁻¹) passivation. (c) EQE spectra for the same devices as in (b). (d) Stability measurement under N₂ atmosphere and under illumination at the maximum power point voltage (V_{MPP}) for the same devices as in (b) and (c).

As shown in the current-density/voltage ($J–V$) curves in Figure 7.4b, devices without passivation layer display good photovoltaic performances and reach 20.2% PCE in the champion device. Passivation of FAPbI₃ with diluted BTaBr (1 mg mL⁻¹) significantly enhances the V_{OC} of the devices from 1.11 to 1.16 V, and slightly improves the short-circuit current density (J_{SC}) and fill factor (FF). As summarized in **Table 1**, FAPbI₃ solar cells passivated with BTaBr reach a PCE of 21.8%. The improved performance of with BTaBr passivation is reproducible over several devices and statistically significant (one-sample *t*-test, *p*-value < 0.001). Based on this statistical data, average photovoltaic parameters are reported in Table 1. When BTaBr passivation is applied using more concentrated solutions (10 mg mL⁻¹), the solar cells show a critical loss in FF and overall worse photovoltaic performances because of poor charge extraction, for reasons that will be described below. We compared the photovoltaic performance of FAPbI₃ passivated with either BTaBr or PEAI, as a more conventional organic spacer, and observed a similar increase in V_{OC} compared to the reference device, but a slightly higher PCE because of enhanced FF when using BTaBr (FF = 0.76 for BTaBr and FF = 0.74 for PEA). Figure 7.4c shows the external quantum efficiency (EQE) spectra of the solar cells. All

devices possess a high EQE with peak values above 95% and an integrated current density (~24 mA cm^{-2}) that closely matches the one obtained *via J–V* measurements. The passivated device shows a slightly higher EQE compared to the reference. The EQE drops in the green region of the spectrum (below 550 nm), which prevents the devices from reaching J_{SC} > 25 mA cm^{-2} and PCE > 22%. We attribute this EQE loss, at least in part, to absorption by the ITO bottom electrode.

A preliminary study of the stability of the solar cells under illumination held at maximum power point voltage (V_{MPP}) is shown in Figure 7.4d. Cells with and without passivation are stable under ~24 h continuous illumination. FAPbI$_3$ retained 98% of the initial PCE, whereas FAPbI$_3$ + BTaBr 1 mg mL^{-1} was slightly more efficient (by about 4%) than at the beginning of the measurement.

Table 1. Photovoltaic parameters of non-passivated and BTaBr-passivated FAPbI$_3$ solar cells with device layout ITO/SnO$_2$/PCBA/FAPbI$_3$/Passivation layer/Spiro-OMeTAD/MoO$_3$/Au. Average values are in parenthesis (N = 10 and N = 17 for reference device and passivated with BTaBr 1 mg mL^{-1}, respectively). For the 10 mg mL^{-1} BTaBr passivation no statistics are reported as few devices were fabricated.

Passivation	J_{SC} (mA cm^{-2})	V_{OC} (V)	FF (-)	PCE (%)
None	24.00 (24.05)	1.11 (1.03)	0.76 (0.78)	20.2 (19.4)
BTaBr 1 mg mL^{-1}	24.16 (24.20)	1.16 (1.10)	0.78 (0.78)	21.8 (20.6)
BTaBr 10 mg mL^{-1}	23.80	1.11	0.60	15.8

7.4 PASSIVATION EFFECT OF BENZOTRIAZOLE BROMIDE

The V_{OC} = 1.16 V of the best BTaBr-passivated FAPbI$_3$ solar cells represents 91% of the radiative limit (1268 mV based on a bandgap of 1.55 eV, calculated *via* inflection point in EQE), indicating small non-radiative losses. To elucidate the effect of the passivation layer on the V_{OC}, we employed absolute photoluminescence (PL) measurements to evaluate differences in the quasi-Fermi level splitting (QFLS) between non-passivated and passivated FAPbI$_3$ films. The QFLS of the non-passivated films is 1161 mV ± 8 mV, *i.e.,* ~100 mV below the radiative limit (1268 mV based on a bandgap of 1.54 eV) (**Figure 7.5**a). Passivation by BTaBr leads to a small increase (~ 4 mV) of the QFLS to 1165 mV ± 7 mV. The enhancement in QFLS is less than the increase in average V_{OC} measured in devices (~70 mV, Table 1). This suggests that the enhanced V_{OC} might also be related to passivation of the perovskite/HTL interface, rather than of the perovskite film itself. To confirm this, we measured the QFLS and V_{OC} of full devices with and without passivation and tracked such quantities over time (Figure 7.5b). The time tracking was necessary because when measuring perovskite/Spiro-OMeTAD films, the absolute PL signal becomes

time-dependent and the peaks in the first few seconds, to then stabilize at a lower value. By tracking QFLS and V_{OC}, we observed a significant increase of both quantities for the passivated devices by about ~20 mV (QFLS) and ~15 mV (V_{OC}). This suggests that BTaBr can have important passivation properties at the perovskite/HTL interface, in agreement with the consistent increase in V_{OC} observed in the solar cells.
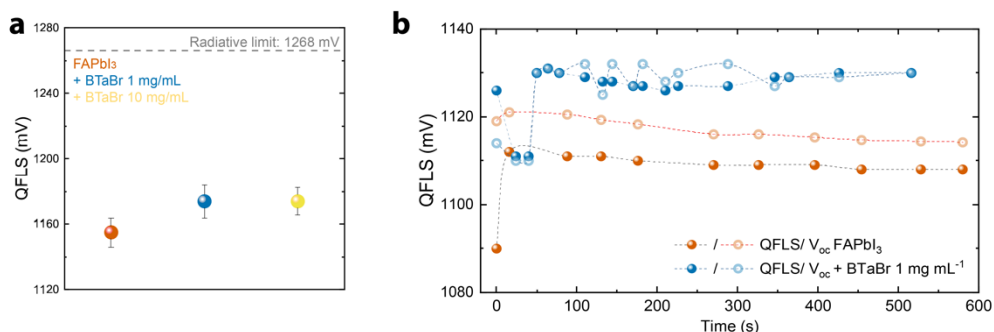

Figure 7.5. (a) The QFLS calculated from absolute PL for neat perovskite films with and without passivation. (b) Time-dependent QFLS and V_{OC} for full devices without and with diluted BTaBr passivation.

To further investigate the passivation effect of BTaBr, we employed scanning-electron microscopy cathodoluminescence (SEM-CL) hyperspectral imaging (**Figure 7.6**a–f). First, merely from a morphology point of view, new crystallites appear on the surface of FAPbI$_3$ after passivation with diluted BTaBr (Figure 7.5a–b). No closed interlayer seems to be formed. Figures 7.6c–d display the 3D perovskite CL emission intensity maps for the 3D perovskite FAPbI$_3$, bandpass filtered at 800 nm ± 10 nm, before and after passivation with diluted BTaBr. For comparison, PbI$_2$ emission mapping (using a bandpass filter at 520 nm ± 10 nm) is shown in Figure 7.6e–f. Both CL hyperspectral maps were acquired under the same conditions, so in each image a more saturated coloring indicates stronger CL. Figure 7.6c–d indicates that before passivation FAPbI$_3$ exhibits a low and inhomogeneous CL emission intensity with most grains being relatively non emissive, and few displaying bright CL emission, sometimes in the proximity of PbI$_2$ grains. After passivation, the 3D perovskite CL emission becomes ~1.5 to 3 times brighter. Additionally, the grain boundaries display stronger emission compared to the non-passivated film. Such an increase of emission, both intra-grain and at grain boundaries after passivation, is in agreement with other reports.[36]
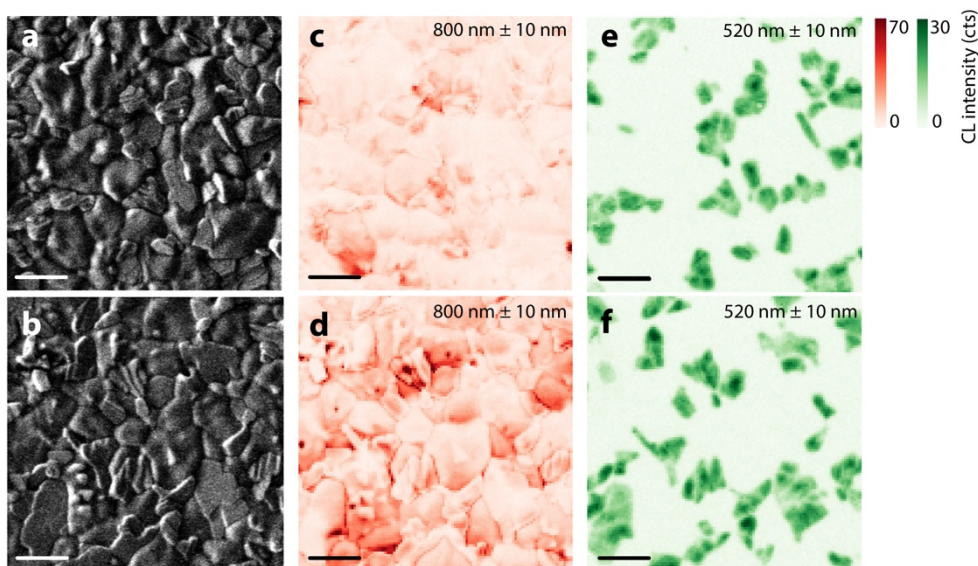
Figure 7.6. (a-b) SEM images of FAPbI$_3$ (c) and FAPbI$_3$ + BTaBr (1 mg mL^{-1}) (d). (c-d) CL emission intensity as shown in the SE images in (a-b). Wavelength of emission is filtered at 800 nm ± 10 nm (c-d) and 520 ± 10 nm (e-f) to visualize emission from 3D perovskite and PbI$_2$, respectively. Scalebar is 1 µm for all images.

Interestingly, for both non-passivated and passivated films, the grain boundaries do not seem to represent a location with enhanced non-radiative recombination, but instead show a relatively high CL emission. This is likely because morphology affects the CL intensity and rougher surfaces (*i.e.*, sharp grain boundaries) can result in brighter CL emission. Just as observed in FAPbI$_3$, also the passivated layer displays a relatively high PbI$_2$ emission, and sometimes it appears that the perovskite emission is stronger at the boundary between perovskite and PbI$_2$. To demonstrate this, we analyzed a passivated perovskite film with higher magnification and found that emission from the 3D perovskite is indeed brighter when the signal overlaps with PbI$_2$ emission, which might suggest a passivation effect from PbI$_2$ itself (**Figure 7.7**). The overlap of signals at 800 nm (FAPbI$_3$) and 520 nm (PbI$_2$) is dictated by the fact that SEM-CL can detect emission not only from the surface, but up to a penetration depth of ~60 nm (at 3 kV electron acceleration voltage), meaning that perovskite crystals under PbI$_2$ superficial grains can be measured.
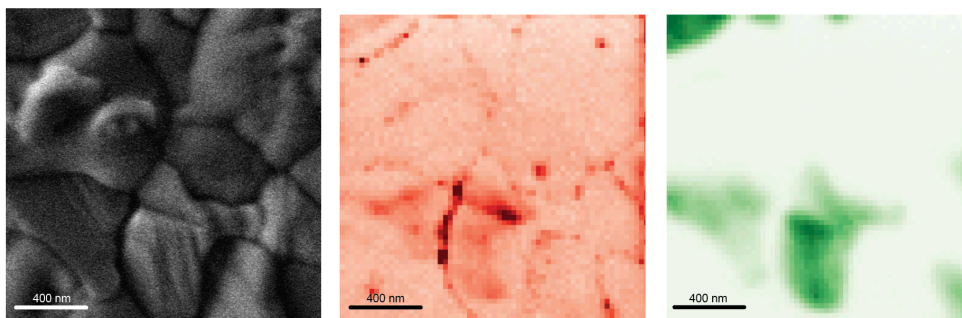
Figure 7.7. SEM-CL image of FAPbI$_3$ + BTaBr 1 mg mL^{-1} at high magnification: SEM image (left), perovskite emission 800 nm ± 10 nm (center), PbI$_2$ emission ± 10 nm (right).
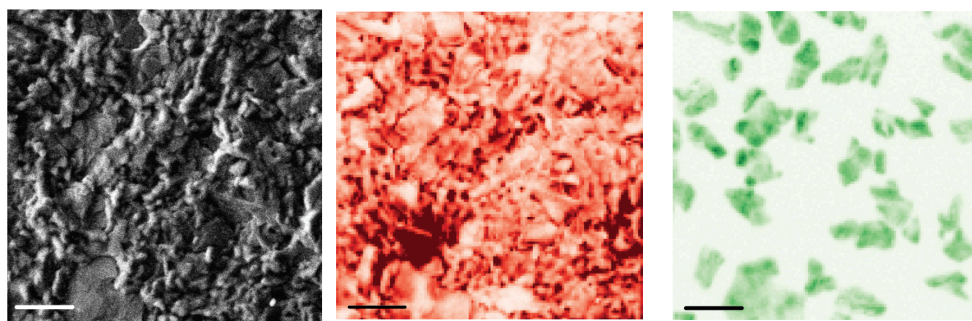
Figure 7.8. SEM-CL image of FAPbI$_3$ + BTaBr 10 mg mL^{-1}: SEM image (left), perovskite emission ~800 nm (center), PbI$_2$ emission ~520 nm (right). Scalebars are 1 µm.

With regard to FAPbI$_3$ passivated with concentrated BTaBr, despite a drastic morphology change because of the presence of a relatively thick 2D interlayer, we could again identify only bright 3D perovskite emission and emission from PbI$_2$ grains (**Figure 7.8**) In all films, no emission from the 2D perovskite phases could be detected. This could be caused by efficient charge or energy transfer mechanism from 2D to 3D phase, which leads to only emission at ~800 nm being observed. No signs of beam-induced damage from the 2D emission were detected either. Nevertheless, both QFLS and SEM-CL suggest that BTaBr has a passivating effect, which reduces non-radiative recombination and leads to stronger CL and PL emission and, as a result, an enhanced V_{OC}.

7.5 2D/3D HETEROSTRUCTURE

Having established the improvement of solar cell performance after 2D passivation, we aimed to characterize in detail the perovskite/BTaBr heterostructure. To do so, we first employed PL spectroscopy. Emission peaks at 530 and 570 nm,

corresponding to 100%-iodide $n = 1$ (2D, $(BTa)_2PbI_4$) and $n = 2$ (quasi-2D, $(BTa)_2FAPb_2I_7$) phases, were observed after spin coating diluted BTaBr (1 mg mL^{-1}) on top of $FAPbI_3$ (**Figure 7.9**a). Hence, despite the use of the bromide salt for passivation, only PL from an iodide-based 2D perovskite was observed. In contrast, $FAPbI_3$ films passivated with concentrated BTaBr (10 mg mL^{-1}) did not display such emission peaks, indicating that no iodide-based 2D or quasi-2D perovskite phases were formed in this case. By analyzing the PL emission spectra at shorter wavelengths (Figure 7.9b), however, we could identify an emission peak at about 400 nm, which corresponds to $(BTa)_2PbBr_4$, as shown in Figure 7.2a. The main, 3D perovskite emission peak is located at 820 nm, which represents a bandgap energy (E_g) of 1.51 eV, in line with the bandgap of 1.55 eV obtained *via* EQE.

The XRD patterns of the 3D $FAPbI_3$ perovskite, without or with BTaBr passivation, show reflections at $2\theta = 14$ and 28° corresponding to α-$FAPbI_3$ (110) and (220) planes (Figure 7.9c). Small reflections at $2\theta = 11.5°$ demonstrate the presence of negligible amounts of δ-$FAPbI_3$, whereas the reflection at $2\theta = 12.7°$ represents PbI_2 and dominates the whole diffractogram. The XRD pattern of the $FAPbI_3$/BTaBr heterostructure showed no reflections at 2θ angles lower than 10°, which are representative of the lower dimensional perovskites, after passivation with the diluted salt (Figure 7.9c). It is plausible that the amount of 2D perovskite phase present on these films is too small to be detected using XRD, which is less sensitive than absorption and photoluminescence spectroscopy to small amounts of low-dimensional perovskite present in a thin film.[34] On the other hand, a peak at $2\theta = 4.8°$ appeared after passivation with concentrated BTaBr. This peak corresponds to the $(BTa)_2PbBr_4$ phase (Figure 7.2b).
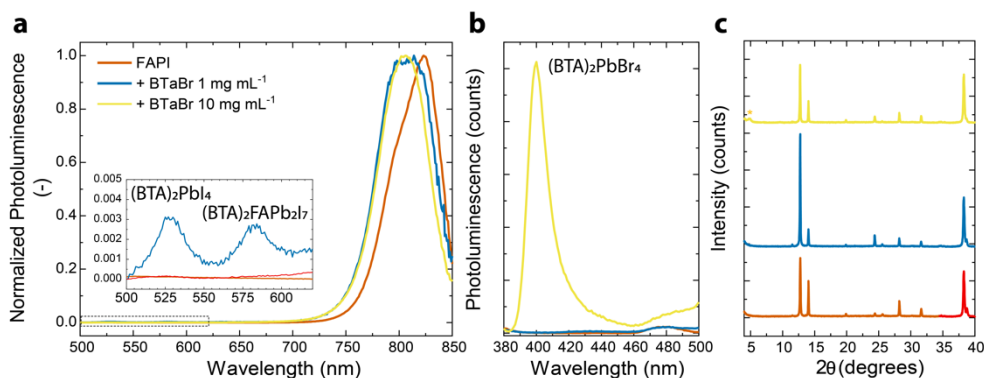

Figure 7.9. (a) PL emission spectra before and after passivation of $FAPbI_3$ with BTaBr at different concentrations (1 and 10 mg mL^{-1}). Inset is same plot but zoomed-in between 500 and 620 nm. (b) Same PL emission spectra as (a), but at lower wavelengths. (c) XRD patterns for the same films as in (a). The asterisk indicates $(BTa)_2PbBr_4$ diffraction peak.

Based on the combination of PL and XRD, we hypothesize that BTaBr first reacts with excess PbI$_2$ or replaces FA from FAPbI$_3$ on the surface to form (BTa)$_2$PbI$_4$, as seen after passivation with the diluted benzotriazole salt. Then, when the concentration of the passivating agent increases, an excess of Br ions replaces I, forming a 100%-Br 2D perovskite structure on top of the 3D perovskite. The presence of Br on the surface is further confirmed by X-Ray photoelectron spectroscopy (XPS), which shows a higher amount of Br with increasing concentration of the passivation salt (Table 2).

To gain more information on the 2D/3D heterostructure and on the presence of PbI$_2$ detected through XRD (Figure 7.9c), we employed angle-resolved grazing-incidence wide-angle X-ray scattering (AR-GIWAXS). The GIWAXS pattern of the FAPbI$_3$ films (**Figure 7.10**a) shows an intense Bragg spot at $q_z = 0.9$ Å^{-1} in the out-of-plane direction, corresponding to PbI$_2$ crystallites with a significant degree of preferential orientation, consistent with the strong reflection at $2\theta = 12.7°$ in the diffractogram shown in Figure 7.9c. Hence, the intense peak of PbI$_2$ in the diffractogram is a consequence of preferential orientation and not only abundance. In contrast, the ring at $q = 1$ Å^{-1} shows that FAPbI$_3$ crystallites are mostly randomly oriented, although a certain degree of preferential orientation is present, as indicated by the higher intensity at about −45, 0, and 45° with respect to q_z. Passivation with dilute BTaBr does not give rise to additional features compared to the reference film, in agreement with XRD.
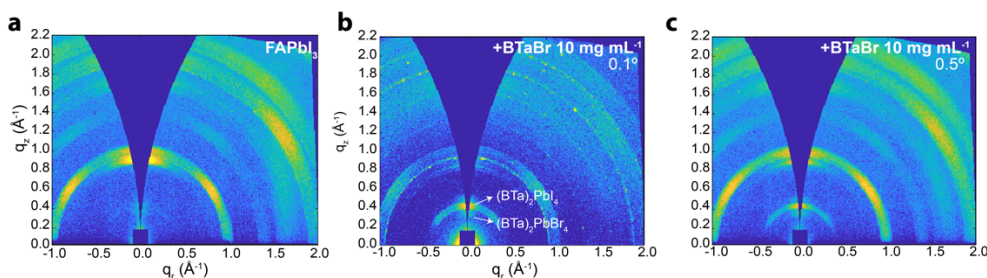
Figure 7.10. GIWAXS 2D pattern for (a) FAPbI$_3$ (b) FAPbI$_3$ + BTaBr 10 mg/mL, 0.1° incidence angle, and (c) FAPbI$_3$ + BTaBr 10 mg mL^{-1}, 0.5° incidence angle.

Angle-resolved GIWAXS allows to characterize the film at different depths, as the penetration of the X-rays in the film is dependent on the angle of incidence. We performed such a measurement on FAPbI$_3$ passivated with concentrated BTaBr. AR-GIWAXS with 0.1° incidence angle (probing the very top surface of the film) displays a Bragg spot at $q_z = 0.45$ Å^{-1} and a less intense one at 0.35 Å^{-1} (Figure 7.10b). These peaks likely correspond to a I- and Br-rich 2D perovskite, respectively. It is unclear why we can discern both I- and Br-rich 2D perovskite *via* GIWAXS, whereas both

XRD and PL hinted at the presence of only $(BTa)_2PbBr_4$. A possible explanation could be the presence of a more complex heterostructure, described as $FAPbI_3/(BTa)_2PbI_4/(BTa)_2PbBr_4$. In such a case, the I-based 2D interlayer would likely not be visible in the PL because of efficient energy transfer to 3D, but visible *via* GIWAXS. The main spot at 0.45 $Å^{-1}$ resembles a half-ring, indicating that the 2D crystals possess a certain degree of disorder with random orientation along the q_z plane. By increasing the incidence angle (until 0.5°, at which the whole film thickness is probed), the abovementioned PbI_2 and $FAPbI_3$ peaks appear as in the reference film (Figure 7.10c). This is in line with the presence of a superficial 2D perovskite layer on top of $FAPbI_3$.

7.6 INTERLAYER CHARACTERIZATION

We further characterized the heterostructure *via* XPS. First, we quantified the atomic concentrations of the elements composing the perovskite layer. As displayed in Table 2, the concentration of carbon (C) and nitrogen (N) at the surface increases with increasing BTaBr concentration. This indicates the presence of passivating molecules on the perovskite surface. Similarly, the bromine (Br) concentration increases from 1.2 at% to 5.7 at%, indicating a Br-richer surface, ideally because of the replacement of iodine (I) from $(BTa)_2PbI_4$ and conversion to $(BTa)_2PbBr_4$, as described above. As expected, the iodine concentration decreases with increasing passivation.

Table 2. Atomic concentrations obtained by XPS for $FAPbI_3$ without and with 2D interlayer passivation.

Atomic conc.	Pb	N	C	I	Cl	Br
$FAPbI_3$	9.6	20.4	18.5	48.5	1.7	1.2
+ BTaBr 1 mg mL^{-1}	5.1	23.8	40.8	24.5	5.0	0.7
+ BTaBr 10 mg mL^{-1}	1.60	27.8	57.0	6.0	1.7	5.7

By analyzing the N $1s$ spectrum and its depth profile, obtained *via* argon ion sputtering at low rates to avoid loss of features in the spectra (see Methods for more details), we gained more information on the formation of a 2D perovskite layer on top of the 3D one. First, non-passivated $FAPbI_3$ shows a single peak slightly above 400 eV for N $1s$ (Figure 7.11a). Then, once BTaBr is spin coated onto the 3D layer, the films display a double peak in the same region. Here, the peak at ~400 eV contains the contributions from both $FAPbI_3$ and BTaBr, whereas the higher energy peak at ~402 eV is only related to BTaBr. In pure BTaBr, the ratio between the low- and high-

energy peaks is equal to 1.2, whereas it goes from 1.9 to 1.2 in the case of BTaBr 1 mg mL^{-1} and 10 mg mL^{-1} deposited onto FAPbI$_3$, respectively. These results indicate that BTaBr is present in both cases on top of the 3D perovskite but in different amounts. It seems that the XPS signal in the case of BTaBr 10 mg mL^{-1} originates prevalently from the 2D interlayer, whereas for the diluted BTaBr salt there is a significant contribution from FAPbI$_3$ as well. Since XPS is a surface-sensitive technique, we speculate that after spin coating diluted BTaBr onto FAPbI$_3$, the passivation layer might be either not closed or in the order of a few nm in thickness, thin enough to pick up signals from the underlying perovskite layer. On the contrary, when passivating with concentrated BTaBr, mostly the 2D layer is probed, indicating the formation a much thicker interlayer that would negatively affect charge transport, as is indeed observed in the FF loss in the solar cells performance.
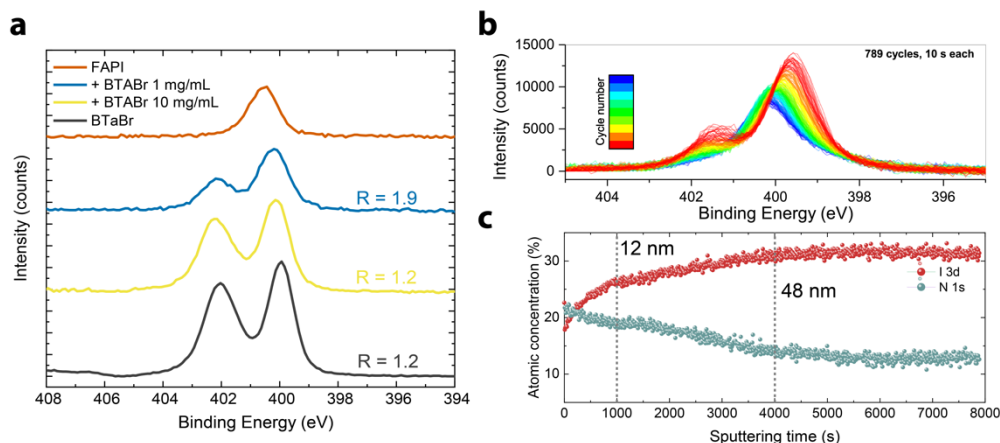
Figure 7.11. (a) N 1s XPS spectra for non-passivated and passivated FAPbI$_3$ films, and for pure BTaBr. (b) Depth-profile N 1s XPS spectra for FAPbI$_3$ + BTaBr 1 mg mL^{-1}. (c) Atomic concentration variation for the same film as in (b).

The depth profile gives additional valuable information on such an interlayer. After passivation with BTaBr 1 mg mL^{-1}, the high-energy peak related to BTaBr decreases with increasing sputtering time, in line with a gradual removal of the passivation layer (Figure 7.11b). The low-energy peak, related to perovskite and BTaBr, shifts to higher binding energy over time and becomes equivalent to the one of pure FAPbI$_3$. Again, this seems to indicate the presence of a rather thin film of BTa-based 2D perovskite or only sparse 2D crystallites on the surface, which would corroborate what was observed in SEM images.

By analyzing the atomic concentration variation of the sample with 1 mg mL^{-1} passivation, we found that the concentrations of iodine increase and those of nitrogen decrease over sputtering time (Figure 7.11c). In comparison, the

concentrations of I and N are stable in the reference film. The atomic concentration of nitrogen seems to follow three regimes, where first it decreases sharply, then linearly, and finally it stabilizes and remains constant. In the first regime (till ~ 1000 s sputtering time), the concentration of BTaBr molecules decreases fast, indicating direct removal of the interlayer. In the second regime (till ~ 4000 s), the concentration of nitrogen decreases more gradually; this might indicate that BTaBr molecules penetrate the perovskite bulk, possibly forming $(BTa)_2FAPb_2I_7$, and such a removal is slower and happens together with the sputtering of the 3D perovskite layer. Finally, in the final regime, the concentration becomes constant, which indicates the presence of a conventional $FAPbI_3$ layer. We additionally measured the thickness of the sputtered area after ~ 790 cycles of 10 s *via* a profilometer and found the thickness to be 93 nm. The etching rate on the perovskite was thus calculated as 0.012 nm s^{-1}. With this information, we calculated that the 2D interlayer is in the order of 12 nm, whereas the penetration of the BTaBr molecules goes as deep as ~ 48 nm.

For $FAPbI_3$ passivated with BTaBr 10 mg mL^{-1}, the two N 1s peaks are still visible even with rougher sputtering conditions and indicate the presence of a thicker 2D interlayer (**Figure 7.12**). The same rougher sputtering conditions for $FAPbI_3$ + BTaBr 1 mg mL^{-1} removed all BTaBr molecules after only one cycle. This confirms the presence of a much thicker 2D interlayer when passivating with concentrated BTaBr.
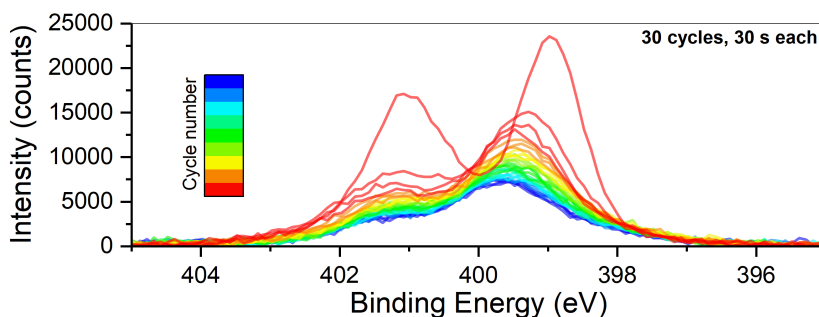
Figure 7.12. Depth-profile N 1s XPS spectra for $FAPbI_3$ + BTaBr 10 mg mL^{-1}. 30 cycles (30 s sputtering each).

7.7 CONCLUSIONS

In conclusion, we introduced a novel benzotriazole-based cation to form 2D and quasi-2D perovskites and showed that it is beneficial to passivate the surface of $FAPbI_3$ perovskite with such a cation to enhance solar cells parameters. A solar cell based on $FAPbI_3$ passivated with an optimal amount of BTaBr reached almost 22% PCE. Mainly, V_{OC} increase is behind enhancement of photovoltaic performance. By

using QFLS and SEM-CL, we demonstrated that BTaBr indeed passivates FAPbI$_3$ and reduces non-radiative recombination at the perovskite/HTL interface. With a variety of characterization methods, we provided insights into the formation of a 2D interlayer. We showed that 2D perovskites, either iodide- or bromide-based are formed even with low amounts of spacers, but the nature of the resulting layer can vary. Low concentration of the 2D spacer leads to the formation of iodide-based 2D and quasi-2D perovskites. It is likely that such a low concentration does not lead to the formation of a closed 2D interlayer, but rather results in sparse crystallites of 2D perovskites being formed on the surface of the 3D perovskite, which are still beneficial to reduce non-radiative recombination and enhance device performance. With increasing concentration of BTaBr, a thicker 2D, bromide-based perovskite layer is formed, which is detrimental for charge extraction. With this study, further knowledge on the formation of 3D/2D heterostructures is developed. Furthermore, the easy-to-functionalize nature of benzotriazole cations suggests that such spacers could pave the way to functionalized 2D interlayers that could push the efficiency and stability of perovskite solar cells even further.

7.8 METHODS

Synthesis of benzotriazole derivatives

Materials. All commercial chemicals and solvents were used without additional purification steps unless stated otherwise. 1,2-diamino-4,5-difluorobenzene (98%), *N*-Boc-ethanolamine, triphenylphosphine, and HBr (48% in water) were purchased from Fluorochem. Triphenylphosphine was recrystallized from methanol before use. 1H-Benzotriazole (99%) was purchased from Alfa Aesar. Di-2-methoxyethyl azodicarboxylate (DMEAD) (≥90%) and sodium nitrite were purchased from Sigma-Aldrich. HI (57% in water, distilled, unstabilized) and tri-n-butyl phosphate (>99%) were purchased from Acros Organics. All solvents were purchased from Fisher Scientific.

2-(2H-benzo[d][1,2,3]triazol-2-yl)ethylamine, Boc protected (2). Boc-ethanolamine (4.5 g, 27.7 mmol) was weighed in a flame-dried 3-neck round-bottom flask; then 1H-Benzotriazole (**1**) (3.0 g, 25.2 mmol), triphenylphosphine (7.3 g, 27.7 mmol), and dry diethyl ether (60 mL) were added. The dispersion was brought under Ar atmosphere and cooled to 0 °C. DMEAD (6.5 g, 27.7 mmol) was dissolved in 30 mL dry diethyl ether and was added dropwise to the reaction mixture. After DMEAD had been added completely, the reaction mixture was slowly brought back to ambient temperature. After 18 h the reaction mixture was extracted with water, and the water fractions were combined and extracted with diethyl ether. The combined ether fractions were dried and filtered, and the solvent was evaporated under reduced pressure. The resulting crude product was purified by column chromatography with gradient elution from DCM to DCM/EtOAc 9:1 to obtain **2** as a white solid (3.63 g, 55% yield).). ¹H NMR (400 MHz, Chloroform-*d*) δ 7.89 – 7.81 (m, 2H), 7.41 – 7.35 (m, 2H), 5.11 (s, 1H), 4.86 –

4.78 (m, 2H), 3.85 (q, J = 5.8 Hz, 2H), 1.41 (s, 9H). ^{13}C NMR (101 MHz, Chloroform-*d*) δ 155.79, 144.51, 126.57, 118.10, 79.89, 56.49, 40.11, 28.41. GC-MS: *m*/*z* = 262. Boc-protected 2-(1*H*-benzo[*d*][1,2,3]triazol-1-yl)ethylamine (asymmetrically alkylated benzotriazole) was also obtained as a side product. ^{1}H NMR (400 MHz, Chloroform-*d*) δ 7.98 (d, *J* = 8.4 Hz, 1H), 7.53 (d, *J* = 8.4 Hz, 1H), 7.45 (ddd, *J* = 8.2, 6.8, 1.0 Hz, 1H), 7.33 (ddd, *J* = 8.0, 6.7, 1.1 Hz, 1H), 4.98 (t, *J* = 6.1 Hz, 1H), 4.74 (t, *J* = 5.8 Hz, 2H), 3.70 (q, *J* = 5.9 Hz, 2H), 1.38 (s, 9H).

2-(2H-benzo[d][1,2,3]triazol-2-yl)ethylammonium iodide (BTaI). HI (57%, unstabilized) was extracted three times with a 9:1 mixture of chloroform and tributyl phosphate to remove impurities. 1.11 mL (8.39 mmol) of this freshly extracted HI was then added with a micropipette to a solution of **2** (1.010 g, 3.81 mmol) in dioxane (25 mL), upon which the color of the mixture changed from colorless to yellow. The reaction mixture was flushed with Ar and was left to react at ambient temperature in the dark for 15 h. The mixture was then concentrated under reduced pressure, and the resulting solid was sonicated with diethyl ether, filtered, and washed several times with diethyl ether. BTaI was obtained as a white solid (1.095 g, 98% yield) and was dried under high vacuum. ^{1}H NMR (400 MHz, DMSO-*d*$_6$) δ 8.04 – 7.87 (m, 5H), 7.48 – 7.40 (m, 2H), 5.02 – 4.94 (m, 2H), 3.56 – 3.48 (m, 2H). ^{13}C NMR (101 MHz, DMSO-*d*$_6$) δ 144.49, 127.26, 118.49, 53.85, 38.99.

2-(2H-benzo[d][1,2,3]triazol-2-yl)ethylammonium bromide (BTaBr). **2** (1.000 g, 3.81 mmol) was dissolved in dioxane (25 mL), after which HBr (48%, 949 μL, 8.39 mmol) was added with a micropipette. The mixture was flushed with Ar and was left to react at ambient temperature for 17 h, during which a precipitate formed. The mixture was then concentrated under reduced pressure, sonicated in diethyl ether, filtered, and washed several times with diethyl ether to yield BTaBr as a white powder (0.890 g, 96% yield), which was dried under high vacuum. ^{1}H NMR (400 MHz, DMSO-*d*$_6$) δ 7.97 (s, 3H), 7.95 – 7.89 (m, 2H), 7.48 – 7.41 (m, 2H), 5.03 – 4.94 (m, 2H), 3.56 – 3.48 (m, 2H). ^{13}C NMR (101 MHz, DMSO-*d*$_6$) δ 144.49, 127.23, 118.48, 53.72, 38.88.

5,6-difluoro-1H-benzo[d][1,2,3]triazole (4). **3** (2.992 g, 20.8 mmol) was dispersed in water (100 mL) and acetic acid (2.4 mL, 42.0 mmol) and was heated under reflux. The mixture was then filtered over a glass filter; the filtrate was slowly cooled down to ambient temperature and was subsequently put in the fridge (5 °C). Meanwhile, sodium nitrite (1.674 g, 24.3 mmol) was dissolved in water (40 mL), and the resulting solution was also put in the fridge. After both solutions had been at 5 °C for 1 h, the sodium nitrite solution was poured into the diamine solution at 5 °C, after which it was slowly brought back to ambient temperature. A precipitate formed, which was filtered off after 1 h. This solid was recrystallized from water and dried under high vacuum to yield **4** as an orange solid (2.45 g, 76% yield). ^{1}H NMR (400 MHz, DMSO-*d*$_6$) δ 15.97 (s, 1H), 8.10 – 7.97 (m, 2H). ^{13}C NMR (101 MHz, DMSO-*d*$_6$) δ 149.67 (dd, *J* = 245.6, 16.7 Hz), 134.99, 102.83. ^{19}F NMR (376 MHz, DMSO-*d*$_6$) δ –137.39. GC-MS: *m*/*z* = 155.

2-(5,6-difluoro-2H-benzo[d][1,2,3]triazol-2-yl)ethylamine,   Boc   protected   (5).   Boc-ethanolamine (1.203 g, 7.46 mmol) was weighed in a flame-dried 3-neck round-bottom flask,

then **4** (1.034 g, 6.67 mmol) and triphenylphosphine (1.957 g, 7.46 mmol) were added. Dry diethyl ether (70 mL) was subsequently added, and the resulting dispersion was sonicated for 1 min to break down **3** to a fine powder. The dispersion was then brought under Ar atmosphere and cooled to 0 °C. DMEAD (1.747 g, 7.46 mmol) was dissolved in a small amount of dry diethyl ether and was added dropwise to the reaction mixture. After DMEAD had been added completely, the reaction mixture was slowly brought back to ambient temperature. The dispersion became a clear solution after about 10 min. After 18 h the reaction mixture was extracted with water, and the water fractions were combined and extracted with diethyl ether. The combined ether fractions were dried and filtered, and the solvent was evaporated under reduced pressure. The resulting crude product was purified by column chromatography with gradient elution from DCM/EtOAc 9:1 to 8:2 to obtain **5** as an off-white solid (1.220 g, 61% yield). Boc-protected 2-(5,6-difluoro-1H-benzo[d][1,2,3]triazol-1-yl)ethylamine (asymmetrically alkylated benzotriazole) was also obtained as a side product (0.230 g, 12% yield). ^{1}H NMR (400 MHz, Chloroform-d) δ 7.58 (t, J = 8.4 Hz, 2H), 4.98 (s, 1H), 4.84 – 4.72 (m, 2H), 3.81 (q, J = 5.8 Hz, 2H), 1.40 (s, 9H). ^{13}C NMR (101 MHz, Chloroform-d) δ 155.74, 151.47 (dd, J = 252.4, 19.2 Hz), 140.23 (t, J = 5.9 Hz), 104.19 – 103.33 (m), 80.01, 56.64, 40.06, 28.38. ^{19}F NMR (376 MHz, Chloroform-d) δ –133.17 (t, J = 8.4 Hz). GC-MS: m/z = 298.

2-(5,6-difluoro-2H-benzo[d][1,2,3]triazol-2-yl)ethylammonium iodide (F$_2$BTaI). HI (57%, unstabilized) was extracted three times with a 9:1 mixture of chloroform and tributyl phosphate to remove impurities. 778 μL (5.90 mmol) of this freshly extracted HI was then added with a micropipette to a solution of **5** (0.797 g, 2.68 mmol) in dioxane (10 mL), upon which the color of the mixture changed from yellow to orange. The reaction mixture was flushed with Ar and was left to react at ambient temperature in the dark for 15 h. The mixture was then concentrated under reduced pressure, and the resulting solid was sonicated with diethyl ether, filtered, and washed several times with diethyl ether. F$_2$BTaI was obtained as a pale-yellow solid (0.863 g, 99% yield) and was dried under high vacuum. ^{1}H NMR (400 MHz, DMSO-d_6) δ 8.07 (t, J = 8.9 Hz, 2H), 7.91 (s, 3H), 5.01 – 4.90 (m, 2H), 3.53 – 3.45 (m, 2H). ^{13}C NMR (101 MHz, DMSO-d_6) δ 151.06 (dd, J = 249.2, 19.4 Hz), 140.52 (t, J = 6.2 Hz), 105.32 – 104.64 (m), 54.29, 39.10. ^{19}F NMR (376 MHz, DMSO-d_6) δ –134.36 (t, J = 8.9 Hz).

2-(5,6-difluoro-2H-benzo[d][1,2,3]triazol-2-yl)ethylammonium bromide (F$_2$BTaBr). **5** (0.498 g, 1.67 mmol) was dissolved in dioxane (10 mL), after which HBr (48%, 417 μL, 3.69 mmol) was added with a micropipette. The mixture was flushed with Ar and was left to react at ambient temperature for 21 h, during which the color changed from yellow to orange and a precipitate formed. The mixture was then concentrated under reduced pressure, sonicated in diethyl ether, filtered, and washed several times with diethyl ether to yield F$_2$BTaBr as an off-white powder (0.460 g, 99% yield), which was dried under high vacuum. ^{1}H NMR (400 MHz, DMSO-d_6) δ 8.10 (t, J = 8.9 Hz, 2H), 7.94 (s, 3H), 5.00 – 4.94 (m, 2H), 3.53 – 3.46 (m, 2H). ^{13}C NMR (101 MHz, DMSO-d_6) δ 150.90 (dd, J = 249.2, 19.3 Hz), 140.36 (t, J = 6.2 Hz), 105.15 – 104.41 (m), 54.00, 38.83. ^{19}F NMR (373 MHz, DMSO-d_6) δ –134.36 (t, J = 8.9 Hz).

2D perovskite thin films and single crystals

Materials. The synthesized organic salts were dried under high vacuum and were stored inside a nitrogen-filled glovebox. Lead(II) iodide (99.99%) was purchased from TCI Chemicals. Lead(II) bromide (99.998%) was purchased from Puratronic. Both lead salts were stored inside a nitrogen-filled glovebox. HBr (48% in water) was purchased from Fluorochem. HI (57% in water, distilled, unstabilized), tri-n-butyl phosphate (>99%), *N,N*-dimethylacetamide (99.5%, dried over molecular sieves) and propylene carbonate (99.5%) were purchased from Acros Organics; all other solvents were purchased from Fisher Scientific.

Thin films fabrication and characterization. Precursor solutions for thin-film synthesis were prepared by dissolving stoichiometric amounts of the corresponding lead halide and organic halide in a mixture of dry *N,N*-dimethylformamide (DMF) and dry *N,N*-dimethylacetamide (DMAc). The amounts are depicted in Table S1. The precursor elements were dissolved at 50 °C and the resulting solutions were filtered through a syringe filter (0.2 μm pore size). The precursor solutions were spin coated on top of quartz substrates, which had been sonicated in dimethyl sulfoxide, deionized water, acetone, and isopropanol respectively (15 min each) and had been treated by UV/ozone for 15 min. Spin coating and subsequent hotplate annealing were performed inside a nitrogen-filled glovebox (<1 ppm O_2, <1 ppm H_2O). Reference thin-films containing only the organic halide were spin coated by omitting the lead halide in the precursor and by drying at 80 °C after spin coating. The resulting perovskite thin-films were stored inside a nitrogen-filled glovebox and were only removed for analysis.

Table S1: Precursor compositions and spin coating conditions.

	Organic halide	Lead halide	Solvents	Spin coating	Annealing (10 min)
$(BTa)_2PbI_4$	0.30 M BTaI	0.15 M PbI_2	DMF/DMAc 9:1 volume ratio	2000 rpm; 2000 rpm s^{-1}; 20 s	120 °C
$(F_2BTa)_2PbI_4$	0.30 M F_2BTaI				
$(BTa)_2PbBr_4$	0.30 M BTaBr	0.15 M $PbBr_2$			130 °C
$(F_2BTa)_2PbBr_4$	0.30 M F_2BTaBr			4000 rpm; 4000 rpm s^{-1}; 20 s	

UV-vis-NIR absorption spectra were measured on a Cary 5000 UV-Vis-NIR spectrophotometer from Agilent Technologies. A cleaned quartz substrate was used as calibration background. Photoluminescence (PL) emission spectra were measured on a Horiba-Jobin Yvon Fluorolog-3 spectrofluorometer, equipped with double-grating excitation

and emission monochromators and a 450 W Xe lamp as a light source. The samples were excited at either 300 nm or 430 nm, which is specified in the relevant figure captions. X-ray diffraction (XRD) measurements were measured at ambient temperature and pressure on a Bruker D8 Discover diffractometer with CuK$_\alpha$ radiation.

Crystallization. Perovskite single-crystals were grown following the solvent conversion-induced crystallization method reported by Fateev *et al.*[1] Stoichiometric amounts of the organic halide and lead halide were dissolved in a mixture of propylene carbonate (PC), water, and HI (57% in water). HI was extracted three times with a 9:1 v/v mixture of chloroform and tri-*n*-butyl phosphate before use. Lead iodide-based mixtures were stirred at 50 °C and lead bromide-based mixtures were stirred at 40 °C until a clear solution was obtained. The solutions were then filtered through a syringe filter into a base-bath cleaned vial and were heated to their crystallization temperature. The vial lid was equipped with a needle to enable CO_2 to escape throughout the solvent degradation process. The exact precursor concentration, solvent mixture and crystallization temperature are summarized in Table S2. $(BTa)_2PbI_4$ and $(F_2BTa)_2PbI_4$ crystallized as orange needles (55% and 64% yield respectively); $(BTa)_2PbBr_4$ and $(F_2BTa)_2PbBr_4$ crystallized as colorless platelets (37% and 24% yield respectively).

Table S2: Summary of precursor compositions and crystallization temperatures.

	Organic halide	Lead halide	Solvents	Crystallization temperature
$(BTa)_2PbI_4$	0.29 M BTaI	0.15 M PbI_2	PC/H_2O/HI (57%) 1:1:0.2 molar ratio	50 °C (24 h)
$(F_2BTa)_2PbI_4$	0.60 M F_2BTaI	0.30 M PbI_2		40 °C (48 h)
$(BTa)_2PbBr_4$	0.17 M BTaBr	0.084 M $PbBr_2$	PC/H_2O/HBr (48%) 1:1:0.2 molar ratio	40 °C (24 h)
$(F_2BTa)_2PbBr_4$	0.11 M F_2BTaBr	0.057 M $PbBr_2$		30 °C (48 h)

X-ray intensity data of single crystals were collected at 100 K on a Rigaku Oxford Diffraction Supernova Dual Source (Cu at zero) diffractometer equipped with an Atlas CCD detector using ω scans and MoK$_\alpha$ (λ = 0.71073 Å) radiation. The images were interpreted and integrated with the program CrysAlisPro.[2] Using Olex2,[3] the structures were solved by direct methods using the ShelXT structure solution program and refined by full-matrix least-squares on F^2 using the ShelXL program package.[4,5] Non-hydrogen atoms were anisotropically refined

and the hydrogen atoms in the riding mode and isotropic temperature factors fixed at 1.2 times U(eq) of the parent atoms.

Crystal data for $(BTa)_2PbI_4$: $C_{16}H_{22}I_4N_8Pb$; MW = 1041.22; orthorhombic, space group *Pnma* (No. 62); a = 12.8383(2) Å, b = 29.6464(4) Å, c = 6.5400(1) Å, α = 90°, β = 90°, γ = 90°; V = 2489.19(6) Å³; Z = 4; ρ = 2.778 g cm⁻³; F(000) = 1872; R_gt = 0.0254 (3156 reflections), wR_ref = 0.0614 (3422 reflections).

Crystal data for $(F_2BTa)_2PbI_4$: $C_{16}H_{18}F_4I_4N_8Pb$; MW = 1113.18; orthorhombic, space group *Pnma* (No. 62); a = 12.8517(2) Å, b = 29.9017(5) Å, c = 6.57340(10) Å, α = 90°, β = 90°, γ = 90°; V = 2526.08(7) Å³; Z = 4; ρ = 2.927 g cm⁻³; F(000) = 2000; R_gt = 0.0210 (3025 reflections), wR_ref = 0.0432 (3350 reflections).

Crystal data for $(BTa)_2PbBr_4$: $C_{16}H_{22}Br_4N_8Pb$; MW = 853.22; monoclinic, space group *C2/c* (No. 15); a = 37.1774(5) Å, b = 5.71880(10) Å, c = 11.36340(10) Å, α = 90°, β = 97.1010(10)°, γ = 90°; V = 2397.44(6) Å³; Z = 4; ρ = 2.364 g cm⁻³; F(000) = 1584; R_gt = 0.0187 (3127 reflections), wR_ref = 0.0460 (3265 reflections).

Crystal data for $(F_2BTa)_2PbBr_4$: $C_{16}H_{18}Br_4F_4N_8Pb$; MW = 925.18; monoclinic, space group *P2₁/c* (No. 14); a = 18.6625(5) Å, b = 11.5643(3) Å, c = 11.5797(3) Å, α = 90°, β = 99.385(2)°, γ = 90°; V = 2465.67(11) Å³; Z = 4; ρ = 2.492 g cm⁻³; F(000) = 1712; R_gt = 0.0361 (4814 reflections), wR_ref = 0.0726 (6236 reflections)

CCDC 2228611-2228614 contain the supplementary crystallographic data for this paper. These data can be obtained free of charge from The Cambridge Crystallographic Data Centre *via* www.ccdc.cam.ac.uk/structures.

FAPbI₃ perovskite solar cells

Materials. The colloidal SnO₂ dispersion (Alfa Aesar), [6,6]-phenyl-C₆₁-butyric acid (PCBA), PbI₂ (TCI Chemicals, 99.99%), formamidinium iodide (FAI) (GreatCell Solar, >99.99%), methylammonium chloride (MACl) (GreatCell Solar, >99.99%), 2,2',7,7'-tetrakis[*N,N*-di(4-methoxyphenyl)amino]-9,9'-spirobifluorene (Spiro-OMeTAD) (Lumtec), tert-butylpyridine (Sigma, 98%), lithium bis(trifluoromethanesulfonyl)imide (Li-TFSI) (Sigma-Aldrich, 99.95% trace metal basis) and tris(2-(1H-pyrazol-1-yl)-4-tert-butylpyridine) cobalt(III) tri[bis(trifluoromethane) sulfonimide] (Co-TFSI) (Sigma, 98%), DMF (Sigma, anhydrous 99.8%), dimethyl sulfoxide (DMSO) (Sigma, anhydrous 99.9%), o-dichlorobenzene (Sigma, anhydrous 99%), and 2-propanol (Sigma, anhydrous 99.8%), were obtained from commercial sources as indicated and used without further purification.

Solution preparation. The SnO₂ colloidal dispersion was diluted with 5 parts H₂O. PCBA was dissolved in *o*-dichlorobenzene (0.2 mg mL⁻¹). PbI₂ (691.5 mg) was dissolved in DMF/DMSO 9:1 (v/v) (1 mL). FAI (90 mg) and MACl (9 mg) were dissolved in 2-propanol (1 mL). BTaX solutions were prepared by dissolving the salts in 2-propanol at concentrations of 1 or 10 mg mL⁻¹. Li-TFSI and Co-TFSI were dissolved in acetonitrile at concentrations of 500 mg mL⁻¹. Spiro-OMeTAD (40 mg) was dissolved in *o*-chlorobenzene (0.5 mL) to which tert-butylpyridine

(14.3 µL) and Li-TFSI in acetonitrile (8.8 µL) were added, followed by addition of Co-TFSI in acetonitrile (10 µL) just before spin coating.

Device fabrication. ITO was sputtered onto glass substrates with a thickness of 90 nm. Substrates were then cleaned by sonication in acetone (15 min), and sodium dodecyl sulfate (99%, Acros) soapy water (15 min), rinsed with deionized water, and then sonicated again in 2-propanol (15 min). Before spin coating, substrates were treated with UV-ozone for 30 min. SnO_2 was spin coated at 2800 rpm for 60 s with 2000 rpm s^{-1} acceleration and annealed at 150 °C for 30 min. ITO/SnO_2 substrates were then transferred to an N_2-filled glovebox after treating them with UV-ozone for 15 min. PCBA was spin coated at 2000 rpm for 30 s with 2000 rpm s^{-1} acceleration and no annealing. PbI_2 was spin coated at 1500 rpm for 30 s with 3000 rpm s^{-1} acceleration and annealed at 70 °C for 1 min. After cooling down, FAI/MACl were spin coated onto PbI_2 layer at 2000 rpm for 30 s with 20,000 rpm s^{-1} acceleration and annealed at 150 °C for 1 min. The passivation layer was dynamically spin coated at 5000 rpm for 45 s. Afterwards, substrates were brought in ambient air and annealed at 150 °C for 15 min. Spiro-OMeTAD was spin coated at 2000 rpm for 50 s with 20,000 rpm s^{-1} acceleration. No annealing was performed. The layers were then doped in air for 20 min. 10 nm MoO_3 and 100 nm Au were thermally evaporated in high vacuum. 100 nm MgF_2 was thermally evaporated on the glass side as anti-reflective coating.

J-V and EQE characterization. A tungsten-halogen lamp combined with a daylight filter (Hoya LB120) and a UV-filter (Schott GG385) were used to simulate the solar spectrum. The light intensity was calibrated *via* a Si photodiode. The solar cell area was defined by a black shadow mask with an aperture of 0.0676 cm^2 or 0.1296 cm^2. *J–V* measurements were performed with a Keithley 2400 source meter to sweep the voltage from –0.5 V (1.5 V) to 1.5 V (–0.5 V) at a scan rate of 0.25 V s^{-1} in both reverse and forward scan. Stability measurements were performed in an N_2-filled glovebox by keeping the devices at the maximum power point voltage under 1-sun illumination and tracking the photocurrent over time. For EQE measurements, a modulated (Oriel, Cornerstone 130) tungsten-halogen lamp (Philips Focusline, 50 W) was used light source. The signal was amplified *via* a current preamplifier (Stanford Research, SR 570) and measured by a lock-in amplifier (Stanford Research, SR 830). Based on a calibrated silicon reference cell, the EQE is then calculated from the spectral response signal. An additional 530 nm LED (Thorlabs) was used to generate a photocurrent in the solar cell during the EQE measurement, which is close to the current measured during *J–V* measurements, to mimic 1-sun condition.

Quasi-Fermi Level Splitting. Absolute photoluminescence spectroscopy was performed using a 455 nm LED (Thorlabs, M455F3-455 fiber coupled LED) source to excite the perovskite film through an optical fiber placed in an integrating sphere (Avantes, AvaSphere-30-REFL) fitted with a 550 nm short-pass filter (Edmund Optics). The excitation intensity was calibrated to 1-sun equivalent intensity. The spectrum was measured through an optical fiber connected to a calibrated AvaSpec-HERO spectrometer (Avantes, AVASPEC- HSC1024X58TEC-EVO) using a 550 nm long-pass filter.

PL characterization. PL spectra were recorded by using an Edinburgh Instruments FLSP920 double-monochromator luminescence spectrophotometer.

X-Ray characterization. XRD patterns were recorded by using a Bruker 2D phaser (CuK$_\alpha$ radiation, $\lambda = 1.5406$ Å): measurements were performed in the range 3-40° with a step size 0.02° and collection time of 1 s. 2D GIWAXS measurements were performed with a Ganesha 300XL+ system from JJ X-ray equipped with a Pilatus 300K detector (pixel side 172 µm × 172 µm). The X-ray source was a Genix 3D Microfocus sealed tube X-ray Cu-source with integrated monochromator. The wavelength used was 1.5408 Å. The detector is in a vacuum chamber with sample-to-detector distance (SDD) of 515.4 mm, as calibrated using silver behenate ($d_{001} = 58.380$ Å). The angle-dependent 2D GIWAXS was conducted *via* controlling incidence angle from 0.1° to 0.5° with 0.1° interval. XPS measurements were performed using a Thermo Scientific K-Alpha with a 180° double focusing hemispherical analyzer and a 128-channel detector. Monochromatic Al Kα (1486.6 eV) radiation was used, and the X-ray spot size was 400 µm. For the surface analysis, a survey spectrum was first measured for 12 scans with a pass energy of 200 eV. High-resolution scan (20 times) of each element was conducted with a pass energy of 50 eV. During the sputtering experiment, the sample was removed layer-by-layer by argon ion etching operated at low current and low ion energy (1000 eV). The sputtering speed corresponds to 0.012 nm s^{-1}. The crater region generated by argon ions is $\sim 2 \times 4$ mm^2. For the depth profiles, snapshot mode was used for each element, and the number of frames was 5×1 s. For the depth profile of N 1*s*, high-resolution scans were used instead of snapshots (20 scans).

SEM and CL characterization. SEM images for Figure S10-11 were measured with a FEI Quanta 3D FEG microscope (5 keV electron beam, secondary electron detector). CL hyperspectral maps from SEM were acquired in an Attolight Allalin 4027 Chronos in continuous wave mode. Spectra were acquired with an iHR320 spectrometer (focal length of 320 mm, 150 gratings per mm blazed at 500 nm, 7000 µm entrance slit) coupled to an Andor 1024 px charge-coupled device (readout rate of 50 kHz, and 4× signal amplification). Measurements were performed at room temperature under a high vacuum. To prevent specimen damage before the measurement, beam focusing was performed away from the areas of interest. All maps were acquired at 3 kV acceleration voltage, 62.5 pA beam current, at 128x128 px resolution in 5.5-µm field of view and 23.8 ms/px acquisition time. These conditions were found to be the optimum balance between electron beam damage and spatial resolution. SE images were acquired after the hyperspectral mapping, at 1024×1024 px resolution and 10 µs/px dwell time. CL maps were background subtracted, processed, and analyzed in LumiSpy 0.2.[6] The artefacts caused by cosmic rays saturating the spectrometer were removed, and the edges of each map were cropped out as they tend to show edge effects and higher CL intensities. Energy bandpass-filtered images were formed by integrating CL intensity over specific energy ranges.

7.9 REFERENCES

[1] M. Kim, G. H. Kim, T. K. Lee, I. W. Choi, H. W. Choi, Y. Jo, Y. J. Yoon, J. W. Kim, J. Lee, D. Huh, H. Lee, S. K. Kwak, J. Y. Kim, D. S. Kim, *Joule* **2019**, *3*, 2179.
[2] G. Yang, H. Zhang, G. Li, G. Fang, *Nano Energy* **2019**, *63*, 103835.
[3] Y. Liu, S. Akin, A. Hinderhofer, F. T. Eickemeyer, H. Zhu, J. Seo, J. Zhang, F. Schreiber, H. Zhang, S. M. Zakeeruddin, A. Hagfeldt, M. I. Dar, M. Grätzel, *Angew. Chem. Int. Ed.* **2020**, *59*, 15688.
[4] T. A. S. Doherty, S. Nagane, D. J. Kubicki, Y.-K. Jung, D. N. Johnstone, A. N. Iqbal, D. Guo, K. Frohna, M. Danaie, E. M. Tennyson, S. Macpherson, A. Abfalterer, M. Anaya, Y.-H. Chiang, P. Crout, F. S. Ruggeri, S. Collins, C. P. Grey, A. Walsh, P. A. Midgley, S. D. Stranks, *Science* **2021**, *374*, 1598.
[5] H. Lu, Y. Liu, P. Ahlawat, A. Mishra, W. R. Tress, F. T. Eickemeyer, Y. Yang, F. Fu, Z. Wang, C. E. Avalos, B. I. Carlsen, A. Agarwalla, X. Zhang, X. Li, Y. Zhan, S. M. Zakeeruddin, L. Emsley, U. Rothlisberger, L. Zheng, A. Hagfeldt, M. Grätzel, *Science* **2020**, *370*, DOI 10.1126/science.abb8985.
[6] T.-S. Su, F. T. Eickemeyer, M. A. Hope, F. Jahanbakhshi, M. Mladenović, J. Li, Z. Zhou, A. Mishra, J.-H. Yum, D. Ren, A. Krishna, O. Ouellette, T.-C. Wei, H. Zhou, H.-H. Huang, M. D. Mensi, K. Sivula, S. M. Zakeeruddin, J. V. Milić, A. Hagfeldt, U. Rothlisberger, L. Emsley, H. Zhang, M. Grätzel, *J. Am. Chem. Soc.* **2020**, *142*, 19980.
[7] Z. Su, C. Wang, G. Zheng, X. Gao, *Coatings* **2021**, *11*, 545.
[8] J. J. Yoo, G. Seo, M. R. Chua, T. G. Park, Y. Lu, F. Rotermund, Y.-K. Kim, C. S. Moon, N. J. Jeon, J.-P. Correa-Baena, V. Bulović, S. S. Shin, M. G. Bawendi, J. Seo, *Nature* **2021**, *590*, 587.
[9] M. Jeong, I. W. Choi, E. M. Go, Y. Cho, M. Kim, B. Lee, S. Jeong, Y. Jo, H. W. Choi, J. Lee, J.-H. Bae, S. K. Kwak, D. S. Kim, C. Yang, *Science* **2020**, *369*, 1615.
[10] J. Jeong, M. Kim, J. Seo, H. Lu, P. Ahlawat, A. Mishra, Y. Yang, M. A. Hope, F. T. Eickemeyer, M. Kim, Y. J. Yoon, I. W. Choi, B. P. Darwich, S. J. Choi, Y. Jo, J. H. Lee, B. Walker, S. M. Zakeeruddin, L. Emsley, U. Rothlisberger, A. Hagfeldt, D. S. Kim, M. Grätzel, J. Y. Kim, *Nature* **2021**, *592*, 381.
[11] H. Min, M. Kim, S.-U. Lee, H. Kim, G. Kim, K. Choi, J. H. Lee, S. I. Seok, *Science* **2019**, *366*, 749.
[12] H. Min, D. Y. Lee, J. Kim, G. Kim, K. S. Lee, J. Kim, M. J. Paik, Y. K. Kim, K. S. Kim, M. G. Kim, T. J. Shin, S. Il Seok, *Nature* **2021**, *598*, 444.
[13] S. Shao, M. A. Loi, *Adv. Mater. Interfaces* **2020**, *7*, 1901469.
[14] A. Fakharuddin, L. Schmidt-Mende, G. Garcia-Belmonte, R. Jose, I. Mora-Sero, *Adv. Energy Mater.* **2017**, *7*, 1700623.
[15] F. Zhang, S. Y. Park, C. Yao, H. Lu, S. P. Dunfield, C. Xiao, S. Uličná, X. Zhao, L. Du Hill, X. Chen, X. Wang, L. E. Mundt, K. H. Stone, L. T. Schelhas, G. Teeter, S. Parkin, E. L. Ratcliff, Y.-L. Loo, J. J. Berry, M. C. Beard, Y. Yan, B. W. Larson, K. Zhu, *Science* **2022**, *375*, 71.
[16] Y.-W. Jang, S. Lee, K. M. Yeom, K. Jeong, K. Choi, M. Choi, J. H. Noh, *Nat. Energy* **2021**, *6*, 63.
[17] H. Zhu, Y. Liu, F. T. Eickemeyer, L. Pan, D. Ren, M. A. Ruiz-Preciado, B. Carlsen, B. Yang, X. Dong, Z. Wang, H. Liu, S. Wang, S. M. Zakeeruddin, A. Hagfeldt, M. I. Dar, X. Li, M. Grätzel, *Adv. Mater.* **2020**, *32*, 1907757.
[18] P. Chen, Y. Bai, S. Wang, M. Lyu, J. Yun, L. Wang, *Adv. Funct. Mater.* **2018**, *28*, 1706923.
[19] S. Sidhik, Y. Wang, M. De Siena, R. Asadpour, A. J. Torma, T. Terlier, K. Ho, W. Li, A. B. Puthirath, X. Shuai, A. Agrawal, B. Traore, M. Jones, R. Giridharagopal, P. M. Ajayan, J. Strzalka, D. S. Ginger, C. Katan, M. A. Alam, J. Even, M. G. Kanatzidis, A. D. Mohite, *Science* **2022**, *377*, 1425.
[20] P. Gao, A. R. Bin Mohd Yusoff, M. K. Nazeeruddin, *Nat. Commun.* **2018**, *9*, 5028.
[21] X. Li, J. M. Hoffman, M. G. Kanatzidis, *Chem. Rev.* **2021**, *121*, 2230.

[22] Y. Liu, S. Akin, L. Pan, R. Uchida, N. Arora, J. V. Milić, A. Hinderhofer, F. Schreiber, A. R. Uhl, S. M. Zakeeruddin, A. Hagfeldt, M. Ibrahim Dar, M. Grätzel, *Sci. Adv.* **2019**, *5*, eaaw2543.
[23] Y. Yang, Z.-G. Zhang, H. Bin, S. Chen, L. Gao, L. Xue, C. Yang, Y. Li, *J. Am. Chem. Soc.* **2016**, *138*, 15011.
[24] J. Min, Z.-G. Zhang, S. Zhang, Y. Li, *Chem. Mater.* **2012**, *24*, 3247.
[25] K. Du, Q. Tu, X. Zhang, Q. Han, J. Liu, S. Zauscher, D. B. Mitzi, *Inorg. Chem.* **2017**, *56*, 9291.
[26] W. T. M. Van Gompel, R. Herckens, M. Mertens, P. H. Denis, B. Ruttens, J. D'Haen, K. Van Hecke, L. Lutsen, D. Vanderzande, *ChemNanoMat* **2021**, *7*, 1013.
[27] P.-H. Denis, M. Mertens, W. T. M. Van Gompel, K. Van Hecke, B. Ruttens, J. D'Haen, L. Lutsen, D. Vanderzande, *Chem. Mater.* **2021**, *33*, 5177.
[28] O. Yaffe, A. Chernikov, Z. M. Norman, Y. Zhong, A. Velauthapillai, A. van der Zande, J. S. Owen, T. F. Heinz, *Phys. Rev. B* **2015**, *92*, 045414.
[29] K. Schötz, A. M. Askar, W. Peng, D. Seeberger, T. P. Gujar, M. Thelakkat, A. Köhler, S. Huettner, O. M. Bakr, K. Shankar, F. Panzer, *J. Mater. Chem. C* **2020**, *8*, 2289.
[30] T. P. A. Pol, K. Datta, M. M. Wienk, R. A. J. Janssen, *Adv. Opt. Mater.* **2022**, *10*, 2102557.
[31] W. Peng, J. Yin, K. T. Ho, O. Ouellette, M. De Bastiani, B. Murali, O. El Tall, C. Shen, X. Miao, J. Pan, E. Alarousu, J. H. He, B. S. Ooi, O. F. Mohammed, E. Sargent, O. M. Bakr, *Nano Lett.* **2017**, *17*, 4759.
[32] N. Kitazawa, *Mater. Sci. Eng. B* **1997**, *49*, 233.
[33] S. A. Fateev, A. A. Petrov, A. A. Ordinartsev, A. Y. Grishko, E. A. Goodilin, A. B. Tarasov, *Chem. Mater.* **2020**, *32*, 9805.
[34] W. T. M. Van Gompel, R. Herckens, K. Van Hecke, B. Ruttens, J. D'Haen, L. Lutsen, D. Vanderzande, *ChemNanoMat* **2019**, *5*, 323.
[35] J. Wang, K. Datta, C. H. L. Weijtens, M. M. Wienk, R. A. J. Janssen, *Adv. Funct. Mater.* **2019**, *29*, 1905883.
[36] D. W. DeQuilettes, S. M. Vorpahl, S. D. Stranks, H. Nagaoka, G. E. Eperon, M. E. Ziffer, H. J. Snaith, D. S. Ginger, *Science* **2015**, *348*, 683.

Summary

Hybrid organic-inorganic, three dimensional (3D) perovskites are a promising material for optoelectronic devices, such as solar cells. With power-conversion efficiencies reaching >25% and >33% for single- and multi-junctions, respectively, this semiconductor technology will likely continue its path towards commercialization.

Two-dimensional (2D) and quasi-2D perovskites have also attracted a great deal of interest because of their higher stability, compared to the traditional, 3D counterpart, and their passivation properties. Solar cells fabricated with quasi-2D perovskites have recently reached power-conversion efficiencies above 21%. The path towards high efficiency photovoltaic devices based on this material is widely discussed in Chapter 2, with a review of the state-of-the-art and an analysis of additive and molecular engineering techniques used for this purpose.

The higher complexity of the (quasi-)2D perovskite precursor solution leads to several crystallization pathways that can lead to a phenomenon of phase distribution, where multiple 2D, quasi-2D, and 3D perovskite phases are formed in the same film. Controlling phase distribution and achieving phase purity is considered one of the main obstacles preventing quasi-2D perovskites from being used in multijunction devices. In Chapter 3, the effect of co-solvents on such phase distribution is studied. It is found that the interaction between the co-solvent and the precursors can change their availability to react. As a result, understanding this interaction is crucial to control phase purity. By means of solvent engineering, films with sensibly higher phase purity are formed and solar cells with efficiency >11% are fabricated.

Phase-distributed quasi-2D perovskite films usually consist of lower-dimensional phases lying at the bottom of the film and 3D ones at the top. In Chapter 4, it is found that the gradient direction is dependent on the length of the alkyl chain when using *n*-alkylammonium spacers. For example, while a traditional 2D-3D graded quasi-2D perovskite is formed when using butylammonium, such gradient is reversed when using a longer cation, such as octyl- or dodecyl-ammonium. The crystallization of these films is studied via in-situ absorption during thermal annealing; here, it is found that crystallization starts at the liquid-N_2 interface as 3D perovskite when using short spacers, as commonly reported in the literature, and as quasi-2D perovskite when using a longer spacer.

The knowledge developed in Chapter 3 and 4 about phase-distributed perovskites is applied to study two different systems. In Chapter 5, a 2D-3D graded

perovskite film is used to increase the interfacial energy barrier between the highest-occupied molecular orbital (HOMO) of the hole-transport-layer (HTL) and the conduction band of the perovskite film in a photodiode. Such increase is proved to inhibit interfacial thermal charge generation and to drastically decrease the dark current of the photodiodes, reaching values of ~10^{-9} mA cm^{-2}. In Chapter 6, a phase-distributed mixed-halide quasi-2D perovskite film is used to investigate the phenomenon of halide segregation under illumination. 2D perovskite phases are found to be stable under illumination, while quasi-2D phases are susceptible, similar to 3D perovskites, to the formation of iodide- and bromide-rich phases when illuminated.

Finally, 2D perovskites are also commonly used as passivation layers in devices consisting of 3D perovskites as the main photo-absorber. In Chapter 7, a novel benzotriazole-based 2D perovskite interlayer is used to passivate defects on the surface of FAPbI$_3$. Such passivation effect, studied *via* both absolute photoluminescence and scanning-electron-microscopy cathodoluminescence, leads to devices of ~22% power-conversion efficiency. By careful characterization of the 2D/3D heterostructure, it is found that a non-uniform 2D perovskite layer onto FAPbI$_3$ is enough to reduce nonradiative recombination and improve the open-circuit voltage.

In summary, this work provides new insights into the crystallization of lower-dimensional perovskites, their peculiar phase distribution, and their integration in optoelectronic devices, such as solar cells or photodiodes.

Curriculum vitae

Alessandro Caiazzo was born on May 3rd, 1994, in Villaricca (Napoli), Italy. He obtained his bachelor's degree in Industrial Chemistry at the Università degli Studi di Napoli "Federico II" in 2016. During his studies, he researched CO_2 capture for carbon capture and storage applications. After that, he moved to Eindhoven University of Technology in 2017 to pursue a master's degree in Chemical Engineering and Chemistry with a specialization in Molecular Systems and Materials Chemistry. During his stay in Eindhoven, his research focused first on photoelectrocatalysis and then on 2D perovskite solar cells. He briefly joined ASML for an internship, where he investigated the effect of plasma on the lifetime of extreme ultraviolet mirrors. Still intrigued by 2D perovskites and driven by curiosity, he started a PhD on the use of lower dimensional perovskites for optoelectronic devices. The main results of his work are presented in this thesis.

List of publications

1. <u>A. Caiazzo</u>, A. Maufort, B. van Gorkom, W. Remmerswaal, J. Orri, J. Li, J. Wang, W. van Gompel, K. Van Hecke, G. Kusch, R. Oliver, C. Ducati, L. Lutsen, M. Wienk, S. Stranks, D. Vanderzande, R. Janssen (2023). 3D Perovskite Passivation with a Benzotriazole-Based 2D Interlayer for High Efficiency Solar Cells. *ACS Applied Energy Materials*, 6, 3933.
2. K. Datta*, <u>A. Caiazzo</u>*, M. Hope, J. Li, A. Mishra, M. Cordova, Z. Chen, L. Emsley, M. Wienk, R. Janssen (2023). Light Induced Halide Segregation in 2D and Quasi-2D Mixed-Halide Perovskites. *ACS Energy Letters*, 8, 1662.
3. <u>A. Caiazzo</u> and R. Janssen (2022). High Efficiency Quasi-2D Ruddlesden-Popper Perovskite Solar Cells. *Advanced Energy Materials*, 12, 2202830.
4. R. Ollearo*, <u>A. Caiazzo</u>*, J. Li, M. Fattori, A. van Breemen, M. Wienk, G. Gelinck, R. Janssen (2022). Multidimensional Perovskites for High Detectivity Photodiodes. *Advanced Materials*, 34, 2205261.
5. <u>A. Caiazzo</u>, K. Datta, J. Jiang, M. Gélvez-Rueda, J. Li, R. Ollearo, J. Vicent-Luna, S. Tao, F. Grozema, M. Wienk, R. Janssen (2021). Effect of Co-Solvents on the Crystallization and Phase Distribution of Mixed-Dimensional Perovskites. *Advanced Energy Materials*, 11, 2102144.
6. <u>A. Caiazzo</u>, K. Datta, M. Wienk, R. Janssen. Impact of Alkyl Chain Length on the Formation of Regular- and Reverse-Graded Quasi-2D Perovskite Thin Films. *In Preparation.*
7. H. Bin, J. Li, <u>A. Caiazzo</u>, M. Wienk, Y. Li, R. Janssen (2023). Preparation of Efficient Organic Solar Cells Based on Terpolymer Donors via Monomer-Ratio Insensitive Side-Chain Hybridization Strategy, *ChemSusChem*, e202300006.

* = shared first authorship

List of conference contributions

1. Multidimensional Perovskites for High Detectivity Photodiodes, *MRS Spring*, San Francisco, 2022 (*Oral Presentation – Best Onsite Student Talk*)
2. Crystallization Mechanism of Regular- and Reverse-Graded Quasi-2D Perovskites, *MRS Spring*, San Francisco, 2022 (*Oral Presentation*)
3. A Novel Benzotriazole-Based 2D Interlayer for Passivation of $FAPbI_3$ Solar Cells, *MRS Spring*, San Francisco, 2022 (*Poster Presentation*)
4. 2D-3D Graded Perovskites: from Film Formation to Optoelectronic Devices. Strain and 2D Perovskites, *NanoGe Online Conference*, 2022 (*Invited Speaker*)
5. Halide Segregation in Ruddlesden-Popper Perovskites, *Next-Generation V+PV Materials*, Groningen, 2022 (*Oral Presentation*)
6. Effect of Co-Solvents on the Crystallization and Phase Distribution of Quasi-2D Perovskites, *Next Generation V+PV Materials*, Groningen, 2022 (*Poster Presentation)*
7. Halide Segregation in Ruddlesden-Popper Perovskites, *MRS Spring*, Honolulu, 2022 (*Poster Presentation*)
8. Exploiting Perovskites Multidimensionality for High Performance Photodiodes, *MRS Spring*, Honolulu, 2022 (*Oral Presentation*)
9. Effect of Co-Solvents on the Crystallization and Phase Distribution of Quasi-2D Perovskites, *MRS Fall*, Boston, 2021 (*Oral Presentation*)

Acknowledgments

Thank you to whoever shared the path with me, even for a little bit. To René, for always showing me a fresh perspective and for your patient dedication. To Martijn, for teaching me how things work in the lab. To the committee members, for giving time to the defense and for reading my thesis. To Kunal, my Jim when I decided to be a Dwight. To Simone, for almost giving up your agenda and for the wonderful camping experience in California. To Ludo, for teaching me how to climb and for being there when I needed it. To Olivera, for being Olivera. To Nicolas, for your enthusiasm for my pizzas. To Lana, for keeping up with my craziness. To Junke, for teaching me how to be an independent researcher. To Tom and Bas, for being such a good sport. To Guus, for the raspberry brownies. To Daniël, for the memes. To Bruno, for being a man of principles and for not trying pastel de nata with Nutella. To Willemijn, for making me understand that I will never want to renovate a house. To Xiao, for your contagious energy. To Haijun, for the delicious Chinese food. To Riccardo, for being my Pizza Lab fellow. To Bruno and Ediz, for your dedication in your master's project. To Laura, for tolerating Salvini-inspired lo-fi music in the office. To Nick, for the crazy dog story. To Wietse, for being so Stefan. To Niels, for the fun questions during M_2N meetings. To Arthur, for bringing organic salts all the way from Belgium. To Maria, for the transient absorption all-day measurements in Delft. To Michael, for not believing in my poster at MRS Spring, which led to solid-state NMR experiments. To Junyu, for the numerous GIWAXS measurements. To Aida and Giorgio, for bringing some of Napoli to Eindhoven. To Federica, for being the sister I've never had. To Giandomenico, for the "oh nous" moments. To the Powerpuff girls, for the first beautiful times in Eindhoven. To George, for a lot of games that were life-sharing moments. To Markella, for being such a caring friend. To my brother, for his outstanding generosity. To my mum and dad – I don't know how you managed. And finally, to me, for writing this whole thesis without completely losing it. That's it, folks.